



Numerical study of fractional topological insulators

Cécile Repellin

► To cite this version:

Cécile Repellin. Numerical study of fractional topological insulators. Physics [physics]. Ecole normale supérieure - ENS PARIS, 2015. English. NNT : 2015ENSU0028 . tel-01229027v2

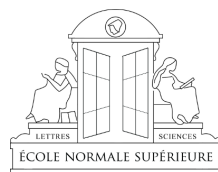
HAL Id: tel-01229027

<https://theses.hal.science/tel-01229027v2>

Submitted on 2 Oct 2017

HAL is a multi-disciplinary open access archive for the deposit and dissemination of scientific research documents, whether they are published or not. The documents may come from teaching and research institutions in France or abroad, or from public or private research centers.

L'archive ouverte pluridisciplinaire **HAL**, est destinée au dépôt et à la diffusion de documents scientifiques de niveau recherche, publiés ou non, émanant des établissements d'enseignement et de recherche français ou étrangers, des laboratoires publics ou privés.



THÈSE DE DOCTORAT

en vue de l'obtention du grade de

Docteur

de l'École Normale Supérieure

Spécialité : **PHYSIQUE**

préparée au **Laboratoire Pierre Aigrain**

dans le cadre de l'école doctorale **Physique en Ile-de-France**

préparée et soutenue publiquement par

Cécile REPELLIN

le 25 Septembre 2015

Titre :

Numerical study of fractional topological insulators

Directeur de thèse : Nicolas REGNAULT

Jury :

<i>Présidente :</i>	Anna MINGUZZI
<i>Rapporteurs :</i>	David CARPENTIER Didier POILBLANC
<i>Examineurs :</i>	Karyn LE HUR Sylvain NASCIMBÈNE
<i>Directeur de thèse :</i>	Nicolas REGNAULT

Remerciements

Je souhaite d'abord remercier les membres du jury pour leur participation à mon jury de thèse et pour leurs questions et commentaires. Je remercie Didier Poilblanc et David Carpentier d'avoir accepté d'être rapporteurs de ce manuscrit, Karyn Le Hur et Sylvain Nascimbène d'avoir joué le rôle d'examineurs, et Anna Minguzzi d'avoir présidé ce jury de thèse.

Je souhaite témoigner ma profonde reconnaissance envers Nicolas Regnault qui a encadré ma thèse avec autant d'exigence que de bienveillance. J'ai bénéficié de sa très grande disponibilité, que ce soit pour discuter des questions physiques les plus philosophiques ou des détails techniques les plus pointus. Ces discussions m'ont appris énormément sur les phases topologiques et sur les méthodes numériques qui permettent de les étudier, et contribuaient toujours à raviver ma curiosité et ma motivation. Je souhaite remercier Nicolas de m'avoir poussée à me dépasser, à faire preuve de toujours plus de ténacité et de rigueur, et de m'avoir offert l'opportunité de rencontrer de nombreux physiciens de par le monde. Merci aussi pour les digressions culinaires, politiques et musicales, les discussions sur la différence entre vanille de Madagascar et de Tahiti, et pour m'avoir fait partager le goût de la cuisine.

Une grande partie de ma thèse s'est déroulée à l'université de Princeton, et cela a été une chance unique pour moi d'être plongée dans cet environnement si stimulant. Cette opportunité a été rendue possible par les efforts conjoints de Nicolas et d'Andrei Bernevig, que je souhaite remercier ici. Je voudrais en particulier exprimer toute ma gratitude à l'égard d'Andrei pour avoir permis ces séjours, et pour l'intérêt qu'il a porté à mes projets. Collaborer avec lui a été une expérience très riche d'enseignement.

À Princeton, j'ai également beaucoup travaillé avec Titus Neupert, que je souhaite remercier ici. Travailler avec Titus a été un grand plaisir, ainsi qu'une belle expérience scientifique qui se poursuivra selon toute vraisemblance dans le futur.

Je remercie également Antoine Sterdyniak, avec qui j'ai partagé un bureau pendant quelques temps, un directeur de thèse, de nombreuses discussions scientifiques, et tant de bons moments. Je souhaite remercier Antoine pour le travail réalisé ensemble, mais aussi et surtout pour son soutien et son amitié.

Durant ma thèse, j'ai eu l'occasion de collaborer avec plusieurs autres personnes que je souhaite remercier ici. Je remercie Zlatko Papic pour nos discussions, en particulier durant la première année de ma thèse, et pour la collaboration qui en a découlé. Je remercie Karyn Le Hur, Benoit Douçot et Tianhan Liu de m'avoir invitée à contribuer à un projet original sur la physique du modèle de Kitaev-Heisenberg, ce qui m'a permis de découvrir un sujet nouveau. Je remercie Joseph Maciejko pour nos discussions sur la phase de Kalmaryer-Laughlin, ainsi que Benoit Estienne pour ses explications sur les liens entre théorie conforme et effet Hall quantique fractionnaire. Je remercie également Dan Arovas d'avoir suggéré un système d'étude de l'effet Hall fractionnaire 4D, et pour sa collaboration sur le sujet. Enfin, je remercie Yang-Le Wu qui m'a fait bénéficier de son expérience des isolants de Chern fractionnaires, et

Tom Iadecola pour nos discussions sur les isolants topologiques fractionnaires.

Je souhaite remercier Jean-Marc Berroir, le directeur du laboratoire Pierre Aigrain pour son accueil au laboratoire, et ses conseils avisés. Je remercie également Anne Matignon et Fabienne Renia, les administratrices du laboratoire Pierre Aigrain, ainsi que Toni Sarchi, côté Princeton, pour avoir facilité les procédures administratives durant ma thèse. Je remercie Rémy Portier et Yann Collin, les informaticiens du département de physique de l'ENS, d'avoir sauvé les données et redémarré à plusieurs reprises les machines dont je dépendais si cruellement, alors que je me trouvais de l'autre côté de l'Atlantique.

Ces années de thèse ont été enrichies de belles rencontres, et d'amitiés durables, dont certaines ont déjà été évoquées. J'ai trouvé au laboratoire Pierre Aigrain une ambiance particulièrement chaleureuse, et je voudrais ici en remercier les acteurs, et en particulier les doctorants et post-doctorants du laboratoire. Je remercie Matthieu, représentant exemplaire des doctorants, qui est toujours présent dès qu'il s'agit de donner un coup de main, de détendre l'atmosphère avec une blague de son cru, ou de discuter des joies et frustrations de la thèse. Merci aussi à Raphaël, tous les deux m'ont soutenue pendant les moments stressants de la rédaction, alors qu'eux-mêmes étaient dans la même galère, et c'était un plaisir que de pouvoir simplement traverser le couloir pour discuter avec eux. Merci à Sarah, pour sa bonne humeur et son énergie, ainsi qu'à Loic, Udson, Feihu, Armand, Anais, Omblin, Adrien, Laure, Quentin, Arthur, je leur souhaite à tous beaucoup de courage pour la suite et beaucoup de réussite. Merci aussi aux plus anciens, qui n'ont pas manqué de transmettre l'esprit LPA aux nouvelles générations de thésards: merci en particulier à Antoine, Kenneth, Michele, Pierrick, Jean, Camille, Simon, Benjamin, Fabien.

Merci à tous ceux qui ont partagé mon quotidien pendant ces années de thèse. Merci aux colloqs et aux colloqs d'adoption, aux amis qu'il était si bon de retrouver lors de mes passages en France. Merci en particulier à ceux qui m'ont offert un toit pendant mes séjours à Paris. Merci à mon frère, qui m'a accueillie tout naturellement de nombreuses fois, merci à Charlotte, Hugo, Clélia, Émilien, Florent, Sylvain, Guilhem, Grégoire, merci aussi à Jérémy, Mélanie, Tom, Thomas, Manon, Phil. Merci à Virginie et aux trois charmantes têtes blondes avec qui j'ai eu le plaisir de partager des repas dans une ambiance familiale. Merci aux amis Princetoniens, qui m'ont tant apporté. Merci au trio de la casa Godfrey, avant tout. Merci à Jess pour tous ses encouragements, pour les footings du petit matin et les bent spoons du soir, merci à Shell, avec qui je referais bien à nouveau le monde dans notre maison en carton qui n'existera bientôt plus, merci à Leenoy, Andras, Alessandra, Kevin, Jack, Margaret, David, merci aux woos, merci aux grimpeurs.

Merci enfin à mes parents, pour leur soutien sans faille et leur confiance.

Résumé

Les isolants topologiques sont des isolants qui ne peuvent être différenciés des isolants atomiques que par une grandeur physique non locale appelée invariant topologique. L'effet Hall quantique – et son équivalent sans champ magnétique, l'isolant de Chern – sont des exemples d'isolant topologique. En présence d'interactions fortes, des excitations exotiques appelées anyons peuvent apparaître dans les isolants topologiques. L'effet Hall quantique fractionnaire (EHQF) est la seule réalisation expérimentale connue de ces phases.

Dans ce manuscrit, nous étudions numériquement les conditions d'émergence de différents isolants topologiques fractionnaires. Nous nous concentrons d'abord sur l'étude de l'E HQF sur le tore. Nous introduisons une méthode de construction projective des états E HQF les plus exotiques, complémentaire par rapport aux méthodes existantes. Nous étudions les excitations de basse énergie sur le tore de deux états E HQF, les états de Laughlin et de Moore-Read. Nous proposons des fonctions d'ondes pour les décrire, et vérifions leur validité numériquement. Grâce à cette description, nous caractérisons les excitations de basse énergie de l'état de Laughlin dans les isolants de Chern. Nous démontrons également la stabilité d'autres états de l'E HQF dans les isolants de Chern, tels que les états de fermions composites, Halperin et NASS. Nous explorons ensuite des phases fractionnaires sans équivalent dans la physique de l'E HQF, d'abord en choisissant un modèle dont l'invariant topologique a une valeur plus élevée, puis en imposant au système la conservation de la symétrie par renversement du temps, ce qui modifie la nature de l'invariant topologique.

Mots-clés:

effet Hall quantique, isolant topologique, isolant de Chern, anyon, fractionalisation

Abstract

Topological insulators are band insulators which are fundamentally different from atomic insulators. Only a non-local quantity called topological invariant can distinguish these two phases. The quantum Hall effect is the first example of a topological insulator, but the same phase can arise in the absence of a magnetic field, and is called a Chern insulator. In the presence of strong interactions, topological insulators may host exotic excitations called anyons. The fractional quantum Hall effect is the only experimentally realized example of such phase.

In this manuscript, we study the conditions of emergence of different types of fractional topological insulators, using numerical simulations. We first look at the fractional quantum Hall effect on the torus. We introduce a new projective construction of exotic quantum Hall states that complements the existing construction. We study the low energy excitations on the torus of two of the most emblematic quantum Hall states, the Laughlin and Moore-Read states. We propose and validate model wave functions to describe them. We apply this knowledge to characterize the excitations of the Laughlin state in Chern insulators. We show the stability of other fractional quantum Hall states in Chern insulators, the composite fermion, Halperin and NASS states. We explore the physics of fractional phases with no equivalent in a quantum Hall system, using two different strategies: first by choosing a model with a higher value of the topological invariant, second by adding time-reversal symmetry, which changes the nature of the topological invariant.

Keywords:

quantum Hall effect, topological insulator, Chern insulator, anyon, fractionalization

List of publications

Fractional Chern Insulators beyond Laughlin states

Tianhan Liu, C. Repellin, B. Andrei Bernevig, N. Regnault
Phys. Rev. B 87, 205136 (2013)

Series of Abelian and Non-Abelian States in $C > 1$ Fractional Chern Insulators

A. Sterdyniak, C. Repellin, B. Andrei Bernevig, N. Regnault
Phys. Rev. B 87, 205137 (2013)

The single mode approximation to the fractional quantum Hall effect on the torus and fractional Chern insulators

C. Repellin, T. Neupert, Z. Papic, N. Regnault
Phys. Rev. B 90, 045114 (2014)

\mathbb{Z}_2 fractional topological insulators in two dimensions

C. Repellin, B. Andrei Bernevig, N. Regnault
Phys. Rev. B 90, 245401 (2014)

Projective construction of the \mathbb{Z}_k Read-Rezayi fractional quantum Hall states and their excitations on the torus geometry

C. Repellin, T. Neupert, B. Andrei Bernevig, N. Regnault
Phys. Rev. B 92, 115128 (2015)

Contents

Introduction	xi
1 Single-particle physics of topological insulators	1
1.1 The integer quantum Hall effect	2
1.1.1 Experimental observation	2
1.1.2 Landau levels	5
1.1.3 Eigenstates in the torus geometry	10
1.1.4 Transport properties of a quantum Hall system	12
1.2 Chern insulators	14
1.2.1 Definitions for the lattice systems	15
1.2.2 Topological nature of the Hall conductance	17
1.2.3 Two microscopic models	20
1.2.4 Experimental realizations	25
1.3 Time reversal symmetric topological insulators	31
1.3.1 Introduction to the quantum spin Hall effect	32
1.3.2 Quantum spin Hall effect in HgTe-CdTe quantum wells	33
1.3.3 Protected helical edge states and \mathbb{Z}_2 invariant	37
2 Strongly interacting topological insulators	41
2.1 Fractional quantum Hall effect	42
2.1.1 Experimental observation and role of the interactions	42
2.1.2 Haldane pseudopotentials	44
2.1.3 The Laughlin wave function and its excitations	46
2.1.4 The composite fermion construction	51
2.1.5 The Moore-Read and Read-Rezayi states	53
2.2 Anyons and topological degeneracy	55
2.2.1 Abelian anyons in the fractional quantum Hall effect	55
2.2.2 Non-abelian anyons in the fractional quantum Hall effect	56
2.2.3 Topological degeneracy on the torus	58
2.2.4 Haldane's exclusion principle	62
2.3 Fractional Chern insulators	63
2.3.1 Motivations and challenges on the experimental side	63
2.3.2 Emergence of a fractional Chern insulator	64
2.3.3 Numerically identifying a Chern insulator phase	68
2.4 Entanglement spectroscopy for the fractional quantum Hall phases	70
2.4.1 Entanglement entropy	70
2.4.2 Particle entanglement spectrum	72
2.5 Exact diagonalization	74

3	The \mathbb{Z}_k Read-Rezayi states and their neutral excitations on the torus	77
3.1	Projective construction of the Read-Rezayi states	78
3.1.1	The bosonic Read-Rezayi states on the torus	78
3.1.2	Numerical challenges	80
3.1.3	The projective construction on genus 0 surfaces	81
3.1.4	The projective construction with a twist	83
3.2	Physics of the neutral modes	87
3.2.1	The collective excitation mode above the Laughlin state . . .	87
3.2.2	The neutral modes above the Moore-Read state	89
3.3	Neutral modes on the torus	89
3.3.1	Neutral mode above the Laughlin state on the torus	90
3.3.2	Neutral mode above the Moore-Read state on the torus . . .	94
4	Fractional Chern insulators beyond the Laughlin state	103
4.1	Magneto-roton mode above the Laughlin state	104
4.1.1	Identification of the neutral mode	104
4.1.2	Scaling of the gap above the Laughlin state	108
4.1.3	Writing a single mode approximation for fractional Chern insulators	109
4.1.4	Numerical benchmarking of the SMA for FCIs	111
4.2	Numerical observation of the composite fermion states in fractional Chern insulators	116
4.2.1	Microscopic model	117
4.2.2	Identifying the composite fermion states	117
4.2.3	Effect of a longer range interaction	121
4.3	Fractional Chern insulators with a Chern number $C > 1$	124
4.3.1	Chern insulators with $C > 1$ in the absence of interactions . .	124
4.3.2	Model $SU(C)$ fractional quantum Hall wave functions	127
4.3.3	Numerical study of some $C > 1$ fractional Chern insulators .	129
5	Fractional topological insulators with time-reversal symmetry	137
5.1	Microscopic model	138
5.1.1	One-body model	139
5.1.2	Coupling via the band structure	140
5.1.3	Form of the interaction	142
5.2	Phase diagram of a fractional topological insulator	145
5.2.1	Stability of the fractional phase at half filling with pseudospin conservation	145
5.2.2	Stability of the fractional phase at half filling without pseudospin conservation	150
5.3	Transition between the time-reversal symmetric FTI and the bilayer FCI	154
5.3.1	The bilayer fractional Chern insulator	154

5.3.2 Interpolation of the bilayer FCI and FTI phases	155
Conclusion	159
A Fourier transform of the density operator on the torus projected onto the lowest Landau level	161
B Factorization of the three-body contact interaction	163
Bibliography	169

Introduction

Categorizing and understanding the different phases of matter is one of the primary goals of physics. Actions as trivial as boiling a pot of water or watching ice melt in a glass provide us with the daily illustration of a phase transition. Even focusing on solids yields countless different phases. A solid can indeed be described by its magnetic properties, or its ability to conduct electricity, among other properties, which all come with many nuances. Condensed matter physics aims at understanding the properties of all different types of condensed phases (solids and liquids). Most often, these properties arise from the collective behavior of many atoms, and have no equivalent in few-particle systems. This illustrates the concept of emergence, whereby "the behavior of large and complex aggregates of elementary particles [...] is not to be understood in terms of a simple extrapolation of the properties of a few particles" [4]. The complexity originates in the interaction between individual constituents (electrons in many cases), and, at large scales, makes it extremely hard to derive any condensed matter property from first principles. To approach condensed matter problems, one thus most often relies on effective models and field theories.

Landau's theory of phase transitions is a paradigmatic example of such an effective theory of condensed matter. Within this framework, one can define a physical quantity called order parameter, whose mean value changes at the phase transition. For example, the net magnetization takes a non-zero value in a ferromagnetic state, and vanishes in the paramagnetic phase. A key property of Landau's order parameter is its local character: in our example, the magnetic nature of the phase is directly related to the fluctuations of the *local* magnetization at the microscopic level. The positive correlation of the local magnetization at two different points of the system define the presence of ferromagnetic order. The notion of order parameter is strongly tied to that of symmetry breaking. Indeed, a disordered system is invariant under a large set of continuous transformations, corresponding to a continuous symmetry group. Upon ordering, the system is no longer invariant under some of these transformations. In a ferromagnetic solid, for example, the non-zero net magnetization spontaneously breaks the rotational invariance of the system by choosing a privileged direction for the orientation of the magnetic moments. Landau's theory of symmetry breaking has been very successful at describing many types of phase transitions, such as the liquid-solid transition, or the transition from the ordinary conductor to the (BCS) superconductor.

The integer and fractional quantum Hall effects, respectively discovered in 1980 [83] and 1982 [162], both fall outside of this paradigm. These phases arise at low temperature when a gas of electrons is confined to two dimensions and subjected to a strong perpendicular magnetic field. In these conditions, an electric current traversing the sample provokes the apparition of an electric voltage in the perpendicular direction. Upon varying the strength of the magnetic field, the associated transverse conductivity – or Hall conductivity – forms plateaus while the

longitudinal conductivity vanishes. On each plateau, the Hall conductivity is equal to a rational (integer in the case of the integer quantum Hall effect) multiple of the quantum of conductance. The bulk of the system behaves like an insulator (characterized by a gap) but differs from an atomic insulator (defined as a solid where the electronic density is highly localized around each atom, with negligible electronic density in between atoms). In spite of this difference, no local measurement can make a distinction between the two phases. In other words, no local order parameter can be defined to distinguish them. However, a global parameter called a topological invariant can be used to characterize these phases. By definition, a topological invariant is a quantum number that can be computed in any gapped system (insulator), and is insensitive to the microscopic details of the system. It stays invariant for any adiabatic perturbation of the system, as long as this perturbation does not close the gap. A phase that is characterized by a non-trivial topological invariant is called a topological phase. In the case of the integer quantum Hall effect, the number of topologically protected edge modes is a topological invariant which is different on each conductivity plateau. It can be determined by a transport experiment, a non-local measurement. The atomic limit insulator is a trivial insulator, since any edge mode it may have can be gapped out.

The quantum Hall effect was the first example of a topological insulator. Recently, more topological insulators have been defined, and sometimes observed experimentally. First, it was predicted in 1988 [60] that phases analogous to the quantum Hall effect could be realized in the absence of a magnetic field. These phases, dubbed Chern insulators, are described by the same topological invariant (the Chern number) as the integer quantum Hall effect, and thus fall in the same universality class. They were observed experimentally for the first time in 2013 in solid state systems [32]. Due to the chirality of their edge modes, integer quantum Hall and Chern insulator systems break time reversal symmetry. The theoretical prediction in 2005-2006 [77, 23] (and subsequent experimental observation in 2007 [85, 84]) of topological insulators preserving this symmetry was a big step in this field. It opened the door to the realization of topological phases in other dimensions, since topological insulators preserving the time-reversal symmetry can also exist in three dimensions, unlike the quantum Hall effect. Moreover, imposing other symmetries on a system – such as charge conjugation or parity – allows to realize other types of topological phases. All non-interacting topological phases have been classified according to the number of spatial dimensions, and their preserved symmetries [145, 80].

Classifying the interacting topological phases is a much more complicated, open problem, which comes at the intersection of two of condensed matter most interesting fields: topological phases, and strongly correlated phases. The fractional quantum Hall effect is the first example of a topological phase where the strong interactions between electrons cause an entirely new topological phase to emerge. The various plateaus of the Hall conductivity attest to the existence of several such fractional phases. One of the most striking features of the fractional quantum Hall effect is the nature of its excitations, which behave like fractions of electrons, called

anyons. Indeed, their charge is a fraction of the electronic charge, and their exchange statistics is neither that of a boson nor that of a fermion. The wave function of a group of identical particles returns to itself up to a phase after two particles are exchanged. This phase is respectively 0 and π for bosons and fermions, but takes different values for anyons. For even more exotic anyons, called non-abelian anyons, the knowledge of each anyon's coordinates is not enough to specify the state of the system, and the form of the wave functions after successive exchanges depends on the order in which these exchanges are performed. The formation of anyons – a process sometimes called *fractionalization* – is accompanied by an extremely robust degeneracy of the ground state, which only depends on the genus of the surface, not on the details of its geometry. The expression *topological order* is often used to qualify a phase where fractionalization takes place. Besides their fascinating properties, non-abelian anyons could have potentially revolutionizing applications in the field of quantum computing. Indeed, as theorized by Kitaev [79], the quantum state formed by a system of non-abelian anyons could be used as a unit storage of information, or qubit. The exchange of two particles – a unitary operation – could be used as a logical gate to modify the state of this qubit. The fact that no local measurement can lift the system degeneracy guarantees that no local perturbation will change its state, and would constitute a protection against decoherence.

Fractional quantum Hall phases may host both abelian and non-abelian anyons. They are in fact the only credible candidate for the realization of these exotic excitations. Following the example of non-interacting topological phases, we can very well imagine that they are merely the representatives of some universality classes, and that analogous phases can be realized in other systems. In the absence of interactions, Chern insulators are extremely similar to the integer quantum Hall effect. When interactions are turned on, they are thus the primary candidates to realize topological order in a different setting. The absence of need for a magnetic field would make them more versatile materials for the engineering of electronic devices. In fact, shortly prior to the beginning of my PhD, several simple Chern insulator lattice models were proposed, and numerically shown to host the simplest of all fractional quantum Hall states [110, 146, 131], the Laughlin state. This fractional phase was dubbed fractional Chern insulator. In this context, several questions related to the realization of topologically ordered phases in the absence of a magnetic field arise.

The first natural question concerns the limits of the analogy between the fractional quantum Hall effect and its lattice realization in Chern insulators. Besides the Laughlin state, is it possible to realize other fractional quantum Hall states in a Chern insulator? It is particularly important to quantify the stability of these new phases, by identifying the lattice models in which they might arise, the form of the interaction that favors them, and the range of parameters that guarantee their stability. The stability of a phase is directly related to the nature of its low energy excitations, and this question should thus also be explored in FCIs. Non-abelian phases have been numerically identified in fractional Chern insulators, but mostly in the presence of rather unrealistic interactions [24, 166]. The question of

the realization of these phases in realistic lattice models is thus also extremely relevant. Also, can Chern insulators host entirely new phases, that have no fractional quantum Hall equivalent? Moving further away from the fractional quantum Hall physics, topological insulators with additional symmetries (such as time-reversal) offer a new ground for the exploration of strongly correlated topological phases, and we will try to identify some of these new phases. The results presented in this manuscript aim at offering a better understanding of these questions.

To explore the physics of topologically ordered phases, I relied on finite size calculations, which are necessary to assess the stability of a phase. In particular, I used exact diagonalization, which allows one to obtain the low energy spectrum and eigenstates of a Hamiltonian without making any assumptions on the nature of the ground state. This is particularly useful to assess the nature and stability of a phase, to avoid any bias towards the fractional phase or any competing phase. The drawback of this method is the limited sizes that can be reached using exact diagonalization. Drawing conclusions that hold in the thermodynamic limit from results obtained with very few particles ($N \simeq 10$) is the main difficulty of this method. In these conditions, one has to work with maximally symmetric systems, to reduce the dimension of the effective spaces to be diagonalized. As a result, I performed all of my numerical simulations in closed systems, which have the maximal symmetry. For a $2D$ lattice system, it means using periodic boundary conditions in both directions, to preserve the translation symmetries. Fortunately, fractional quantum Hall systems are known to have a short correlation length, allowing the observation of the signatures of these phases even in very small systems.

The physics of the fractional quantum Hall effect on the torus can be an extremely useful guide to the physics of fractional Chern insulators. We will see that not all Chern insulators can become fractional Chern insulators when interactions are turned on. It can therefore be insightful to clarify the properties of the fractional quantum Hall effect in the system where it appears in its purest, most stable form. The torus is an appropriate choice for many reasons: it is a closed surface and has a non-trivial genus 1. Most importantly, it has the same genus as a lattice system with periodic boundary conditions, the geometry that I used for all FCI numerical simulations. This point is crucial, since the physics of topologically ordered phases depends on few parameters but the genus of the surface. To explore the low energy excitations above the Laughlin state on the torus, I developed a generalization of the single mode approximation on the torus [138]. This approach [49, 50] describes the low energy excitations of a fractional quantum Hall state as some density modulations of the ground state. This study served mostly as a guide to replicate the single mode approximation in FCIs. Finding a realistic model for the realization of non-abelian excitations in a FCI is a complicated task, the completion of which goes beyond the scope of this manuscript. However, the projective construction [30] of the non-abelian quantum Hall states in a continuous system might be a promising first step. Indeed, as proposed in Refs. [128, 112, 139, 17, 119, 163, 183, 47, 99, 123], non-abelian order could emerge in bilayer systems thanks to this construction. It builds the non-abelian Read-Rezayi states of the fractional quantum Hall effect us-

ing the simpler Laughlin state as a building block. While the construction is well known on the sphere, difficulties arise on the torus. I realized that the projective construction was not complete in finite size on the torus, and participated in building the tools that would make it complete in the bosonic case [137]. I numerically implemented these new tools, and generated the trial states, so that they could be systematically compared to the states obtained from exact diagonalization. To that end, I wrote an optimized exact diagonalization code for the n -body contact interaction on the torus, which is the model interaction for the Read-Rezayi states. I used this code to generate the Read-Rezayi states on the torus, as well as all numerically accessible quasihole states, which allowed me to prove the validity and completeness of the construction. I also used this code to obtain the low energy excitations of the Moore-Read state, one of the states of the Read-Rezayi series. Representing this spectrum in a meaningful way allowed me to identify the low energy mode above the Moore-Read state as a single mode. I also showed that the trial states obtained using the single mode approximation were excellent approximations of these exact states.

Focusing on fractional Chern insulators, I first worked on the identification of the composite fermion states, which are fractional quantum Hall states different from the Laughlin state, in these models. Using the models that had already been identified as good hosts to the Laughlin state, I used exact diagonalization to find evidence of the composite fermion states in the low energy spectrum of these systems [98]. The comparison of the number of quasihole states of these phases to their number in the equivalent FQH system was a strong test for the recently developed mapping [24]. Entanglement spectroscopy [97, 153] – a numerical method to obtain information on the excited states using only the ground state – proved especially helpful to confirm the nature of the phase. I also performed an extensive numerical study of the Laughlin state on the ruby lattice Chern insulator model. I further developed and numerically implemented the method introduced in Ref. [89] to define tilted boundary conditions of the lattice. This method allows for a large freedom in the choice of the geometric aspect ratio of the system, a quantity that can greatly influence the value of the manybody gap. I used this method to show that even small systems have very little finite size effect, and thus justify the extrapolation of finite size results to the thermodynamic limit. Using this exact diagonalization study, I worked on generalizing the single mode approximation to fractional Chern insulators, thus providing insight into the nature of the low energy excitations of this phase. The dispersion relation of these low energy excitations was previously hidden in the incomplete information provided by the energy spectrum. After pointing out the similarities of fractional Chern insulators with the fractional quantum Hall effect, I worked on the fractional phases that were supported by Chern insulators with a Chern number larger than one [154]. In some conditions, these systems host phases that have no fractional quantum Hall effect analog. Some of these phases were not completely understood at the time, but prompted more analytical as well as numerical research [174, 176, 152] that unveiled their subtle properties.

Finally, I studied an interacting topological insulator where time-reversal sym-

metry is preserved. A simple model for such a system consists in gluing together two copies of a Chern insulator with opposite chiralities. By adding strong interactions in each copy, one can realize two Laughlin states with opposite chiralities. This system is trivially gapped, since the copies are decoupled, and the existence of a gap in the total system is guaranteed by the presence of a gap in each individual copy. I studied the influence of different types of coupling between the two copies on the stability of this phase [136]. I performed an extensive exact diagonalization study, and showed that the chosen model hosted a very robust phase, even more robust than the phase realized by gluing together two copies of the Laughlin state with the same chirality.

This manuscript is organized as follows. The first chapter introduces the physics of non-interacting topological insulators, focusing on the integer quantum Hall effect, Chern insulators, and topological insulators preserving time reversal symmetry. The second chapter is an introduction to the physics of strongly interacting topological phases. The third chapter focuses on the Read-Rezayi states of the fractional quantum Hall effect and their low energy excitations, as realized on the torus. The fourth chapter is devoted to fractional Chern insulators. The fifth chapter proposes a strongly interacting topological insulator model preserving the time reversal symmetry and analyses its stability. This manuscript is based on the five articles that I have contributed to [154, 138, 137, 98, 136]. The fifth chapter is solely based on Ref. [136], but the third and fourth chapters present different aspects of the remaining articles to provide a more unified perspective on the topics I have worked on.

Single-particle physics of topological insulators

Contents

1.1 The integer quantum Hall effect	2
1.1.1 Experimental observation	2
1.1.2 Landau levels	5
1.1.3 Eigenstates in the torus geometry	10
1.1.4 Transport properties of a quantum Hall system	12
1.2 Chern insulators	14
1.2.1 Definitions for the lattice systems	15
1.2.2 Topological nature of the Hall conductance	17
1.2.3 Two microscopic models	20
1.2.4 Experimental realizations	25
1.3 Time reversal symmetric topological insulators	31
1.3.1 Introduction to the quantum spin Hall effect	32
1.3.2 Quantum spin Hall effect in HgTe-CdTe quantum wells	33
1.3.3 Protected helical edge states and \mathbb{Z}_2 invariant	37

Condensed matter physics aims at understanding the ways in which matter organizes itself depending on the external conditions such as temperature, pressure, electric or magnetic field, etc. Gases, liquids, solids or magnets are some of the most commonly known phases of matter but a closer examination using the laws of quantum mechanics yields a multitude of other phases. Superconductors, Bose-Einstein condensates, charge density waves, antiferromagnets are among the many examples of phases that have been theoretically studied and experimentally observed in the twentieth century. All of these phases share a fundamental property: they can be understood using the concept of symmetry breaking introduced by Landau in the 1930s. This theory postulates that different phases of matter can be characterized by a local order parameter, which is invariant under the transformations of a given symmetry group. For instance, the density distribution in a liquid has a continuous rotational invariance, which is broken when the atoms order to form a solid.

The discovery of the integer quantum Hall effect shed light on a new type of phases, which could not be described within the theory of Landau symmetry breaking. The integer quantum Hall effect is indeed the first example of a topological

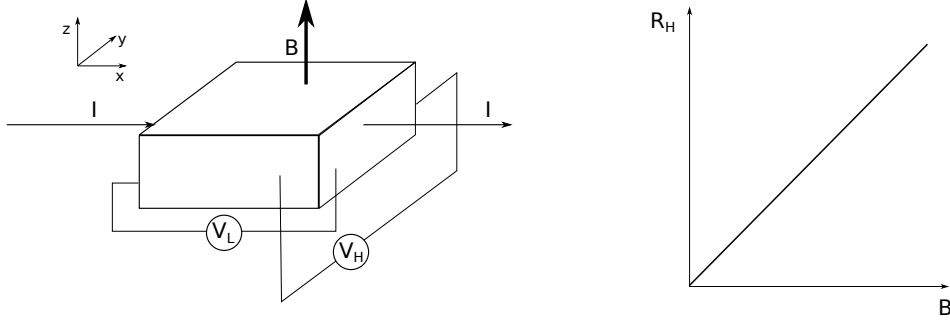


Figure 1.1: Basic setup for a Hall experiment. A voltage difference V_L is applied on the sample, resulting in current I . A magnetic field B applied along the z direction results in a voltage drop V_H in the direction transverse to the current I . The Hall resistance $R_H = V_H/I$ thus measured is proportional to the magnetic field.

phase, a phase that cannot be described by a local order parameter, but is rather defined by a topological invariant. The goal of this chapter is to introduce the physics of non-interacting quantum Hall systems, and to understand how it fits in the more general framework of phases that share the same topological invariant, the Chern number. I will also present its time-reversal equivalent, the quantum spin Hall effect, and show that it can be described by another type of topological invariant.

1.1 The integer quantum Hall effect

1.1.1 Experimental observation

In 1879, E. Hall discovered [63] that applying a magnetic field and an electric field on a conductor leads to a current perpendicular to these two fields. Conversely, applying a current I to a sample subjected to a magnetic field creates a transverse voltage drop V_H . Fig. 1.1 gives the basic experimental setup for this observation. This phenomenon now called the classical Hall effect can be entirely understood using classical mechanics: as it is accelerated through the sample by an electric field \mathbf{E} , an electron of charge $-e$ is subjected to the influence of the Lorentz force

$$\mathbf{F}_L = -e(\mathbf{E} + \mathbf{v} \times \mathbf{B}) \quad (1.1)$$

For transverse electric and magnetic fields $\mathbf{E} = E\mathbf{e}_x$ and $\mathbf{B} = B\mathbf{e}_z$ (see Fig. 1.1), it results, in stationary regime, in a drift velocity perpendicular to the current direction

$$\mathbf{v} = \frac{\mathbf{E} \times \mathbf{B}}{B^2} \quad (1.2)$$

The resulting Hall current density is $\mathbf{j} = -e\rho\mathbf{v}$ where ρ is the electronic density. Hence the Hall resistivity (which in two dimensions is equal to the resistance)

$$R_H = \rho_{xy} = \frac{E}{J_y} = -\frac{B}{\rho e} \quad (1.3)$$

Measuring the Hall resistance $R_H = V_H/I$ as shown in Fig. 1.1 is a convenient way to obtain the charge sign and density ρ of carriers, since R_H is proportional to these quantities. Thanks to this relation, the Hall effect enabled the discovery of holes as carriers in p -conducting semiconductors. To this day, using a Hall effect sensor is still one of the preferred ways to measure the amplitude of a magnetic field.

About a century after the discovery of E. Hall, in 1980, Von Klitzing et. al. [83] discovered that the electric response in a Hall experiment could drastically differ from the classical behavior in some specific conditions. When the geometry of the conducting sample is such that the electrons are confined to two dimensions, at very low temperature ($T < 4K$) and high magnetic field (a few tesla), the integer quantum Hall effect occurs: the Hall resistivity $\rho_{xy} = R_H$ is not proportional to the magnetic field, but rather quantized, forming plateaus at values $\frac{h}{pe^2}$, where p is an integer, and h is the Planck constant. Meanwhile, the longitudinal resistivity ρ_{xx} vanishes. The results of the experiment of Ref. [83] are shown in Fig. 1.2. It is also useful to define the conductivity tensor σ_{ij} , which is the inverse of the resistivity tensor ρ_{ij} . When the longitudinal resistivity vanishes, the Hall conductivity σ_{xy} is just the inverse of the Hall resistivity ρ_{xy} .

Realizing an integer quantum Hall effect experiment calls for the confinement of an electronic gas in two dimensions. Among the different implementations, this can be achieved by carefully growing (using molecular beam epitaxy – MBE) one type of semiconductor (GaAs) on top of another ($\text{Al}_x\text{Ga}_{1-x}\text{As}$). These two materials are chosen for their similar lattice constants, accompanied by slightly different band gaps. Upon doping, the electrons are trapped in the atomically thin interface between the two compounds, thus effectively creating a 2D gas of electrons.

The quantized value of the Hall resistivity is achieved with an extreme accuracy, to a degree that is unprecedented in condensed matter physics (a relative error of the order of 10^{-9} is observed [9, 39, 75, 70, 124]). This accuracy is so remarkable, that it is now used in metrology to define the fundamental unit of resistance, or Von Klitzing constant

$$R_K = \frac{h}{e^2} = 25.812806k\Omega \quad (1.4)$$

This value is independent of the device in which the integer quantum Hall effect occurs: it does not depend on the disorder or concentration of impurities in the sample. Nor does it depend on the material itself: the integer quantum Hall effect has been observed in materials as diverse as AlGaAs, GaN heterostructures, strained Si quantum wells in Si-SiGe heterostructures, and graphene. A quantity whose value does not depend on the microscopic details of the material is the physical definition of a well defined mathematical concept: the topological invariant. This point will be further detailed later in the manuscript.

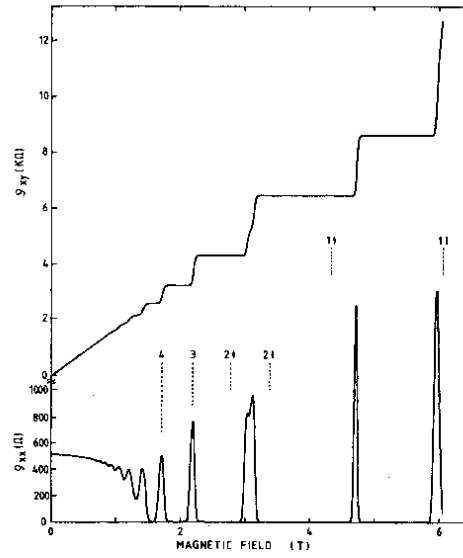


Figure 1.2: Results of the Von Klitzing experiment, reporting the discovery of the integer quantum Hall effect in Ref. [164]. The graph shows the evolution of the transverse resistivity $\rho_{xy} = R_H$ and of the longitudinal resistivity $\rho_{xx} = R_L = V_L/I$ as a function of the magnetic field. At low magnetic field, ρ_{xy} is proportional to B : this is the classical Hall effect. For higher fields, ρ_{xy} becomes quantized and ρ_{xx} vanishes.

1.1.2 Landau levels

1.1.2.1 Energy spectrum

The quantization of the Hall resistance, as well as its expression in terms of the Planck constant \hbar are clear signs that quantum mechanics is needed to explain the discovery of Von Klitzing *et. al.*. In this paragraph, we solve the Hamiltonian of a non-relativistic single electron confined in the (x, y) plane, in a transverse magnetic field $\mathbf{B} = B\mathbf{e}_z$. The Hamiltonian writes

$$H = \frac{1}{2m_e} (\hat{\mathbf{p}} + e\mathbf{A}(\hat{\mathbf{r}}))^2 \quad (1.5)$$

where m_e is the mass of the electron, $-e$ the charge of the electron, \mathbf{A} is the vector potential that generates the magnetic field $\mathbf{B} = \nabla \times \mathbf{A}(\hat{\mathbf{r}})$. $\hat{\mathbf{p}} = (\hat{p}_x, \hat{p}_y)$ and $\hat{\mathbf{r}} = (\hat{x}, \hat{y})$ are the conjugate momentum and position operators of the electron, that verify the canonical commutation relations

$$\begin{aligned} [\hat{x}, \hat{p}_x] &= i\hbar, & [\hat{x}, \hat{p}_y] &= 0 \\ [\hat{y}, \hat{p}_y] &= i\hbar, & [\hat{y}, \hat{p}_x] &= 0 \end{aligned} \quad (1.6)$$

For a uniform magnetic field, $\mathbf{A}(\mathbf{r})$ is a linear function of the particle coordinates. As a result of this spatial dependency, the momentum does not commute with the Hamiltonian, and the system is not translationally invariant. Additionally, $\hat{\mathbf{p}}$ is a gauge dependent operator (since $\mathbf{A}(\hat{\mathbf{r}})$ is defined up to a gauge choice). We define the operator

$$\mathbf{\Pi} = (\Pi_x, \Pi_y) = \hat{\mathbf{p}} + e\mathbf{A}(\hat{\mathbf{r}}) \quad (1.7)$$

which is a more physically relevant quantity, since it is proportional to the electron velocity, and thus gauge independent. In terms of the gauge independent momentum, the Hamiltonian simply writes

$$H = \frac{1}{2m_e} (\Pi_x^2 + \Pi_y^2) \quad (1.8)$$

The two components of $\mathbf{\Pi}$ have a non-vanishing commutator:

$$\begin{aligned} [\Pi_x, \Pi_y] &= e([\hat{p}_x, A_y] - [\hat{p}_y, A_x]) \\ &= e\left(\frac{\partial A_y}{\partial x}[\hat{p}_x, \hat{x}] + \frac{\partial A_y}{\partial y}[\hat{p}_x, \hat{y}] - \frac{\partial A_x}{\partial x}[\hat{p}_y, \hat{x}] - \frac{\partial A_x}{\partial y}[\hat{p}_y, \hat{y}]\right) \end{aligned} \quad (1.9)$$

where we have used the relation

$$[O_1, f(O_2)] = \frac{df}{dO_2} [O_1, O_2] \quad (1.10)$$

which is valid for any operators O_1, O_2 whose commutator is a number. Using Eq. (1.6), we find that

$$\begin{aligned}
 [\Pi_x, \Pi_y] &= -ie\hbar \left(\frac{\partial A_y}{\partial x} - \frac{\partial A_x}{\partial y} \right) \\
 &= -ie\hbar (\nabla \times \mathbf{A}) \cdot \mathbf{e}_z \\
 &= -ie\hbar B \\
 &= -i \frac{\hbar^2}{l_B^2}
 \end{aligned} \tag{1.11}$$

where we have introduced the magnetic length

$$l_B = \sqrt{\frac{\hbar}{eB}} \tag{1.12}$$

As a result, Π_x and Π_y are canonically conjugate operators, and the Hamiltonian Eq. (1.8) is that of a one-dimensional harmonic oscillator, where Π_x and Π_y play the respective roles of a standard oscillator's position and momentum operators. A convenient way to solve this Hamiltonian is to introduce ladder operators

$$a = \frac{l_B}{\hbar\sqrt{2}} (\Pi_x - i\Pi_y) \quad a^\dagger = \frac{l_B}{\hbar\sqrt{2}} (\Pi_x + i\Pi_y) \tag{1.13}$$

such that they obey the canonical commutation relation

$$[a, a^\dagger] = 1. \tag{1.14}$$

In terms of the ladder operators, the Hamiltonian writes

$$\begin{aligned}
 H &= \frac{\hbar^2}{m_e l_B^2} \left(a^\dagger a + \frac{1}{2} \right) \\
 &= \hbar\omega_c \left(a^\dagger a + \frac{1}{2} \right)
 \end{aligned} \tag{1.15}$$

where ω_c is the cyclotron frequency and writes

$$\omega_c = \frac{\hbar}{m_e l_B^2} \tag{1.16}$$

It follows that the eigenvalues of the Hamiltonian are those of the number operator $a^\dagger a$. The spectrum of the two-dimensional non-interacting electron gas in a magnetic field thus consists of a series of energy levels, all separated by the same energy gap $\hbar\omega_c$, called Landau levels, and labeled by a positive integer n

$$E_n = \hbar\omega_c \left(n + \frac{1}{2} \right) \tag{1.17}$$

The lowest energy level ($n = 0$) is also called lowest Landau level (LLL).

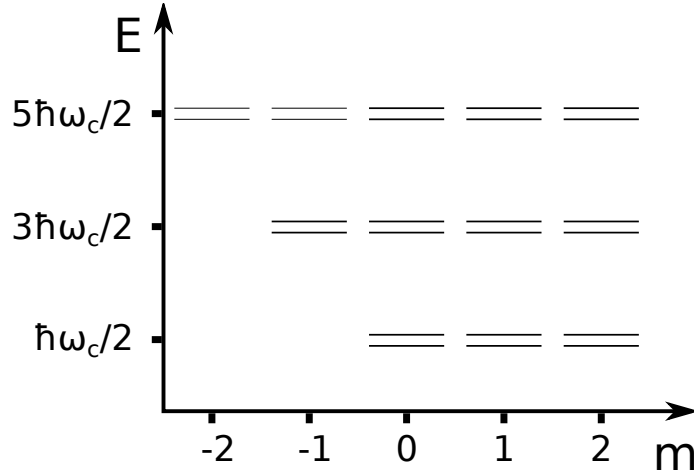


Figure 1.3: Energy spectrum of a non-interacting bidimensional gas of electrons immersed in a transverse magnetic field. The spectrum consists of perfectly flat, degenerate Landau levels. Each level is split into two due to the Zeeman effect. In the symmetric gauge (see Eq. (1.22)), the states in each Landau level are labeled with a positive integer m .

Note that we have omitted the Zeeman term in the Hamiltonian, which lifts the degeneracy between electrons of opposite spin:

$$H_Z = g\mu_B \mathbf{S} \cdot \mathbf{B} = -g\mu_B S_z B \quad (1.18)$$

where μ_B is the Bohr magneton, g is the Landé g -factor, and \mathbf{S} is the spin angular momentum of the electron. In GaAs, the value of the g -factor is $g \simeq -0.4$, causing a splitting of the Landau levels $\Delta E_Z \simeq 0.33B [T] K$, which is much smaller than the Landau level separation in this same material: $\hbar\omega_c \simeq 24B [T] K$. As a result, each Landau level will split into two bands with a given value of S_z , but the Landau levels will not mix due to the Zeeman effect. Note that this small energy splitting is actually increased by the interactions. The electronic many-body wave function must be antisymmetric, which can be achieved if the spatial part is antisymmetric (with a symmetric spin part of the wave function), or symmetric (in which case the spin part must be antisymmetric). Since a repulsive interaction is better screened by a spatially antisymmetric wave function, there is a tendency towards a ferromagnetic ordering, and double occupations correspond to a higher energy. The Zeeman gap is thus increased, with a corrective factor of the order of the Coulomb interaction

$$\frac{e^2}{\varepsilon l_B} \simeq 4.6\sqrt{B [T]} \quad (1.19)$$

The split Landau levels are represented in Fig. 1.3.

1.1.2.2 Degeneracy

Defining the ladder operators is enough to obtain the eigenvalues of the Hamiltonian, but it does not suffice to fully determine the quantum states. Indeed, the initial Hamiltonian (1.5) was written in terms of *two* commuting pairs of conjugate operators: \hat{x}, \hat{p}_x , and \hat{y}, \hat{p}_y . Eq. (1.15) uses only *one* such pair (a, a^\dagger), so there must be an additional pair of conjugate operators that commute with H , a and a^\dagger , and the Landau levels must be degenerate. In a similar manner to Eq. (1.7), we define the pseudo-momentum

$$\tilde{\Pi} = (\tilde{\Pi}_x, \tilde{\Pi}_y) = \hat{\mathbf{p}} - e\mathbf{A}(\hat{\mathbf{r}}) \quad (1.20)$$

whose components, while being separately gauge dependent, have canonical commutation relations:

$$[\tilde{\Pi}_x, \tilde{\Pi}_y] = i \frac{\hbar^2}{l_B^2} \quad (1.21)$$

$\tilde{\Pi}_x$ and $\tilde{\Pi}_y$ do not generally commute with Π_x, Π_y , and thus with the Hamiltonian. However, the treatment of the Hamiltonian was completely gauge independent until this point, and we can choose a gauge that fixes this issue. The mixed commutators $[\tilde{\Pi}_i, \Pi_j]$ vanish in the symmetric gauge, which is defined as:

$$\mathbf{A}_S(\hat{\mathbf{r}}) = \frac{B}{2} (-\hat{y}, \hat{x}, 0) \quad (1.22)$$

Thanks to the canonical commutation relation (1.21) of $\tilde{\Pi}_x$ and $\tilde{\Pi}_y$, we can define the new ladder operators similarly to those of Eq. (1.13)

$$b = \frac{l_B}{\hbar\sqrt{2}} (\tilde{\Pi}_x + i\tilde{\Pi}_y) \quad b^\dagger = \frac{l_B}{\hbar\sqrt{2}} (\tilde{\Pi}_x - i\tilde{\Pi}_y) \quad (1.23)$$

which again verify the canonical commutation relation $[b, b^\dagger] = 1$. Since the system is invariant under any rotation around the z axis, the z component of the angular momentum L_z is conserved, and commutes with the Hamiltonian. In terms of the number operators $a^\dagger a$ and $b^\dagger b$, it writes:

$$L_z = \hbar (a^\dagger a - b^\dagger b) \quad (1.24)$$

We can thus diagonalize H and L_z simultaneously. We call $-m\hbar$ the eigenvalue of L_z : m is an integer that can take any value superior to the opposite of the Landau level index $-n$ (see Fig. 1.3 for a representation of the energy levels as a function of n and m). In the symmetric gauge, the eigenstates of H are thus labeled with two integers n, m , and write:

$$|n, m\rangle = \frac{(b^\dagger)^{m+n}}{\sqrt{(m+n)!}} \frac{(a^\dagger)^n}{\sqrt{(n)!}} |0, 0\rangle \quad (1.25)$$

In the lowest Landau level, the wave functions write:

$$\phi_{0,m}(\mathbf{r}) = \langle \mathbf{r} | 0, m \rangle = \frac{z^m e^{-\frac{1}{4l_B^2} z \bar{z}}}{l_B^m \sqrt{2\pi 2^m m!}} \quad (1.26)$$

where $z = x - iy$ ¹ and $\bar{z} = x + iy$. In the lowest Landau level, apart from a Gaussian factor, the eigenstates of L_z and H are monomials in z . Any wave function can be written in this basis, and is thus a polynomial in z . The corresponding density only depends on the distance to the center r , and writes

$$\rho_m(r) = |\phi_{0,m}(r)|^2 = \frac{r^{2m} e^{-\frac{1}{2l_B^2} r^2}}{l_B^{2m} 2\pi 2^m m!} \quad (1.27)$$

The maximum density of probability for an electron in the orbital m of the symmetric gauge is along a circle of radius $\sqrt{2m}l_B$, and most of the electronic density is localized along this circle.

While the physical meaning of $\tilde{\Pi}$ is not obvious from the definition of Eq. 1.20, the pseudo-momentum has a semi-classical interpretation. Let us first express the position operator as a function of the gauge independent momentum and the pseudo-momentum, in the symmetric gauge:

$$\begin{aligned} \hat{y} &= \frac{\tilde{\Pi}_x}{eB} - \frac{\Pi_x}{eB} \\ \hat{x} &= -\frac{\tilde{\Pi}_y}{eB} + \frac{\Pi_y}{eB} \end{aligned} \quad (1.28)$$

The classical equation of motion for an electron in a magnetic field writes

$$m_e \ddot{\mathbf{r}} = -e \dot{\mathbf{r}} \times \mathbf{B} \quad (1.29)$$

We obtain the expression of the velocity by integrating this equation

$$\begin{aligned} \dot{x} &= -\omega_c (\hat{y} - Y) \\ \dot{y} &= \omega_c (\hat{x} - X) \end{aligned} \quad (1.30)$$

where $\mathbf{R} = (X, Y)$ are integration constants, and represent a constant of motion: it is the guiding center of the electron. Moreover, we know from Eq. (1.8) that the velocity can also be expressed as a function of the gauge independent momentum $\dot{\mathbf{r}} = \mathbf{\Pi}/m_e$. Consequently

$$\begin{aligned} \hat{y} &= Y - \frac{\Pi_x}{eB} \\ \hat{x} &= X + \frac{\Pi_y}{eB} \end{aligned} \quad (1.31)$$

¹One could easily absorb the minus sign in the definition of z by changing the sign of the magnetic field, to obtain the more conventional $z = x + iy$.

Comparing Eqs. (1.28) and (1.31), we immediately see that in the symmetric gauge, the pseudo-momentum is proportional to the guiding center coordinates

$$X = -\frac{\tilde{\Pi}_y}{eB} \quad Y = \frac{\tilde{\Pi}_x}{eB} \quad (1.32)$$

We can thus deduce the commutation relation of the coordinates of the guiding center from those of $\tilde{\Pi}_x$ and $\tilde{\Pi}_y$ (see Eq.(1.21)), associated with the corresponding Heisenberg inequality

$$[X, Y] = i l_B^2 \quad \Delta X \Delta Y \geq 2\pi l_B^2 \quad (1.33)$$

In a quantum Hall system, a quantum state thus occupies a minimal surface of $2\pi l_B^2$: in a given Landau level, the electron can never be fully localized. This inequality allows us to compute the number of states allowed on a given area \mathcal{A}

$$N_\phi = \frac{\mathcal{A}}{\Delta X \Delta Y} = \frac{\mathcal{A}}{2\pi l_B^2} = \frac{\mathcal{A}B}{h/e} \quad (1.34)$$

where h/e is the magnetic quantum flux unit, and $\mathcal{A}B$ is the magnetic flux through the surface \mathcal{A} . The number of states in a Landau level for a given surface is thus equal to the number of magnetic flux quanta that pierce this surface.

1.1.3 Eigenstates in the torus geometry

In the previous section, we derived the spectrum of a free electron confined in two dimensions in a magnetic field using a gauge-independent method, and introduced the symmetric gauge (1.22) so that we could define the ladder operators b, b^\dagger , and have a complete set of quantum numbers to determine the eigenstates. While very convenient for rotationally invariant systems, this treatment is more cumbersome for systems with a translational invariance. This is the case of many of the systems presented in this thesis: among the diverse two-dimensional systems that I have studied during my PhD, most have periodic boundary conditions. To reflect this orientation, I will derive here the wave function for a single electron on a rectangular torus spanned by the vectors $L_x \mathbf{e}_x$ and $L_y \mathbf{e}_y$, subjected to a magnetic field $B \mathbf{e}_z$.

The Landau gauge is the most convenient one for a system with translational invariance

$$\mathbf{A}_L(\hat{\mathbf{r}}) = B(0, -\hat{x}, 0) \quad (1.35)$$

In this gauge, the Hamiltonian (1.5) does not depend on the second position coordinate y , and the eigenvalue $\hbar k_y$ of the momentum operator \hat{p}_y is a good quantum number. The y -dependent part of the wave function is thus a plane wave $e^{ik_y y}$. We obtain the Hamiltonian of a one-dimensional harmonic oscillator:

$$H = \frac{1}{2m_e} \left(\hat{p}_x^2 + (-eB\hat{x} + \hbar k_y)^2 \right), \quad (1.36)$$

and the corresponding eigenfunction writes

$$\phi_{n,k_y}(x, y) = \mathcal{N}_n e^{ik_y y} e^{-\frac{1}{2l_B^2}(x - l_B^2 k_y)^2} H_n \left(\frac{x - l_B^2 k_y}{l_B} \right) \quad (1.37)$$

where n is the Landau level index, \mathcal{N}_n is a normalization constant, and H_n are Hermite polynomials.

The wave function (1.37) takes into account the periodicity of the system along the y direction, but not along the x direction: it is thus a valid wave function on the cylinder, but not on the torus. We now need to impose the periodic boundary conditions of the torus. Let us denote $T_{\mathbf{a}} = e^{i\mathbf{a}\cdot\hat{\mathbf{p}}}$ the operator that translates the electron by a vector \mathbf{a} in real space. The usual boundary conditions, defined in terms of $T_{\mathbf{a}}$, cannot be consistently enforced, because $T_{\mathbf{a}}$ does not commute with the Hamiltonian. Instead, we define the magnetic translation operator

$$\mathcal{T}_{\mathbf{a}} = e^{i\frac{e}{\hbar c}\mathbf{A}(\mathbf{a})\cdot\hat{\mathbf{r}}}T_{\mathbf{a}} \quad (1.38)$$

which verifies $[H, \mathcal{T}_{\mathbf{a}}] = 0$. The magnetic translation operators associated with different vectors \mathbf{a} and \mathbf{b} do not necessarily commute, but rather follow the Girvin-Platzmann-MacDonald [50] (GMP) algebra

$$[\mathcal{T}_{\mathbf{a}}, \mathcal{T}_{\mathbf{b}}] = -2 \sin\left(\frac{1}{2l_B^2}\mathbf{e}_z \cdot (\mathbf{a} \times \mathbf{b})\right) \mathcal{T}_{\mathbf{a}+\mathbf{b}} \quad (1.39)$$

This fundamental property of the quantum Hall effect can be seen as another manifestation of the impossibility to fully localize a wave function (see the uncertainty principle (1.33) concerning the guiding center coordinates). Indeed, $\mathcal{T}_{\mathbf{a}}$ can be interpreted as the operator that translates the guiding center by a vector \mathbf{a} . Note that $\mathbf{e}_z \cdot (\mathbf{a} \times \mathbf{b})$ is the area enclosed in the parallelogram (\mathbf{a}, \mathbf{b}) . The argument of the sine function in Eq. (1.39), which is equal to

$$\frac{\mathbf{e}_z \cdot (\mathbf{a} \times \mathbf{b}) B}{h/e} \pi \quad (1.40)$$

is the number of flux quanta enclosed in the parallelogram (\mathbf{a}, \mathbf{b}) times π . As a result, $\mathcal{T}_{\mathbf{a}}$ and $\mathcal{T}_{\mathbf{b}}$ commute as soon as the flux enclosed in (\mathbf{a}, \mathbf{b}) is an integer. Another interesting consequence of the GMP algebra is the Aharonov-Bohm phase that a single-particle wave function picks up when it goes around a loop. Eq. (1.38) implies that

$$\mathcal{T}_{\mathbf{a}}\mathcal{T}_{\mathbf{b}} = \mathcal{T}_{\mathbf{b}}\mathcal{T}_{\mathbf{a}}e^{-\frac{i}{l_B^2}\mathbf{e}_z\cdot(\mathbf{a}\times\mathbf{b})}. \quad (1.41)$$

For a closed cycle $\mathbf{ab}(-\mathbf{a})(-\mathbf{b})$, the product of magnetic translation operators thus writes

$$\mathcal{T}_{\mathbf{a}}\mathcal{T}_{\mathbf{b}}\mathcal{T}_{\mathbf{a}}^{-1}\mathcal{T}_{\mathbf{b}}^{-1} = e^{-\frac{i}{l_B^2}\mathbf{e}_z\cdot(\mathbf{a}\times\mathbf{b})} \quad (1.42)$$

The wave function of the electron thus picks up a phase equal to the magnetic flux enclosed by its path when it goes around a loop. Note that while these results were derived in specific gauges, they stay valid in any gauge because they only involve gauge invariant quantities.

After a translation of the electron around the full torus, the wave function may accumulate some phase. We want to impose that this phase does not depend on the order of translations along the two directions of the torus. This constraint imposes

$[\mathcal{T}_{L_x \mathbf{e}_x}, \mathcal{T}_{L_y \mathbf{e}_y}] = 0$. For a rectangular torus ($\mathbf{e}_x \cdot \mathbf{e}_y = 0$), this writes $\frac{B}{h/e} L_x L_y = N_\phi$, where N_ϕ is an integer. We recognize the unit flux quantum h/e in this equation: the number of flux quanta N_ϕ piercing the torus must be integer valued. We can write the previous equality in terms of the magnetic length, such that for a rectangular torus

$$L_x L_y = 2\pi N_\phi l_B^2 \quad (1.43)$$

The wave functions $\phi_{n,k_y}(x, y)$ of Eq. (1.37) do not respect the periodic boundary conditions in both directions, but can be recombined into states that do. We note Φ_{n,k_y} the eigenstates of both the Hamiltonian and the translation operators. Using the expression of the magnetic translation operator Eq. (1.38), this writes

$$\begin{aligned} \Phi_{n,k_y}(x, y) &= \mathcal{T}_{L_x \mathbf{e}_x} \Phi_{n,k_y}(x, y) = e^{iL_x y / l_B^2} \Phi_{n,k_y}(x + L_x, y) \\ \Phi_{n,k_y}(x, y) &= \mathcal{T}_{L_y \mathbf{e}_y} \Phi_{n,k_y}(x, y) = \Phi_{n,k_y}(x, y + L_y) \end{aligned} \quad (1.44)$$

The second equation imposes the quantization of the momentum quantum number: $k_y = \frac{2\pi}{L_y} \mathbf{k}_y$, where \mathbf{k}_y is an integer. To obey the first equation, it is necessary to make the wave function of Eq. (1.37) periodic. This writes

$$\Phi_{n,k_y}(x, y) = \mathcal{N}_n \sum_{m=-\infty}^{\infty} e^{i(l_B^2 k_y + m L_x) y / l_B^2} e^{-\frac{1}{2l_B^2} (l_B^2 k_y + m L_x - x)^2} H_n \left(\frac{l_B^2 k_y + m L_x - x}{l_B} \right) \quad (1.45)$$

where \mathcal{N}_n is a normalization constant. It is easy to see that \mathbf{k}_y and $\mathbf{k}_y + N_\phi$ yield the same wave function (the additional term can always be absorbed by shifting the sum index m by one). All the Landau levels thus have the same degeneracy N_ϕ on the torus. In the lowest Landau level ($n = 0$), $H_0 = 1$, and the wave functions are localized at positions $x = l_B^2 k_y$, with a gaussian decay, while being completely delocalized in the y direction.

1.1.4 Transport properties of a quantum Hall system

The discussion in Sec. 1.1.2 is the basis to understand the integer quantum Hall effect. Let us define the filling fraction ν , the number of occupied Landau levels (a non integer value of ν corresponds to partially filled Landau levels)

$$\nu = \rho \frac{h/e}{B} \quad (1.46)$$

where ρ is the density of electrons. It can also be expressed as a function of the total number of electrons in the sample N divided by the number of flux quanta piercing it

$$\nu = \frac{N}{N_\phi} \quad (1.47)$$

In terms of the filling fraction, the classical Hall conductance (see Eq. (1.3)) writes

$$R_H = \frac{h}{\nu e^2} \quad (1.48)$$

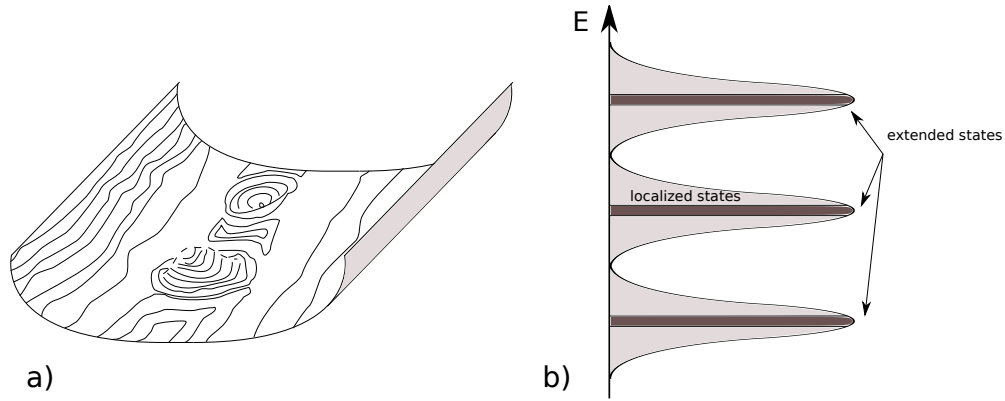


Figure 1.4: Effect of disorder on the quantum Hall effect. a) Schematic potential landscape for a finite sample with charged impurities. The equipotential lines are closed in the bulk (localized states), and open at the edge (extended states). b) Density of states in a disorder system. The degenerate Landau levels broaden into bands in the presence of disorder, with extended states in the center, separated by localized states.

The plateaus of the Hall resistivity observed experimentally correspond to ν integer, and thus to fully filled Landau levels. While this draws a connection between the plateaus and the energy levels, it does not explain the quantization of the resistivity when the Landau levels are partially filled. For that, it is essential to take into account the disorder that exists in any sample, as well as its finite extent.

Let us consider a semiconducting heterostructure – such as AlGaAs – that realizes a good approximation of a two dimensional electron gas. The potential landscape is not perfectly flat unlike what was implicitly assumed in Sec. 1.1.2. Fig. 1.4a represents the equipotential lines of a plausible potential landscape. First, there is a confinement potential associated with the finite extent of the sample. Also, the presence of charged impurities in the material creates potential hills (for negative impurities), as well as as potential valleys (for positive impurities). This space-dependent potential causes the Landau levels to widen. However, not all states within the broadened Landau levels contribute to the transport in the same way. The confinement potential, which is constant in the bulk, dramatically increases at the edge of the system. The equipotential lines reflect this behavior by staying open, connecting one end of the sample to the other. The edge states are thus delocalized (or extended), and contribute to the conductance. Due to the magnetic field, the edge states are chiral: the current flows in one direction on one edge of the sample, in the opposite direction on the opposite edge. In the bulk, however, most equipotential lines are closed, resulting in localized states that do not contribute to the electrical conductance of the sample. The gap that separates two Landau levels is thus filled with localized states, and called a mobility gap (see Fig. 1.4b). The chirality of the edge states can be understood using the semi-classical picture of an

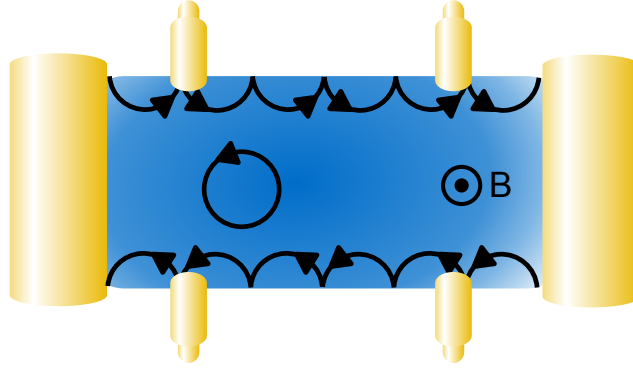


Figure 1.5: Semi-classical picture of the motion of an electron in a finite two-dimensional sample in a magnetic field. In the bulk, the electron goes around closed orbits and thus does not contribute to transport. At the edge, the confinement potential prevents the electron from undergoing a closed loop, resulting in a "bouncing" motion. The direction of the magnetic field imposes a counterclockwise loop, resulting in the chirality of the edge transport modes.

electron in a magnetic field performing skipping orbits at the edge, as depicted in Fig. 1.5. To explain the behavior of the Hall resistivity, let us consider a system with an integer filling fraction ν . As the electron density increases, more localized states become occupied, with no modification to the Hall conductance, until the extended states start filling up. The Hall conductance then increases linearly with the electron density, until the narrow band of extended states is completely filled, and the next plateau has been reached.

These arguments explain the qualitative behavior of the transverse and longitudinal conductivities σ_{xx} and σ_{xy} , but does not explain why the value of the Hall conductivity is so perfectly quantized to the same value in all systems. This latter phenomenon relies on the topological nature of the Hall conductance, which will be explored in the next section.

1.2 Chern insulators

In the previous section, I have explained the apparition of plateaus of the Hall conductivity σ_{xy} when a strong magnetic field is applied to a two-dimensional electron gas. While this argument is correct, it does not convey the topological character of σ_{xy} . In Ref. [158], Thouless, Kohmoto, Nightingale and den Nijs (TKNN) showed that the Hall conductance could be expressed as a function of an integer – the Chern number – independent of the details of the microscopic model, thus fitting the definition of a topological invariant. This insensitivity to microscopic details is the origin of the robust quantization of the Hall conductance mentioned in Sec. 1.1.1. This property makes the integer quantum Hall effect the first example of a topological phase, a phase not characterized by a local order parameter, but by

a topological invariant. As shown by Haldane [60] in 1988, the argument of TKNN can be generalized to systems that have a zero net magnetic field, but still break time-reversal symmetry (which a magnetic field does for free). This phenomenon – non-zero Hall conductance in the absence of Landau levels – is called anomalous quantum Hall effect, and appears in systems named Chern insulators. Chern insulators are band insulators, where one (or more) Bloch bands have a non-zero Chern number and play the role of Landau levels. They could potentially be observed in easier experimental conditions: since the cyclotron energy is proportional to the magnetic field B , both a high magnetic field and a very low temperature are required to observe the quantum Hall effect. Chern insulators, on the other hand, do not require any magnetic field, and could even be observed at high temperature if the band gap is large enough. Their first experimental observation in a solid state system is very recent: Ref. [32] reported the observation of the anomalous quantum Hall effect in magnetic insulators in 2013. Even more recently, they were engineered in cold atoms by a few independent groups [76, 2, 102].

In this section, I focus on lattice – rather than continuous – systems. I show that the Hall conductivity is related to a number that does not depend on the microscopic details of the system. This derivation constitutes a definition of the Chern number as a topological invariant. I give an interpretation of the Chern number as an obstruction to the Stokes theorem, which serves as a proof that the Chern number is an integer. I then describe two simple microscopic lattice models with a non-trivial topology, with and without a net magnetic flux through the lattice. Finally, I give two examples of the experimental observation of a Chern insulator, one in a solid state system, the other in a cold atom lattice.

1.2.1 Definitions for the lattice systems

1.2.1.1 Lattice Hamiltonian

We consider non-interacting electrons on a $N_x \times N_y$ two-dimensional translationally invariant lattice with m orbitals per unit cell. The only other constraint on the Hamiltonian is that it must have a band gap (the system is an insulator). We implement periodic boundary conditions, resulting in the quantization of the pseudo-momentum \mathbf{k} :

$$\mathbf{k} = (k_x, k_y) = \left(\frac{2\pi}{N_x} k_x, \frac{2\pi}{N_y} k_y \right), \quad k_x = 0, \dots, N_x - 1, \quad k_y = 0, \dots, N_y - 1 \quad (1.49)$$

Thanks to the discrete translational invariance, the Hamiltonian is block-diagonal in momentum space. It writes

$$H = \sum_{\mathbf{k}} c_{\mathbf{k},\alpha}^\dagger h^{\alpha\beta}(\mathbf{k}) c_{\mathbf{k},\beta} \quad (1.50)$$

where $c_{\mathbf{k},\alpha}^\dagger$ (respectively $c_{\mathbf{k},\alpha}$) creates (respectively annihilates) an electron in the orbital $\alpha = 1, \dots, m$, at momentum \mathbf{k} , and $h(\mathbf{k})$ is a $m \times m$ matrix (there is an

implicit summation on the orbital indexes α and β). Diagonalizing $h(\mathbf{k})$ gives us the dispersive bands of the Hamiltonian $\varepsilon_\mu(\mathbf{k})$, as well as the Bloch vectors $|\mu, \mathbf{k}\rangle$, where μ is the band index. The diagonalized Hamiltonian writes

$$H = \sum_{\mathbf{k}} \sum_{\mu=1}^m \varepsilon_\mu(\mathbf{k}) |\mu, \mathbf{k}\rangle \langle \mu, \mathbf{k}| \quad (1.51)$$

We call $|0\rangle$ the vacuum. $c_{\mathbf{k},\alpha}^\dagger |0\rangle$ is a state of momentum \mathbf{k} , localized on the atoms α of the lattice, while $|\mu, \mathbf{k}\rangle$ represents a state of momentum \mathbf{k} in the band μ . These two types of orbitals are related by the matrix $u(\mathbf{k})$, whose elements write

$$u_\mu^\alpha(\mathbf{k}) = \langle 0 | c_{\mathbf{k},\alpha} | \mu, \mathbf{k} \rangle \quad (1.52)$$

For each value of the band index μ , the vector $u_\mu(\mathbf{k})$ is an eigenvector of the matrix $h(\mathbf{k})$.

$$h(\mathbf{k})u_\mu(\mathbf{k}) = \varepsilon_\mu(\mathbf{k})u_\mu(\mathbf{k}) \quad (1.53)$$

1.2.1.2 Flat-band limit

The goal of this paragraph is to introduce a useful mathematical trick, the flat-band limit, which consists in flattening the bands of a dispersive Hamiltonian. By definition, the topological properties of the Hamiltonian do not depend on its energies, only its eigenstates. Thanks to this property, working in the flat-band limit does not affect the topological properties of the Hamiltonian.

We consider a system with a finite bulk gap, and place the Fermi level ε_F inside the insulating gap. We call p the number of filled bands, such that for all \mathbf{k} :

$$\varepsilon_1(\mathbf{k}) \leq \dots \leq \varepsilon_p(\mathbf{k}) < \varepsilon_F < \varepsilon_{p+1}(\mathbf{k}) \leq \dots \leq \varepsilon_m(\mathbf{k}) \quad (1.54)$$

We pick two arbitrary energies ε_G (for ground state) and ε_E (for excited) respectively below and above the Fermi level

$$\varepsilon_G < \varepsilon_F < \varepsilon_E \quad (1.55)$$

We are now equipped to define the interpolation of all energies below (respectively above) the Fermi level to ε_G (respectively ε_E), controlled by the interpolation parameter t :

$$E_\mu(\mathbf{k}, t) = \begin{cases} \varepsilon_\mu(\mathbf{k})(1-t) + \varepsilon_G t & 1 \leq \mu \leq p \\ \varepsilon_\mu(\mathbf{k})(1-t) + \varepsilon_E t & p+1 \leq \mu \leq m \end{cases} \quad (1.56)$$

It is crucial that the gap remain open throughout the interpolation procedure, as is that none of the energy bands cross the Fermi level for any t . The Hamiltonian interpolates between the original system of Eq. (1.51) and the flat-band system, but with unchanged eigenstates

$$\begin{aligned} H(t) &= \sum_{\mathbf{k}} h_t(\mathbf{k}) \\ h_t(\mathbf{k}) &= \sum_{\mu=1}^m E_\mu(\mathbf{k}, t) |\mu, \mathbf{k}\rangle \langle \mu, \mathbf{k}| \end{aligned} \quad (1.57)$$

The flat-band Hamiltonian corresponds to the $t = 1$ limit:

$$h_1(\mathbf{k}) = \varepsilon_G \underbrace{\sum_{\mu=1}^p |\mu, \mathbf{k}\rangle \langle \mu, \mathbf{k}|}_{P_G} + \varepsilon_E \underbrace{\sum_{\mu=p+1}^m |\mu, \mathbf{k}\rangle \langle \mu, \mathbf{k}|}_{P_E} \quad (1.58)$$

where we have defined two operators, P_G and P_E as the projectors onto the occupied and empty bands. As per their projectors nature, they verify the following properties:

$$P_G + P_E = I \quad P_G P_E = 0 \quad P_G^2 = P_G \quad P_E^2 = P_E \quad (1.59)$$

1.2.2 Topological nature of the Hall conductance

1.2.2.1 Hall conductivity and Chern number

The Hall conductance can be computed using the Kubo formula, in the framework of the linear response theory [111]. We consider a many-body Hamiltonian with eigenstates $|\Psi_n\rangle$ and associated eigenenergies E_n . For a non-interacting insulator at integer filling p , the ground state $|\Psi_0\rangle$ is obtained by writing the Slater determinant of all the states $|\mu, \mathbf{k}\rangle$ in the p lowest band, and is non-degenerate. The Hall conductance writes

$$\sigma_{xy} = \frac{ie^2\hbar}{L_x L_y} \sum_{n>0} \frac{\langle \psi_0 | \hat{v}_x | \psi_n \rangle \langle \psi_n | \hat{v}_y | \psi_0 \rangle - \langle \psi_0 | \hat{v}_y | \psi_n \rangle \langle \psi_n | \hat{v}_x | \psi_0 \rangle}{(E_0 - E_n)^2} \quad (1.60)$$

where $\mathbf{v} = (v_x, v_y)$ is the velocity operator. Using this formalism, TKNN [158] have shown that the Hall conductance can be expressed as the integral over the whole phase space of a vector field \mathbf{F} . In the case of a lattice system, the integral runs over the Brillouin zone. \mathbf{F} is called the Berry curvature and writes

$$\mathbf{F} \cdot \mathbf{e}_z := \frac{-i}{2\pi} \sum_{\mu=1}^p \left(\frac{\partial}{\partial k_x} \langle \mu, \mathbf{k} | \right) \left(\frac{\partial}{\partial k_y} | \mu, \mathbf{k} \rangle \right) - \left(\frac{\partial}{\partial k_y} \langle \mu, \mathbf{k} | \right) \left(\frac{\partial}{\partial k_x} | \mu, \mathbf{k} \rangle \right) \quad (1.61)$$

where the sum runs over all p occupied bands. It is remarkable that this quantity depends only on the Bloch states $|\mu, \mathbf{k}\rangle$, and not on their energies. The Berry curvature \mathbf{F} writes as the curl of a vector potential \mathbf{A}_B called the Berry potential

$$\mathbf{F} = \nabla \times \mathbf{A}_B \quad (1.62)$$

where the Berry potential writes

$$\mathbf{A}_B := \frac{-i}{2\pi} \sum_{\mu=1}^p \begin{pmatrix} \langle \mu, \mathbf{k} | \frac{\partial}{\partial k_x} | \mu, \mathbf{k} \rangle \\ \langle \mu, \mathbf{k} | \frac{\partial}{\partial k_y} | \mu, \mathbf{k} \rangle \\ 0 \end{pmatrix} \quad (1.63)$$

The Hall conductivity is thus the integral of the Berry curvature over the Brillouin zone, for all occupied bands.

$$\sigma_{xy} = \frac{e^2}{h} \int dk_x dk_y (\nabla \times \mathbf{A}_B) \cdot \mathbf{e}_z \quad (1.64)$$

This quantity does not depend on the energies of the system: the spectrum can be continuously deformed into a different one, as long as the band gap does not close in the process. In particular, the flat-band limit introduced in the previous paragraph can be used to compute the Hall conductivity, thus greatly simplifying the calculation [20]. If we allowed the gap to close, the Bloch states of the occupied bands would be able to mix with those of the excited bands, thus modifying the value of the Berry curvature. The integral in Eq. (1.64) is thus a topological invariant, called the Chern number.

1.2.2.2 Edge states of a Chern insulator

The relation of the Hall conductivity with a topological invariant explains the extremely precise quantization of σ_{xy} , which is measured to be exactly the same in diverse materials. Indeed, no perturbation (such as a disorder Hamiltonian) can change the value of the Chern number – as long as it does not close the bulk gap.

In the Landauer-Buttiker approach to transport, the quantization of σ_{xy} reveals that the transport occurs in C distinct chiral conduction channels, without any dissipation. The absence of dissipation indicates that backscattering is impossible in the edge states, which is due to the chirality of the edge states. Numerically, the simplest way to observe the edge states is to use the cylinder geometry. The cylinder has periodic boundary conditions in the x direction, such that the momentum quantum number k_x is still a good quantum number, but open boundary conditions in the y direction. The edge states are thus localized at both ends of the cylinder (see Fig. 1.6a). The typical spectrum of a Chern insulator is shown in Fig. 1.6b. It reveals that the two edge states traversing the bulk gap have opposite velocity, and are thus chiral. In the case of a trivial insulator, there are no edge states traversing the bulk gap (see Fig. 1.6c).

1.2.2.3 The Chern number as an obstruction to Stokes' theorem over the Brillouin zone

The Bloch wave functions in the filled band of an insulator have a $U(1)$ gauge degree of freedom. The topological character of a Chern band is characterized by the fundamental impossibility to define a smooth gauge throughout the whole Brillouin zone. We explore this obstruction in this paragraph by studying a generic two-orbital model, the simplest example of a band insulator. In such system, the vector $u_\mu(\mathbf{k})$ defined in Eq. (1.52) is two-dimensional. To remove the phase ambiguity, we choose the first component $u_\mu^0(\mathbf{k})$ to be real and positive. This choice only makes sense when u_μ^0 is non-zero, and we need to define an alternative gauge choice when this is not the case. At any point in the Brillouin zone, at least one of the vector components u_μ^0 or u_μ^1 must be non-zero. For any momentum \mathbf{k}_s such that $u_\mu^0(\mathbf{k}_s) = 0$, there is thus a vicinity of \mathbf{k}_s where $u_\mu^1(\mathbf{k}) \neq 0$. We regroup all such vicinities in one subset R_s^ε of the Brillouin zone:

$$R_s^\varepsilon = \{\mathbf{k} \in BZ \mid |\mathbf{k} - \mathbf{k}_s| < \varepsilon, u_\mu^0(\mathbf{k}_s) = 0, u_\mu^1(\mathbf{k}) \neq 0\} \quad (1.65)$$

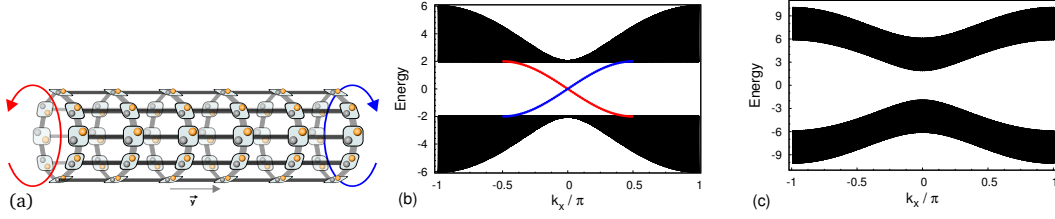


Figure 1.6: Chern insulator lattice system on a cylinder. a) The transport in a Chern insulator is due to the presence of edge states at both ends of the cylinder, represented by the blue and red arrows at either end of the cylinder. b) Band structure of a typical Chern insulator on the cylinder, represented as a function of the momentum k_x in the periodic direction. Two edge states with opposite chiralities connect the valence and conduction band of the bulk. The edge states are physically separated, and they respectively correspond to the blue and red edge states of a), with the same color code. c) Typical band structure of a trivial insulator on the cylinder. Note the absence of edge states.

where ε is the smallest radius of all vicinities. The gauge can be fixed to one convention on R_s^ε ($u_\mu^1(\mathbf{k})$ real and positive), and a different one on the rest of the Brillouin zone ($u_\mu^0(\mathbf{k})$ real and positive). More formally, this writes

$$\begin{cases} u_\mu^0(\mathbf{k}) \in \mathfrak{R}^+ & \text{if } \mathbf{k} \in BZ - R_s^\varepsilon \\ u_\mu^1(\mathbf{k}) \in \mathfrak{R}^+ & \text{if } \mathbf{k} \in R_s^\varepsilon \end{cases} \quad (1.66)$$

We are now set up with a zoning of the Brillouin zone, with one well defined Berry potential in each zone. On the boundary between the two zones, these potentials are related by a gauge transformation

$$\mathbf{A}_{R_s^\varepsilon} = \mathbf{A}_{BZ-R_s^\varepsilon} + \nabla\chi(\mathbf{k}) \quad (1.67)$$

where $\chi(\mathbf{k})$ is the phase that differentiates the vectors in the two regions

$$u_\mu(\mathbf{k})_{R_s^\varepsilon} = e^{i2\pi\chi(\mathbf{k})} u_\mu(\mathbf{k})_{BZ-R_s^\varepsilon} \quad (1.68)$$

We can now determine the Hall conductance (which, as an observable quantity, is gauge invariant) using the Stokes theorem in both domains (they have identical boundaries with opposite orientations):

$$\begin{aligned} \sigma_{xy} &= \frac{e^2}{h} \left(\int_{BZ-R_s^\varepsilon} \nabla \times \mathbf{A}_{BZ-R_s^\varepsilon} + \int_{R_s^\varepsilon} \nabla \times \mathbf{A}_{R_s^\varepsilon} \right) \\ &= \frac{e^2}{h} \oint_{\mathcal{O}} d\mathbf{k} \cdot (\mathbf{A}_{R_s^\varepsilon} - \mathbf{A}_{BZ-R_s^\varepsilon}) \end{aligned} \quad (1.69)$$

where \mathcal{O} is the oriented boundary of the R_s^ε zone. As a result, the Chern number is equal to

$$C = \oint_{\mathcal{O}} d\mathbf{k} \cdot \nabla\chi(\mathbf{k}) \quad (1.70)$$

The Bloch wave functions must be single-valued: they return to their initial value after a closed loop in the Brillouin zone. This property must be true in any gauge, which implies (using Eq. (1.68)) that $e^{i2\pi\chi}$ must return to its initial value after a loop. This writes:

$$\chi(\mathbf{k}^+) - \chi(\mathbf{k}^-) = n \quad (1.71)$$

where $\chi(\mathbf{k}^+)$ and $\chi(\mathbf{k}^-)$ are the values of $\chi(\mathbf{k})$ after and before going around the loop, and n is an integer, called the winding number of χ . Since the contour \mathcal{O} is made of one or more closed loops, the Chern number is the sum of all winding numbers around each loop of the contour \mathcal{O} , and is thus an integer.

More generically, the integral of the Berry potential on a given path \mathcal{P} is called the Berry phase.

$$\gamma_B = \int_{\mathcal{P}} \mathbf{A}_B \cdot d\mathbf{l} \quad (1.72)$$

For an adiabatic evolution in parameter space, the ground state of the Hamiltonian picks up a phase that is the sum of the dynamical phase $\frac{1}{\hbar} \int E(t)dt$ and the Berry phase γ_B . Per the above argument, the Berry phase for a closed path \mathcal{P} is gauge independent and an integer. For instance, the Aharonov-Bohm phase of Sec. 1.1.3 is a form of Berry phase, emphasizing the similar nature of the Berry potential \mathbf{A}_B and the vector potential \mathbf{A} .

1.2.3 Two microscopic models

While the considerations in the previous paragraph apply to a quantum Hall system, there is no explicit reference to the magnetic field. Rather, the Chern number appears as a property of the Bloch states, independently of the underlying system. In the next paragraph, I describe how the presence of a magnetic field modifies the Hamiltonian of a lattice system. This will give us the ingredients to build a lattice model with non-zero Chern number in the absence of a magnetic field.

1.2.3.1 Square lattice in a magnetic field

As detailed in Sec. 1.1.3, applying a magnetic field onto a system modifies its translation properties dramatically, as the usual translation operators do not commute with the Hamiltonian. Instead, we have defined magnetic translation operators (see Eq.(1.38)), which commute with the Hamiltonian, and obey the GMP algebra defined in Eq. (1.39). It is insightful to investigate the implications of these properties for a lattice Hamiltonian.

We consider a square lattice spanned by the vectors $a\mathbf{e}_x$ and $a\mathbf{e}_y$, where a is the lattice constant. In the Landau gauge (as defined in Eq.(1.35)), the magnetic operators that translate a particle by a lattice vector respectively write

$$\begin{aligned} \mathcal{T}_x(m, n) &= e^{-i\frac{a^2 n}{l_B^2}} \mathcal{T}_x(m, n) \\ \mathcal{T}_y(m, n) &= \mathcal{T}_y(m, n) \end{aligned} \quad (1.73)$$

where T_x and T_y are the lattice translation operators, and (m, n) are the lattice coordinates. The lattice Hamiltonian in the absence of a magnetic field can be fully expressed in terms of T_x and T_y . For instance, the simplest tight-binding Hamiltonian consists of a square lattice with only nearest neighbor hopping terms and writes

$$\begin{aligned} H &= -t \sum_{m,n} c_{m+1,n}^\dagger c_{m,n} + c_{m,n+1}^\dagger c_{m,n} + h.c. \\ &= -t \sum_{m,n} T_x(m, n) + T_y(m, n) + h.c. \end{aligned} \quad (1.74)$$

To take the magnetic field into account, one can simply substitute the magnetic translation operators for the usual translation operators. This operation, called a Peierl's substitution, results in the one-particle wave function accumulating the Aharonov-Bohm phase due to the presence of the magnetic field when it goes around a lattice unit cell. Note that if the magnetic flux enclosed in the lattice unit cell is a multiple of the flux quantum ($a^2/l_B^2 = 2\pi n_\phi$, n_ϕ integer), the phase in the definition of \mathcal{T}_x cancels, and there is no change to the Hamiltonian. If, however, this quantity is a rational fraction ($a^2/l_B^2 = 2\pi p/q$, p and q relative primes), the magnetic translation operators do not commute, but only a power of them does

$$\mathcal{T}_x^q \mathcal{T}_y = \mathcal{T}_y \mathcal{T}_x^q \quad (1.75)$$

The presence of the magnetic field thus results in a change of the periodicity of the lattice: the magnetic unit cell is enlarged q times such that it contains an integer number of magnetic quantum fluxes. Consequently, the area of the first Brillouin zone is reduced by a factor of q , and the number of bands is multiplied by q . This model is called Hofstadter model, and gives rise to the celebrated Hofstadter butterfly energy spectrum when the number of magnetic flux quanta piercing a lattice unit cell is an irrational number.

1.2.3.2 The two-orbital square lattice Chern insulator model

In 1988, Haldane introduced the first model of a Chern insulator [60], which consists of a honeycomb lattice with complex next nearest neighbor hopping. This complex hopping is the essential ingredient that allows the Chern number to be nonzero: it is the equivalent of the Peierl's substitution introduced in the last paragraph, in the absence of a net magnetic field. Instead of the Haldane model, we introduce a simpler model, the square lattice model with two orbitals, and complex inter-orbital hopping.

Let us consider a system made of a square Bravais lattice and 2 orbitals per unit cell. As noted in the last paragraph, a complex hopping term is equivalent to enclosing a non trivial magnetic flux inside the lattice plaquettes. While the Peierl's substitution breaks translational invariance, it is possible to choose the hopping amplitudes phases in such a way that the lattice periodicity is preserved. This can be achieved by enclosing a staggered magnetic flux, instead of a homogeneous one:

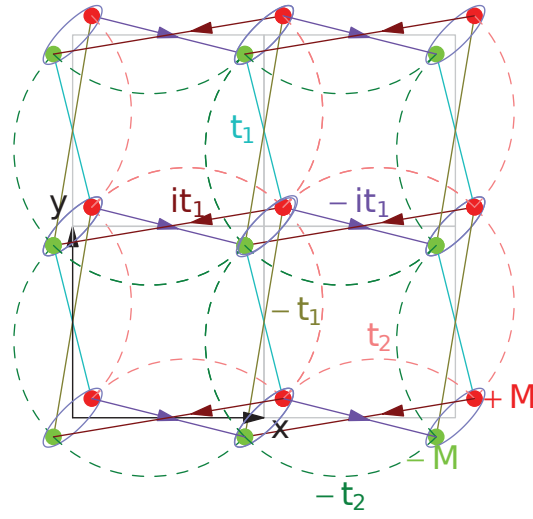


Figure 1.7: The two-orbital square lattice model. The two orbitals A and B are colored in red and green, respectively. The nearest neighbor hopping terms between orbitals of the same type have an amplitude $\pm t_2$. The amplitude of the interorbital nearest neighbor hopping term is $\pm it_1$ in the x direction, along the arrow, $\pm t_1$ in the y direction. The counterclockwise (respectively clockwise) arrow cycles enclose a $\pi/2$ (respectively $-\pi/2$) flux, resulting in a zero net magnetic field. This figure was slightly adapted from Ref. [172]

the opposite contributions of the magnetic flux in adjacent plaquettes add up to a zero net magnetic field. This is such system that I describe here. The Hamiltonian consists of a mass term of amplitude M and of nearest neighbor hopping terms, whose amplitude is real for the hopping between orbitals of the same type, and can be complex or real for the hopping between orbitals of a different type depending on the hopping direction.

$$\begin{aligned}
H = & t_2 \sum_{m,n} \left(c_{m+1,n,A}^\dagger c_{m,n,A} + c_{m,n+1,A}^\dagger c_{m,n,A} - c_{m+1,n,B}^\dagger c_{m,n,B} - c_{m,n+1,B}^\dagger c_{m,n,B} \right) \\
& + it_1 \sum_{m,n} \left(c_{m+1,n,A}^\dagger c_{m,n,B} - c_{m+1,n,B}^\dagger c_{m,n,A} + h.c. \right) \\
& + t_1 \sum_{m,n} \left(c_{m,n+1,A}^\dagger c_{m,n,B} - c_{m,n+1,B}^\dagger c_{m,n,A} + h.c. \right) \\
& + M \sum_{m,n} \left(c_{m,n,A}^\dagger c_{m,n,A} - c_{m,n,B}^\dagger c_{m,n,B} \right)
\end{aligned} \tag{1.76}$$

where $c_{m,n,\alpha}^\dagger$ (respectively $c_{m,n,\alpha}$) creates (respectively annihilates) an electron at lattice coordinates (m,n) on orbital $\alpha = A, B$. Fig. 1.7 represents the two-orbital square lattice model, with the various hopping terms. The lattice has a finite size, with respectively N_x and N_y unit cells in the x and y direction, and periodic boundary conditions.

To diagonalize this Hamiltonian, we write it in Fourier space (see Eq. (1.50)). The 2×2 Bloch Hamiltonian writes

$$h(\mathbf{k}) = 2t_1 \sin k_x \sigma_x + 2t_1 \sin k_y \sigma_y + (M - 2t_2 (\cos k_x + \cos k_y)) \sigma_z \tag{1.77}$$

where the σ_i are the Pauli matrices, and k_i was defined in Eq. (1.49). This two-band Hamiltonian is gapped except at the values of M where $(M - 2t_2 (\cos k_x + \cos k_y))^2 = 4t_1^2 (\sin^2 k_x + \sin^2 k_y)$. This equation has solutions in the Brillouin zone when

- $M = 4t_2 : (k_x, k_y) = (0, 0)$
- $M = 0 : (k_x, k_y) = (0, \pi), (\pi, 0)$
- $M = -4t_2 : (k_x, k_y) = (\pi, \pi)$

We want to determine the value of the Chern number in the lowest band, for the different values of M . A change in the Chern number is a topological phase transition, which can only happen if the gap closes. The gap remains consistently open for $M > 4t_2$ and $M < -4t_2$: these phases are thus respectively equivalent to the $M \rightarrow \pm\infty$ limits, i.e. the atomic limit. In this limit, the two sublattices A and B can be completely decoupled into two independent single-band insulators, and the insulator is a trivial one. As a consequence, all bands carry a zero Chern number in the intervals $M > 4t_2$ and $M < -4t_2$. We only need to determine the band topology in the interval $-4t_2 < M < 4t_2$. As M decreases from the atomic limit

$M \rightarrow \infty$ to $M = 4t_2$, the gap collapses at the $\Gamma = (0,0)$ point, while all the other points remain gapped. Consequently, the Berry curvature is a continuous function of M through the gap closing and reopening everywhere but at the Γ point, and we only need to analyze its evolution in the vicinity of that particular point. The linearized Hamiltonian reads

$$h(\mathbf{k}) = 2t_1 k_x \sigma_x + 2t_1 k_y \sigma_y + (M - 4t_2) \sigma_z \quad (1.78)$$

The ground state is characterized by the following energy and eigenfunction:

$$\begin{cases} E_- &= -\sqrt{4t_1^2 \mathbf{k}^2 + (M - 4t_2)^2} \\ \Psi_- &= \frac{1}{\sqrt{2\sqrt{4t_1^2 \mathbf{k}^2 + (M - 4t_2)^2}(\sqrt{4t_1^2 \mathbf{k}^2 + (M - 4t_2)^2} - (M - 4t_2))}} \begin{pmatrix} (M - 4t_2) - \sqrt{4t_1^2 \mathbf{k}^2 + (M - 4t_2)^2} \\ 2t_1(k_x - ik_y) \end{pmatrix} \end{cases} \quad (1.79)$$

From the eigenfunction, we analytically derive the expression of the Berry potential:

$$\begin{aligned} A_x &= \frac{-2t_1 k_y}{2\sqrt{4t_1^2 \mathbf{k}^2 + (M - 4t_2)^2}(\sqrt{4t_1^2 \mathbf{k}^2 + (M - 4t_2)^2} + (M - 4t_2))} \\ A_y &= \frac{2t_1 k_x}{2\sqrt{4t_1^2 \mathbf{k}^2 + (M - 4t_2)^2}(\sqrt{4t_1^2 \mathbf{k}^2 + (M - 4t_2)^2} + (M - 4t_2))} \end{aligned} \quad (1.80)$$

which yields for the Berry curvature:

$$F_{xy} = \frac{(M - 4t_2)}{2((M - 4t_2)^2 + 4t_1^2 k^2)^{3/2}} \quad (1.81)$$

We integrate this over a disk \mathcal{D} of center Γ and radius K .

$$\begin{aligned} \frac{1}{2\pi} \int_{\mathcal{D}} d^2 \mathbf{k} F_{xy} &= \frac{(M - 4t_2)}{4} \int_0^{K^2} \frac{d(k^2)}{((M - 4t_2)^2 + 4t_1^2 k^2)^{3/2}} \\ &= \frac{1}{2} \left(\text{sign}(M - 4t_2) - \frac{(M - 4t_2)}{\sqrt{(M - 4t_2)^2 + 4t_1 K^2}} \right) \\ &\xrightarrow{M \rightarrow 4t_2} \frac{\text{sign}(M - 4t_2)}{2} \end{aligned} \quad (1.82)$$

K should be chosen such that \mathcal{D} is included in the Brillouin zone ($0 < K < \pi$), but its particular value is not important, as we only need to compute the difference of Chern numbers at the transition

$$\begin{aligned} \Delta C &= C_{M-4t_2 < 0} - C_{M-4t_2 > 0} \\ &= \frac{1}{2\pi} \int_{BZ} d^2 \mathbf{k} (F_{xy}^{M-4t_2 < 0} - F_{xy}^{M-4t_2 > 0}) \end{aligned} \quad (1.83)$$

and not their absolute value. Since the Berry curvature is a continuous function of M everywhere but at the Γ point, the Berry curvature difference is only non-zero

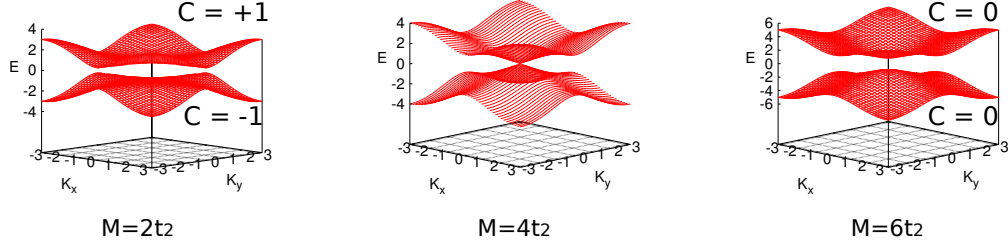


Figure 1.8: Bulk band structure of the two-orbital square lattice model at masses $M = 2t_2$, $4t_2$, $6t_2$. Both phases at $M = 2t_2$ and $6t_2$ are gapped, and the gap closes for $M = 4t_2$, at the Γ point $(0,0)$. The phase at $M = 6t_2$ is trivial, while the one at $M = 2t_2$ is topological, but it is impossible to deduce this from the band structure.

at the Γ point. Consequently, the integration interval can be reduced to \mathcal{D} , and the choice of K is arbitrary. At the gap closing and reopening transition, the change in Chern number is thus:

$$\begin{aligned} \Delta C &= \frac{1}{2\pi} \int_{\mathcal{D}} d^2\mathbf{k} (F_{xy}^{<0} - F_{xy}^{>0}) \\ &= \frac{\text{sign}(M - 4t_2)_{<0}}{2} - \frac{\text{sign}(M - 4t_2)_{>0}}{2} \\ &= -1 \end{aligned} \tag{1.84}$$

Since the state $M > 4t_2$ has zero Chern number, the Chern number of the phase $0 < M < 4t_2$ is $C = -1$. Similarly, to compute the Chern number of the $-4t_2 < M < 0$ phase, we increase M from the atomic limit $M \rightarrow -\infty$, until the gap closes at $M = -4t_2$ and (π, π) . Examining what happens at this point, we conclude to a Chern number $C = +1$ for that phase. Fig. 1.8 gives the bulk band structure of the square lattice Chern insulator for different values of M . There is no way to tell that these spectra correspond to Hamiltonians with different topological properties, since the Chern number is a property of the eigenstates alone, as seen in Sec. 1.2.2. The Chern number can however be deduced from the energy spectrum on the cylinder, which is represented in Fig. 1.6: the number of edge states at either end of the cylinder gives the value of the Chern number.

1.2.4 Experimental realizations

The prediction of the quantum anomalous Hall effect raises numerous experimental possibilities. Since there is no need for a magnetic field, it could be observed in easier experimental conditions than the integer quantum Hall effect. This motivated the engineering of solid state Chern insulators, which have been observed very recently for the first time in ferromagnetic semiconductors. Ultracold atomic gases are another experimental route for the realization of Chern bands, and are sometimes favored for their versatility, which allows a fine-tuning of the band parameters. While the observation of the insulating behavior remains elusive because

of a too large temperature, the Chern number of each band can be measured using indirect methods. In this paragraph, I give an example of both types of systems, and explain how the non-trivial topology of the system is measured.

1.2.4.1 Observation of the quantum anomalous Hall effect in ferromagnetic materials

Two main ingredients are needed to obtain a Chern insulator: a large gap (compared to the temperatures that can be reached experimentally), and a breaking of time-reversal symmetry, with a complex hopping lattice tunneling term that encloses a non-trivial flux. With decades of experience in the field of semiconductors, condensed matter experimentalists have already produced many solutions to find the first ingredient in a solid state system. Ferromagnetic long range order is then required to break time-reversal symmetry. The complex hopping term arises from spin-orbit coupling through a mechanism called band inversion that will be detailed in Sec. 1.3.2.1. The quantum anomalous Hall effect has been observed in Cr-doped thin films of magnetic semiconductors [33, 86, 34, 87], where Cr plays the role of a magnetic impurity that creates ferromagnetic order. To detect the topology of the electrons in the film, one can simply conduct a four-point transport experiment similar to the one used to detect the quantum Hall effect. When the magnetic field is varied, the magnetization of the ferromagnetic thin film follows a hysteresis cycle, and consequently, so do the Hall (σ_{xy}) and the longitudinal (σ_{xx}) conductivities, as shown in Fig. 1.9, which reports the experimental results of Ref. [87]. For a negative magnetic field, the Hall conductivity is on a $\sigma_{xy} = -e^2/h$ plateau, which persists when $B = 0$, revealing a topological insulating band with Chern number $C = -1$. At the coercive field ($B \simeq 0.15T$), it goes through a short $\sigma_{xy} = 0$ plateau, corresponding to the vanishing of magnetization (and thus to a trivial insulator). The topology of the insulator is restored for non-zero magnetization, and the Hall conductance jumps to a plateau corresponding to a $C = 1$ Chern band. When B decreases, the plateau persists for vanishing magnetic field. At low temperature, the longitudinal conductivity σ_{xx} is almost zero, in agreement with a dissipationless conducting mode. It increases dramatically at the approach of the coercive field, and reaches a sharp maximum at the transition between the various plateaus. Note that the temperatures required to observe the $\sigma_{xy} = 0$ plateau are still much lower than those employed in a regular integer quantum Hall effect experiment. Indeed, as shown in Fig. 1.9, $T = 1.9K$ is the highest temperature at which σ_{xy} shows an inflection at a zero value, while even the original results of Von Klitzing et. al. were obtained at $T = 4K$.

1.2.4.2 Measuring the Chern number in optical lattice systems

Ultracold atoms in optical lattices constitute ideal systems to study condensed matter models in a well-controlled environment. The atoms can be trapped in a three-dimensional lattice corresponding to a tight-binding Hamiltonian whose tunneling

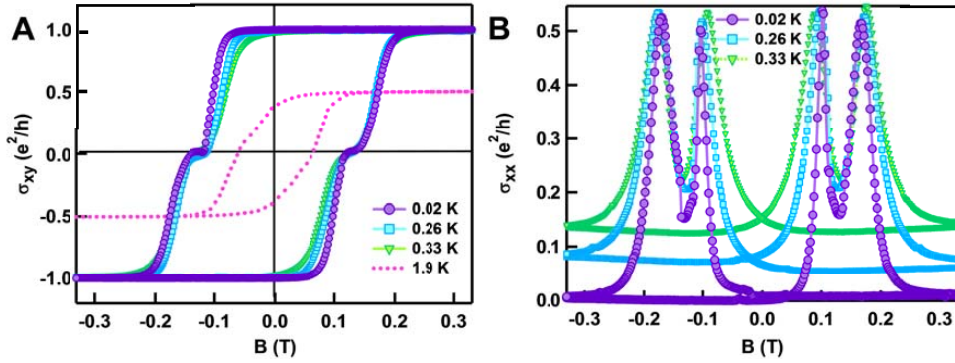


Figure 1.9: Evolution of the transverse (A) and longitudinal (B) conductivities of the Cr-doped $(\text{BiSb})_2\text{Te}_3$ magnetic topological insulator with varying magnetic fields, as reported in Ref. [87]. Three Hall plateaus can be clearly distinguished, corresponding to $C = -1, 0, 1$. The inversion of the Chern number is due to the inversion of the magnetization of the topological insulator. The longitudinal conductivity reaches a sharp peak at each plateau transition, and is otherwise negligible at low temperature.

terms can be tuned with a high degree of precision. Simulating magnetic fields in neutral cold atom systems is a challenge that can be resolved by creating artificial gauge fields [37]. These methods take advantage of the geometric phase that can result, for instance, from atom-light interaction, and that mimics the Aharonov-Bohm phase induced by a magnetic field. Periodically driven systems (described by Floquet theory) are an example of such methods. Several theoretical works [82, 54, 113, 51] have proven that a circularly polarized light could open a gap at the Dirac cones of a honeycomb lattice, leading to a Chern insulator akin to the Haldane model. The Chern number of the lowest band of this model was recently experimentally measured [76] in a system of ultracold fermions. Jaksch and Zoller [74] proposed another way of producing artificial gauge fields, which realizes the Hofstadter model of Sec. 1.2.3.1. It consists in tuning the phase difference between the two Raman lasers creating the optical lattice in such a way that the hopping term between adjacent sites has a well-determined phase. In this paragraph, I describe the principle of the proposal of Jaksch and Zoller, and its recent experimental realizations in Refs. [2, 1, 102].

The basic idea of the proposal of Ref. [74] is to first create a standard two-dimensional xy optical lattice, inhibit the hopping in the x direction and restore it in a controlled way (with a complex amplitude), with the use of additional lasers. The resulting system realizes the Harper-Hofstadter Hamiltonian with complex hopping in the x direction, and real hopping in the y direction. The initial (trivial) lattice is created by standing wave laser fields that generate a potential of the form

$$V(\mathbf{r}) = V_{0x} \sin(k_s x)^2 + V_{0y} \sin(k_s y)^2 + V_{0z} \sin(k_s z)^2 \quad (1.85)$$

where $k_s = 2\pi/\lambda_s$ is the wavevector of the light. The depth of the lattice in the z

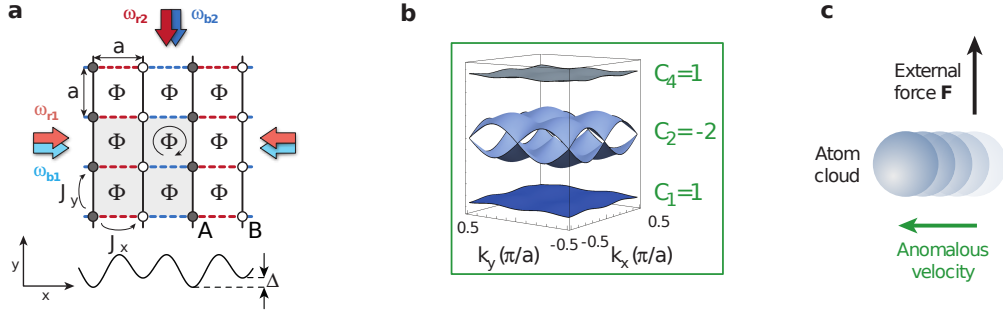


Figure 1.10: Measuring a Chern number in an optical lattice. a: Optical lattice setup. Standing wave fields create a two-dimensional square lattice with lattice constant a . Tunneling along the x direction is inhibited by a staggered potential of amplitude Δ , which creates two types of orbitals, A (filled dots) and B (empty dots). The resonant tunneling is restored independently on the red and blue links by two pairs of running wave ω_r and ω_b lasers, creating a $\Phi = \pi/2$ flux in each plaquette. The magnetic unit cell is highlighted in gray. b: Band structure of the $\Phi = \pi/2$ Hofstadter model. The two intermediate bands touch at several points in the Brillouin zone, thus forming one effective superband. c: The measurement of the Chern number relies on the anomalous (transverse) velocity resulting from the force F . These figures were reproduced from Ref. [2].

direction is assumed to be so large that hopping along this direction due to kinetic energy is prohibited, and the analysis can be restricted to a single xy plane. Moreover, we assume that the atomic gas is very dilute, so that the interactions between atoms can be neglected. For a fairly deep lattice potential, each atom is mainly localized around one lattice site, and we can describe this set up with a tight-binding Hamiltonian:

$$H_0 = - \sum_{m,n} J_{0x} c_{m+1,n}^\dagger c_{m,n} + J_{0y} c_{m,n+1}^\dagger c_{m,n} + h.c. \quad (1.86)$$

where $c_{m,n}^\dagger$ and $c_{m,n}$ are bosonic creation and annihilation operators at the site of lattice coordinates (m, n) . The terms $J_{0i=x,y}$ correspond to the tunneling amplitudes between adjacent sites

$$J_{0i} = \int dr_i w^*(r_i + l_i a) \left[-\frac{\hbar^2}{2m} \frac{d^2}{dr_i^2} + V_{0i} \sin(k_s r_i)^2 \right] w(r_i + (l_i - 1)a) \quad (1.87)$$

where $\phi(\mathbf{r}) = w(x)w(y)$ is the wave function describing a single atom of mass m subjected to the lattice potential, and $a = \lambda_s/2$ is the lattice constant.

An additional standing wave laser with a twice larger wavelength $\lambda_L = 2\lambda_s$ is superimposed in the x direction to create a staggered potential in this direction. The energy amplitude Δ of this staggered potential is much larger than the bare lattice hopping J_{0x} , thus doubling the lattice constant $a_x = \lambda_L/2$, and effectively

separating the lattice sites into two groups A and B (see Fig. 1.10a). The next step is to restore resonant tunneling, through the use of two additional pairs of lasers, each pair i generating a moving wave of the form

$$V_i(\mathbf{r}) = \kappa \cos(k_L x + \phi_i) \cos(-k_L y + \omega_i t) \quad (1.88)$$

where κ is the driving amplitude, $k_L = \frac{2\pi}{\lambda_L}$. The frequencies ω_i are set to $\omega_i = \pm\Delta/\hbar$ so that the tunneling induced by one pair of lasers is resonant for half the x bonds (in Fig. 1.10a, ω_r is resonant for the red bonds, ω_b is resonant for the blue bonds). The phases ϕ_i can be tuned independently so as to adjust the phase of the hopping term for each type of bond. In the high frequency limit $\hbar\omega \gg J_{0x}, J_{0y}$, this system can be described by the following time-independent tight-binding Hamiltonian:

$$H = - \sum_{m,n} J_x e^{in\Phi} c_{m+1,n}^\dagger c_{m,n} + J_y c_{m,n+1}^\dagger c_{m,n} + h.c. \quad (1.89)$$

where $J_x = \frac{J_{0x}\kappa}{\sqrt{2}\Delta}$ and $J_y \simeq J_{0y}$, and Φ is fixed to $\pi/2$ in Ref. [2]. This corresponds to a Hofstadter model where each lattice plaquette is pierced by one quarter of a magnetic flux quantum. This fractional number of flux quanta results in the doubling of the lattice unit cell in both directions, to include a full flux quantum in the new unit cell. Consequently, the first Brillouin zone is reduced, and the energy bands split into four subbands (the band structure of this model is represented in Fig. 1.10b). The lowest band is separated by an energy gap from the rest of the spectrum, and its Chern number is 1, which was recently observed experimentally in Ref. [2].

Before reporting the findings of Ref. [2], we should note that it does not constitute an observation of a Chern insulator *per se*: the optical lattice was loaded with bosons, which would condense at very low temperature, not form an insulator (the point here is rather to use the condensate as a probe of the band structure topology). More generally, reaching low temperatures compared to the band gap remains a challenge of this field, preventing the observation of an insulating behavior, even in fermionic systems. However, it is possible to measure the Chern number of the lowest band by measuring the transverse (Hall) drift resulting from the application of a force \mathcal{F} (see Fig. 1.10c). A force of strength \mathcal{F} applied in the y direction has a contribution to the velocity $v_x^\mu(\mathbf{k})$ along the x direction of a particle in the μ band that is proportional to the Berry curvature F_μ of this band:

$$v_x^\mu(\mathbf{k}) = -\frac{\mathcal{F}}{\hbar} F_\mu(\mathbf{k}) \quad (1.90)$$

The band dispersion relation causes an additional velocity $v_{band}^\mu(\mathbf{k})$, which averages out in the uniformly filled band configuration of Ref. [2]. The contribution of an atom in the μ^{th} band to the center of mass motion perpendicular to the force thus writes in terms of the band Chern number C_μ

$$x_\mu(t) = -\frac{4a^2\mathcal{F}}{\hbar} C_\mu t = -4aC_\mu \frac{t}{\tau_B} \quad (1.91)$$

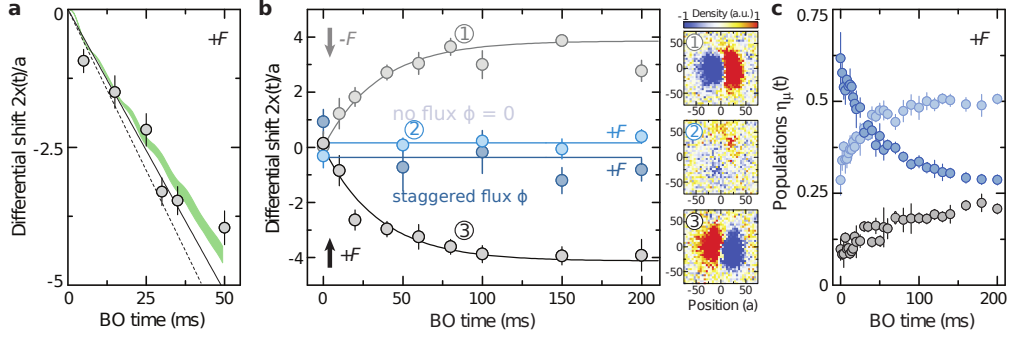


Figure 1.11: Differential center-of-mass displacements and band populations $\eta_\mu(t)$ versus Bloch oscillation (BO) time, as reported in Ref. [2]. a) The black solid line is a linear fit to the data for $t \leq 35\text{ms}$. The dashed line depicts the ideal evolution for $C_1 = 1$ and the same initial band populations. b) Three different situations are depicted: no flux ($\Phi = 0$), staggered flux ($\Phi = (-1)^m\pi/2$) (blue points), and $\Phi = \pi/2$ (gray points). The band structure is expected to be trivial in the first two cases, and the absence of Hall drift reflects this prevision. For $\Phi = \pi/2$, the drift profile is symmetric with respect to the force \mathbf{F} , and has been fitted with an exponential. The small figures on the right hand side represent the density profile of the atomic gas. c) Evolution of the band populations.

where the factor $4a^2$ comes from the fourfold enlargement of the unit cell due to the $\Phi = \pi/2$ flux, and $\tau_B = h/(Fa)$ is the characteristic time scale of the Bloch oscillations. The center of mass shift and the band population η_μ (supposed to be constant for short drift times, and homogeneous in k space) are measured independently. The total shift writes

$$\begin{aligned} x(t) &= \sum_{\mu=1}^4 \eta_\mu x_\mu(t) \\ &= -\frac{4at}{\tau_B} \sum_{\mu=1}^4 \eta_\mu C_\mu \end{aligned} \quad (1.92)$$

For a particle-hole symmetric non-interacting Hamiltonian with n bands, the Chern number of bands μ^{th} and $(n - \mu)^{\text{th}}$ bands are the same. Consequently, we can use the fact that the Harper-Hofstadter Hamiltonian is particle-hole symmetric to affirm that the lowest and highest bands have the same Chern number $C_1 = C_4$. Moreover, the bands 2 and 3 are actually not separated by a gap, and form one superband with twice as many states, and a Chern number C_2 . Since our model has a finite number of bands, the sum of the Chern numbers of all bands has to be zero [8], such that $C_2 = -2C_1$. Consequently, the total Hall displacement writes

$$x(t) = -\frac{4at}{\tau_B} C_1 (\eta_1 + \eta_4 - \eta_2) \quad (1.93)$$

The observations of Ref. [2] are reproduced in Fig. 1.11, and yield $C_1 = 0.9(2)$. The experimental Chern number comes closer ($C_1 = 0.98(12)$) to the expected unit value when the evolution of the band populations, as well as the saturation of the transverse velocity are taken into account.

In this section, I have shown the connection between the Hall conductance and an integer topological invariant, the Chern number. This connects the quantum Hall phases with a larger class of topological phases, the Chern insulators. These systems may have non-zero Hall conductance, and thus break time-reversal symmetry, but the presence of a magnetic field is not required. While the concept of a Chern insulator at zero magnetic field was introduced as early as 1988 by Haldane [60], it only sparked modest interest until the late 2000s. Then, the prediction and subsequent experimental observation of time-reversal preserving topological insulators revived the field of topological phases, and Chern insulators became a central topic in this field. This explains the more recent experimental realization of Chern insulators. In spite of this chronology, Chern insulators can also be seen as one of the building blocks of time-reversal symmetric topological insulators. I will explain this image in the next section.

1.3 Time reversal symmetric topological insulators

Time reversal symmetric (TRS) systems were long considered unsuitable for the apparition of topologically non-trivial physics. Since the Hall conductance σ_{xy} is odd under time-reversal \mathcal{T} (changing the direction of the magnetic field will reverse the sign of σ_{xy}), the Chern number of a TRS system is always zero. TRS insulators can nonetheless host a variety of interesting topological phases. TRS topological insulators are observed in bidimensional materials, but also in 3D, where no quantum Hall effect exists. By definition of a topological insulator, they have a charge excitation gap in the bulk, and they support topologically protected edge states (or surface states in 3D). The topological protection is ensured by time-reversal symmetry, meaning that only a time-reversal breaking perturbation may gap out the edge states without closing the bulk gap. In 2D, this phenomenon is called quantum spin Hall (QSH) effect, and closely resembles the quantum Hall effect. A spin current replaces the charge current of the quantum Hall (QH) effect, and is associated with counterpropagating pairs of edge modes. 3D topological insulators, on the other hand, support metallic surface states in the form of spin locked Dirac cones.

Beyond the exciting search for new phases of matter, TRS topological insulators could have powerful technological applications. They allow for the direct electric manipulation of the spin degrees of freedom without a magnetic field, making them good candidates for the construction of spintronic devices. Moreover, the associated spin current flows without dissipation, opening the route to reversible quantum computation. 3D topological insulators more specifically offer even more exotic possibilities with the potential emergence of non-Abelian topological order at their

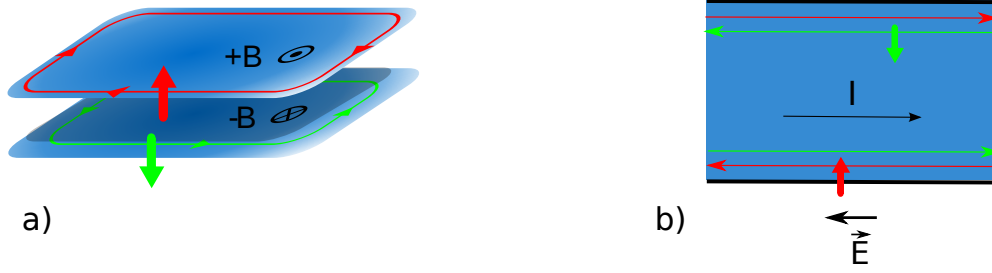


Figure 1.12: Toy model for the quantum spin Hall effect. (a) A bilayer system where electrons in each layer experience an opposite magnetic field realizes the quantum spin Hall effect. (b) When an electric field is applied to the sample, spin up electrons accumulate on the upper edge of the sample, while the same number of spin down electrons accumulate on the other side.

boundary with an ordinary superconductor, another stepping stone on the way to building a fault-tolerant quantum computer.

In this section, I will give an introduction to the physics of non-interacting two dimensional topological insulators. 3D topological insulators are beyond the scope of this manuscript, therefore I will not explore this topic any further. I will give a brief description of the first experimental observation of the quantum spin Hall effect. This phase is characterized by a topological invariant that admits only two different values. I will give a definition of the \mathbb{Z}_2 invariant for 2D systems, as well as its relation to measurable physical properties.

1.3.1 Introduction to the quantum spin Hall effect

The simplest model of a 2D TRS topological insulator consists of two decoupled copies of the quantum Hall effect, or a 2D gas of electrons with a spin 1/2 degree of freedom (see Fig. 1.12 for a schematic representation of this toy model). In the following, we will refer to this degree of freedom as a spin, even though it is not necessarily a physical spin. The spin up and spin down electrons are subjected to opposite magnetic fields, to ensure that there is no net magnetic field traversing the sample (and consequently that time-reversal symmetry is preserved). The spectrum of this system is composed of spin degenerate Landau levels (see Sec. 1.1.2). We consider the case where the lowest Landau level is filled with an equal number of spin up and spin down electrons, thus constituting two copies of the integer quantum Hall effect with opposite chiralities. As seen in Sec. 1.2.2, the electron gas of each spin species has a chiral mode at the edge. Since they experience opposite magnetic fields, electrons with different spins are associated with edge modes with opposite chiralities. The pair of spin-polarized, counterpropagating modes – also called helical edge states – is responsible for the conduction in the sample. Fig. 1.12b represents a situation where a current I flows through the sample. Unlike the quantum Hall effect, there is no charge accumulation on either side of the sample, and the Hall conductance σ_{xy} is zero. Rather, there is an accumulation of spin up on one edge

(the upper edge in our example), and of spin down on the other edge. Let us call S_z the projection of the total spin along the quantization axis (given by the direction of the magnetic field in this example). The spin imbalance corresponds to a spin Hall conductance σ_{xy}^H , defined as

$$\sigma_{xy}^H = \frac{e^2}{h} (\langle S_z \rangle_L - \langle S_z \rangle_R) \quad (1.94)$$

where $\langle S_z \rangle_L$ (respectively $\langle S_z \rangle_R$) is the expectation value of S_z for the left moving (respectively right moving). $\langle S_z \rangle_L = -\langle S_z \rangle_R$ to maintain time-reversal symmetry. In our example, $\langle S_z \rangle_L = 1/2$, since there is a single conduction channel for each spin, resulting in a spin Hall conductance $\sigma_{xy}^H = \frac{e^2}{h}$. Note that the quantization of the spin Hall conductance is specific to our simplified model, and not a general feature of the QSH effect. Indeed, the QSH effect does not require the conservation of spin [78], and could still exist if a mixing term was introduced (fortunately so: in a realistic material, S_z can never be an exact quantum number due to the existence of spin-orbit coupling). Finally, note that the current I flows without dissipation, as long as time-reversal symmetry is preserved. Indeed, the only backscattering allowed would have to be accompanied by a spin flip, which only a time-reversal breaking (magnetic) impurity can trigger (this point will be further justified in a later paragraph). Rather than a particular value of the spin Hall conductance, it is the stability of the edge states against localization that defines the QSH effect. We will define how this stability is related to a topological invariant in Sec. 1.3.3.

The toy model presented in this section is convenient to lay out the theoretical foundations of the QSH effect, but is of course in no way realistic. Engineering materials where a theoretically predicted effect will arise is one of the biggest challenges of the field of topological phases. In the next paragraph, we describe the first experimental realization of a 2D topological insulator, HgCdTe quantum wells.

1.3.2 Quantum spin Hall effect in HgTe-CdTe quantum wells

Kane and Mele [77] showed that spin-orbit coupling in graphene could create a TRS insulating phase with a non-zero spin current. While their prediction provided a useful theoretical framework for the QSH effect, it was later shown [101, 179] that the gap opened by spin-orbit coupling in graphene was too small (of the order of 10^{-3} meV) to be experimentally noticeable. Following the theoretical proposal of Bernevig, Hughes and Zhang [23] in 2006, the QSH effect was experimentally observed for the first time in HgCdTe quantum wells by König *et al.* [85, 84] in 2007. In the following paragraph, I give a simplified account of this historic experiment.

1.3.2.1 Band inversion in HgTe/CdTe quantum wells

Let us consider a semiconductor quantum well made of a thin layer of HgTe encapsulated in a CdTe barrier (see Fig 1.13a). The gap of both of these semiconductors is smallest in the vicinity of the Γ point, with energy scales such that the low energy

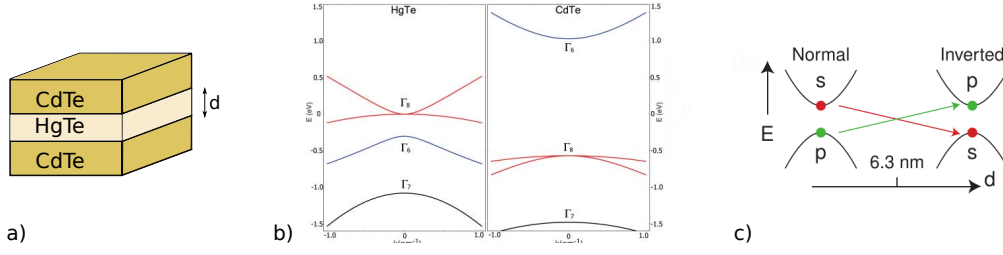


Figure 1.13: (a) HgTe/CdTe quantum well. A thin layer of HgTe constitutes the well, while CdTe is the barrier material. (b) Bulk band structure for HgTe and CdTe around the Γ point. (c) Simplified bulk band structure of HgTe/CdTe quantum wells. A band inversion occurs for a well thickness of $d_c = 6.3 \text{ nm}$. (Figures adapted from Ref. [23])

physics of the quantum well can be understood from considerations around the Γ point alone. In this region of the Brillouin zone, both materials feature an s -type Γ_6 and a p -type Γ_8 bands around the typical Fermi level, but these bands differ in their respective order. In CdTe, the succession of different bands around the Fermi level is considered "normal", with Γ_6 lying above Γ_8 . In contrast, the band order in HgTe is called inverted, as Γ_6 lies below Γ_8 . This particular band configuration is crucial to the emergence of the QSH effect, because it guarantees that a band inversion will occur: for a thin well, the band structure is mostly that of the barrier material (e.g. CdTe), and is thus normal. As the well grows thicker, the physics becomes dominated by the (inverted) band structure of the well material (e.g. HgTe). There is thus a critical thickness d_c of the quantum well, for which the bulk gap closes.

Following Ref. [23], we can derive a simplified Hamiltonian for this system, based on symmetry considerations. We consider a translationally invariant system, such that we can write the Hamiltonian in the Bloch form $H = \sum_{\mathbf{k} \in \text{BZ}} H(\mathbf{k})$, where the sum is over all momentum vectors \mathbf{k} in the Brillouin zone. Time reversal \mathcal{T} is an antiunitary operator, meaning that for any two states $|\Psi_1\rangle$ and $|\Psi_2\rangle$ in the Hilbert space, the following equality is verified

$$\langle \mathcal{T}\Psi_1 | \mathcal{T}\Psi_2 \rangle = \langle \Psi_2 | \Psi_1 \rangle \quad (1.95)$$

For half integer spins, time-reversal moreover verifies the property

$$\mathcal{T}^2 = -1 \quad (1.96)$$

\mathcal{T} acts on any operator as the product of complex conjugation and the reversal of spin. For the Hamiltonian H to be time-reversal invariant, the Bloch Hamiltonian $H(\mathbf{k})$ must satisfy the equality

$$\mathcal{T}H(\mathbf{k})\mathcal{T} = H(-\mathbf{k}) \quad (1.97)$$

We want to write the simplest Hamiltonian that respects these constraints and is a good model for the HgTe/CdTe quantum well. First, we simplify the model by

neglecting spin mixing, in which case the Hamiltonian can be written as a block matrix. Taking into account the constraint of time-reversal symmetry, this writes

$$H(\mathbf{k}) = \begin{pmatrix} & |\uparrow\rangle & |\downarrow\rangle \\ h(\mathbf{k}) & 0 \\ 0 & h^*(-\mathbf{k}) \end{pmatrix} \begin{pmatrix} |\uparrow\rangle \\ |\downarrow\rangle \end{pmatrix} \quad (1.98)$$

We now need to write $h(\mathbf{k})$ in a way that reflects the physics of the HgTe/CdTe quantum well. The band structure of HgTe/CdTe results from the combination of the following six basic atomic states of HgTe and CdTe (see Fig. 1.13b), given by their band and angular momentum:

$$|\Gamma_6, 1/2\rangle, |\Gamma_6, -1/2\rangle, |\Gamma_8, 1/2\rangle, |\Gamma_8, -1/2\rangle, |\Gamma_8, 3/2\rangle, |\Gamma_8, -3/2\rangle \quad (1.99)$$

These six bands combine to give the spin-up and spin-down states of the three quantum well subbands. One of these bands is well separated from the other two and can be neglected in this analysis. The resulting model is a twofold degenerate two-band model, whose spin-up part is represented by the Bloch Hamiltonian $h(\mathbf{k})$, a 2×2 matrix. Conversely, the spin-down part of the Bloch Hamiltonian is $h^*(-\mathbf{k})$. Without loss of generality, a two band Bloch Hamiltonian can always be written

$$h(\mathbf{k}) = \varepsilon(\mathbf{k})I + \sum_{\alpha=1}^3 d_{\alpha}(\mathbf{k})\sigma_{\alpha} \quad (1.100)$$

where I is the identity matrix and σ_{α} are the Pauli matrices. The quantum well band structure comes from the coupling of two types of atomic orbitals with opposite symmetries under two-dimensional spatial reflection: the s atomic orbitals are even under this reflection, and the p orbitals are odd. As a result, the coupling between the s and p orbitals must be an odd function of the momentum \mathbf{k} (since the contribution of any even term would average out). This imposes that the off-diagonal elements of $h(\mathbf{k}) - d_1(\mathbf{k})$ and $d_2(\mathbf{k})$ – be odd functions of \mathbf{k} . Likewise, the diagonal terms – $\varepsilon(\mathbf{k})$ and $d_3(\mathbf{k})$ – must be even. Around the Γ point, these constraints translate into a Bloch Hamiltonian of the form of Eq. (1.77), the square lattice Hamiltonian analyzed in Sec. 1.2.3.2. The quantum well is thus similar to a bilayer square lattice, with opposite chirality for the two layers. The inverted regime corresponds to the region of the Chern insulator, where the lowest band is non-trivial ($0 < M < 4t_2$). The lowest bands $|s, \pm\rangle$ of the effective model thus respectively carry Chern numbers $+1$ and -1 , and the system is topologically equivalent to the toy-model of the previous paragraph.

1.3.2.2 Experimental observation

The QSH effect can be detected in HgTe/CdTe quantum wells through a series of electrical experiments, spin measurements being more difficult to conduct. To this end, devices in a Hall bar geometry (see Fig. 1.14a) were constructed [84] with

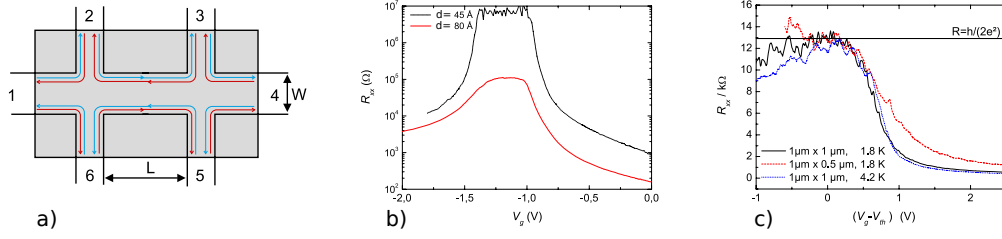


Figure 1.14: Observation of the quantum spin Hall effect in HgTe/CdTe quantum wells, as reported in Ref. [84]. a) Schematic sketch of the device showing the QSH edge states. The longitudinal resistance R_{xx} is measured between contacts 2 and 5 as a current flows from 1 to 4, while a gate voltage V_g is applied on the sample. b) Longitudinal resistance as a function of the gate voltage in the normal ($d = 45 \text{ Å}$ – black) and inverted ($d = 80 \text{ Å}$ – red) regimes. c) Longitudinal resistance as a function of the gate voltage in the inverted regime, for samples of sizes $L \times W = 1 \mu\text{m} \times 1 \mu\text{m}$ and $1 \mu\text{m} \times 0.5 \mu\text{m}$, at temperatures $T = 1.8 \text{ K}$ and 4.2 K . The threshold voltage V_{th} is defined such that the Fermi level falls at the bottom of the conducting band for $V_g = V_{th}$.

various thickness d . A gate voltage V_g is applied on the device to control the Fermi level ε_F and drive it from the n -conducting regime (ε_F in the conduction band) to the p -conducting regime (ε_F in the valence band). The longitudinal voltage drop $\mu_3 - \mu_2$ is measured as a current flows through the sample. The corresponding longitudinal resistance R_{xx} is represented as a function of the gate voltage in Fig. 1.14b. It is minimal in the n - and p -conducting regimes, where the density of states is large. There is an intermediary regime when ε_F is inside the bulk gap, where R_{xx} is larger, and differs greatly for quantum wells with a thickness d above or below the critical thickness $d_c \simeq 63 \text{ Å}$. For $d < d_c$, the band structure is normal, and the insulator is trivial, resulting in a large resistance R_{xx} of several $\text{M}\Omega$. For $d > d_c$, the band structure is inverted, and the insulator is topological. As can be seen in Fig. 1.14b, the conducting edge states result in a finite resistance. Note that the scattering of electrons with the voltage probes at the contact points results in an increase of the resistance.

To have a clear observation of the QSH effect, one also has to prove that the current in the inverted regime is due to the edge modes. Fig. 1.14c shows the evolution of the longitudinal resistance as a function of the gate voltage for samples in the inverted regime with various widths W (see Fig. 1.14a for the definition of W). The resistance in the n -conducting regime varies greatly when W goes from $0.5 \mu\text{m}$ to $1 \mu\text{m}$. For smaller gate voltage, however, the resistance is the same in both devices even though their widths differ by a factor 2, proving that the bulk transport is negligible compared to the edge transport. Moreover, the value of the resistance in this regime proves – through the Landauer-Buttiker formula – that the current is transported in two almost perfect canals. Finally, we also note that the QSH signal

is robust against a change of temperature, as long as $k_B T$ is small compared to the the bulk gap.

1.3.3 Protected helical edge states and \mathbb{Z}_2 invariant

1.3.3.1 Kramer's degeneracy

Kramer's theorem is a fundamental theorem for all TRS systems, at the origin of the topological protection of the edge states in topological insulators. It states that any single-particle state in a TRS system with $\mathcal{T}^2 = -1$ has to be doubly degenerate. Consequently, all states appear as pairs, called Kramer's doublets.

For half integer spins, the time-reversal operator verifies the equality $\mathcal{T}^2 = -1$. Let us write $|\Psi\rangle$ an eigenstate of the Hamiltonian H , with energy E . Since \mathcal{T} commutes with the Hamiltonian, $\mathcal{T}|\Psi\rangle$ is also an eigenstate of H with energy E . Let us now compute the overlap between these two states, using first the antiunitarity of \mathcal{T} (see Eq. (1.95)), and then $\mathcal{T}^2 = -1$:

$$\begin{aligned}\langle\Psi|\mathcal{T}\Psi\rangle &= \langle\mathcal{T}(\mathcal{T}\Psi)|\mathcal{T}\Psi\rangle \\ &= -\langle\Psi|\mathcal{T}\Psi\rangle\end{aligned}\tag{1.101}$$

As a result, $|\Psi\rangle$ and $\mathcal{T}|\Psi\rangle$ are orthogonal, and the spectrum of H is doubly degenerate. For a system with translational invariance, the degeneracy relates states of opposite momentum. For the points in the Brillouin zone where \mathbf{k} and $-\mathbf{k}$ are the same (modulo a translation of the lattice reciprocal vectors), there is a doubly degenerate state. In 2D, this guarantees that no gap can be open between the two states of a Kramer's pair at momenta $(k_x, k_y) = (0, 0), (\pi, 0), (0, \pi), (\pi, \pi)$. We have thus proven that the minimal model for a TRS topological insulator is a four-band model, since a TRS two-band model cannot be gapped, and all bands must appear in pairs.

1.3.3.2 Backscattering in the edge states of a TRS system

The existence of metallic edge states that are robust against localization is the key feature of 2D topological insulators. To explore this property, let us now consider an open bidimensional, TRS system. As we just showed in the last paragraph, each edge mode has to be accompanied by its Kramer's conjugate, with these two bands being mirror symmetric of one another in k -space. It means that around any given momentum \mathbf{k} , one member of the pair corresponds to a left-moving excitation, and the other one to a right-moving excitation. If these edge states cross the Fermi level, the edge states are metallic. To examine whether disorder can gap out the edge states, we compute the backscattering amplitude of a single-particle state $|\Psi\rangle$

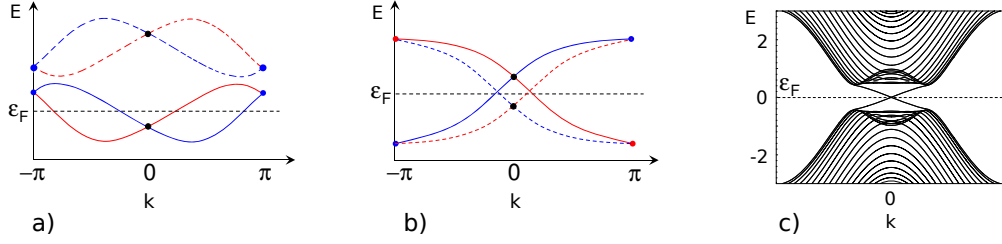


Figure 1.15: a), b): Edge states of a 2D time-reversal invariant insulator. Periodic boundary conditions are implemented in one direction (corresponding to the momentum k on the x axis of the graphs), while open boundary conditions are in effect in the other direction. There is one pair (red/blue) of Kramer's pairs on one side (solid line), one pair on the other side (dashed line). a) Trivial insulator: no matter what the position of the Fermi level ε_F is, each edge state crosses it an even number of times. b) Topological insulator: each edge state crosses the Fermi level an odd number of times. c) Simplified band structure of the quantum well HgTe/CdTe, in the quantum spin Hall effect regime, as derived in Ref. [23]. Figures are adapted from Ref. [84]

into its time-reversal conjugate $|\mathcal{T}\Psi\rangle$ by a TRS perturbation H_{per}

$$\begin{aligned}
 \langle \mathcal{T}\Psi | H_{per} | \Psi \rangle &= \langle \mathcal{T}(H_{per}\Psi) | \mathcal{T}^2\Psi \rangle \\
 &= -\langle \mathcal{T}(H_{per}\Psi) | \Psi \rangle \\
 &= -\langle H_{per}(\mathcal{T}\Psi) | \Psi \rangle \\
 &= -\langle \mathcal{T}\Psi | H_{per}^\dagger | \Psi \rangle \\
 &= -\langle \mathcal{T}\Psi | H_{per} | \Psi \rangle
 \end{aligned}$$

where we have used the antiunitarity of \mathcal{T} at the first step, and the hermiticity of H_{per} at the last one. It follows that the probability of a left-moving electron to be backscattered into a right-moving electron vanishes. The time-reversal operator can be defined to act on a many-body Hilbert space, instead of the single particle space. For a N -body Hilbert space of non-interacting spin-1/2 fermions, it verifies the property

$$\mathcal{T}_N^2 = (-1)^N \quad (1.102)$$

Consequently, if an odd number N of pairs of edge states crosses the Fermi level of a TRS insulator, these edge states will remain gapless thanks to the time-reversal symmetry. On the other hand, if the number of Kramer's pairs crossing the Fermi level is even, they can always be gapped out by disorder. The parity of N is thus a \mathbb{Z}_2 topological invariant, defining two categories of TRS insulators: topological for N odd, trivial for N even (see Fig. 1.15). In a topological insulator, protection against backscattering differentiates the edge states of a topological insulator from the "accidental" conducting edge states of a trivial insulator.

To illustrate this definition, we can go back to the introductory example of Sec. 1.3.1. Since the total spin S_z is a conserved quantum number in this example, the Kramer's degeneracy is equivalent to the spin degeneracy. There is one edge state for each spin: in other words, $N = 1$, and the insulator is topological. Had we chosen a four-layer system with two copies of the quantum Hall effect for each spin, we would have $N = 2$ Kramer's pairs of edge states, corresponding to a trivial insulator. An approximate tight-binding model for HgTe-CdTe quantum wells was derived in Ref. [23]. Diagonalizing this model for open boundary conditions in the inverted regime ($d > d_c$) leads to the single-particle spectrum of Fig. 1.15c. There is a single Kramer's pair of edge states traversing the bulk gap, which leads to the prediction of the observation of the QSH effect in this material.

In this Chapter, we have introduced the physics of the quantum Hall effect, as well as its two zero magnetic field cousins, Chern insulators and the quantum spin Hall effect. The gapped bands of these phases are characterized by a topological invariant, respectively the Chern number and a \mathbb{Z}_2 topological invariant, which makes them topological insulators. A crucial property of topological insulators is their protected dissipationless edge transport modes, which may have important applications in the field of low-consumption electronic devices. Adding interactions into a topological insulator may lead to even more exciting properties, with potentially revolutionizing applications for quantum computing. Strongly interacting topological insulators share some properties with their non-interacting counterparts, such as the quantization of conductance and the protection of edge states against localization. However, their charged excitations have a completely different nature: instead of having the same braiding statistics as the individual constituents, they can fractionalize into quasiparticles that are neither bosons nor fermions. These particularly interesting properties are the focus of the next chapter.

Strongly interacting topological insulators

Contents

2.1 Fractional quantum Hall effect	42
2.1.1 Experimental observation and role of the interactions	42
2.1.2 Haldane pseudopotentials	44
2.1.3 The Laughlin wave function and its excitations	46
2.1.4 The composite fermion construction	51
2.1.5 The Moore-Read and Read-Rezayi states	53
2.2 Anyons and topological degeneracy	55
2.2.1 Abelian anyons in the fractional quantum Hall effect	55
2.2.2 Non-abelian anyons in the fractional quantum Hall effect	56
2.2.3 Topological degeneracy on the torus	58
2.2.4 Haldane's exclusion principle	62
2.3 Fractional Chern insulators	63
2.3.1 Motivations and challenges on the experimental side	63
2.3.2 Emergence of a fractional Chern insulator	64
2.3.3 Numerically identifying a Chern insulator phase	68
2.4 Entanglement spectroscopy for the fractional quantum Hall phases	70
2.4.1 Entanglement entropy	70
2.4.2 Particle entanglement spectrum	72
2.5 Exact diagonalization	74

Non-interacting topological phases may host an array of properties that distinguish them from trivial phases, such as the existence of protected dissipationless edge modes. They are characterized by a topological invariant, a quantity that takes quantized values and can be related to a physically measurable quantity. Different types of topological invariants (such as the integer Chern number, or the \mathbb{Z}_2 invariant discussed in the previous chapter) correspond to different classes of topological phases, which have been studied systematically to give rise to a classification of topological insulators [145, 80]. As a result, we now have a good understanding of which topological invariants can be defined (and thus which topological phases can

be expected to arise) for a system with a given number of spatial dimensions that is invariant under a given discrete symmetry group. The interplay of topology and strong interactions, however, gives rise to a much lesser known physics, described by the notion of topological order. Topological order is a term that is mainly used to describe the many-body quantum states supporting fractionalized excitations. By definition, their intrinsic quantum numbers (such as the electric charge, or the spin) may be fractionalized (i.e. a fraction of the value of the microscopic constituent's quantum numbers), and their statistics is neither fermionic nor bosonic. While there is no comprehensive classification of topological order, it is observed in a well known experimental system, the fractional quantum Hall effect.

The first part of this chapter focuses on the fractional quantum Hall effect. I will introduce the concept of a model wave function, a powerful tool to understand the fractional quantum Hall physics. I will use the model states' excitations as examples to discuss the concept of fractionalization. We will see that similar properties can in principle be observed in a strongly correlated Chern insulator in the absence of a magnetic field. Finally, I will introduce some numerical tools that can be used to detect topological order.

2.1 Fractional quantum Hall effect

2.1.1 Experimental observation and role of the interactions

Only two years after the discovery of the integer quantum Hall effect, Tsui, Stormer and Gossard [162] reported the observation of a new plateau of the Hall resistance, at $R_H = 3h/e^2$, in a heterostructure of GaAs submitted to a strong magnetic field at very low temperature. More generically, the fractional quantum Hall effect corresponds to the observation of a plateau of the Hall resistance at

$$R_H = \frac{h}{\nu e^2} \quad (2.1)$$

where ν is a rational number. With the improvement of experimental conditions (higher mobilities in the sample due to perfected growing techniques, stronger magnetic field and lower temperature), a multitude of new fractions ν were observed (see Fig. 2.1). To this day, more than fifty fractions below unity have been observed.

The results of the previous chapter do not allow us to understand the fractional quantum Hall effect: the plateaus observed at non-integer ν correspond to partially filled Landau levels, and thus to phases expected to be compressible in the non-interacting picture. The Coulomb interaction between electrons must cause the opening of a mobility gap inside a Landau level (impurities acting at the single-particle level cannot be invoked because the fractional quantum Hall effect is only observed in high mobility samples). The ground state of a completely filled Landau level is a single non-degenerate state, and any excitation involves a transition of an electron into the next Landau level. In this context, the interaction may be treated perturbatively compared to the excitation energy, the cyclotron energy $\hbar\omega_c$.

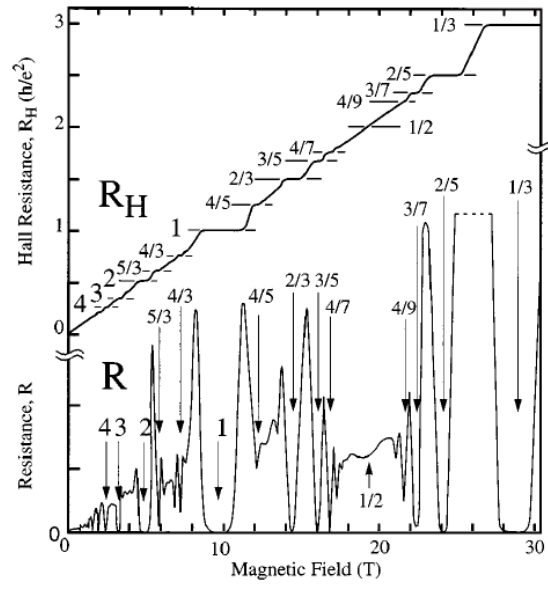


Figure 2.1: Evolution of the transverse resistance R_H and its longitudinal counterpart R as a magnetic field is applied onto the sample. R_H shows plateaus at values $h/(\nu e^2)$, where ν is a rational number printed on the figure. R vanishes on the plateaus, and shows sharp peaks at the transition between plateaus. Figure reproduced from Ref. [155]

This constitutes the limit of the approach of the previous chapter, which stays valid as long as the amplitude of the Coulomb interaction V is small compared to the cyclotron energy. For a partially filled Landau level, however, there are plenty of zero energy excitations, as one electron can always go from one orbital to the other with no kinetic energy cost. The fractional quantum Hall effect appears when the cyclotron energy is large compared to V , which must be itself dominant compared to the impurity potential strength t

$$\hbar\omega_c \gg V \gg t \quad (2.2)$$

The typical distance between two electrons in the presence of a magnetic field is given by the magnetic length $l_B = \sqrt{\hbar/(eB)}$, leading to a typical Coulomb energy

$$V = \frac{e^2}{\epsilon l_B} \simeq 50\sqrt{B(T)}K \quad (2.3)$$

while the cyclotron energy writes

$$\hbar\omega_c \simeq 20B(T)K \quad (2.4)$$

The constraint of Eq. (2.2) can thus be respected for large enough magnetic fields. In this case, the interaction can never be treated perturbatively: the analysis can be restricted to the highest partially filled Landau level, and V becomes the only energy scale in the problem, which makes it irrelevant. Unless otherwise noted, we will restrict our analysis to the lowest Landau level ($\nu < 1$). We will also assume that the interaction between electrons of opposite spins causes a Landau level splitting large compared to V , such that the lowest Landau level is fully polarized. Our system consists of N particles interacting via a pairwise potential, projected onto the lowest Landau level. In terms of the projection operator \mathcal{P}_{LLL} , the effective Hamiltonian writes

$$H = \mathcal{P}_{LLL} \left(\sum_{1 \leq i < j \leq N} V(|\mathbf{r}_i - \mathbf{r}_j|) \right) \mathcal{P}_{LLL} \quad (2.5)$$

This very simple Hamiltonian is also very difficult to solve: the interaction cannot be perturbatively handled, starting from an initial non-interacting ground state, since the Hamiltonian only contains one term. Consequently, the only way to find its energies and eigenstate is to numerically diagonalize the N -body problem, or to guess them (variational approach). A few ansatz have been proposed to describe the fractional quantum Hall effect, the most successful of which are presented in this section.

2.1.2 Haldane pseudopotentials

Haldane [57] introduced a way to parametrize any pairwise interaction projected onto the lowest Landau level (LLL), as long as it only depends on the distance between two particles. It can be used to write a realistic interaction (such as Coulomb)

in terms of an infinite – but discrete – number of parameters, or to define a simplified Hamiltonian.

As we will see, the fractional quantum Hall effect can arise in both bosonic and fermionic systems. For this reason, we consider the two statistics in this section. The wave function for a system of two non-interacting bosonic (respectively fermionic) particles can be written as the symmetrized (respectively antisymmetrized) product of two single-particle wave functions. For a rotationally invariant system, in the lowest Landau level, these wave functions have a respective angular momentum m_1 and m_2 and are defined in Eq. (1.26). A generic two-body wave function writes

$$\Psi_{m_1, m_2}(z_1, z_2) = \mathcal{N} (z_1^{m_1} z_2^{m_2} \pm z_2^{m_1} z_1^{m_2}) e^{-\frac{1}{4l_B^2}(|z_1|^2 + |z_2|^2)} \quad (2.6)$$

where z_1 and z_2 are the complex coordinates of particles 1 and 2, and \mathcal{N} is a normalization constant. It can be rewritten in terms of the relative and center of mass coordinates $z = (z_1 - z_2)/\sqrt{2}$ and $Z = (z_1 + z_2)/\sqrt{2}$

$$\Psi_{M, m}(z, Z) = \langle z, Z | M, m \rangle = \mathcal{N}' Z^M z^m e^{-\frac{1}{4l_B^2}(|z|^2 + |Z|^2)} \quad (2.7)$$

where the integers m and M are the relative and center of mass angular momenta. Note that m must be odd (respectively even) for fermionic (respectively bosonic) particles to respect the antisymmetry (symmetry) of the wave function. We can write the LLL-projected two-body interaction \hat{V} in this basis. Since it only depends on the relative coordinate, \hat{V} does not depend on M . For an isotropic interaction, the relative angular momentum is also conserved, yielding

$$\begin{aligned} \langle M', m' | \hat{V} | M, m \rangle &= \langle M' | M \rangle \langle m' | \hat{V} | m \rangle \\ &= \delta_{M', M} \delta_{m', m} \langle m | \hat{V} | m \rangle \end{aligned} \quad (2.8)$$

We note V_m the expectation value of the interaction for a two-particle state with relative momentum m .

$$V_m = \langle m | \hat{V} | m \rangle \quad (2.9)$$

The coefficients V_m are called Haldane pseudopotentials, and represent the energy penalty to populate a state with relative momentum m . In other words, they are the energy spectrum of the two-body problem in the lowest Landau level. They completely specify the interaction in the LLL:

$$\begin{aligned} \hat{V} &= \sum_{M, m} \sum_{M', m'} |M', m'\rangle \langle M', m' | \hat{V} | M, m \rangle \langle M, m| \\ &= \sum_{M, m} V_m |M, m\rangle \langle M, m| \end{aligned} \quad (2.10)$$

Note that depending on their bosonic or fermionic statistics, identical particles are only sensitive to the pseudopotentials with a given parity of m . Two fermions cannot have an even relative momentum (otherwise the wave function would be

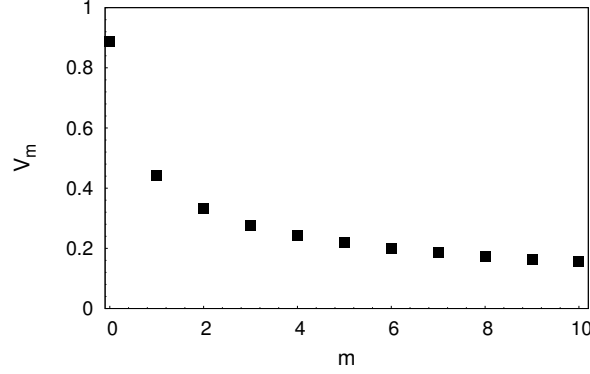


Figure 2.2: Pseudopotentials of the Coulomb interaction on the sphere geometry in the lowest Landau level.

symmetric under the exchange of these two fermions), and thus only sense the m odd pseudopotentials. Equivalently, bosons only sense the m even pseudopotentials.

As an example of the use of this parametrization, let us give the pseudopotentials decomposition of the Coulomb interaction projected onto the LLL on the sphere geometry:

$$V_m = \frac{\Gamma(m+1/2)}{2l_B \Gamma(m+1)} \quad (2.11)$$

where Γ is the Euler Gamma function. They are represented in Fig. 2.2.

Conversely, one can write the interaction $\hat{V}_l = \sum_M V_l |M, l\rangle \langle M, l|$ corresponding to a given pseudopotential V_l in real space. V_0 is associated with the contact interaction between two particles

$$\hat{V}_0(\mathbf{r}_1, \mathbf{r}_2) = V_0 \delta^{(2)}(\mathbf{r}_1 - \mathbf{r}_2) \quad (2.12)$$

\hat{V}_1 is a slightly longer range interaction, which is sometimes called the hollow core interaction, since it does not penalize having two particles at the same position. In real space, it writes [160]

$$\hat{V}_1(\mathbf{r}_1, \mathbf{r}_2) = -V_1 \nabla^2 \delta^{(2)}(\mathbf{r}_1 - \mathbf{r}_2) \quad (2.13)$$

2.1.3 The Laughlin wave function and its excitations

2.1.3.1 The Laughlin ground state

The impossibility to find an approximate solution to the fractional quantum Hall problem perturbatively only leaves us with options such as the guessing of plausible ansatzs. In 1983, Laughlin proposed a wave function [91] to describe the incompressible states observed at fractions $1/q$, q odd (remember that $1/3$ was the first observed fraction).

Single-particle states in the LLL are written in the symmetric gauge in Eq. (1.26) as monomials of the complex coordinate $z = x - iy$, up to a Gaussian factor.

This implies that a many-body wave function in the lowest Landau level must be analytical in all of the particle coordinates z_i , and write

$$\Psi(z_1, \dots, z_N) = F_A(\{z_j\}) e^{-\frac{1}{4l_B^2} \sum_j |z_j|^2} \quad (2.14)$$

where $F_A(\{z_j\})$ is a polynomial of the z_j s antisymmetric under the exchange of any two z_i and z_j . Among the many polynomials verifying this constraint, the goal is to find one that minimizes the Coulomb interaction. The approach of Laughlin roughly follows these steps:

- Laughlin was influenced by the success of Jastrow-type wave functions to describe superfluid helium. These states have pairwise correlations, leading to the following form for the polynomial

$$F_A(\{z_j\}) = \prod_{j < k} f(z_j - z_k) \quad (2.15)$$

- The wave function should be an eigenstate of the total angular momentum \hat{L}_z (because \hat{L}_z commutes with the Coulomb interaction). $\prod_{j < k} f(z_j - z_k)$ should thus be a polynomial of the same degree L for each z_j , which is only possible if each term $f(z_j - z_k)$ has a definite angular momentum.
- The function f must be antisymmetric to ensure the antisymmetry of the full wave function: $f(z) = -f(-z)$

This set of constraints imposes that

$$f(z) = z^q \quad (2.16)$$

where q is an odd integer. This produces the Laughlin wave function

$$\Psi_{1/q}^L(z_1, \dots, z_N) = \left(\prod_{j < k} (z_j - z_k)^q \right) e^{-\frac{1}{4l_B^2} \sum_j |z_j|^2} \quad (2.17)$$

Note that our system is a priori infinite, even for a finite number of particles, as we have not defined any confinement potential. However, it is effectively finite, because of the limited extension of the single-particle wave functions in the symmetric gauge. Indeed, we have seen in Eq. (1.27) that the electronic density in an orbital m in the symmetric gauge was mainly located around a circle of radius $\sqrt{2m}l_B$. The system is thus effectively limited to a disk of radius $\sqrt{2m_{\max}}l_B$, where m_{\max} is the largest index of any occupied orbital. In the symmetric gauge, m_{\max} is given by the degree of the polynomial of the many-body wave function. The polynomial $\prod_{j < k} (z_j - z_k)^q$ has a degree $(N-1)q$ in each variable z_j . The maximal momentum of a single-particle state involved in this wave function is thus $m_{\max} = (N-1)q$. As a consequence, the system supporting the Laughlin state (2.17) is effectively limited to a disk of radius $\sqrt{2(N-1)q}l_B = \sqrt{2N_\phi}l_B$. The density profile of the Laughlin

state is actually uniform on a disk of radius $\sqrt{2N_\phi}l_B$ (see Fig. 2.3), as can be derived by computing the density numerically.

The sphere [57] is another finite geometry that is convenient to study the fractional quantum Hall effect. On this geometry, both the radius of the sphere ($\propto \sqrt{N_\phi}$) and the number of orbitals in the lowest Landau level $N_\phi + 1$ are fixed by the strength of the magnetic monopole at its center. Through the stereographic projection, all wave functions written on the disk may easily be written on the sphere by setting $z = u/v$, where $u = \cos(\theta/2)e^{i\phi/2}$ and $v = \sin(\theta/2)e^{-i\phi/2}$ are the spinor coordinates with spherical coordinates θ and ϕ . There is also a global factor that replaces the Gaussian factor such that the sphere Laughlin wave function reads

$$\Psi_{1/q}^{L,\text{sphere}}(u_1, v_1, \dots, u_N, v_N) = \prod_{j < k} (u_j v_k - u_k v_j)^q \quad (2.18)$$

An advantage of working on the sphere is the additional $SU(2)$ symmetry which is respected by the Hamiltonian on this geometry. As a result, the total angular momentum L is a good quantum number, and many-body wave functions on the sphere are labeled by both L_z and L .

The Laughlin phase corresponds to N particles occupying $(N - 1)q + 1$ orbitals. This defines the relation between the number of flux quanta N_ϕ and the number of particles for the Laughlin state on the disk (or equivalently sphere) geometry

$$N_\phi = Nq - q \quad (2.19)$$

The filling fraction was defined in Eq. (1.47) as the ratio of the number of particles living on a surface and the number of flux quanta piercing it in the thermodynamic limit. Taking Eq. (2.19) to the thermodynamic limit leads to a filling fraction $\nu = 1/q$ for the Laughlin $1/q$ state. The discrepancy between the filling fraction, which is defined in the thermodynamic limit, and the ratio N/N_ϕ in finite size corresponds to the shift δ defined as

$$N_\phi = N\nu^{-1} - \delta \quad (2.20)$$

The shift of the Laughlin state on the disk or the sphere is $\delta = q$. While it appears here as some finite size artefact, the shift has important physical significance, since it is related to the Hall viscosity [130], a topological quantity. Going back to the thermodynamic limit, for $q = 3$, the Laughlin wave function describes the state observed by Tsui, Stormer and Gossard at filling fraction $\nu = 1/3$ (see Fig. 2.1) with high accuracy. The exact diagonalization of the Coulomb interaction yields a state with a very large overlap with the Laughlin state [61, 43] (99% for $N = 12$). This is remarkable, especially in the absence of any variational parameter.

It is interesting to note that the Laughlin wave function can be written in terms of the non-interacting many-body wave function at $\nu = 1$. We consider an electron gas on a disk (or a sphere) pierced by N_ϕ flux quanta. The lowest Landau level of this finite system has a degeneracy $(N_\phi + 1)$. We completely fill the lowest Landau

level with $N = N_\phi + 1$ particles. The many-body wave function of this system writes as a Slater determinant of all lowest Landau level single-particle states

$$\Psi_{\nu=1}(z_1, \dots, z_N) = \begin{vmatrix} \langle z_1|0\rangle & \dots & \langle z_1|N-1\rangle \\ \langle z_2|0\rangle & \dots & \langle z_2|N-1\rangle \\ \dots & \dots & \dots \\ \langle z_N|0\rangle & \dots & \langle z_N|N-1\rangle \end{vmatrix} \quad (2.21)$$

Substituting the single-particle wave functions by their expression leads to (up to a normalization constant)

$$\Psi_{\nu=1}(z_1, \dots, z_N) = \begin{vmatrix} 1 & z_1 & \dots & z_1^{N-1} \\ 1 & z_2 & \dots & z_2^{N-1} \\ \dots & \dots & \dots & \dots \\ 1 & z_N & \dots & z_N^{N-1} \end{vmatrix} \times e^{-\frac{1}{4l_B^2} \sum_j |z_j|^2} \quad (2.22)$$

The first factor of this product is a Van der Monde determinant, which is equal to $\prod_{j < k} (z_j - z_k)$. The fully filled LLL wave function is thus no other than the Laughlin wave function for $q = 1$. Conversely, for a generic q , the polynomial part of the Laughlin wave function is just the polynomial part of a filled Landau level raised to the power q .

Finally, one of the most important properties of the Laughlin state is to be the exact ground state of some model Hamiltonian, expressed very simply in terms of the Haldane pseudopotentials. The wave function of a pair of particles with relative momentum q and total momentum $M = 0$, writes $(z_1 - z_2)^q$. It follows that q is the smallest relative momentum that two particles can carry in the Laughlin wave function. Let us define the family of model Hamiltonians that penalize only the pairs of particles with relative angular momentum lower than q

$$V_l > 0, l < q \quad V_l = 0, l \geq q \quad (2.23)$$

The Laughlin state is an eigenstate of this Hamiltonian, with energy 0. It is moreover a ground state, since the Hamiltonian is positive semi-definite. It is in fact the unique ground state of the Hamiltonian Eq. (2.23) at filling fraction $\nu = 1/q$. We can easily see that the Laughlin state is the densest zero energy eigenstate of (2.23): for all pairs of particles j and k , the difference $(z_j - z_k)$ must enter the ground state Ψ at (at least) the power q , otherwise there would be pairs of particles with relative momentum lower than q . This sets $\nu = 1/q$ as the lowest filling factor for a zero energy eigenstate of (2.23). The above property also imposes that the ground state wave function can be factorized into the product of $\prod_{j < k} (z_j - z_k)^q$ and another factor. The other factor $F_S(\{z_j\})$ must be symmetric, since $\prod_{j < k} (z_j - z_k)^q$ is symmetric (respectively antisymmetric) for q even (respectively q odd). The general lowest Landau level wave function excluding pairs with momentum $l < q$ thus has the form:

$$F_S(\{z_j\}) \prod_{j < k} (z_j - z_k)^q e^{-\frac{1}{4l_B^2} \sum_j |z_j|^2} \quad (2.24)$$



Figure 2.3: Approximate electronic density of the Laughlin ground state (*left*, see Eq. (2.17)) and the Laughlin wave function with one added quasihole (*right*, see Eq. (2.25))

If F_S supplied any additional power of z_j , it would lower the filling fraction of the overall wave function. As a result, F_S must be equal to one, and the Laughlin state is the unique densest ground state of the model interaction Eq. (2.23). Using this, and the decomposition of the Coulomb interaction into a series of pseudopotentials, one can understand why the $1/3$ Laughlin state reproduces the Coulomb ground state at $\nu = 1/3$ with such high accuracy. Indeed, V_1 is much larger than V_3 , and that higher l V_l pseudopotentials [83], as can be seen in Fig. 2.2 (we recall that electrons are only sensitive to odd index pseudopotentials). For bosonic systems, the Laughlin function $q = 2$ is the unique ground state of a Hamiltonian whose only non-zero pseudopotential is V_0 , the contact delta interaction (2.12).

2.1.3.2 Charged excitations to the Laughlin state

Elementary excitations to the Laughlin state are obtained by shifting the filling factor slightly away from $\nu = 1/m$. This can be done by changing either the electronic density, the magnetic field, or the sample area, to have a different number of flux quanta piercing the sample. Let us consider the following excited state ansatz introduced by Laughlin, where w_0 is a complex parameter:

$$\Psi_{1/q}^{qh}(z_1, \dots, z_N) = \left(\prod_j (z_j - w_0) \right) \left(\prod_{j < k} (z_j - z_k)^q \right) e^{-\frac{1}{4l^2 B} \sum_j |z_j|^2} \quad (2.25)$$

The additional factor $\prod_j (z_j - w_0)$ (compared to Eq. (2.17)) raises the degree of the polynomial part of the $1/q$ Laughlin wave function by 1 for each coordinate z_j . This is equivalent to changing the number of flux quanta by one. An important property of this ansatz is that it is an exact zero energy ground state of the Hamiltonian of Eq. (2.23), since the additional factor does not supply any pair of particles with relative angular momentum lower than q .

If $w_0 = 0$, this excited state is equal to a Laughlin wave function where all single-particle orbitals have been pushed by one unit, and no particle has a momentum $m = 0$. More generically, the electronic density in the excited state $\Psi_{1/q}^{qh}$ has a zero at complex coordinate w_0 , and describes a quasihole localized at w_0 (see Fig. 2.3). To compensate the addition of a quantum flux unit and go back to a filling $1/q$, one would need to add a fraction $1/q$ of an electron. Consequently, the Laughlin

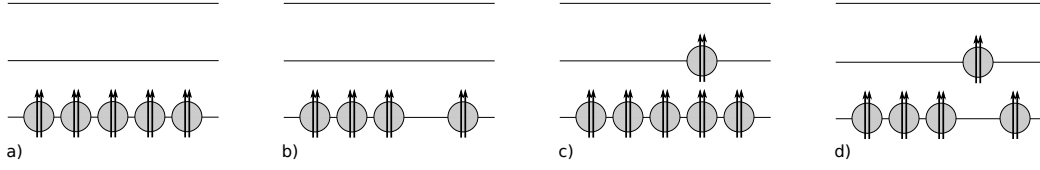


Figure 2.4: The composite fermion construction with $n = 2$ flux quanta attached to each fermion. a) One filled Lambda level ($p = 1$). This corresponds to the Laughlin $\nu = 1/3$ ground state. b) The Laughlin $\nu = 1/3$ state with one quasihole. c) The Laughlin $\nu = 1/3$ state with one quasielectron. d) The Laughlin $\nu = 1/3$ state with one exciton (neutral excitation). A model wave function for any of these configurations can be written within the composite fermion formalism.

quasihole described in Eq. (2.25) has a charge

$$e_{qh}^* = \frac{e}{q} \quad (2.26)$$

The charge of the Laughlin quasihole can also be derived by calculating the Aharonov-Bohm phase accumulated by the wave function of Eq. (2.25) when the quasihole goes around a loop, as pointed out in Ref. [7]. The fractional nature of the elementary charged excitations in the quantum Hall effect has been confirmed experimentally in shot-noise experiments [144, 38], where one measures the square fluctuations of the current to infer the carrier charge by a proportionality relation.

Conversely, adding a quasiparticle of charge $-e/m$ (opposite to that of the Laughlin quasihole) into the system can be done by lowering the number of flux quanta N_ϕ by one. Laughlin proposed an ansatz to describe this excited state, but the overlap of this state with the exact quasielectron states actually decreases rapidly with the system size. The composite fermion description of the fractional quantum Hall effect, which will be detailed in the next paragraph, provides better variational wave functions for the quasielectron states.

2.1.4 The composite fermion construction

Laughlin's ansatz wave function was a breakthrough that greatly improved the understanding of the fractional quantum Hall effect. However, it does not give a full account of this phenomenon, as it does not explain all of the observed fractions, even in the lowest Landau level¹. Jain proposed a simple heuristic picture [73] to explain the series of incompressible states observed at filling fraction $\nu = \frac{p}{2p+1}$. Jain's idea was to replace interacting electrons by weakly interacting composite quasiparticles, called composite fermions (CF), formed by the binding of an electron and n magnetic flux quanta. The CF play the role of the electrons in the integer quantum Hall

¹The so-called hierarchy construction [57, 64, 65] takes the Laughlin state as a building block to explain the odd denominator fractions of the fractional quantum Hall effect. However, it does not predict the phenomenon observed at half filling, which will be detailed in this section

effect: they form Lambda levels, a new type of Landau levels, such that completely filled Lambda levels correspond to an incompressible state. For p filled Lambda levels, Jain's wave function writes

$$\Psi_{p,n}^{CF}(z_1, \dots, z_N) = \mathcal{P}_{LLL} \left(\prod_{j < k} (z_j - z_k)^n \Psi_{\nu^*=p}(z_1, \dots, z_N) \right) \quad (2.27)$$

where $\prod_{j < k} (z_j - z_k)^n$ attaches n magnetic flux quanta to each electron, and $\Psi_{\nu^*=p}$ is the wave function describing N non-interacting CF completely filling p Lambda levels. $\Psi_{\nu^*=p}$ is easily obtained by writing a Slater determinant with the single-particle states obtained in the previous chapter. After the flux attachment, the CF are subjected to a reduced magnetic field

$$B^* = B - n\rho\phi_0 \quad (2.28)$$

where ρ is the electronic density, and ϕ_0 the unit flux quantum. This results in a Lambda level filling fraction

$$\nu^* = \frac{N}{N_\phi^*} = \frac{N}{N_\phi(1 - n\nu)} = \frac{\nu}{1 - n\nu} \quad (2.29)$$

where N_ϕ and N_ϕ^* are respectively the original and effective numbers of flux quanta. For fully filled Lambda levels $\nu^* = p$, this yields the filling fraction

$$\nu = \frac{p}{np + 1} \quad (2.30)$$

Fig. 2.4a shows a schematic representation of this construction for $n = 2$ and $p = 1$.

Note that the CF indeed have to be of fermionic statistics (otherwise they would not form an incompressible state by filling an integer number of Lambda levels). In the case where the underlying particles are fermions (which is the case for the fractional quantum Hall effect of electrons), this implies that the number of attached fluxes n must be even. Similarly, if the elementary particles are bosons, n must be odd. For one Lambda level fully filled ($p = 1$) with composite fermions made by attaching $n = q - 1$ fluxes to each electron, the CF wave function (2.27) is exactly the $\nu = 1/q$ Laughlin wave function (2.17). Indeed, this case corresponds to $\Psi_{\nu^*=1}(z_1, \dots, z_N) = \prod_{j < k} (z_j - z_k)$ (i.e. the wave function of a fully filled lowest Landau level, which was derived in Eq. (2.22)). The projection onto the lowest Landau level acts trivially onto this state. With two fluxes attached per electron ($n = 2$), and respectively $p = 2$ or $p = 3$ filled Lambda levels, one gets the fractions $\nu = 2/5$ and $\nu = 3/7$, which can be observed in Fig. 2.1.

The CF construction thus provides a simple picture to explain most of the observed plateaus. Its main advantage is that it provides a practical way to write many fractional quantum Hall wave functions, including those for the $\nu = 1/3, 2/5, 3/7$ plateaus. These functions are not in general the exact eigenstates of a model microscopic Hamiltonian (except for $\nu = 1/3$), but they have a very good overlap with

the exact states in finite size. The CF construction also provides an accurate way to describe the elementary excitations of the ground state. In Fig. 2.4, we show some examples, including the CF representation of quasihole, quasielectron, and neutral exciton.

2.1.5 The Moore-Read and Read-Rezayi states

The CF wave function proposed by Jain is very successful in explaining the existence of a number of incompressible states. It also predicts the existence of a compressible state at $\nu = 1/2$. It corresponds to a situation, for $n = 2$ attached fluxes per electron, where all the magnetic flux quanta have been absorbed to form composite fermions, such that the effective cyclotron gap between Landau levels vanishes. This state can thus be described as a Fermi liquid of CF, and is metallic. This is consistent with the absence of a Hall conductivity plateau at $\nu = 1/2$, as well as the fact that most Hall fractions have an odd denominator. In 1987, however, Willett et. al [169] discovered a plateau at $\nu = 5/2$ (see also Ref. [117]), corresponding to a half filled second Landau level. While the first interpretations leaned towards a spin-single state [62], it is now a consensus that the state at $5/2$ is spin polarized. The partially filled second Landau level can be modeled as the lowest Landau level, with a modified Coulomb interaction (assuming the lower Landau levels are completely filled and inert). This effective interaction may cause the pairing of composite fermions, at the origin of the instability of the Fermi liquid, similar to the BCS (Bardeen-Cooper-Schrieffer) instability giving rise to superconductivity. A wave function was proposed by Moore and Read [105] (and independently by Greiter, Wen, Wilczek [52, 53]) to describe the incompressible state at $\nu = 5/2$. The Moore-Read wave function was subsequently proven [66] to be a p-wave paired state of composite fermions. It writes

$$\Psi_{1/2}^{Pf}(z_1, \dots, z_N) = Pf\left(\frac{1}{z_i - z_j}\right) \prod_{i < j} (z_i - z_j)^2 e^{-\frac{1}{4l_B^2} \sum_j |z_j|^2} \quad (2.31)$$

where Pf stands for Pfaffian. The Pfaffian is defined for any N -dimensional (with N even) antisymmetric matrix A as

$$Pf(A) = \sum_{\sigma} \varepsilon_{\sigma} A_{\sigma(1)\sigma(2)} A_{\sigma(2)\sigma(3)} \dots A_{\sigma(N-1)\sigma(N)} \quad (2.32)$$

where the sum runs over all permutations of indexes σ , and ε_{σ} is the signature of the permutation. $Pf\left(\frac{1}{z_i - z_j}\right)$ is antisymmetric under the exchange of two particles, such that the Moore-Read wave function describes a fermionic state. This wave function can always be divided by a Jastrow factor $\prod_{i < j} (z_i - z_j)$ to describe a bosonic state. The fermionic and bosonic Moore-Read wave functions respectively describe a state at filling fractions $1/2$ and 1 . Numerical simulations in finite size systems [140] have shown that the Moore-Read Pfaffian state was a very realistic candidate to describe the $5/2$ quantum Hall plateau. While the filling fraction $1/2$ is its own particle-hole conjugate, the Pfaffian wave function is not particle-hole symmetric.

Its particle-hole conjugate, the anti-Pfaffian, is also a good candidate to describe the $5/2$ phase. Indeed, finding out which one of the Pfaffian and anti-Pfaffian wave functions provide the best description for the $5/2$ plateau is still a very active field of research [165, 141, 116, 120].

Several years after the proposal of Moore and Read, Cappelli [29] showed that their wave function could be written as the antisymmetrized product of two correlated Laughlin states. Omitting the Gaussian factors, this writes

$$\Psi_{1/2}^{Pf}(z_1, \dots, z_N) = \mathcal{A} \left(\prod_{1 \leq i < j \leq N/2} (z_i - z_j)^3 \prod_{N/2 < i < j \leq N} (z_i - z_j)^3 \prod_{1 \leq i \leq N/2 < j \leq N} (z_i - z_j) \right) \quad (2.33)$$

where \mathcal{A} operates the antisymmetrization over all particle coordinates. The bosonic Moore-Read state at $\nu = 1$ is, even more simply, written as the symmetrized product of two decoupled Laughlin liquids

$$\Psi_1^{Pf}(z_1, \dots, z_N) = \mathcal{S} \left(\prod_{1 \leq i < j \leq N/2} (z_i - z_j)^2 \prod_{N/2 < i < j \leq N} (z_i - z_j)^2 \right) \quad (2.34)$$

where \mathcal{S} operates the symmetrization over all particle coordinates. Cappelli et al. [30] showed that this can be generalized to the symmetrized product of k Laughlin liquids, yielding the \mathbb{Z}_k Read-Rezayi [129] state at filling fraction $\nu = k/2$

$$\Psi_k(z_1, \dots, z_N) = \mathcal{S} \left(\prod_{0 \leq j < k} \Psi_{1/2}^L(z_{1+jN/k}, \dots, z_{N+jN/k}) \right) \quad (2.35)$$

where $\Psi_{1/2}^L$ is the Laughlin state $\nu = 1/2$ defined in Eq. (2.17). The bosonic Read-Rezayi states are the exact densest ground states of a model interaction, the $(k+1)$ -body contact interaction

$$H_B^{k+1} = \sum_{i_1 < \dots < i_{k+1}} \prod_{j=1}^k \delta^{(2)}(z_{i_j} - z_{i_{j+1}}) \quad (2.36)$$

This is the $(k+1)$ -body generalization of Eq. (2.12), the two-body contact interaction corresponding to the pseudopotential V_0 . The Read-Rezayi states obey some very specific vanishing properties: all bosonic \mathbb{Z}_k Read-Rezayi wave functions vanish when $(k+1)$ of the N bosons are brought to the same position. For instance, the bosonic Laughlin and Moore-Read wave functions respectively vanish when a cluster of two (respectively three) particles is formed. These properties are the origin of the Read-Rezayi states being exact ground states of the Hamiltonian 2.36. The fermionic Read-Rezayi states can be deduced from their bosonic counterparts by multiplication by a Jastrow factor. They are the exact ground states of the $(k+1)$ -body hollow core interaction, the generalization of the V_1 pseudopotential interaction (2.13) [129]. Consequently, for each bosonic Read-Rezayi state at filling fraction ν_B , there is a fermionic Read-Rezayi state verifying $\nu_F^{-1} = 1 + \nu_B^{-1}$. The $k = 3$ Read-Rezayi state (or, more precisely, its particle-hole conjugate) is one of the candidates to explain the Hall conductivity plateau observed at $\nu = 12/5$ [177, 182, 104].

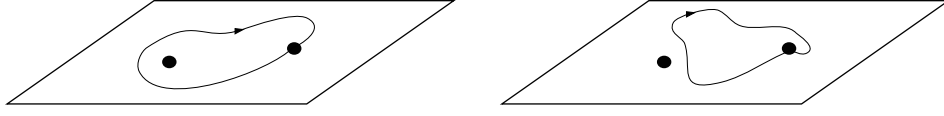


Figure 2.5: Two indistinguishable particles in 2D. A closed path taking one particle around the other (*left*) is not equivalent to the loop that does not encircle the other particle (*right*)

2.2 Anyons and topological degeneracy

In the previous section, we have reported the experimental observation of the fractional quantum Hall effect, and given some ansatz wave functions to understand this phenomenon. While it is important to understand the origin of the fractions, we have left out the most interesting and novel aspect of the fractional quantum Hall effect, which is its anyonic – abelian and non-abelian – excitations.

2.2.1 Abelian anyons in the fractional quantum Hall effect

In three dimensions, particles are characterized by an exchange statistics that can only be bosonic or fermionic. Let us picture, for two indistinguishable particles, the possible paths that bring back one particle to its original position. All such closed paths can be continuously deformed into a point without enclosing the second particle. As a result, the wave function of this two-particle system must be unchanged after one particle goes around a loop. We consider a translationally invariant system: as a result, having one particle go around the other is equivalent to permuting the two particles twice. The two-particle wave function must be the same (if the particles are bosons), or the opposite (if they are fermions) after one permutation, so that it is unchanged after two permutations. In two dimensions, however, not all closed loops are equivalent [93, 168] (see Fig. 2.5): a path through which one particle encircles the other is not equivalent to a path through which it does not (these paths cannot be transformed into one another without going over the second particle). As a result, the wave function describing this two-particle state need not return to itself after the loop, but rather can be modified by any phase 2θ

$$\Psi(\mathbf{r}_1, \mathbf{r}_2) \rightarrow e^{2i\theta} \Psi(\mathbf{r}_1, \mathbf{r}_2) \quad (2.37)$$

θ is the exchange phase picked up by the wave function under the counterclockwise exchange of the two particles.

$$\Psi(\mathbf{r}_1, \mathbf{r}_2) \rightarrow e^{i\theta} \Psi(\mathbf{r}_2, \mathbf{r}_1) \quad (2.38)$$

If $\theta = 0$ or π , the particles are bosons or fermions, respectively. Particles with a different value of the statistical angle θ are called anyons. This shows that the existence of anyons is possible in principle in two dimensions. Since we live in a

three-dimensional world, no elementary particle can be anyonic. Rather, fractional statistics may appear as an emergent property in a many-body system.

The fractional quantum Hall effect provided the first experimental realization of anyonic particles. The Laughlin quasiholes, for example, are anyons with a statistical angle $\theta = \pi/q$. Let us show this property by considering a $\nu = 1/q$ Laughlin liquid with two quasiholes at complex coordinates w_0 and w_1 . Using the construction of Eq. (2.25), we can write the wave function of this system as

$$\Psi_{1/q}^{2qh}(z_1, \dots, z_N) = \mathcal{N} \cdot (w_0 - w_1)^{1/q} \cdot \left(\prod_j (z_j - w_0)(z_j - w_1) \right) \cdot \Psi_{1/q}^L(z_1, \dots, z_N) \quad (2.39)$$

where \mathcal{N} is a normalization constant. It can be shown [90, 65, 55, 147, 127] that \mathcal{N} does not depend on the different quasihole positions as long as they stay far apart ($|w_0 - w_1| \gg l_B$). When exchanging the two quasiholes w_0 and w_1 , we see that $\Psi_{1/q}^{2qh}$ picks up a factor $e^{i\pi/q}$ from the factor $(w_0 - w_1)^{1/q}$. The Laughlin quasiholes thus have an anyonic statistics [7], with a statistical angle π/q .

Topological field theory provides a more general framework to discuss the anyonic properties of the fractional quantum Hall elementary excitations. Zhang, Hans and Kivelson [181], following a seminal work by Girvin and MacDonald [48], described the Laughlin fractions in terms of a Chern-Simons field theory. Lopez and Fradkin [100] extended this theory to arbitrary composite fermion fractions using a mean field approach of Jain's construction. In this language, the binding of flux to the electrons is represented by a Chern-Simons term in the Lagrangian. It is then possible to recover the braiding statistics of the states' excitations using general principles of topological field theory. The elementary excitations of a $\nu = p/q$ (p and q relatively prime) composite fermion ground state are found to be π/q anyons. Note that this approach relies on the existence of a gap above the quantum Hall ground state, which is related to the properties of the Coulomb Hamiltonian, not just the properties of the ground state.

2.2.2 Non-abelian anyons in the fractional quantum Hall effect

Non-abelian statistics occur when the position of the particles is not sufficient to specify a quantum state. Let us consider a g dimensional degenerate subspace of the N -body Hilbert space, spanned by the orthonormal basis $\{\Psi_\alpha\}_{1 \leq \alpha \leq g}$. The exchange of two of the N particles can result in more than a phase change of each wave function Ψ_α , but can send the system into a different state with the same particle configuration. Generically, particle exchange corresponds to a linear transformation on the basis $\{\Psi_\alpha\}_{1 \leq \alpha \leq g}$ (the group of such transformations is called the braid group). If the subspace is non-degenerate ($g = 1$), then the braid group is the unitary group $U(1)$, and all transformations commute. However, for $g > 1$, the representations of the braid group are $g \times g$ matrices, and do not necessarily commute. We call \mathcal{E}_{ij} the representation of the braid group that exchanges particles i and j . The exchange of

particles i and j results in the following wave function change:

$$\Psi_\alpha \rightarrow \sum_{\beta} \mathcal{E}_{ij}^{\alpha\beta} \Psi_\beta \quad (2.40)$$

If the \mathcal{E}_{ij} matrices do not commute, the braid group is non-abelian. The quasiparticles described by this braid group are then called non-abelian anyons. Braiding them will cause non-trivial rotations within the subspace of degenerate states $\{\Psi_\alpha\}_{1 \leq \alpha \leq g}$. Furthermore, no local operation can lift the degeneracy between these states (by definition, all Ψ_α are described by the same quantum numbers). Braiding is thus the only way to perform a non-trivial operation on these states. Non-abelian anyons were mostly a very interesting physical curiosity until Kitaev [79] proposed to exploit this property to build a quantum computer. He showed that the degrees of freedom of degenerate non-abelian anyons could be used for non-local storage of information (qubits). In this context, a braiding operation would act as a unitary quantum gate. Since the degeneracy of non-abelian anyons is extremely robust (no local perturbation can lift it), these qubits could be used to build a fault-tolerant quantum computer. This justifies the current experimental and theoretical interest in non-abelian anyons, and the search for a system that would support them.

Moore and Read predicted [105] that the excitations of their candidate wave function for the 5/2 plateau were non-Abelian anyons. Likewise, the Read-Rezayi states may support non-abelian anyons of a different nature. The zero energy ground states of the model Hamiltonian Eq. 2.36 for each value of k (in other words the Laughlin, Moore-Read and Read-Rezayi wave functions) all can be written [45, 105] as the correlators of some conformal field theory [18, 106, 40] (CFT) operators. The braiding statistics of their quasiholes were predicted by using a conjecture [105] that links the braiding statistics of the quasiholes with the nature of the corresponding CFT. Note that a system with anyonic particles generally has different types of anyons. For example, the bound state of two abelian anyons with statistics θ form an abelian anyon with statistics 4θ . The process of bringing together two anyons to form a new one is called fusion. A complete description of the system must include the higher order anyons resulting from the fusion of two anyons. The fusion of two anyons may result in more than one type of anyon: these different possibilities are called fusion channels. Multiple fusion channels are the hallmark of a non-abelian anyon. For example, the Moore-Read state is described by an Ising CFT, which has three different types of anyons, noted $\mathbf{1}$, σ and Ψ . We note $a \times b$ the fusion of two anyons a and b , $+$ separates different fusion channels. The fusion rules of the Ising anyons are

$$\begin{aligned} \sigma \times \sigma &= \mathbf{1} + \Psi, & \sigma \times \Psi &= \sigma, & \Psi \times \Psi &= \mathbf{1}, \\ \mathbf{1} \times \Psi &= \Psi, & \mathbf{1} \times \sigma &= \sigma, & \mathbf{1} \times \mathbf{1} &= \mathbf{1} \end{aligned} \quad (2.41)$$

One can note a similarity of these rules with the fusion rules of two $SU(2)$ angular momenta, where $\mathbf{1}$, σ and Ψ respectively correspond to a total momentum $S = 0$, $1/2$ and 1 , with a truncation at $S = 1$. For this reason, these fusion rules are also

called $SU(2)_2$. More generically, the \mathbb{Z}_k Read-Rezayi states are written as correlators of CFT whose anyons follow $SU(2)_k$ fusion rules, the analog of the $SU(2)$ fusion rules of angular momentum, with a truncation at $S = k/2$.

Analytical arguments can be used to derive the braiding properties of the Laughlin (see previous section) and Moore-Read [55, 127, 28] wave functions. However, these arguments rely on the screening properties of the system to localize the quasiholes, which can only be verified numerically. The statistics of FQH quasiholes can also be verified directly by numerical braiding. The limited system sizes accessible to numerical simulation often limit these computer experiments, especially since the braiding is only well defined for distant quasiholes, a constraint that requires relatively large systems. The increasing complexity of the fusion rules of the \mathbb{Z}_k anyons makes this even more challenging for higher k , since a larger number of quasiholes is required to explore the increasing number of fusion channels. The braiding properties of the Moore-Read quasiholes have been verified numerically using exact diagonalization and Monte Carlo techniques [161, 125, 10]. These techniques do not allow to reach the system sizes necessary to detect the braiding properties of the \mathbb{Z}_3 quasiholes. These were thus only verified recently [173], with the help of matrix product states, a numerical method that was only developed in recent years for the fractional quantum Hall effect. In spite of the great experimental advances [3, 170] to determine whether the $5/2$ state supports non-abelian Ising excitations, direct conclusive evidence is still lacking. However, given the success of the Moore-Read state to describe the $\nu = 5/2$ state in numerical simulations, it is likely to be the case. Likewise, the $12/5$ fractional quantum Hall state (which is likely well described by the \mathbb{Z}_3 state) is a plausible candidate for the realization of $SU(2)_3$ (Fibonacci) anyons.

2.2.3 Topological degeneracy on the torus

The existence of fractionalized (abelian or non-abelian) excitations in a system is associated with a type of order called *topological order*. Like the topological invariant of the non-interacting phases studied in the first chapter of this thesis, topological order cannot be detected by any local measurement. The presence of topological order in a system is signaled by the non-trivial degeneracy of the low energy states, which depends on the genus of the surface on which it is defined. Most strikingly, the ground state of any topologically ordered phase is degenerate on a non-zero genus surface. This degeneracy is particularly robust, and cannot be lifted by any local perturbation. The torus is the simplest example of a surface where the topological degeneracy occurs, and is particularly convenient for numerical simulations, since it simply corresponds to periodic boundary conditions.

2.2.3.1 Many-body quantum numbers on the torus and center of mass degeneracy

Quantum Hall systems at a rational filling fraction $\nu = p/q$, where p and q are relative primes have an exact q -fold degeneracy on the torus geometry. This degeneracy is a consequence of the magnetic translation algebra (Eq. (1.39)), which can be seen, following Haldane [58], by analyzing the many-body symmetries of the Hamiltonian on the torus.

In a system of N particles, we can decompose the translation of a particle i by a vector \mathbf{a} into a center of mass (CM) and a relative (rel) part $\mathcal{T}_i(\mathbf{a}) = T_{rel,i}(\mathbf{a}) T_{CM}(\mathbf{a}/N)$

$$\begin{aligned} T_{rel,i}(\mathbf{a}) &= \mathcal{T}_i(\mathbf{a}) \prod_{j=1}^N \mathcal{T}_j(-\mathbf{a}/N) \\ T_{CM}(\mathbf{a}) &= \prod_{i=1}^N \mathcal{T}_i(\mathbf{a}/N) \end{aligned} \quad (2.42)$$

The center of mass translation by an arbitrary vector commutes with the Hamiltonian, but not necessarily with the single-particle operators $\mathcal{T}_i(L_j \mathbf{e}_j)$, $j = x, y$. Since we used these operators to define a single-particle basis, it is useful to define the following center of mass operators, which commute with all $\mathcal{T}_i(L_j \mathbf{e}_j)$

$$T_{CM,x} = T_{CM} \left(\frac{L_x \mathbf{e}_x}{N_\phi} \right), \quad T_{CM,y} = T_{CM} \left(\frac{L_y \mathbf{e}_y}{N_\phi} \right) \quad (2.43)$$

We also define the following set of relative translation operators

$$T_{rel,x} = T_{rel,i}(p L_x \mathbf{e}_x), \quad T_{rel,y} = T_{rel,i}(p L_y \mathbf{e}_y) \quad (2.44)$$

We note that $T_{rel,x} = ((T_{CM,x})^q)^\dagger$ (and likewise with $T_{rel,y}$). This justifies dropping the index i , since these relative operators do not depend on the particle i . As powers of center of mass operators, the above defined relative translation operators commute with the Hamiltonian. The center of mass translation operators themselves do not commute, but have a simple commutation relation, which follows from the algebra of magnetic translations, the GMP algebra Eq. (1.39). Their commutation relation writes

$$T_{CM,y} T_{CM,x} = T_{CM,x} T_{CM,y} e^{-i2\pi p/q} \quad (2.45)$$

We choose to label the many-body eigenstates of the Hamiltonian with the center of mass momentum \mathbf{k}_y , which is just the sum of the single-particle momenta modulo N_ϕ , such that $e^{-2\pi i \mathbf{k}_y / N_\phi}$ is an eigenvalue of $T_{CM,y}$. Since $[T_{CM,y}, T_{rel,x}] = 0$, we can also diagonalize $T_{rel,x}$ simultaneously. We call N_0 the greatest common divisor of N and N_ϕ

$$N_0 = \text{GCD}(N, N_\phi) \quad (2.46)$$

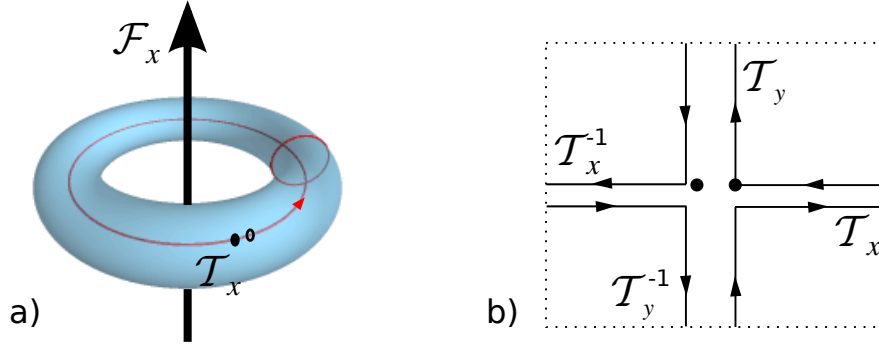


Figure 2.6: Quasiparticle braiding and topological degeneracy on the torus. a) \mathcal{F}_x represents the threading of a unit flux quantum in the hole of the torus. \mathcal{T}_x corresponds to the creation of a quasiparticle-quasihole pair, followed by the translation around the torus of the quasiparticle, and their annihilation. For anyonic quasiparticles, these operations do not commute (see Eq. (2.48)). b) Braiding a quasiparticle around another on the torus. The torus is symbolized by a rectangle whose parallel sides are related by periodic boundary conditions.

We note that $(T_{rel,x})^{N_0} = T_{rel,i}(NL_x \mathbf{e}_x) = \mathbf{1}$. $T_{rel,x}$ thus has N_0 distinct eigenvalues $e^{2\pi i k_x / N_0}$, where $k_x = 0, \dots, N_0 - 1$ is an integer. We are equipped with a two-dimensional momentum quantum number, defined in a $N_0 \times N_\phi$ Brillouin zone, to label the many-body eigenstates of the Hamiltonian.

Finally, we can use the commutation relation Eq. (2.45) to derive the center of mass degeneracy on the torus. Let us consider an eigenstate $\Psi_{\mathbf{k}_x, \mathbf{k}_y}$ of the Hamiltonian and of the relative and center of mass operators $T_{CM,y}$ and $T_{rel,x}$. Eq. (2.45) implies

$$\begin{aligned} T_{CM,y}(T_{CM,x}\Psi_{\mathbf{k}_x, \mathbf{k}_y}) &= T_{CM,x}e^{-i2\pi p/q}T_{CM,y}\Psi_{\mathbf{k}_x, \mathbf{k}_y} \\ &= e^{-i2\pi p/q}e^{-2\pi i k_y / N_\phi}T_{CM,x}\Psi_{\mathbf{k}_x, \mathbf{k}_y} \end{aligned} \quad (2.47)$$

One can thus create q different eigenstates of $T_{CM,y}$ by successive applications of $T_{CM,x}$. Since $[T_{rel,x}, T_{CM,x}] = 0$, \mathbf{k}_x is not affected by the action of $T_{CM,x}$. Moreover, all q states have the same energy, since $T_{CM,x}$ commutes with the Hamiltonian. The state $(T_{CM,x}\Psi_{\mathbf{k}_x, \mathbf{k}_y})$ has a center of mass momentum $(\mathbf{k}_y + N_0)$ modulo N_ϕ . The $N_0 \times N_\phi$ magnetic Brillouin zone can thus be divided into q degenerate zones of size $N_0 \times N_0$. The region $N_0 \times N_0$ is called reduced Brillouin zone.

2.2.3.2 Topological degeneracy from fractionalization

In the previous section, the degeneracy of fractional quantum Hall states on the torus appeared as a consequence of the many-body magnetic translation algebra. For instance, this tells us that the Laughlin $1/m$ state must have a degeneracy that is a multiple of m . In fact, the Laughlin state is exactly m -fold degenerate. Likewise,

the composite fermion states at $\nu = p/(2np + 1)$ are $2np + 1$ -fold degenerate on the torus. For non-abelian states, the degeneracy is higher than the center of mass degeneracy: for instance, the bosonic Moore-Read state at filling fraction $\nu = 1$ is threefold degenerate. Generically, the degeneracy of a state on the torus geometry is equal to the number of different quasiparticles (anyons) that constitute the theory. For example, Laughlin $1/q$ has q different quasiparticles, characterized by the statistical angles $2\pi l/q$ where l is a positive integer smaller than q ($0 \leq l < q$). The bosonic Moore-Read state has three quasiparticles $\mathbf{1}$, σ and Ψ (see Eq. (2.41)), and is indeed threefold degenerate on the torus. I will not demonstrate the general property here, but I would like to give some arguments, following Refs. [115, 114], to illustrate the fundamental connection between fractionalization of the quantum numbers (charge and statistical angle) and topological degeneracy.

We consider a system of electrons on the torus, with a finite gap above the ground state(s), and elementary quasihole/quasiparticle excitations of fractional charge $e^* = e\frac{p}{q}$ (where p and q are coprimes). We note \mathcal{F}_x the operator that realizes the insertion of a unit flux quantum through the hole of the torus, thus inducing a vector potential in the x direction. We call \mathcal{T}_x the operation of creating a quasiparticle-quasihole pair, thread the quasiparticle around the torus along the x direction and pair-annihilate it with the quasihole. A schematic representation of these two operators is given in Fig. 2.6a). \mathcal{F}_x and \mathcal{T}_x do not commute, due to the Aharonov-Bohm phase collected by the quasiparticle when encircling the additional flux caused by \mathcal{F}_x . Rather, we have

$$\mathcal{T}_x \mathcal{F}_x = \mathcal{F}_x \mathcal{T}_x e^{2\pi i p/q} \quad (2.48)$$

where the non-trivial phase is caused by the fractional charge p/q carried by the quasiparticle. Note that, strictly speaking, the Hamiltonian is not intact after the unit flux insertion, but is related to the initial Hamiltonian by a unitary transformation (the same thing happens to \mathcal{T}_x). The above relation is thus correct if the flux insertion is accompanied by a gauge transformation. The two processes \mathcal{T}_x and \mathcal{F}_x should map a ground state to a ground state. The algebra Eq. (2.48) leads to a degeneracy of the ground state that is a multiple of q . The same construction in the y direction yields

$$\mathcal{T}_y \mathcal{F}_y = \mathcal{F}_y \mathcal{T}_y e^{2\pi i p/q} \quad (2.49)$$

If the operations in the x and y directions were independent, this would lead to a degeneracy that is a multiple of q^2 . Depending on the particle statistics, this may not be the case. In the case of an abelian quasiparticle of statistical angle θ , the braiding of two such anyons leads to

$$\mathcal{T}_x \mathcal{T}_y = \mathcal{T}_y \mathcal{T}_x e^{2i\theta} \quad (2.50)$$

(this can easily be understood by considering one anyon performing a loop $\mathcal{T}_x^{-1} \mathcal{T}_y^{-1} \mathcal{T}_x \mathcal{T}_y$ around the other one, as represented in Fig. 2.6b) Note that here, the non-trivial commutation relation of \mathcal{T}_x and \mathcal{T}_y comes from the fractional statistics of the quasiparticles. In the case of fermions $\theta = \pi$ or bosons $\theta = 0$, the two algebra Eqs. (2.48)(2.49) are equivalent, and the degeneracy of the ground state

must be a multiple of q^2 . For anyonic quasiparticles, however, this not be the case. In fact, we know that the degeneracy of the Laughlin state is q . In this case, Wen and Niu [167] have argued that \mathcal{T}_x induces a flux through the torus, just as \mathcal{F}_y does. Therefore, as far as the action on the ground state is concerned, we can identify \mathcal{T}_x and \mathcal{F}_y together (likewise with \mathcal{T}_y and \mathcal{F}_x^{-1}). This leads to the result of Ref. [115]: on the torus: the degeneracy of a ground state supporting excitations with a fractionalized charge ep/q must be a multiple of q -fold degenerate. This highlights the intricate connection between fractional charge, fractional statistics, and topological degeneracy on the torus: these three properties cannot exist separately.

2.2.4 Haldane's exclusion principle

Fermionic and bosonic statistics are associated with constraints on the occupation of the single-particle orbitals (the Pauli exclusion principle), which determine the dimension of the associated many-body Hilbert space. This concept translates to anyonic systems: a system with a given number of anyonic particles has a specific Hilbert space dimension, which depends on the nature of the anyonic nature of the excitations. One says that the number of states associated with a given number of anyonic particles is a signature of the topological order. In 1991, Haldane [56] introduced the concept of a generalized exclusion principle for particles with anyonic statistics. Let us consider a N -body system whose single-particle orbitals can be labeled by an extensive quantum number. Haldane's exclusion principle aims at predicting the counting of anyonic excitations in this system by imposing rules on the orbital occupation. A (k, r) -admissible partition labels a Fock state, whose occupation configuration has no more than k particles in r consecutive orbitals. The (k, r) exclusion principle is thus a generalization of the Pauli principle, which limits the occupation of each orbital to a single fermion, i.e. $k = 1, r = 1$.

The number of zero modes in a fractional quantum Hall system with a given number of quasiholes is a signature of its topological order. The generalized exclusion principle predicts the number of quasihole excitations of a fractional quantum Hall state in many situations. On the plane, Bernevig and Haldane [22, 21] showed that several bosonic quantum Hall states are equal (up to a Gaussian factor) to symmetric polynomials called the Jack polynomials, and verify a (k, r) clustering property. A (k, r) clustered state is a state that vanishes at power r when a cluster of $(k + 1)$ particles is brought to the same position, and corresponds to a filling fraction $\nu = k/r$. They showed that the number of (k, r) clustered states is equal to the number of (k, r) -admissible partitions. The $\nu = 1/q$ Laughlin state is a clustered state with $k = 1, r = q$. The number of Laughlin quasiholes for a given number of particles N and number of flux quanta N_ϕ can thus be predicted by the $(1, q)$ generalized exclusion principle. For instance, the Laughlin $1/3$ ground state with $N = 6$ fermions corresponds to a unique $(1, 3)$ -admissible partition on the plane, which writes

$$1\ 0\ 0\ 1\ 0\ 0\ 1\ 0\ 0\ 1\ 0\ 0\ 1\ 0\ 0\ 1 \quad (2.51)$$

where each integer represents the occupation of an orbital (here, 0 or 1 since we

are considering fermions). In the partition above, the orbitals are implicitly labeled with their angular momentum $l_z = 0, 1, \dots, N_\phi$, from left to right. Since the angular momentum is an extensive, conserved quantum number, each admissible partition has a well defined total angular momentum L_z , and the exclusion principle yields a counting that is resolved in L_z . The Moore-Read and \mathbb{Z}_k Read-Rezayi states also are clustered states, and the number of their quasihole excitations is given by a $(k, r = 2)$ counting rule. The Haldane exclusion principle can be generalized to the torus geometry in the case of the Laughlin, Moore-Read, and Read-Rezayi states. In this case, one has to take into account the periodic boundary conditions on the torus to determine the admissibility of a partition, in order to obtain the number of quasihole excitations. For instance, the threefold degeneracy of the $1/3$ Laughlin state on the torus is related to the existence of three admissible particle partitions. A partition is written as a series of integers, each describing the occupation of an orbital of momentum quantum number $k_y = 0, \dots, N_\phi - 1$. For $N = 6$, the admissible partitions of the $1/3$ Laughlin state on the torus write

$$\begin{array}{cccccccccccc} 1 & 0 & 0 & 1 & 0 & 0 & 1 & 0 & 0 & 1 & 0 & 0 & 1 & 0 & 0 & 1 & 0 & 0 \\ 0 & 1 & 0 & 0 & 1 & 0 & 0 & 1 & 0 & 0 & 1 & 0 & 0 & 1 & 0 & 0 & 1 & 0 \\ 0 & 0 & 1 & 0 & 0 & 1 & 0 & 0 & 1 & 0 & 0 & 1 & 0 & 0 & 1 & 0 & 0 & 1 \end{array} \quad (2.52)$$

Note that for a configuration on the torus, the exclusion principle should be understood with periodic boundary conditions, i.e. the first and last orbitals of the configurations are considered consecutive.

2.3 Fractional Chern insulators

2.3.1 Motivations and challenges on the experimental side

In the previous chapter, we saw that the physics of the quantum Hall effect could be observed in a lattice system in the absence of a magnetic field. More precisely, the Bloch bands of a lattice system may be described by a non-zero Chern number, and a band characterized by a Chern number $C = 1$ is akin to the lowest Landau level of a two-dimensional system subjected to a magnetic field. Given these similarities in the non-interacting regime, we expect Chern insulators to host features similar to those of the fractional quantum Hall effect once interactions are turned on and the Chern band is partially filled. For a lattice with $N_x \times N_y$ unit cells and periodic boundary conditions, the number of single-particle orbitals in a given band is equal to $N_x N_y$. The filling factor in a Chern insulator is defined by reference to its quantum Hall effect analog, as

$$\nu^{FCI} = \frac{N}{N_x N_y} \quad (2.53)$$

When ν^{FCI} is a rational number, in the presence of strong interactions, Chern insulators may host phases with fractionalized excitations. Indeed, the absence of need for a magnetic field would make these materials more suitable than the fractional

quantum Hall effect to be used as qubits. While there is an array of analytical and numerical evidence to support the existence of fractional Chern insulators, they have not yet been observed experimentally. This is not surprising, given the difficulty to observe the Hall plateaus in a Chern insulator at integer filling (see Sec. 1.2.4.1). Indeed, the gaps opened at fractional filling in the fractional quantum Hall effect are much smaller than the gaps observed at integer filling, and their observation requires smaller temperature and higher mobility samples. Currently, the conditions of observation of the quantum anomalous Hall effect are much harder to achieve than those for the fractional quantum Hall effect. There might be more hopeful perspectives in realizing fractional Chern insulators in optical lattices, with the help of artificial gauge fields (see Sec. 1.2.4.2), since these are more controlled systems. Still, diverse heating processes [36] currently prevent suitably low temperatures from being reached in these systems.

2.3.2 Emergence of a fractional Chern insulator

Even at zero temperature, in a perfect system with no disorder, the existence of an incompressible phase at fractional filling in a strongly interacting Chern insulator is not guaranteed. For example, no numerical evidence [172] of such a phase has been found in the two-orbital square lattice model of Sec. 1.2.3.2. The conditions for the emergence of such a phase are a rich and active topic of theoretical condensed matter physics. The general idea is that an incompressible phase is most likely to appear in a Chern band when its properties make it most similar to a Landau level. Since the Laughlin state is one of the most stable FQH states, one can expect that it might be the easiest phase to realize in a fractional Chern insulator. We consider the two operators that translate a particle by a lattice vector, projected onto the topological band of a Chern insulator. The algebra formed by these operators (the analog of the GMP algebra (1.39)) does not close [121]. As a result, the pseudopotential construction 2.1.2 does not hold. While it is possible to write the Laughlin wave function in the Bloch basis of a Chern insulator [174], writing a microscopic model Hamiltonian for this wave function is a complicated task [92], and the resulting Hamiltonian strongly depends on the lattice. On the lattice, the contact interaction (2.12) of bosons can be replaced by an on-site Hubbard term

$$H_{int}^b = U \sum_i : \rho_i \rho_i : \quad (2.54)$$

where $\rho_i = c_i^\dagger c_i$ is the density operator on site i , and $::$ represents normal ordering. For fermions, a nearest-neighbor interaction

$$H_{int}^f = U \sum_{\langle i,j \rangle} : \rho_i \rho_j : \quad (2.55)$$

is a good approximation of the hollow core interaction (2.13) V_1 .

As for the kinetic part of the Hamiltonian, one can choose among the multiple lattice Chern insulator models that have been proposed. Historically, the Haldane

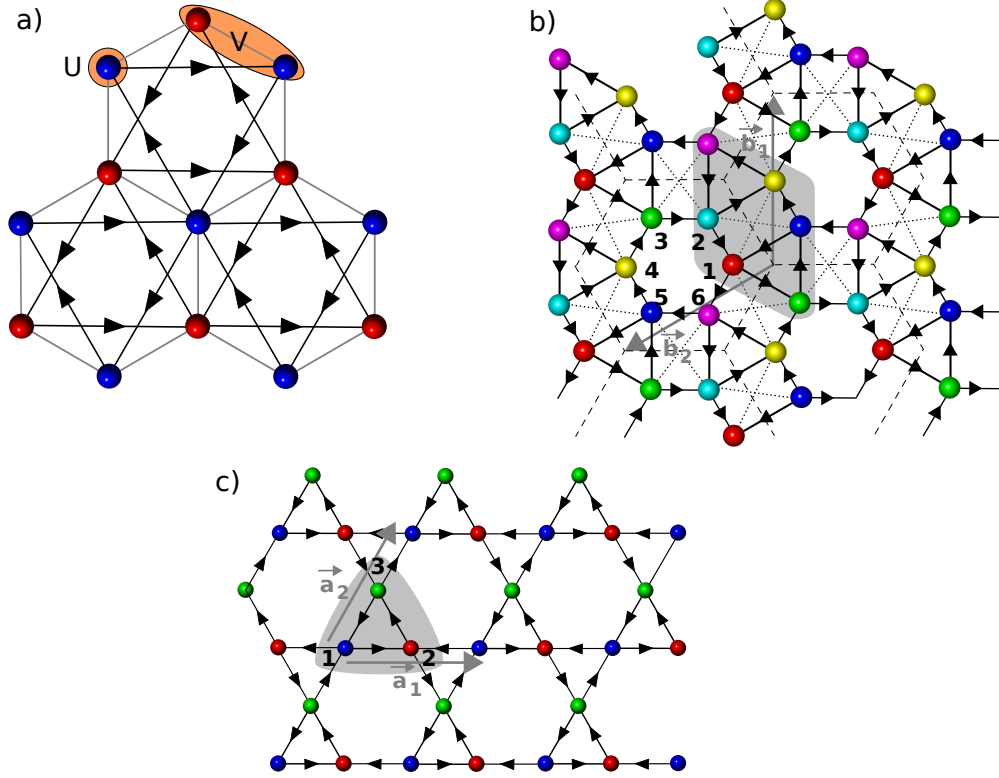


Figure 2.7: The Haldane (a) and ruby (b) and kagome (c) lattice Chern insulator models. a) The Haldane model is based on the honeycomb lattice (triangular Bravais lattice with two atoms per unit cell). It consists of nearest neighbor and next nearest neighbor hopping terms of respective amplitudes t_1 and $t_2 e^{i\phi}$, as well as a mass term $\pm M$. b) The ruby lattice is based on a triangular lattice with 6 atoms per unit cell, with nearest and next nearest neighbor hopping terms. c) The kagome lattice is based on a triangular lattice with 3 atoms per unit cell. We limit ourselves to nearest neighbor hopping of complex amplitude $t_1 + i\lambda_1$. In all three figures, the direction of the arrows gives the convention for the sign of the phase of the complex hopping terms. The gray An on-site (U) and nearest neighbor (V) Hubbard interaction are represented by an orange ellipse on top of the lattice structure of the Haldane model.

model [60] is the first example of a Chern insulator. It is supported by a honeycomb lattice (see Fig. 2.7a), which is a triangular lattice with two atoms per unit cell. The hopping between nearest neighbors on the lattice has a real amplitude t_1 , while the hopping between next nearest neighbors has a complex amplitude $t_2 e^{i\phi}$ in the direction of the arrows of Fig. 2.7a. Another example of a Chern insulator, which will appear a lot in this manuscript is the ruby lattice model [71]. The ruby lattice model has 6 atoms per unit cell and is spanned by \mathbf{b}_1 and \mathbf{b}_2 (see Fig. 2.7b). The six sites are denoted from 1 to 6, and the Bloch Hamiltonian is

$$h(\mathbf{k}) = \begin{pmatrix} & |1\rangle & |2\rangle & |3\rangle & |4\rangle & |5\rangle & |6\rangle \\ \begin{pmatrix} 0 & & & & \text{h.c.} & \\ t_1^* & 0 & & & & \\ t & t_1^* e^{-i(k_1+k_2)} & 0 & & & \\ t_4(1+e^{ik_1}) & t & t_1^* e^{ik_1} & 0 & & \\ t^* & t_4(1+e^{-i(k_1+k_2)}) & t & t_1 & 0 & \\ t_1 e^{ik_1} & t^* & t_4(e^{ik_1} + e^{i(k_1+k_2)}) & t & t_1^* e^{i(k_1+k_2)} & 0 \end{pmatrix} & \begin{matrix} |1\rangle \\ |2\rangle \\ |3\rangle \\ |4\rangle \\ |5\rangle \\ |6\rangle \end{matrix} \end{pmatrix} \quad (2.56)$$

where $k_1 = \mathbf{k} \cdot \mathbf{b}_1$ and $k_2 = \mathbf{k} \cdot \mathbf{b}_2$. We also define the kagome lattice Chern insulator model [156], which is defined on a triangular lattice with 3 atoms per unit cell (see Fig. 2.7c). The original model of Ref. [156] had nearest neighbor as well as next nearest neighbor tunneling terms, but we restrict ourselves to the former. We write $t_1 + i\lambda_1$ the complex amplitude of this tunneling term. The Bloch Hamiltonian of the kagome Chern insulator model is

$$h(\mathbf{k}) = \begin{pmatrix} & |1\rangle & |2\rangle & |3\rangle \\ \begin{pmatrix} 0 & (t_1 + i\lambda_1)(1 + e^{-ik_x}) & (t_1 - i\lambda_1)(1 + e^{-ik_y}) \\ & 0 & (t_1 + i\lambda_1)(1 + e^{i(k_x - k_y)}) \\ \text{h.c.} & & 0 \end{pmatrix} & \begin{matrix} |1\rangle \\ |2\rangle \\ |3\rangle \end{matrix} \end{pmatrix} \quad (2.57)$$

The Hamiltonian resulting from a Chern insulator tight-binding model and the interaction H_{int}^b for bosons (respectively H_{int}^f for fermions) may have, in some conditions, at filling fraction 1/2 (respectively 1/3), a ground state with the same topological nature as the Laughlin state. Numerical simulations are necessary to confirm the existence of such a fractional Chern insulator phase in a given system.

Using analogies with the quantum Hall effect can guide us to find the emergence conditions of a fractional Chern insulator, through simple energetic arguments. The band mixing due to the interaction between particles should be minimal, so that the system can be approximated by a single $C = 1$ band resembling the lowest Landau level. This requires the interaction strength V to be small compared to the energy gap Δ between the lowest and second bands. At the same time, the interactions

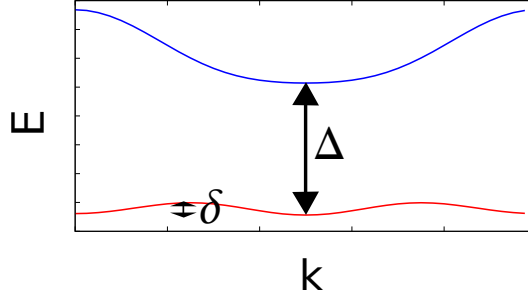


Figure 2.8: Typical low energy band structure of an ideal Chern insulator that would mimic a single Landau level. δ is the band width of the lowest band, and Δ the gap to the next band.

should be strong enough to open a gap at fractional filling. In the fractional quantum Hall effect the Landau levels are perfectly flat, so that no interaction can be treated perturbatively. On the other hand, in a lattice system, the dispersion of the band causes a finite band width δ . It is thus preferable that the band width be small compared to the gap, so that the following inequality can be respected (see Fig. 2.8)

$$\delta \ll V \ll \Delta \quad (2.58)$$

While the above inequality ensures conditions similar to the fractional quantum Hall effect, it should not be understood as a strict constraint. Indeed, numerical simulations [88] have shown that a fractional Chern insulator phase could arise in some particular models for interactions far exceeding the band gap ($V \gg \Delta$). In the rest of this manuscript, we will however choose to respect Eq. (2.58).

While it is possible to fine-tune the tunneling parameters of a given model so that the band width is smaller than the gap, it can be advantageous to work in the ideal limit of a dispersionless model, or flat-band limit, as described in Sec. 1.2.1.2, to avoid the effects of band dispersion altogether. Further, we can get rid of band mixing by projecting the interaction onto the lowest band, leading to the projected, flat-band Hamiltonian

$$H = \varepsilon_G \sum_{\mathbf{k} \in BZ} |0, \mathbf{k}\rangle \langle 0, \mathbf{k}| + \sum_{\mathbf{k}, \mathbf{k}' \in BZ} |0, \mathbf{k}\rangle \langle 0, \mathbf{k}| \hat{V} |0, \mathbf{k}'\rangle \langle 0, \mathbf{k}'| \quad (2.59)$$

where \hat{V} is the interaction operator. Even in this ideal limit, the emergence of a gapped phase at fractional filling is not guaranteed, which is precisely why working in this limit is useful. Indeed, it can allow us to understand the influence of different parameters independently, without the complications brought by band mixing and band dispersion.

Besides the existence of band dispersion, the difference between a Landau level and a $C = 1$ Chern band in a Chern insulator is the Berry curvature, which fluctuates a lot in the topological band of a Chern insulator, while it is concentrated at one point of the magnetic Brillouin zone in a Landau level. Chern insulator models

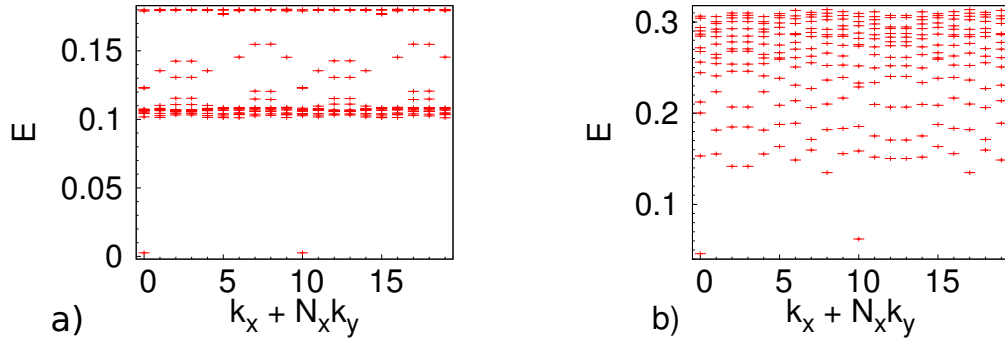


Figure 2.9: Low energy spectrum of the fractional Chern insulators with $N = 10$ bosons on a 5×4 lattice (half filling of the lowest band), obtained by exact diagonalization of an on-site Hubbard interaction projected onto the lowest band. The twofold almost degenerate ground state with a many-body gap to higher energy excitations is characteristic of the Laughlin $1/2$ phase. a) Ruby lattice Chern insulator model. b) Haldane Chern insulator model. The ground state degeneracy is clearly lifted.

generally do not have a uniform Berry curvature in finite size, but numerical simulations have shown that the fractional Chern insulator phases seem to be most stable in systems where its fluctuations are relatively small [172]. This is in agreement with the idea that fractional phases are stable in a Chern insulator system when the Chern band most closely resembles a Landau level.

2.3.3 Numerically identifying a Chern insulator phase

Numerical simulations are necessary to assess the stability of a fractional Chern insulator phase. In particular, the stability of a Laughlin-like phase has been extensively studied in several tight-binding Chern insulator models with periodic boundary conditions [110, 146, 131] (see also Refs. [19, 122] and references therein). A gapped phase appears at filling $\nu = 1/3$ for fermions ($\nu = 1/2$ for bosons), when \hat{V} takes the form of a short range Hubbard interaction, such as a nearest-neighbor two-body interaction, or on-site interaction for bosons (see Fig. 2.7a).

The first numerical signature of a Laughlin-like fractional Chern insulator is a q -fold almost degenerate ground state at filling $\nu = 1/q$, separated by a gap from higher energy excitations. The approximate degeneracy has the same origin as the topological degeneracy of the Laughlin state on the torus, since a lattice system with periodic boundary conditions is topologically equivalent to a torus. Due to the fluctuations of the Berry curvature in a Chern band, the lattice translation operators projected onto the Chern band have different properties than their FQH counterparts, the magnetic translations. In particular, their commutations relations are not described by the GMP algebra (1.39) (in the thermodynamic limit, it can be shown [121, 108] that the translation operators projected onto a topological Chern

band form a closed algebra reminiscent of the GMP algebra, but only approximately, in the long wavelength limit). For FQH systems, we have seen in Sec. 2.2.3.1 that the GMP algebra leads to the exact q -fold degeneracy of each state in the spectrum. For fractional Chern insulators, the degeneracy of the ground state is thus not exact in finite size because there is no exact center of mass degeneracy. It is expected (and numerically supported) that the exact degeneracy be recovered in the thermodynamic limit. In Fig. 2.9, we have represented the spectrum of two bosonic fractional Chern insulators, respectively based on the Haldane (see Fig. 2.7a) and ruby lattice models (see Fig. 2.7b), with well chosen microscopic parameters, at filling fraction $\nu = 1/2$. Since there is no magnetic field, the lattice translation symmetry (as long as they are not projected onto a given band) are preserved and commute. The center of mass momentum in the x and y directions k_x and k_y are thus good quantum numbers, and the spectrum can be represented as a function of the linearized lattice quantum number $k_x + N_x k_y$. In Fig. 2.9, it is apparent that the degeneracy lifting of the ground state in finite size is highly model dependent.

On top of the topological degeneracy of the ground state, the non-trivial degeneracy of charged (quasihole and quasiparticle) excitations is a hallmark of topological order. Quasiholes can be added to the system by removing particles, or by adding unit cells, starting from the system with a fixed filling fraction $\nu = p/q$, p and q coprime numbers. Exact diagonalization gives us access to the low energy manifold, which contains the quasihole or quasiparticle states. In the cases where the gap is well defined, we can count the number of states below it: a total counting identical to the number of charged excitations in the corresponding fractional quantum Hall effect phase is a sign that these states have the same topological order. While these two systems do not have the same symmetries, it is possible to relate their respective quantum numbers, to predict the momentum resolved FCI counting. The fractional quantum Hall Brillouin zone is a $GCD(N, N_\phi) \times N_\phi$ rectangle, and thus has more momentum sectors than the FCI $N_x \times N_y = N_\phi$ Brillouin zone. As shown in Ref. [24], mapping the FQH Brillouin zone onto the FCI one consists in folding the reduced FQH Brillouin zone onto a region of smaller size. Let us define two integers

$$N_{x0} = GCD(N, N_x) \quad N_{y0} = GCD(N, N_y) \quad (2.60)$$

The reduced FQH Brillouin zone is folded onto a reduced FCI Brillouin zone of size $N_{x0} \times N_{y0}$, such that the folded quantum numbers write

$$\mathbf{k}_x^{\text{FCI}} = \mathbf{k}_x \text{ modulo } N_{x0} \quad \mathbf{k}_y^{\text{FCI}} = \mathbf{k}_y \text{ modulo } N_{y0} \quad (2.61)$$

where $\mathbf{k}_j^{\text{FCI}}$, \mathbf{k}_j , $j = x, y$ are integers related to the momentum quantum numbers by $k_j^{\text{FCI}} = 2\pi \mathbf{k}_j^{\text{FCI}} / N_j$, $k_j = 2\pi \mathbf{k}_j / L_j$ (the lattice constant is equal to 1). The full $N_x \times N_y$ FCI Brillouin zone is then paved by repeating this reduced zone $q_x = N_x / N_{x0}$ times in the x direction and $q_y = N_y / N_{y0}$ times in the y direction. Finally, the q -fold topological degeneracy of the FQH on the torus is taken into account by attributing an additional $q / (q_x \times q_y)$ degeneracy onto each state. An example of the mapping is given in Fig. 2.10, corresponding to the systems whose spectra are

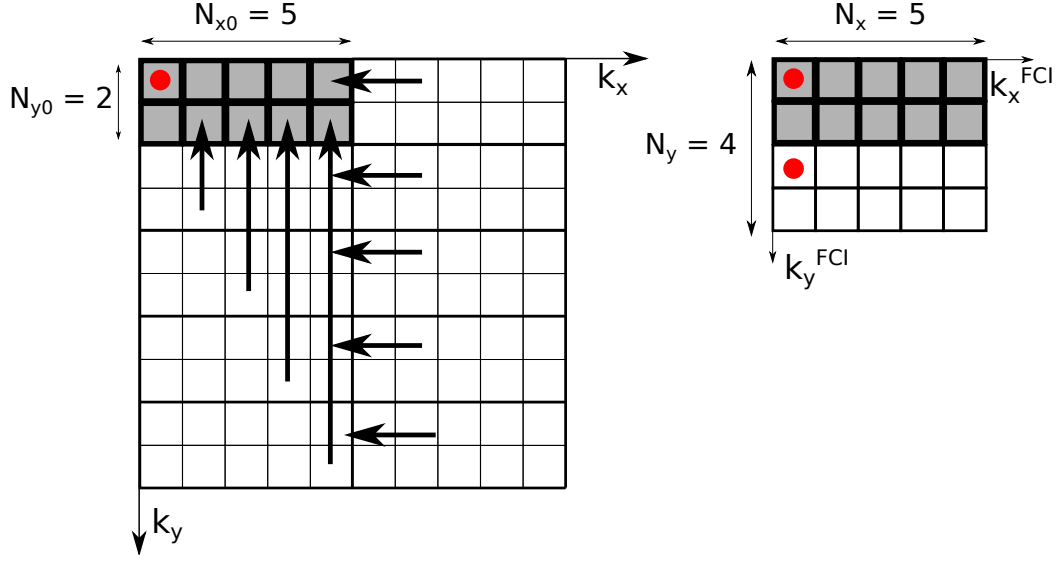


Figure 2.10: Folding of the FQH reduced Brillouin zone of a system with $N = 10$ particles and $N_\phi = 20$ flux quanta (left) onto the 5×4 lattice first Brillouin zone (right). The FQH reduced Brillouin zone is folded onto a $N_{x0} \times N_{y0}$ zone, where $N_{x0} = \text{GCD}(10, 5) = 5$ and $N_{y0} = \text{GCD}(10, 4) = 2$. This zone is doubled to form the 5×4 first Brillouin zone. The red dots represent the position of the Laughlin ground state, showing how their lattice momentum can be predicted from their FQH quantum numbers. The validity of this mapping can be observed in the spectra obtained numerically for the same system size, and shown in Fig. 2.9.

shown in Fig. 2.9. This mapping allows to relate the momentum resolved counting of charged excitations of the Laughlin state in the FQH and FCI cases, as long as they are well separated from the higher energy excitations.

2.4 Entanglement spectroscopy for the fractional quantum Hall phases

2.4.1 Entanglement entropy

Topological order is a new type of order that cannot be detected using any local measurement. It is thus crucial to define new quantities to detect its presence in a system, at least numerically (if not experimentally). The degeneracy of the ground state on a non-zero genus surface, as well as the degeneracy of the charged excitations are signatures of a given type of topological order. However, the energy spectrum of some other (non-topological) phases – for example a symmetry breaking phase such as a charge density wave – may have the same features (at least in finite size). Also, the degeneracy of excitations may be difficult to obtain numerically. Entanglement entropy is a promising quantity to extract information about the

2.4. Entanglement spectroscopy for the fractional quantum Hall phases

topological order of a given phase, starting from the ground state. We consider the bipartite entanglement between two parts A and B of a system, described by its ground state $|\Psi\rangle$. The partition is described by the reduced density matrix

$$\rho_A = \text{Tr}_B |\Psi\rangle \langle \Psi| \quad (2.62)$$

In its most popular definition, the entanglement entropy is the Von Neumann entropy associated with ρ_A and writes

$$S_A = -\text{Tr}_A [\rho_A \ln \rho_A] \quad (2.63)$$

For a system in d dimensions with a finite correlation length l , the entanglement entropy grows linearly with the area of the boundary between A and B [149]. This property is called the area law, and writes

$$S_A \simeq \alpha \mathcal{L}^{d-1} \quad (2.64)$$

where $\mathcal{L} \gg l$ is the typical length of A , and α is a non-universal constant. For two-dimensional phases, Refs. [81, 96] showed that the first correction to the area law γ is a signature of the topological order

$$S_A \simeq \alpha \mathcal{L} - \gamma \quad (2.65)$$

γ is called the topological entanglement entropy and is related to the topological nature of the ground state via its total quantum dimension \mathcal{D} , which is associated to the growing rate of the Hilbert space per number of quasiparticles. For the topological sector associated with the quasiparticle i , the total quantum dimension writes

$$\gamma = \ln \mathcal{D} / d_i \quad (2.66)$$

where d_i is the quantum dimension of the quasiparticle i . It can be computed knowing the quantum dimension d_i of all of its quasiparticles

$$\mathcal{D} = \sqrt{\sum_i d_i^2} \quad (2.67)$$

This relation can be especially useful to identify a given phase. However, note that different types of topological order can have the same topological entanglement entropy. For instance, the quantum dimension of an abelian quasiparticle is 1, and the Laughlin $1/q$ state has a topological entanglement entropy $\gamma = \sqrt{q}$ (since it has q abelian quasiparticles). The bosonic Moore-Read phase has two abelian quasiparticles, and one non-abelian quasiparticle with quantum dimension $\sqrt{2}$. As a result, both the bosonic Laughlin $1/4$ and bosonic Moore-Read (at filling $\nu = 1$) phases have a topological entanglement entropy $\gamma = \ln 2$ in the vacuum sector. Knowing the filling fraction (or the topological entanglement entropy in the other topological sector) would allow us to distinguish them, but it might not be the case in more complicated examples. The other limitation of this technique to detect and identify

topological order, is that it requires the computation of γ by linear interpolation with a great quantitative precision. This is only possible if the entanglement entropy S_A is computed for several different system sizes, which can be numerically challenging. For instance, exact diagonalization only allows the computation of the ground state for a small number of system sizes, as will be discussed in the last section of this chapter. Entanglement spectroscopy can bring a solution to this problem, by analyzing the full spectrum of ρ_A , instead of reducing all of the information to a single number.

2.4.2 Particle entanglement spectrum

The entanglement spectrum was introduced by Li and Haldane [97] in the context of the fractional quantum Hall effect, and has triggered numerous studies concerning different topological phases. Various system partitions can be made, probing different properties of the phase. For instance, Li and Haldane have conjectured that the entanglement spectrum of a gapped phase for a real space partition is directly related to the energy spectrum of the edge states along this cut, and that these spectra are identical in the thermodynamic limit. This conjecture can be verified numerically in many cases, including the fractional quantum Hall states. The orbital entanglement spectrum introduced by the same authors, where the cut is made in orbital space, is another powerful tool to probe the topological nature of the system. Indeed, orbital and real space cuts are closely related in the specific case of the fractional quantum Hall effect. Here, we focus on another type of bipartition, the particle cut, whereby the geometry of the system is kept intact, while the density matrix is traced over the positions of $N_B = N - N_A$ particles. The particle partition was introduced as an entanglement entropy bipartition in Refs. [67, 185], and later applied to compute entanglement spectra in Ref. [153] to probe the bulk excitations of a phase from its ground state. For a generic wave function written in first-quantized notation $\Psi(x_1, \dots, x_N)$, the reduced density matrix for a particle partition writes

$$\rho_A(x_1, \dots, x_{N_A}, x'_1, \dots, x'_{N_A}) = \int \left(\prod_{i=1}^{N_B} dx_{N_A+i} \Psi(x_1, \dots, x_{N_A}, x_{N_A+1}, \dots, x_N) \right. \\ \left. \times \Psi(x'_1, \dots, x'_{N_A}, x'_{N_A+1}, \dots, x'_N) \right) \quad (2.68)$$

The advantage of the particle partition is that it preserves all of the spatial symmetries of the original system. In the case of a q -fold degenerate ground state (think, for instance of the Laughlin state defined on the torus), the following density matrix commutes with the symmetry operators (such as the magnetic translation operator)

$$\rho = \frac{1}{q} \sum_{i=1}^q |\Psi_i\rangle \langle \Psi_i| \quad (2.69)$$

After dividing the particles into two groups A and B , we trace over the particles belonging to B to obtain the reduced density matrix $\rho_A = \text{Tr}_B \rho$. Since this operation preserves the symmetries of the system, the eigenvalues $e^{-\xi}$ of ρ_A can be

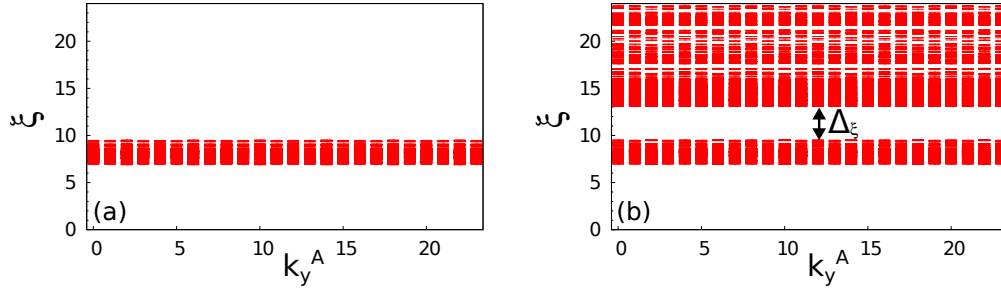


Figure 2.11: Particle entanglement spectrum (PES) of the threefold degenerate groundstate of $N = 8$ fermions on a torus pierced by $N_\phi = 24$ flux quanta on the torus, and a particle partition $N_A = 4$. a) Laughlin state (exact ground state of the model two-body interaction Eq. (2.23)) b) Coulomb ground state. There is a finite entanglement gap Δ_ξ between the low entanglement energies (universal part of the entanglement spectrum) and the high entanglement energies. The number of states per k_y^A sector below the entanglement gap is the same as in the Laughlin PES.

labeled by the same quantum numbers as the energy spectrum. In particular, for a fractional quantum Hall state on the torus, the entanglement spectrum is labeled with the value of the center of mass momentum k_y^A .

For a model wave function, the counting of non-zero eigenvalues of the reduced density matrix is non-trivial (i.e. it does not saturate the Hilbert space dimension) and does not depend on the geometry, only on the genus of the surface. This property, already demonstrated in the case of an orbital cut [97] is also true for a particle cut [153]. Further, Ref. [153] noticed that this number is equal (per momentum sector) to the number of quasi-hole states in the system with an equal number of flux quanta and N_A particles. When the state is the exact, unique ground state of a model Hamiltonian, one can prove that the counting of non-zero entanglement eigenvalues must be bounded by the number of quasiholes, but the saturation of the counting remains a conjecture. Since this conjecture was verified numerically in a large number of cases, it is generally admitted to hold in most cases. This is an extremely powerful tool for the identification of a topological phase.

When the wave function is not the exact ground state of a model Hamiltonian, the non-universal part of the entanglement spectrum appears at finite entanglement energy. The separation between the universal and non-universal parts of the entanglement spectrum defines an entanglement gap Δ_ξ . For instance, the particle entanglement spectrum of the Coulomb state, which is very similar to the Laughlin $1/3$ state, has a finite entanglement gap. But the counting of states below it is exactly the same as the number of non-zero eigenvalues of the reduced density matrix for the Laughlin $1/3$ state (see Fig. 2.11). More generically, as long as the entanglement gap does not close, the counting can be used to identify a given topological order by comparing the counting with that of the corresponding model state. For instance, one can identify the Laughlin state in a fractional Chern insulator by com-

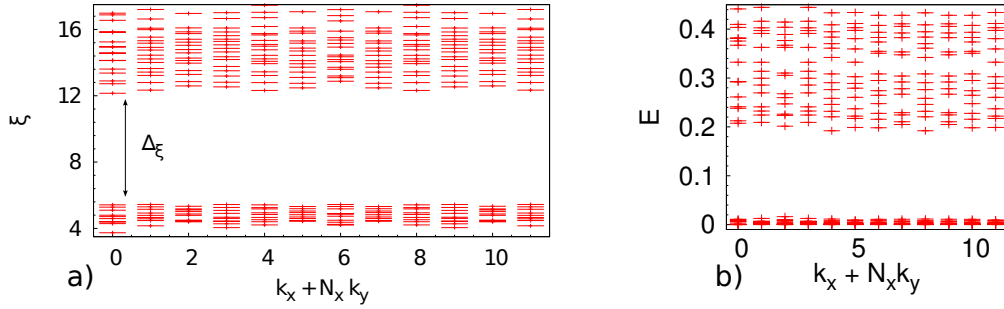


Figure 2.12: Characterization of the Laughlin $1/2$ state in a bosonic fractional Chern insulator, realized in a 4×3 kagome lattice. a) Particle entanglement spectrum of the $N = 6$ twofold ground state at $\nu = 1/2$, with a particle partition $N_A = 3$. There is a finite entanglement gap Δ_ξ between the universal (low ξ) and non-universal parts of the spectrum. The counting of states per momentum sector below the entanglement gap is equal to the number of quasi-hole excitations in the $N = 3$ system, shown in b). b) Low energy spectrum of the fractional Chern insulator with $N = 3$ bosons.

puting and diagonalizing the reduced density matrix of the q -fold quasi-degenerate ground state. Since this ground state is not exactly the Laughlin state, there is a finite entanglement gap in the entanglement spectrum. Using the FQH-to-FCI mapping of quantum numbers (see Sec. 2.3.3), one can verify that the counting below the entanglement gap is the same per momentum sector as the counting for the exact Laughlin state. It also corresponds to the counting of quasi-hole excitations in the system with N_A particles and the same geometry (see Fig. 2.12). Note that in finite size, the energy spectrum of the system with quasi-hole excitations might not always be gapped, as the degeneracy splitting between low energy states can cause the gap to close for a large number of quasi-hole states. The PES thus appears as a way to probe the charged excitations of the system directly from the ground state. Moreover, it allows to distinguish the topological phase from a charge density wave, which may have the same energetic signatures [26].

2.5 Exact diagonalization

Numerical simulations are an essential tool of the study of strongly correlated systems, due to the extreme difficulty to do any analytical calculation. The fractional quantum Hall effect is no exception to this rule. Model wave functions and field theory are powerful methods to investigate the topological order of the FQHE, but cannot be used to predict the existence of an incompressible phase at a given filling fraction, or compute any energetic quantity. To obtain both the eigenstates and energy spectrum of a Hamiltonian, one can use exact diagonalization (ED).

The principle of ED is fairly simple. First, one has to generate all the Hilbert space configurations corresponding to a number of particles, a number of flux quanta,

and, optionally, the value of some quantum number (if the Hamiltonian commutes with a given operator, they can be both diagonalized simultaneously). One then computes the matrix elements that connect all space configurations, and finally use a diagonalization algorithm (such as Lanczos) to obtain the lowest eigenenergies and eigenvectors of this matrix. If the Hamiltonian is invariant under some symmetry, fixing the value of the corresponding quantum number results in a block-diagonal Hamiltonian whose blocks can be diagonalized separately. This method is especially helpful to obtain the low energy spectrum of a Hamiltonian, but is limited by the exponential growth of the Hilbert space dimension. On the torus geometry, the number of single-particle orbitals in the lowest Landau level is given by the number of flux quanta N_ϕ that pierce the torus. If there are N fermions interacting on the torus, the total number of states is thus the binomial coefficient $C_{N_\phi}^N$. For instance, the Laughlin state can be observed for $N = 8$ fermions living on the torus pierced by $N_\phi = 24$ flux quanta, which corresponds to a dimension of 735471. By taking into account the translational invariance on the torus, one only has to diagonalize blocks with a dimension of the order of 3840.

When considering the feasibility of an ED calculation, there are two main factors that one has to consider. The first is the amount of memory that is needed to store all of the Hamiltonian matrix elements. Since Lanczos is an iterative algorithm that uses these matrix elements at each iteration, it is often advantageous to store them in the random-access memory (RAM) of the computer, so that they only have to be computed once. This criterion can appear to be quite restrictive: storing the matrix elements of the two-body hollow core interaction for $N = 13$ and $N_\phi = 39$ (to obtain the fermionic Laughlin state) requires 125Gb of RAM, a capacity only available on some powerful work stations or specialized computing clusters. Note that the model interaction for the fractional quantum Hall states is highly local, resulting in a quite sparse Hamiltonian matrix (but still much denser than, say, the Hubbard model or a spin chain with nearest neighbor couplings). This makes the FQHE a good candidate to be studied with ED, since a more dense Hamiltonian would result in more matrix elements to be stored. The second factor to consider is the speed of the processors: if storing all of the matrix elements is not an option, one can envision recomputing them at every step, which is only viable if the processors are fast enough. In any case, ED codes are parallelized so that multiple processors can perform simultaneous operations.

The interpretation of ED results inevitably relies on the analysis of finite size data. As a sanity check, it is thus necessary to compare the results obtained for the few accessible system sizes. A similar behavior across various system sizes may justify the extrapolation to the thermodynamic limit. The short correlation length (i.e. large gap) compared to the size of the system is an essential ingredient of the FQHE physics that ensures a rapid convergence of the measurable quantities (such as the energy gap) as we will see in the next chapters.

The \mathbb{Z}_k Read-Rezayi states and their neutral excitations on the torus

Contents

3.1 Projective construction of the Read-Rezayi states	78
3.1.1 The bosonic Read-Rezayi states on the torus	78
3.1.2 Numerical challenges	80
3.1.3 The projective construction on genus 0 surfaces	81
3.1.4 The projective construction with a twist	83
3.2 Physics of the neutral modes	87
3.2.1 The collective excitation mode above the Laughlin state . . .	87
3.2.2 The neutral modes above the Moore-Read state	89
3.3 Neutral modes on the torus	89
3.3.1 Neutral mode above the Laughlin state on the torus	90
3.3.2 Neutral mode above the Moore-Read state on the torus . . .	94

In this chapter, we explore the physics of a series of fractional quantum Hall states in the continuum. We are particularly interested in the low energy excitations of the Laughlin state, as well as the Read-Rezayi states and their low energy excitations. These wave functions are interesting in that they are excellent approximations of some phases of the fractional quantum Hall effect. The Read-Rezayi states present an additional, more exotic interest, since they host anyonic excitations with non-abelian statistics. The complexity of the fractional quantum Hall effect calls for the use of numerical methods, to evaluate the accuracy of the proposed ansatz, or test the validity of effective field theories. As pointed out at the end of the previous chapter, exact diagonalization – the numerical method used throughout this manuscript – is limited by the exponentially growing size of the Hilbert space of the described system, and is best at describing closed systems, with maximal spatial symmetry. The sphere introduced by Haldane [57] and the torus are the simplest closed two-dimensional surfaces, and are used in many numerical simulations. The sphere is a simpler choice than the torus in many respects, which explains why most preexisting works focus on the sphere. There is a simple mapping of the single-particle orbitals from the plane to the sphere geometry (only

the normalization differs), leading to polynomial many-body wave functions on the sphere. On the torus, there are also some numerical complications due to the periodic boundary conditions, which make the brute force calculation of the interaction Hamiltonian extremely costly for a n -body interaction. On the other hand, the topological degeneracy of the ground state appears on the torus, but not on a genus 0 surface like the sphere. The similarity of the torus with lattice systems (which are typically defined with periodic boundary conditions, and will be the focus of the next two chapters) constitutes an additional motivation to study the fractional quantum Hall effect on the torus.

This chapter is structured in the following way: first, we focus on the Read-Rezayi states (ground state and quasihole excitations) on the torus, and see how they can be written in terms of simpler quantum Hall wave functions, using a projective construction. Then, we review the general properties of the neutral low energy modes above the two simplest of the Read-Rezayi states, the Laughlin and Moore-Read states. Finally, we study the specificities of the low energy excitations above the Laughlin and Moore-Read states on the torus, and propose approximate wave functions for these modes. The accuracy of the approximation is tested through an extensive numerical study.

3.1 Projective construction of the Read-Rezayi states

3.1.1 The bosonic Read-Rezayi states on the torus

The bosonic \mathbb{Z}_k Read-Rezayi state Ψ_k is the densest zero-energy ground state at $\nu = k/2$ of the $(k+1)$ -body contact interaction expressed in Eq. (2.36) projected into the lowest Landau level. This model Hamiltonian can also be written in second quantized notations

$$H_{\text{int},k} = \int d^2\mathbf{r} : [\hat{\rho}(\mathbf{r})]^{k+1} : \quad (3.1)$$

where

$$\hat{\rho}(\mathbf{r}) = \psi^\dagger(\mathbf{r})\psi(\mathbf{r}), \quad (3.2)$$

is the density operator written in terms of the field operator $\psi^\dagger(\mathbf{r})$, that creates a boson in the lowest Landau level at position \mathbf{r} , and $::$ represents the normal ordering.

On the torus the \mathbb{Z}_k Read-Rezayi ground state appears at filling fraction $\nu = k/2$, that is to say if the number of particles N and the number of flux quanta N_ϕ obey

$$kN_\phi = 2N. \quad (3.3)$$

This relation cannot be satisfied for all system sizes, since both N and N_ϕ have to be integer. For example, if k is odd and N_ϕ is odd, there exists no ground state. If a ground state exists, it can exhibit a topological degeneracy on the torus. This degeneracy is a hallmark of the specific topological order, as was discussed in Sec. 2.2.2. The topological order realized by a bosonic \mathbb{Z}_k Read-Rezayi state is labelled by the affine Lie algebra $\text{SU}(2)_k$ and contains $(k+1)$ irreducible representations, corresponding to $(k+1)$ topological anyon excitations. Thus, on the torus

	k odd (k_x, k_y)	deg.	k even (k_x, k_y)	deg.
N_ϕ odd	—		(0, 0)	1
N_ϕ even	(0, 0)	$\frac{k+1}{2}$	(0, 0)	$\frac{k}{2}$
	(0, $N_\phi/2$)	$\frac{k+1}{2}$	(0, $N_\phi/2$)	1
			($N_\phi/2$, 0)	1
			($N_\phi/2$, $N_\phi/2$)	$\frac{k}{2} - 1$

Table 3.1: Ground state degeneracies and momenta of the \mathbb{Z}_k Read-Rezayi state on the torus. For k odd (respectively even), the momentum quantum numbers k_x, k_y thus belong to a $N_\phi/2 \times N_\phi$ (respectively $N_\phi \times N_\phi$) Brillouin zone. These momentum quantum numbers are defined in the Landau x -gauge with vector potential $\mathbf{A}(\mathbf{r}) = (0, -Bx)$. See Sec. 2.2.3.1 for the definition of the momentum quantum numbers.

with an even number of flux quanta N_ϕ , any \mathbb{Z}_k Read-Rezayi state is $(k + 1)$ -fold degenerate. The momentum quantum numbers of the degenerate ground states are given in Tab. 3.1. There is a fundamental difference between k even and k odd. For k odd, N must be a multiple of k for the filling fraction to be $\nu = k/2$. When k is even, there are two alternatives: N is either an integer multiple of k (and N_ϕ is even) or a half-integer multiple of k (and N_ϕ is odd). In the latter case, there is a unique \mathbb{Z}_k state. Note that this feature is specific to the torus geometry (or any surface of genus 1), and absent on the sphere (a surface of genus 0). This discrepancy is rooted in the topological order of the Read-Rezayi states, but simple considerations on the filling factor can help understand it. We have defined the shift δ in Eq. (2.20) in relation to the discrepancy between the filling fraction in finite size and in the thermodynamic limit. There is no shift on the torus, such that Eq. (3.3) is true for any system size. On the sphere, however, the shift for the bosonic Read-Rezayi states is $\delta = 2$, resulting in the following equality

$$N = \frac{k}{2} (N_\phi + \delta) \quad (3.4)$$

Consequently, the particle density of the bosonic \mathbb{Z}_k Read-Rezayi states is larger on the sphere than on the torus. This imposes stronger constraints on the number of particles for which these states can be observed. On the sphere, the \mathbb{Z}_k Read-Rezayi states (in their densest version that verifies Eq. (3.4)) appear only when the number of particles N is a multiple of k , and it is not degenerate.

Finally, if one deviates from the filling factor $\nu = k/2$ by increasing the number of flux quanta, quasihole excitations are nucleated. Their wave functions correspond to the zero energy states of the model Hamiltonian (3.1). The number of zero energy states (and their quantum numbers) for a given number of particles and a given number of flux quanta can be deduced from the clustering properties of these states [22, 21]. This number is also related to the number of partitions obeying the $(k, 2)$ generalized exclusion principle, as detailed in Sec. 2.2.4.

3.1.2 Numerical challenges

To perform an exact diagonalization calculation, we need to write the Hamiltonian in the occupation basis. The $(k+1)$ -body contact interaction Hamiltonian (2.36) can be written generically as a function of the Fourier transform of the density operator projected onto the lowest Landau level $\rho_{\mathbf{q}}$. For simplicity, we define $n = k + 1$ in this section. The Hamiltonian writes

$$H = \sum_{\mathbf{q}_1 \dots \mathbf{q}_n} : \hat{\rho}_{\mathbf{q}_1} \dots \hat{\rho}_{\mathbf{q}_n} : \delta_{\mathbf{q}_1 + \dots + \mathbf{q}_n, 0} \quad (3.5)$$

where $::$ represents normal ordering, and $\delta_{\mathbf{q}_1 + \dots + \mathbf{q}_n, 0}$ is a Kronecker symbol that enforces the conservation of momentum. The sum runs over discrete momenta

$$\mathbf{q}_i = (q_{xi}, q_{yi}) = \left(\frac{2\pi s_i}{L_x}, \frac{2\pi t_i}{L_y} \right) \quad (3.6)$$

where s_i and t_i can take any integer value (positive or negative). By definition, $\hat{\rho}_{\mathbf{q}}$ is the Fourier transform of the projected density operator $\hat{\rho}(\mathbf{r})$

$$\hat{\rho}_{\mathbf{q}} = \int d^2\mathbf{r} e^{-i\mathbf{q}\cdot\mathbf{r}} \hat{\rho}(\mathbf{r}) \quad (3.7)$$

and – using the expression Eq. (1.45) of the single-particle eigenstates on the torus – can be conveniently expressed as

$$\hat{\rho}_{\mathbf{q}} = e^{-l_B^2 |\mathbf{q}|^2 / 4} \sum_{j=0}^{N_\phi-1} e^{-\frac{2\pi i s}{N_\phi} (j+t/2)} c_j^\dagger c_{j+t} \quad (3.8)$$

where c_j^\dagger (respectively c_j) creates (respectively annihilates) a boson in the orbital j of momentum $2\pi j/L_y$ (see Appendix A for the derivation of this formula). The generic expression for any n -body Hamiltonian is the following

$$H = \sum_{j_1, j_2, \dots, j_{2n}} V_{j_1 j_2 \dots j_{2n}} c_{j_1}^\dagger \dots c_{j_n}^\dagger c_{j_{n+1}} \dots c_{j_{2n}} \quad (3.9)$$

In the case of the contact interaction, the coefficient $V_{j_1 j_2 \dots j_{2n}}$ can be derived using Eq. 3.8. We need to compute the value of $V_{j_1 j_2 \dots j_{2n}}$ for all sets of $0 \leq j_i < N_\phi$ that respect the conservation of momentum $j_1 + \dots + j_n = (j_{n+1} + \dots + j_{2n}) \bmod N_\phi$. We call $\rho_{j,s,t}$ the amplitude of the contribution of $c_j^\dagger c_{j+t}$ to $\hat{\rho}_{\mathbf{q}}$, where the relation between s, t and \mathbf{q} is given in Eq. (3.6).

$$\rho_{j,s,t} = e^{-|\mathbf{q}|^2 / 4} e^{-\frac{2\pi i s}{N_\phi} (j+t/2)} \quad (3.10)$$

such that the projected density operator writes

$$\hat{\rho}_{\mathbf{q}} = \sum_{j=0}^{N_\phi-1} \rho_{j,s,t} c_j^\dagger c_{j+t} \quad (3.11)$$

Note that while the orbital indexes j_i are defined modulo N_ϕ , and can only take a finite number of values ($0 \leq j_i < N_\phi$), the projected density operator can be written for an infinite number of momenta \mathbf{q} , such that the sums that appear in Eq. (3.5) are infinite. The expression $V_{j_1 j_2 \dots j_{2n}}$ in terms of the coefficients $\rho_{j,s,t}$ must reflect this and contain infinite sums. The interaction coefficient writes

$$\begin{aligned} V_{j_1 j_2 \dots j_{2n}} &= \sum_l \delta_{j_1 + \dots + j_n, j_{n+1} + \dots + j_{2n} + l N_\phi} \\ &\times \sum_{s_1 \dots s_n} \sum_{t_1 \dots t_n} \rho_{j_1, s_1, t_1} \dots \rho_{j_n, s_n, t_n} \delta_{s_1 + \dots + s_n, 0} \delta_{t_1 + \dots + t_n, 0} \end{aligned} \quad (3.12)$$

where all summation coefficients can take any integer (positive or negative) value. Because of the Kronecker symbol, three of the summation coefficients are actually constrained to a unique value. This leaves us with $2(n-1)$ nested infinite sums. For small N_ϕ , the amplitude of the density operator decreases rapidly with the momentum, thanks to the rapid decay of the Gaussian factor. This limits the actual number of terms to be added to obtain the sum. For $n=2$ (model interaction to generate the Laughlin state and its excitations), computing the interaction coefficients is not the limiting factor to determine the maximal number of flux quanta N_ϕ that can be reached, but for $n \geq 3$, the complexity $O(N_\phi^{2(n-1)})$ of computing $V_{j_1 j_2 \dots j_{2n}}$ limits the system sizes that can be simulated.

To remedy this problem, one can take advantage of the translational symmetry of the system to factorize the sums into two factors involving $n-1$ nested sums each. This approach was used in Ref. [118] to factorize the two-body interaction ($n=2$). We give in Appendix B the factorized interaction coefficient for a contact n -body interaction with no demonstration (the case $n=3$ is derived). In the factorized expression of the Hamiltonian, the translational invariance of the system appears explicitly, since center of mass and relative momentum coordinates can be separated. The complexity of the calculation has been reduced to $O(N_\phi^{n-1})$. This is a crucial improvement, especially since we need to compute the n -body interaction for $n \geq 3$.

Note that once this factorization is implemented, the diagonalization of the Hamiltonian matrix itself becomes the most time consuming part of the calculation, for any n or N_ϕ . For Hilbert spaces of comparable dimensions, the diagonalization time increases with the value of n . This is due to the fact that the Hamiltonian is less and less sparse as n grows.

3.1.3 The projective construction on genus 0 surfaces

In Sec. 2.1.5, we introduced the bosonic \mathbb{Z}_k Read-Rezayi states as the result of the symmetrization [30] over the copy index of k independent copies of the Laughlin state. The procedure of Eq. (2.35) is in fact generic, and the bosonic \mathbb{Z}_{gk} Read-Rezayi state can be obtained by symmetrizing over g copies of the \mathbb{Z}_k state. To make things more specific, we call $\mathcal{S}_{g \rightarrow 1}$ the operator that symmetrizes over g copies

of the \mathbb{Z}_k Read-Rezayi state.

$$|\Psi_{gk}\rangle = \mathcal{S}_{g \rightarrow 1} \left(\underbrace{|\Psi_k\rangle \otimes \cdots \otimes |\Psi_k\rangle}_{g \text{ times}} \right). \quad (3.13)$$

The action of $\mathcal{S}_{g \rightarrow 1}$ was written explicitly in real space in Eq. (2.35), with $\mathcal{S} \equiv \mathcal{S}_{g \rightarrow 1}$ for $k = 1$. Here, we can picture the direct product of $|\Psi_k\rangle$ states as being defined on g layers of the same manifold. For instance, we can construct a \mathbb{Z}_g Read-Rezayi state for any g by symmetrizing over g layers of $\nu = 1/2$ bosonic Laughlin states. As a simple example, consider two layers of the $\nu = 1/2$ bosonic Laughlin state with two particles each. We focus on the polynomial part of the wave function only, given by $\Psi_1(z_1, z_2; z_3, z_4) \equiv (z_1 - z_2)^2 (z_3 - z_4)^2$, when particles 1 and 2 are in one layer and particles 3 and 4 are in the other. Here, $z_i = x_i - iy_i$ is the complex coordinate of particle i on the disk. Symmetrization amounts to summation over all possible even distributions of the four particles over the two layers

$$\begin{aligned} \Psi_1(z_1, z_2; z_3, z_4) &\xrightarrow{\mathcal{S}_{2 \rightarrow 1}} \Psi_1(z_1, z_2; z_3, z_4) + \Psi_1(z_1, z_3; z_2, z_4) \\ &\quad + \Psi_1(z_1, z_4; z_2, z_3) \\ &= 2 \text{Pf} \left(\frac{1}{z_i - z_j} \right) \prod_{i < j}^4 (z_i - z_j). \end{aligned} \quad (3.14)$$

We recognize the last line of Eq. (3.14) as the Moore-Read state of Eq. (2.31) for 4 particles, up to a normalization factor. This gives a practical definition of the symmetrization operator for first-quantized many-body wave functions: sum the wave function over all possible distributions of the particles in the g layers that keep the particle number in each layer fixed. From this definition, we can easily see why the construction works, based on the vanishing properties of the Read-Rezayi states, expressed in Sec. 2.1.5. We consider a system made of two copies of the Laughlin $\nu = 1/2$ state, and bring three particles of this system to the same position. In every distribution of the particles between the two copies, one of the copies hosts a cluster of at least two particles, ensuring that all terms in the symmetrization sum vanish (since each term is a product of two Laughlin states). If we bring only two particles to the same place, some terms of the sum (corresponding to one of these particles in each layer) do not vanish. The resulting state thus has the vanishing properties of the Moore-Read state (it vanishes when at least three particles are brought to the same position), and is a zero energy eigenstate of the model Hamiltonian Eq. (2.36). Since the filling factor is doubled by the symmetrization procedure, the symmetrized state is characterized by $\nu = 1$, and is equal to the Moore-Read state.

In second quantization, the equivalent operation acting on single-particle operators can be defined as follows: Let $\Phi_{j,l}^\dagger$ be the single-particle operator that creates a boson in orbital j of layer $l = 0, \dots, g-1$. (We assume that all layers are equivalent and the orbitals are labeled in the same way.) Then, the symmetrization $\mathcal{S}_{g \rightarrow 1}$

$$\Phi_{j,l}^\dagger \xrightarrow{\mathcal{S}_{g \rightarrow 1}} \Phi_j^\dagger. \quad (3.15)$$

maps these operators to the single-particle operators ϕ_j^\dagger in a single layer system (hence we can suppress the layer index), i.e., it simply erases the layer index of the operators.

We note that there is a fundamental problem with the symmetrization construction (3.13) for systems of finite size. If a densest ground state $|\Psi_{gk}\rangle$ has a particle number N that is not divisible by g , this particle number cannot be spread equally over g densest states $|\Psi_k\rangle$. To give a simple example, consider the bosonic Moore-Read state $|\Psi_2\rangle$ with $N = 7$ particles, which is a zero-energy ground state of the Hamiltonian (3.1) on a torus with $N_\phi = 7$ flux quanta (filling $\nu = 1$). On the same torus, the bosonic $\nu = 1/2$ Laughlin state $|\Psi_1\rangle$ does not exist as a zero energy ground state, since $N_\phi = 7$ is not divisible by two. One could consider symmetrizing over a Laughlin quasihole state with $N = 3$ and a Laughlin quasielectron state with $N = 4$ (the latter being at finite energy since its filling factor is larger than that of the Laughlin state). However, this construction can at best yield an approximation of the desired $|\Psi_2\rangle$ ground state (we checked numerically that the corresponding overlap was of the order of 0.998 for $N = 17$). It might be possible to obtain the exact state by using the composite fermion [72] expression of the quasielectron states, but these are very hard to obtain on the torus [69, 44]. A similar obstruction appears for all \mathbb{Z}_k Read-Rezayi states with k even on a torus with odd N_ϕ .

This obstruction to build the \mathbb{Z}_k Read-Rezayi states from a layered construction also occurs when looking at quasihole excitations. Adding flux quanta to the original $\nu = k/2$ system is a way to nucleate quasihole excitations of the \mathbb{Z}_k Read-Rezayi states. While the obstruction disappears for a sufficient number of added flux quanta, not all quasihole states are immune to this issue. The system with 7 particles on a torus pierced by $N_\phi = 5$ flux quanta has a filling fraction strictly lower than $3/2$, and thus admits zero energy states of the 4-body interaction of the \mathbb{Z}_3 Read-Rezayi state. However, the 7 particles can at best be spread into two layers with 2 particles (Laughlin quasihole state) and one layer with 3 particles (Laughlin quasielectron), resulting in a non-zero energy state after symmetrization. In general, we see that for odd N_ϕ and the largest N such that $N/N_\phi \leq k/2$, the \mathbb{Z}_k states cannot be constructed using the symmetrization technique.

3.1.4 The projective construction with a twist

In this section, we will demonstrate that an alternative symmetrization scheme on the torus can remedy this obstruction. The key idea is to change the boundary conditions between the layers from periodic to twisted, as depicted in Fig. 3.1. Equivalently, this can be seen as introducing a topological defect line that permutes the layer indices [14, 12, 13, 11, 157]. Similarly to the symmetrization over multiple independent layers, our construction with twisted boundary conditions in one direction between the layers alone does not yield the complete \mathbb{Z}_k manifold. To obtain the complete manifold, two of the three symmetrization schemes (untwisted multilayer, twist in x direction, twist in y direction) have to be combined. This construction is valid not only on the torus, but in any geometry. More details can

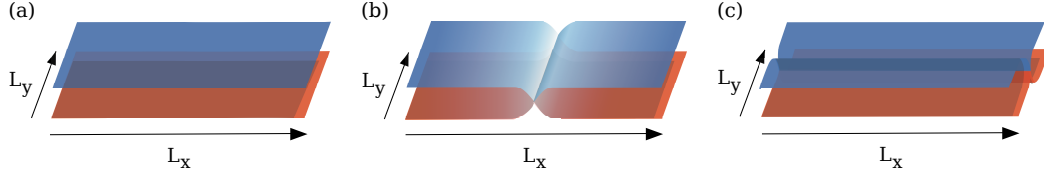


Figure 3.1: Bilayer system with different types of topological defects. a) Bilayer system with no defect. b) Bilayer system with a twist defect along the y direction. If the system has periodic boundary conditions, it is transformed into a monolayer torus with a doubled length in the x direction. c) Bilayer system with a defect along the x direction. If the system has periodic boundary conditions, it is transformed into a single layer torus with a doubled length in the y direction.

be found in Ref. [137].

As a manifold, a double layer torus of size $L_x \times L_y$ with twisted boundary conditions in the x -direction (respectively y -direction) is equivalent to a single layer torus of size $2L_x \times L_y$ (respectively $L_x \times 2L_y$). Note that the magnetic field is preserved, and the number of flux quanta piercing the two times enlarged torus is thus $2N_\phi$. It is possible to show that this equivalence between manifolds is also respected by the model Hamiltonian (3.1) for the Read-Rezayi state. To be more precise, let us focus on $k = 1$ and consider a bilayer system of size $L_x \times L_y$ with twisted boundary conditions in the x -direction. Because of the twist, it is not possible to label the two layers with a global index, but locally, one can always distinguish two different layers. The N bosons living on this manifold interact via the two-body contact interaction, which acts on two bosons with the same layer index. On the other hand, we consider N bosons living on a single layer torus of size $2L_x \times L_y$, interacting via the two-body contact interaction of Eq. (3.1). The two systems described here are in fact equivalent, and the absence of interlayer interaction in the original Hamiltonian is key to proving it. This equivalence carries over to the g layer torus (see Fig. 3.2 for an illustration of different possible boundary conditions of three layers). Rather than proving this property (the detailed demonstration was provided in Ref. [137]), we will focus on giving a practical definition of the symmetrization procedure on the g times enlarged torus, in first and second quantized notations. In fact, we will see that simple arguments – based on writing the action of the symmetrization operator in real space – allow us to derive the vanishing properties of the symmetrized states.

We define T as the rectangular torus of size $L_x \times L_y$, and $(gT)_i$ as the torus enlarged g times in the i direction (for example, $(gT)_x$ is the rectangular torus of size $gL_x \times L_y$). The symmetrization operator $\mathcal{S}_{(gT)_i \rightarrow T}$ acts on a many-body wave function defined on $(gT)_i$, $i = x, y$ and yields a many-body wave function defined on the torus T . We start by writing the action of $\mathcal{S}_{(gT)_i \rightarrow T}$ in first quantized notation. The translation operator $\mathcal{T}_{L_i \mathbf{e}_i}^j$ (as defined in Sec. 2.2.3.1) translates the particle j by $L_i \mathbf{e}_i$ on $(gT)_i$, $i = x, y$. The symmetrization identifies positions that are related by any translation of a vector $\delta L_i \mathbf{e}_i$, where $0 \leq \delta < g$, $\delta \in \mathbb{Z}$. Starting from a

many-body wave function Ψ on a $(gT)_i$ torus, the symmetrized wave function reads

$$\mathcal{S}_{(gT)_i \rightarrow T} \Psi(\mathbf{r}_1, \dots, \mathbf{r}_N) = \sum_{\{0 \leq \delta_j < g\}} \left(\prod_{j=1}^N \mathcal{T}_{\delta_j L_i \mathbf{e}_i}^j \right) \Psi(\mathbf{r}_1, \dots, \mathbf{r}_N). \quad (3.16)$$

where \mathbf{r}_j denotes the coordinates of the j -th particle restricted to the $L_x \times L_y$ region. With our gauge choice (see Eq. (1.44)), magnetic translations in the y direction $\mathcal{T}_{\delta_j L_y \mathbf{e}_y}^j$ identify with simple spatial (not magnetic) translations. As a result, the translations in the y direction are not accompanied by a phase change, and Eq. (3.16) has an even more explicit expression for $\mathcal{S}_{(gT)_y \rightarrow T}$

$$\mathcal{S}_{(gT)_y \rightarrow T} \Psi(\mathbf{r}_1, \dots, \mathbf{r}_N) = \sum_{\{0 \leq \delta_j < g\}} \Psi(\mathbf{r}_1 + \delta_1 L_y \mathbf{e}_y, \dots, \mathbf{r}_N + \delta_N L_y \mathbf{e}_y) \quad (3.17)$$

The vanishing properties of the symmetrized wave function can immediately be deduced from those of Ψ . Indeed, if Ψ is a Laughlin wave function (or one of its quasihole excitations), it vanishes when two particles are at the same point. There are terms in the sum of Eq. (3.17) where $\delta_1, \dots, \delta_g$ are all distinct integers. If we put the g first particles at the same position, these terms do not need to vanish. We now bring the $(g+1)$ -th first particles at the same position. In each term of the sum, at least two integers δ_i among $\delta_1, \dots, \delta_{g+1}$ are equal, ensuring that Ψ is evaluated at a position including two equal coordinates. Thus $\mathcal{S}_{(gT)_y \rightarrow T} \Psi$ vanishes when $g+1$ particles are at the same position, proving it is a zero energy eigenstate of the $(g+1)$ -body contact interaction (3.1), i.e. a \mathbb{Z}_g Read-Rezayi wave function (or one of its quasihole excitations). A similar argument holds true for the symmetrization on the $(gT)_x$ torus, including Eq. (3.16).

Writing the action of the symmetrization operators in real space is useful to derive the vanishing properties of the symmetrized states, but it is not very practical for numerical purposes. For that, we need to derive their action on the single-particle operators. Starting from the single-particle states $\Phi_j^{(gT)_i}$, $j = 0, \dots, gN_\phi - 1$ on the g times enlarged torus $(gT)_i$, we want to build a basis of single-particle wave functions Φ_j^T , $j = 0, \dots, N_\phi - 1$ on the torus T . First, we focus on $(gT)_x$, the torus enlarged g times in the x direction. Using the commutation properties (1.41) of the single-particle translation operators, we write

$$\begin{aligned} \mathcal{T}_{\mathbf{e}_y} \mathcal{T}_{L_x \mathbf{e}_x} \Phi_j^{(gT)_x} &= e^{2\pi i N_\phi / L_y} \mathcal{T}_{L_x \mathbf{e}_x} \mathcal{T}_{\mathbf{e}_y} \Phi_j^{(gT)_x} \\ &= e^{2\pi i (j + N_\phi) / L_y} \mathcal{T}_{L_x \mathbf{e}_x} \Phi_j^{(gT)_x} \end{aligned} \quad (3.18)$$

Thus on the $(gT)_x$ torus, a translation of a particle by a vector $L_x \mathbf{e}_x$ shifts the orbital index by N_ϕ .

$$\mathcal{T}_{L_x \mathbf{e}_x} \Phi_j^{(gT)_x} = \Phi_{(j+N_\phi) \bmod (gN_\phi)}^{(gT)_x} \quad (3.19)$$

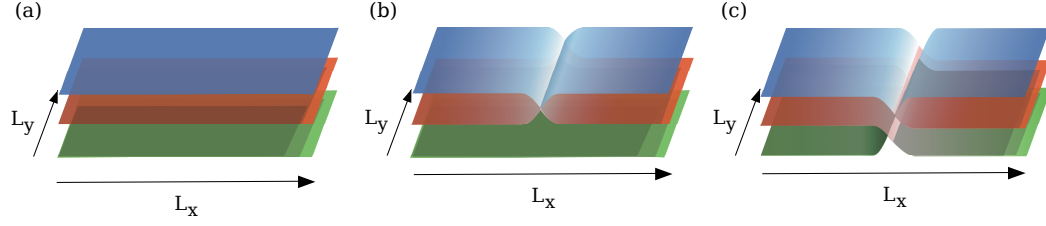


Figure 3.2: Trilayer system with different types of topological defects. a) Trilayer system with no defect. b) Trilayer system with a defect along the y direction connecting the two upper layers. With periodic boundary conditions, this system is equivalent to a bilayer torus, with the first layer having aspect ratio 2, and the second layer having aspect ratio 1. c) Trilayer system with a defect along the y direction connecting respectively layers 1 (blue) and 2 (red), 2 and 3 (green), 3 and 1. With periodic boundary conditions, this system is equivalent to a torus with aspect ratio 3.

A valid single-particle state on the T torus must verify the periodic boundary conditions of Eq. (1.44), in particular

$$\mathcal{T}_{L_x \mathbf{e}_x} \Phi_j^T = \Phi_j^T \quad (3.20)$$

(the periodic boundary conditions in the y direction are automatically verified by definition of $\Phi_j^{(gT)_x}$). Φ_j^T can thus be written as a linear combination with equal coefficients of g single-particle states on $(gT)_x$ regularly distributed in momentum space (see Fig. 3.3b for an example with $g = 2$).

$$\Phi_j^T = \frac{1}{\sqrt{g}} \sum_{s=0}^{g-1} [\mathcal{T}_{L_x \mathbf{e}_x}]^s \Phi_j^{(gT)_x} \quad (3.21)$$

$$= \frac{1}{\sqrt{g}} \sum_{s=0}^{g-1} \Phi_{(j+sN_\phi)}^{(gT)_x} \quad (3.22)$$

To write these states as a function of the single-particle states on the $(gT)_y$ torus, we can use the fact that in the y direction, the single-particle wave functions behave like plane waves. This implies

$$\mathcal{T}_{L_y \mathbf{e}_y} \Phi_j^{(gT)_y} = e^{2\pi i j/g} \Phi_j^{(gT)_y} \quad (3.23)$$

As a result, $\Phi_j^{(gT)_y}$ is invariant under a magnetic translation $\mathcal{T}_{L_y \mathbf{e}_y}$ whenever the particle momentum j is a multiple of g , and the wave functions

$$\Phi_j^T = \Phi_{gj}^{(gT)_y} \quad (3.24)$$

are valid single-particle states on the torus T .

The above discussion of the translational properties of the single-particle states holds for the single-particle operators, and gives a practical implementation of the symmetrization operator in second quantized notation. For a g times enlarged torus in the x direction, the added occupations of the g orbitals $(j + N_\phi) \bmod (gN_\phi)$ give the occupation of the j^{th} orbital on the T torus. On the other hand, the occupation of the $(gj)^{\text{th}}$ orbital on the $(gT)_y$ torus becomes that of the j^{th} orbital on j^{th} . These constructions are summarized in the case of a twice enlarged torus in Fig. 3.3.

This practical implementation of the symmetrization allowed us to test it in finite size systems. To benchmark our construction, two separate questions are relevant. First, what are the properties of the constructed states, and in particular, are these states the exact states that we are trying to reproduce, or some approximation? If Ψ is a zero energy eigenstates of the $(k+1)$ contact interaction (3.1) we know from the vanishing properties that the symmetrized states must be zero energy eigenstates of the $(gk+1)$ contact interaction. This answers the question in the case of a Read-Rezayi ground state or quasihole state: the construction yields states that are exactly the \mathbb{Z}_{gk} states. When Ψ is a low (but non-zero) energy excitation of a \mathbb{Z}_k Read-Rezayi state, we will show in Sec. 3.3.2.2 that the symmetrized states are good approximations of the neutral low energy excitations of the \mathbb{Z}_{gk} Read-Rezayi state. The second question concerns the completeness of the description. As pointed out in Sec. 2.2.4, the number of quasihole states for a given fractional quantum Hall state is a signature of the topological order. Being able to write all quasihole states within the projective construction is thus crucial. This also brings us back to our original motivation for this study, the fact that some states were missing in the decoupled multilayer construction. We thus generated numerically (using exact diagonalization) the \mathbb{Z}_k quasihole manifolds for $k = 1, 2, 3, 4$ and all accessible N and N_ϕ . We compared the manifolds resulting from the symmetrization of the \mathbb{Z}_k quasihole states with the \mathbb{Z}_{gk} quasihole manifolds obtained using exact diagonalization, and found that these manifolds were identical, i.e. the description is complete (see Ref. [137] for details).

In this section, we presented an exact construction of the \mathbb{Z}_k Read-Rezayi states, focusing on the zero modes of the model Hamiltonian (3.1). In the rest of the chapter, we will turn to the physics of the low energy excitation above these ground states. We look at $k = 1$ and $k = 2$, i.e. the neutral excitations above the Laughlin and Moore-Read ground states. Most of the existing literature studies these excited states on the sphere geometry, and will give an account of previous results on the sphere in the following section, before moving on to the torus geometry.

3.2 Physics of the neutral modes

3.2.1 The collective excitation mode above the Laughlin state

The ground state of the Coulomb interaction at $\nu = 1/3$ is understood to be gapped, since it corresponds to a plateau of the Hall conductivity. It is interesting to investigate its lowest energy excitations, to gain some insight as to why there is a gap,

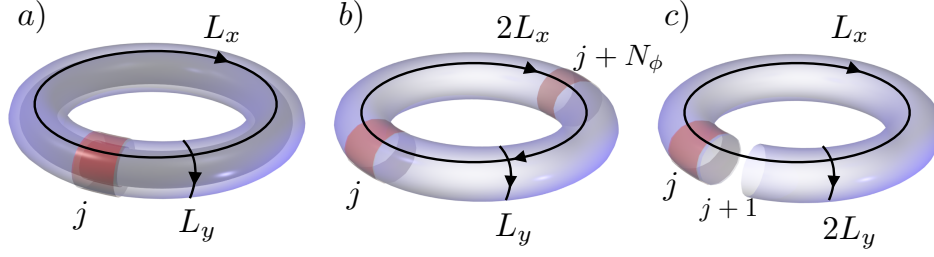


Figure 3.3: Schematic representation of the symmetrization procedure to obtain the ground state on the T torus of dimensions $L_x \times L_y$ pierced by N_ϕ flux quanta. The orbitals colored in red have become equivalent after symmetrization. a) The T torus bilayer of lengths $L_x \times L_y$, pierced by N_ϕ flux quanta. b) The $(2T)_x$ torus of lengths $2L_x \times L_y$, pierced by $2N_\phi$ flux quanta. c) The $(2T)_y$ torus of lengths $L_x \times 2L_y$, pierced by $2N_\phi$ flux quanta.

and what mechanism may compromise the stability of this gap. Girvin, MacDonald, Platzman [49, 50] proposed a trial wave function to describe the low energy excitation above the ground state at filling $1/3$. Their approach was inspired by Feynman's construction of phonon-like excitations in superfluid Helium. The principle of this construction, called single mode approximation (SMA) is that the low energy excitation should be a density modulation of the ground state. Assuming the neutral excited states indeed form a density wave, the SMA gives us their wave function as a function of the ground state wave function

$$\Psi^{SMA}(\mathbf{k}) = \frac{1}{\sqrt{N}} \hat{\rho}_{\mathbf{k}} \Psi(\mathbf{r}_1, \dots, \mathbf{r}_N) \quad (3.25)$$

where $\hat{\rho}_{\mathbf{k}}$ is the Fourier transform of the density operator projected into the lowest Landau level, and $\Psi(\mathbf{r}_1, \dots, \mathbf{r}_N)$ is an ansatz for the ground state. One can use the exact ground state, as obtained by exact diagonalization, or a model wave function such as the Laughlin state of Eq. (2.17). The lowest Landau level projection is useful to ensure there is no mixing with higher Landau levels, as should be the case for a low energy excitation at high magnetic field. Considerations on the neutral mode, as well as the SMA extend to bosonic systems, with filling fraction $\nu = 1/2$.

The energy of this trial wave function was evaluated numerically on the sphere geometry for the Coulomb and the model Hamiltonian of Eq. (2.23), and shows great agreement [178] with the exact energies of these models, especially at long wavelength. In particular, it reproduces correctly the roton minimum that appears in the dispersion relation, and that gives its name to the neutral mode: magneto-roton (see Fig. 3.4a for a plot of the magneto-roton in finite size). The GMP approach predicts a deepening of the roton minimum as the filling fraction decreases, and a closing of the gap at $\nu \simeq 1/6.5$ at a wave vector amplitude k_W (see Ref. [49]). This is compatible with the symmetry breaking that occurs at low filling, corresponding to the formation of a Wigner crystal. In particular, the position of the roton minimum

k_W is compatible with the lattice constant of the Wigner crystal.

The success of the GMP approach validates the understanding of the magneto-roton mode as a density wave. It is a sign that the magneto-roton mode emerges from the interaction of a quasielectron-quasihole pair with the Laughlin liquid background. Within this interpretation, the magneto-roton states can be viewed as states that minimally violate the generalized exclusion principle of Sec. 2.2.4. Ref. [178] validated this interpretation by proposing trial wave functions for the neutral mode within this approach. This provides model wave functions agreeing with the SMA at long wavelength, and are even better approximations of the magneto-roton states for all momenta.

3.2.2 The neutral modes above the Moore-Read state

Like the Laughlin state, the Moore-Read state has a well defined collective excitation mode. The Moore-Read state being a paired state (see Sec. 2.1.5), its properties and that of its excitations dramatically depend on the parity of the number of particles. On the sphere, the Moore-Read only appears at even numbers of particles. There is a neutral mode above this state, which is also called magneto-roton mode, because it bears strong similarities to the magneto-roton mode above the Laughlin state. Indeed, it is well described by the single-mode approximation [178]. For an odd number of particles, no zero energy ground state of the three-body contact (respectively hollow core) Hamiltonian is found at filling fraction $\nu = 1$ for bosons (respectively $\nu = 1/2$ for fermions) on the sphere. In spite of the absence of zero energy state, there is a neutral low energy mode with a dispersion different from that of the magneto-roton mode, as numerically shown in Refs. [103, 27]. This mode was dubbed neutral fermion mode. Both the magneto-roton and the neutral fermion modes can be viewed as states that minimally violate the generalized exclusion principle. In the magneto-roton mode, the violation appears as a quasielectron-quasihole pair, similar to the Laughlin case. In the neutral fermion mode, the violation consists of a single unpaired particle in a background of paired particles. The Jack polynomial approach of Ref. [178] was also adapted in the same work to the neutral modes above the Moore-Read state, thus validating the above interpretation.

Finally, trial states for the magneto-roton and neutral fermion modes can be written on the sphere using the projective construction of fractional quantum Hall states presented in Sec. 3.1.3. Within the projective construction, the neutral modes can be approximated [142, 150, 151] using elementary excitations of the Laughlin state (quasielectron, quasihole and exciton). Note that the quasielectron and exciton (quasielectron - quasihole pair) states can be approximated using the composite fermion construction on the sphere, thus facilitating the projective approach.

3.3 Neutral modes on the torus

In this section, we study the properties of the neutral mode above the Laughlin and Moore-Read states on the torus. We want to give the dispersion relation of the

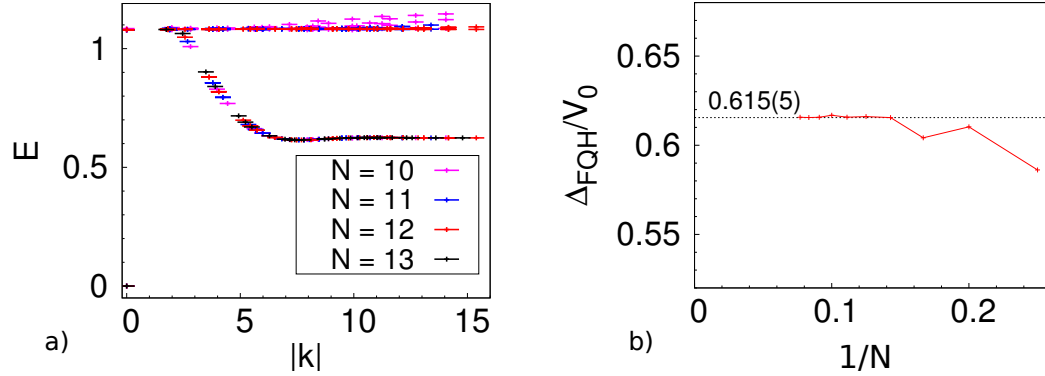


Figure 3.4: Exact diagonalization results for the model two-body interaction on the torus at filling $\nu = 1/2$. a) Low energy spectrum for up to $N = 13$ bosons and $N_\phi = 2 \times N$ flux quanta, as a function of the modulus of the momentum \mathbf{k} , which was defined in Eq. (3.28). b) Scaling of the many-body gap as a function of the inverse number of particles. We see that the finite size effects become negligible for relatively small systems ($N > 7$)

collective modes corresponding to the model Hamiltonian of Eq. (3.1) (the bosonic Laughlin and Moore-Read states are exact ground states of this Hamiltonian for respectively $k = 1$ and $k = 2$). We use the model interaction for simplicity. Also, in bosonic systems, the contact two-body interaction is more realistic than any longer range interaction, since the most relevant experimental system for the bosonic fractional quantum Hall phases are cold atomic gases. Moreover, on the sphere, Ref. [103] showed that the neutral modes appeared most clearly if one used the model three-body interaction instead of any more realistic two-body interaction. This motivates using the three-body interaction on the torus as well. We start by diagonalizing the model Hamiltonians of the bosonic Laughlin and Moore-Read states, at respective filling factors $\nu = 1/2$ and $\nu = 1$, as written and factorized in Sec. 3.1.2. We show that the single mode approximation (SMA) can easily be adapted to the torus geometry. Also, the new form of the projective construction can be used to approximate the neutral modes above the Moore-Read state with a high accuracy.

3.3.1 Neutral mode above the Laughlin state on the torus

3.3.1.1 Exact diagonalization results

We focus on a filling fraction $\nu = 1/2$ of the lowest Landau level. Note that while all numerical results are given for $\nu = 1/2$, the analytical expressions in this section are valid generically for any filling fraction $\nu = 1/q$ where q is an even integer. We need to properly choose the quantum numbers against which to plot the spectrum, to unveil the dispersion relation of the neutral mode. As seen in Sec. 2.2.3.1, the translations on the torus can be factorized into the product of a center of mass (CM)

and a relative translation. The CM translation operator along the y axis and the relative translation operator along the x axis commute with each other and with the Hamiltonian. The eigenstates of the Hamiltonian thus carry the corresponding momentum quantum numbers \mathbf{k} that belong to the FQH Brillouin zone BZ_{FQH}

$$\text{BZ}_{\text{FQH}} \equiv \left\{ \mathbf{k} = \frac{2\pi}{L_x} k_x \tilde{\mathbf{e}}_x + \frac{2\pi}{L_y} k_y \tilde{\mathbf{e}}_y \mid \right. \\ \left. k_x = 0, \dots, \text{GCD}(N, N_\phi) - 1; k_y = 0, \dots, N_\phi - 1 \right\}. \quad (3.26)$$

where GCD stands for the greatest common divisor, and $\tilde{\mathbf{e}}_x, \tilde{\mathbf{e}}_y$ are two unit vectors in the reciprocal lattice, such that $\mathbf{e}_i \cdot \tilde{\mathbf{e}}_j = \delta_{i,j}$. In the following, we shall only consider cases where $N_\phi = qN$ (corresponding to the filling fraction $1/q$ of the Laughlin state), so that BZ_{FQH} consist of $N \times N_\phi$ points. The center of mass degeneracy introduced in Sec. 2.2.3.1 relates q states that differ by a CM momentum translation $\mathbf{k}_y \rightarrow \mathbf{k}_y + N$ modulo N_ϕ . On the sphere, the magneto-roton is observed when the spectrum is plotted as a function of the angular momentum L . Analogously, on the torus, the spectrum should be plotted as a function of $|\mathbf{k}|$. To avoid redundancies due to the center of mass degeneracy, \mathbf{k} should be chosen in the reduced Brillouin zone [59], which is of size $N \times N$ at filling $\nu = 1/q$

$$\text{BZ}_{\text{FQH}}^{\text{red}, 1/q} \equiv \left\{ \mathbf{k} = \frac{2\pi}{L_x} k_x \tilde{\mathbf{e}}_x + \frac{2\pi}{L_y} k_y \tilde{\mathbf{e}}_y \mid \right. \\ \left. k_x = 0, \dots, N - 1; k_y = 0, \dots, N - 1 \right\}. \quad (3.27)$$

While the q topologically degenerate ground states appear at different momenta $\mathbf{K}_\alpha \in \text{BZ}_{\text{FQH}}$, with $\alpha = 0, \dots, q - 1$, they all map to momentum $\mathbf{k} = 0$ in $\text{BZ}_{\text{FQH}}^{\text{red}, 1/q}$. This way, all their magneto-roton dispersions coincide at the same momenta. Collapsing data for various system sizes, Fig. 3.4a clearly exposes the magneto-roton mode as an excitation mode above the ground state and below the continuum of higher energy excitations. The data is then plotted as a function of $|\mathbf{k}|$, i.e.,

$$|\mathbf{k}| = \frac{2\pi}{\sqrt{N} \sin \theta} \sqrt{r^{-1} k_x^2 + r k_y^2 - 2 \cos \theta k_x k_y}, \quad (3.28)$$

where $r = L_x/L_y$ is the aspect ratio, and θ is the angle formed by \mathbf{e}_x and \mathbf{e}_y , the vectors spanning the torus. We observe in Fig. 3.4a that the magneto-roton dispersion does not show a magneto-roton minimum, but rather flattens out for momenta $|\mathbf{k}| > 2$. This behavior can be attributed to the short-range nature of the pseudopotential interaction. In contrast, for the Coulomb interaction, a deep minimum would be visible (see Ref. [178] for a comparison between short range interactions and the Coulomb interaction). For a wide range of system sizes, the FQH magneto-roton modes all fall on the same curve, as shown Fig. 3.4a. Indeed, the gap between the ground state and the first excited state (which belongs to the magneto-roton mode) exhibits almost no finite size effect, starting from $N = 7$. We extract the many-body gap of the FQH systems and plot it as a function of $1/N$ in Fig. 3.4b. The thermodynamic extrapolation of the gap yields a value of

$\Delta = 0.615(5) \times V_0$, where V_0 is the scale of the two-particle interaction energy. The scaling of the gap on the sphere geometry was studied in Refs. [132, 133], and shows a more important finite size effect than we observe on the torus. The extrapolated gap of the Laughlin $\nu = 1/2$ system on the sphere is $0.60(1) \times V_0$, in agreement with our value on the torus geometry. Note that the scaling on the sphere assumed a linear behavior as a function of $1/N$, which may underestimate the thermodynamic value of the gap.

3.3.1.2 Single mode approximation on the torus

To use the SMA (3.25) on the torus, we have to take into account the q -fold degeneracy of the Laughlin state on this geometry. In this context, the SMA provides a variational expression for the low energy excitations above the topologically degenerate ground states $|\Psi_\alpha\rangle$, $\alpha = 0, \dots, q-1$ of the $1/q$ Laughlin state. The trial state is given by

$$|\Psi_{\mathbf{k},\alpha}^{\text{SMA}}\rangle = \hat{\rho}_{\mathbf{k}} |\Psi_\alpha\rangle. \quad (3.29)$$

where the Fourier transform of the density operator projected onto the lowest Landau level $\hat{\rho}_{\mathbf{k}}$ was expressed on the torus in Eq. (3.11). The momentum of $|\Psi_{\mathbf{k},\alpha}^{\text{SMA}}\rangle$ is given by the momentum \mathbf{K}_α of $|\Psi_\alpha\rangle$ shifted by \mathbf{k} . Given the states $|\Psi_{\mathbf{k},\alpha}^{\text{SMA}}\rangle$, one can obtain an approximation to the dispersion of the magneto-roton mode via

$$E_{\mathbf{k}}^{\text{mr}} = \frac{\langle \Psi_{\mathbf{k},\alpha}^{\text{SMA}} | H | \Psi_{\mathbf{k},\alpha}^{\text{SMA}} \rangle}{\langle \Psi_{\mathbf{k},\alpha}^{\text{SMA}} | \Psi_{\mathbf{k},\alpha}^{\text{SMA}} \rangle}, \quad (3.30)$$

where H is the many-body Hamiltonian of the FQH system.

In the expression of $\hat{\rho}_{\mathbf{k}}$ (3.11), we do not restrict \mathbf{k} to belong to BZ_{FQH} , as was pointed out in Refs. [31, 109]. Rather, for every $\mathbf{k} \in \text{BZ}_{\text{FQH}}$, there exist several linearly independent operators $\hat{\rho}_{\mathbf{k}+\mathbf{G}}$ with the reciprocal lattice vectors

$$\mathbf{G} = 2\pi N (\mathbf{G}_x/L_x, q\mathbf{G}_y/L_y)^\top, \quad (\mathbf{G}_x, \mathbf{G}_y) \in \mathbb{Z}^2. \quad (3.31)$$

More precisely, $\hat{\rho}_{\mathbf{k}+\mathbf{G}} = \hat{\rho}_{\mathbf{k}+\mathbf{G}'}$ if there exists a pair of integers $(\mathbf{g}_x, \mathbf{g}_y)$ such that

$$\begin{aligned} \mathbf{G}_x - \mathbf{G}_x' &= q \mathbf{g}_x \\ \mathbf{G}_y - \mathbf{G}_y' &= \mathbf{g}_y \end{aligned} \quad (3.32)$$

This gives rise to q distinct density operators $\hat{\rho}_{\mathbf{k}+\mathbf{G}}$ for every $\mathbf{k} \in \text{BZ}_{\text{FQH}}$. Hence, the $\hat{\rho}_{\mathbf{k}}$ span the same N_ϕ^2 -dimensional space of operators as the boson bilinears $c_{\mathbf{q}_y'}^\dagger c_{\mathbf{q}_y}$, with $\mathbf{q}_y, \mathbf{q}_y' = 0, \dots, N_\phi - 1$. Acting with the $\hat{\rho}_{\mathbf{k}}$ operators on the q -fold degenerate ground states according to Eq. (3.29) thus yields a basis of qN_ϕ^2 linearly independent variational states $\left\{ |\Psi_{\mathbf{k}+\mathbf{G},\alpha}^{\text{SMA}}\rangle \right\}$, spanning what we call the bilinear subspace. That is, for every of the $N \times N_\phi$ good quantum numbers $\mathbf{k} \in \text{BZ}_{\text{FQH}}$, we can build q^2 variational states with the help of the density operator (3.11). Here, one factor of

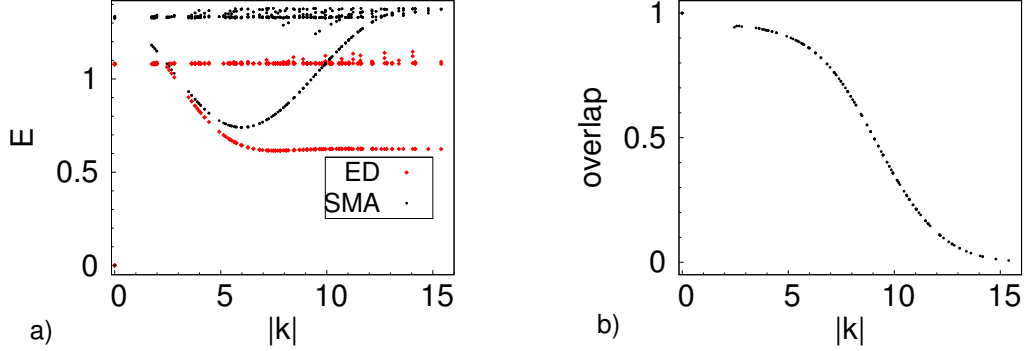


Figure 3.5: a) Low energy spectrum of the FQH systems with up to $N = 13$ bosons on the torus, at half filling. The variational energy of the SMA states are compared to the energies obtained through exact diagonalization (ED) of the Hamiltonian. For $N = 13$, only one eigenvalue per sector has been computed via ED. c) The dots show the overlap between the SMA trial state and each exact magneto-roton state, as a function of $|\mathbf{k}|$, for the FQH on the torus with up to $N = 13$ bosons at half filling.

q is due to the q degenerate ground states labeled by α that one can act on, and a second factor of q comes from the distinct shifts by reciprocal lattice vectors \mathbf{G} .

In contrast, the magneto-roton mode consists of at most one state in every of the $N \times N_\phi$ sectors of \mathbf{k} (see Ref. [138] for details). Thus, the naive SMA as given by Eq. (3.29) provides a factor of q^2 more variational states than needed to describe the magneto-roton mode. For each $\mathbf{k} \in \text{BZ}_{\text{FQH}}$, we propose the following rule to select one of the q^2 SMA states

$$|\Psi_{\mathbf{k}+\mathbf{G},\alpha}^{\text{SMA}}\rangle \equiv \hat{\rho}_{\mathbf{k}+\mathbf{G}} |\Psi_\alpha\rangle, \quad \alpha = 0, \dots, q-1, \quad (3.33a)$$

as the variational state for the magneto-roton mode: The variational magneto-roton state is given by

$$|\Psi_{\mathbf{k}}^{\text{mag-SMA}}\rangle = |\Psi_{\mathbf{k}+\mathbf{G}_0,\alpha_0}^{\text{SMA}}\rangle, \quad (3.33b)$$

where α_0 labels the ground state at momentum $\mathbf{K}_\alpha \in \text{BZ}_{\text{FQH}}$ and \mathbf{G}_0 is the reciprocal lattice vector for which the momentum-space distance

$$|\mathbf{k} + \mathbf{G} - \mathbf{K}_\alpha| \quad (3.33c)$$

is minimized for fixed $\mathbf{k} \in \text{BZ}_{\text{FQH}}$. An illustration of this selection rule for the simplest case of $q = 2$ is given in Fig. 3.6. This rule is motivated by the fact that the SMA is an approximation at small momentum $|\mathbf{k}|$ of the magneto-roton mode.

We tested the validity of this approach by computing the energy of the states $|\Psi_{\mathbf{k}}^{\text{mag-SMA}}\rangle$. It is represented on the same graph as the exact diagonalization results in Fig. 3.5a. We observe that the SMA variational energies only slightly

overestimate the magneto-roton mode energy at small momenta $|\kappa| < 2\pi$, in a way that accurately preserves the shape of the dispersion relation. For momenta $|\kappa| > 2\pi$, the SMA energies increase and finally merge with the continuum of excited states, while the magneto-roton mode flattens out to constant values. Note that neither the magneto-roton mode nor its approximation show any visible finite size effect. The estimated value of the excitation gap from the SMA dispersion is $0.74(2)$, which corresponds to a relative error of 20% as compared to the exact diagonalization result. In accordance with the behavior of the SMA variational energies, the overlap between the SMA state selected by criterion (3.33) and the respective exact magneto-roton eigenstate at a given $\mathbf{k} \in \text{BZ}_{\text{FQH}}$ is high ($\simeq 0.9$) for small magnitudes of $|\kappa| < 2\pi$ of the rescaled momentum κ , and drops significantly for $|\kappa| > 4\pi$ (see Fig. 3.5b). Finally, to check the validity of the selection criterion (3.33) for SMA states, we diagonalized the interacting Hamiltonian at every $\mathbf{k} \in \text{BZ}_{\text{FQH}}$ in the full q^2 subspace of SMA states (3.33a). The q^2 energy eigenvalues per momentum sector are superimposed with the exact and SMA spectra in Fig. 3.5a. We observe that the enlarged space of variational states does not further improve the approximation to the magneto-roton dispersion that was obtained with the variational states selected by criterion (3.33). In particular, the flattening of the magneto-roton dispersion at large $|\kappa|$ is not captured in this approach either. This is supported by the overlaps of the full SMA subspace with the magneto-roton mode being not significantly larger than the overlap of the single SMA state selected by criterion (3.33) in each momentum sector (see Fig. 3.5b).

3.3.2 Neutral mode above the Moore-Read state on the torus

3.3.2.1 Exact diagonalization results

We now characterize the neutral modes above the Moore-Read state via the exact diagonalization of the three-body contact interaction. As reported in Ref. [120], on the torus, both types of neutral excitation modes above the Moore-Read state appear irrespective of the parity of N . We show that they are actually different parts of one common neutral excitation mode (see Fig. 3.7).

Generically, in the low energy spectrum of the three-body contact interaction, we observe patterns of low energy modes, with up to four distinct dispersing branches that merge with the continuum of states near the four inversion symmetric momenta of the FQH Brillouin zone BZ_{FQH}

$$\mathbf{k}_0 = 0, \quad \mathbf{k}_1 = \pi \tilde{\mathbf{e}}_x, \quad \mathbf{k}_2 = \pi \tilde{\mathbf{e}}_y, \quad \mathbf{k}_3 = \pi \tilde{\mathbf{e}}_x + \pi \tilde{\mathbf{e}}_y. \quad (3.34)$$

Note that \mathbf{k}_1 , \mathbf{k}_2 and \mathbf{k}_3 are not valid accessible momenta when N is odd, but rather are defined as reference points in the Brillouin zone.

On the torus, the continuous rotational symmetry of the quantum Hall problem is only broken by the boundary conditions. Still, the physics governing the neutral excitation modes should be dominated by shorter length scales comparable to the magnetic length. We can thus expect that the dispersion of the neutral excitation

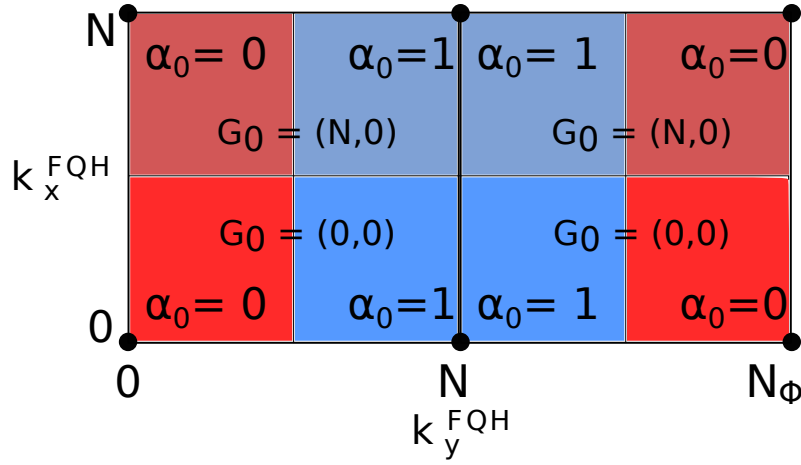


Figure 3.6: Schematic representation of the SMA construction rule Eq. (3.33c) in the FQH Brillouin zone BZ_{FQH} . The position of the ground states is marked by black dots. In the vicinity of the origin (red), the magneto-roton states are well approximated by SMA states stemming from the first ground state ($\alpha_0 = 0$). Conversely, around $(k_x, k_y) = (0, N)$ (blue), the magneto-roton states are approximated by SMA states originating from the second ground state ($\alpha_0 = 1$). In the upper area, one should use the density operator at $\mathbf{k} + \mathbf{G}_0$ with $\mathbf{G}_0 = (N, 0)$ to obtain the magneto-roton state. In the lower area, one should use the density operator at $\mathbf{k} + \mathbf{G}_0 = \mathbf{k}$, where $\mathbf{k} \in BZ_{\text{FQH}}$.

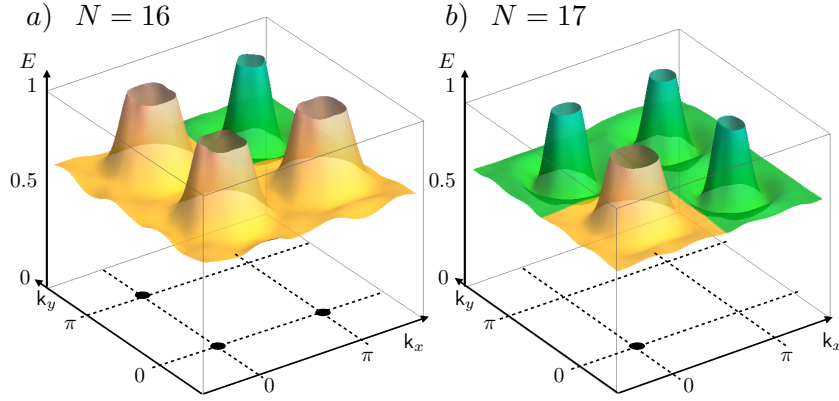


Figure 3.7: Dispersion of the neutral excitation mode above the Moore-Read ground states on the torus as a function of the center of mass and relative momenta of the many-body states in the FQH Brillouin zone. Interpolations of the dispersions are obtained from energy eigenvalues of finite size systems for a) $N = N_\phi = 16$ and b) $N = N_\phi = 17$. In accordance with the momentum sectors Tab. 3.1, these systems feature three ground states and one ground state, respectively (black dots). For energies larger than $E \sim 1$, a continuum of excited states appears (not shown). The dispersions are centered around the inversion symmetric momenta. The slight anisotropy of the dispersive part of each mode near these momenta is a finite size effect. We clearly observe two types of neutral excitations depending on the presence or absence of a zero energy state at the center of the dispersive part. In the presence of a ground state at the inversion symmetric point, the neutral mode is represented in yellow and called magneto-roton mode. In the absence of a ground state, the neutral mode has a much more pronounced minimum. It is represented in green and called neutral fermion mode.

modes is almost rotationally symmetric and can be plotted as a function of a one-dimensional momentum κ . To unveil this dispersion, we have to account for the momentum shifts with respect to the inversion symmetric momenta (3.34). We also include the geometric factor $\sqrt{L_x L_y / N}$ that was introduced in Eq. (3.28), in order to obtain the data collapse with all system sizes. We thus define κ as the minimal distance to any of the inversion symmetric momenta

$$\kappa := \min \{ |\mathbf{k} - \mathbf{k}_i| \mid i = 0, \dots, 3 \}. \quad (3.35)$$

We show the low energy spectrum of the three-body contact interaction in Fig. 3.8 for systems with up to $N = 17$ bosons. For clarity, we represent the three inequivalent regions of the Brillouin zone centered around \mathbf{k}_0 , $\mathbf{k}_1 / \mathbf{k}_2$, and \mathbf{k}_3 in separately panels a), b) and c), respectively. We can clearly identify two modes with different dispersion relations. Above the four ground states, there is a mode flattening out at large momentum without forming an energy minimum [seen in Fig. 3.8 a) for all N and in Fig. 3.8 b) for N even]. This mode is similar to the magneto-roton mode observed above the Laughlin state [49, 50]. Secondly, around inversion symmetric momenta that do not harbor a ground state for a given N , there is another type of neutral mode that features a clear but soft energy minimum before flattening out [seen in Fig. 3.8 c) for all N and in Fig. 3.8 b) for N odd].

These characteristics of a mode without minimum and a mode with minimum are similar to those of the magneto-roton and the neutral fermion modes as observed for the three-body contact interaction on the sphere geometry, for an even and odd number of particles, respectively. Further, we observe that the first mode shows a noticeable finite size effect, while the second one is far better defined. This is consistent with the interpretation given to either mode in terms of weakly interacting elementary excitations on the sphere. In a background of paired quasiparticles, the magneto-roton mode is interpreted as the dispersion relation of an interacting quasiparticle-quasihole pair (i.e., two σ quasiparticles of the underlying Ising field theory), while the neutral fermion mode corresponds to the energy of an unpaired quasiparticle (i.e., one ψ Ising quasiparticle). Since two quasiparticles induce more finite size effect in a system than one, the magneto-roton mode shows more finite size effects than the neutral fermion mode, as was observed for example in Ref. [103]. This interpretation is relatively natural on the sphere, where the magneto-roton mode (respectively the neutral fermion mode) only appears at an even (respectively odd) number of particles. It is however less obvious that this holds on the torus geometry where both the magneto-roton and the neutral fermion modes are observed at the same filling.

3.3.2.2 Approximating the neutral mode using the projective construction

In Refs. [142, 150, 151], trial wave functions for the neutral modes above the Moore-Read state were obtained by symmetrizing over excitations of the Laughlin state on the sphere. If one layer is in a Laughlin ground state, while the other is in a

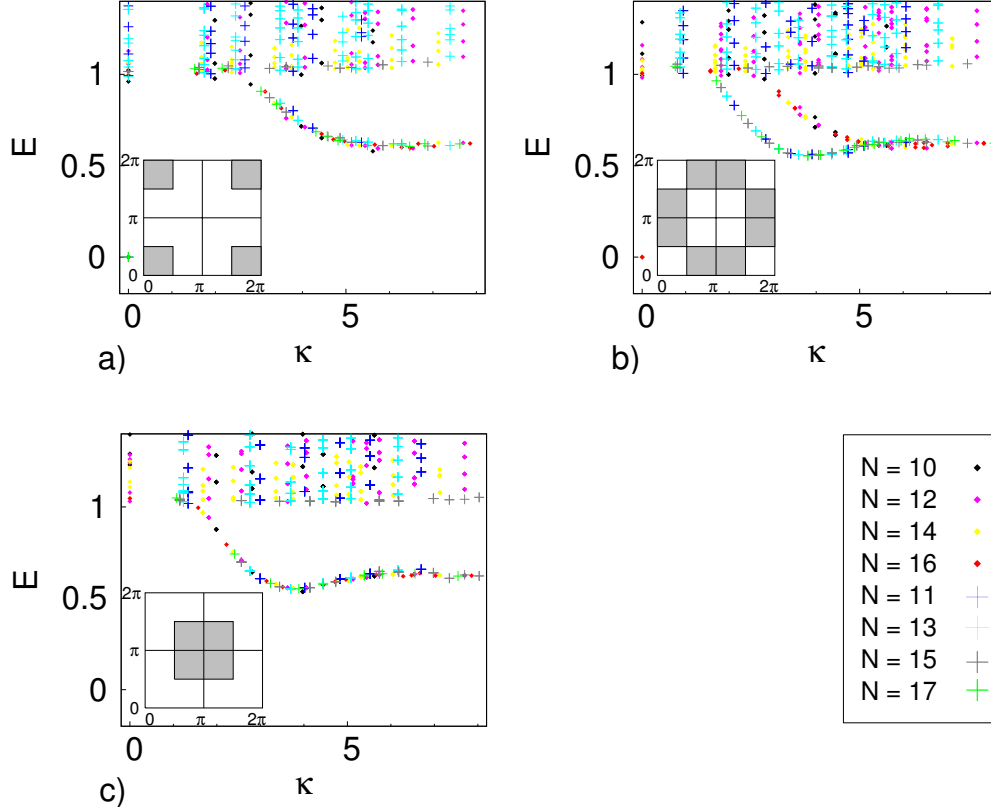


Figure 3.8: Low energy spectrum of the model three-body contact interaction (Moore-Read state) on the torus as a function of the one-dimensional momentum κ defined in Eq. (3.35). In each graph, we show a different domain of the Brillouin zone, which is highlighted in grey in the inset. The black dots (respectively crosses) in the inset represent the Moore-Read ground states for N even (respectively odd). a) For both N even (dots) and N odd (crosses), there is a zero energy eigenstate lying at $\mathbf{k}_0 = 0$. All points fall onto the same curve, defining a neutral excitation (the magneto-roton mode). b) A zero energy state is found at each inversion symmetric momentum in this domain for N even only. The neutral excitation energies fall onto two distinct curves, with the repartition determined by the parity of N . c) No zero energy ground state is found at $\mathbf{k}_3 = (\pi, \pi)$. All neutral excitation energies fall onto the same curve.

magneto-roton state, one obtains an approximation to the Moore-Read magneto-roton state [142, 150]. On the other hand, if one layer is in a Laughlin quasihole state and the other is in a Laughlin quasielectron state, the symmetrized state approximates a neutral fermion state [151].

To test this bilayer construction on the torus geometry, we have performed an extensive numerical study. We found that either periodic boundary conditions or twisted boundary conditions can be used to obtain a complete set of trial states for the entire neutral excitation branch of the Moore-Read state on the torus. We obtained good quantitative agreement both regarding the dispersion of the neutral excitation modes as well as the wave function overlap.

We now compare the symmetrization construction of the neutral modes with the results from exact diagonalization.

–*Neutral excitations from the bilayer torus with periodic conditions* We start with the bosonic Moore-Read state on the torus with an even number of particles N . As a trial wave function for its neutral excitations we use

$$|\Psi_2^{\text{ex}}\rangle = \mathcal{S}_{2 \rightarrow 1}(|\Psi_1\rangle \otimes |\Psi_1^{\text{ex}}\rangle), \quad (3.36)$$

i.e., the symmetrized product of one layer with the Laughlin ground state $|\Psi_1\rangle$ and one layer with its neutral excitation $|\Psi_1^{\text{ex}}\rangle$, the magneto-roton mode.

In Refs. [142, 151], $|\Psi_1\rangle$ and $|\Psi_1^{\text{ex}}\rangle$ were obtained using the composite fermion construction [72]. Here, we use the states resulting from exact diagonalization of the model two-body contact interaction, since the composite fermion construction on the torus is at best a tedious task [69], and is restricted to really small sizes. Note that the symmetrization procedure does not preserve the \mathbf{k}_x quantum number. Specific linear combinations of the resulting states have to be formed to obtain eigenstates of the corresponding translation operator $\mathcal{T}_x^{\text{rel}}$. The overlap of the states constructed this way with the Moore-Read neutral excitation mode is of the order of 0.99 for well-defined magneto-roton states, i.e., states below the continuum of excitations that are found above a critical κ . This is the same order of magnitude as the overlaps obtained on the sphere in Refs. [142, 151].

When the number of particles N is odd, we use the following trial state

$$|\Psi_2^{\text{ex}}\rangle = \mathcal{S}_{2 \rightarrow 1}(|\Psi_1^{\text{qh}}\rangle \otimes |\Psi_1^{\text{qe}}\rangle), \quad (3.37)$$

i.e., the symmetrized product of one layer with one Laughlin quasihole state $|\Psi_1^{\text{qh}}\rangle$ and one layer with a Laughlin quasielectron state $|\Psi_1^{\text{qe}}\rangle$ (obtained using exact diagonalization). Equation (3.37) can be used to generate trial states for the Moore-Read ground state $|\Psi_2\rangle$ as well as its neutral excitations $|\Psi_2^{\text{ex}}\rangle$. Although this method does not yield any exact zero energy state of the three-body contact interaction, the approximation it provides for the Moore-Read ground state is fairly good (with an overlap of 0.998 with the Moore-Read ground state for $N = 17$). Likewise, $|\Psi_2^{\text{ex}}\rangle$ is a good approximation of the neutral excitation states (with overlaps of the order of 0.99 for states well into the neutral mode). The energies of the trial states for both

N even and odd are represented in Fig. 3.9 along with the exact energies. Hence, this method yields very satisfactory trial states for the neutral excitations above the Moore-Read state on the torus.

In the following, we will see that the alternative symmetrization with twisted boundary conditions developed in Sec. 3.1.4 also yields a good approximation of the neutral modes above the Moore-Read state.

–*Neutral excitations from the bilayer torus with twisted boundary conditions* As a trial wave function for the neutral excitation states above the Moore-Read state, we now use the following wave function

$$|\Psi_{2,x}^{\text{ex}}\rangle = \mathcal{S}_{(2T)_x \rightarrow T} |\Psi_1^{\text{ex}}\rangle. \quad (3.38)$$

This is the result of the action of the symmetrization operator on a Laughlin magneto-roton state defined on a twice enlarged torus $(2T)_x$. Similarly, applying the symmetrization operator $\mathcal{S}_{(2T)_y \rightarrow T}$ on a Laughlin magneto-roton state defined on the $(2T)_y$ torus yields another trial state for the Moore-Read neutral mode.

These states have high overlap with the exact neutral mode states (of the order of 0.99 for $N = 13$). For a given system size, the overlaps with the trial states provided by the different symmetrization constructions [see Eqs. (3.36), (3.37), and (3.38)] have very similar values. We plot the energies of $|\Psi_{2,x}^{\text{ex}}\rangle$ in Fig. 3.9 ($|\Psi_{2,y}^{\text{ex}}\rangle$ yields the same spectrum up to one percent accuracy), and compare them to the exact spectrum of the three-body Hamiltonian.

We have thus verified that the symmetrization methods provided satisfactory approximations to the neutral modes above the Moore-Read state on the torus. As expected, the symmetrization scheme previously known on the sphere is equally valid on the torus, but can also be extended to a torus with twisted boundary conditions. It is however harder to reach large system sizes with this new scheme, because it would imply calculating the Laughlin magneto-roton states for larger number of particles, a great numerical challenge. The same limitation arises when approximating the neutral mode for larger k : we expect the symmetrized Laughlin magneto-roton states on a g times enlarged torus to yield good trial states for the \mathbb{Z}_g neutral mode. However, it is numerically very difficult to compute the Laughlin neutral mode for more than $N = 13$ particles. For this number of particles, the neutral modes above the \mathbb{Z}_g states with $g > 2$ still show large finite size effects.

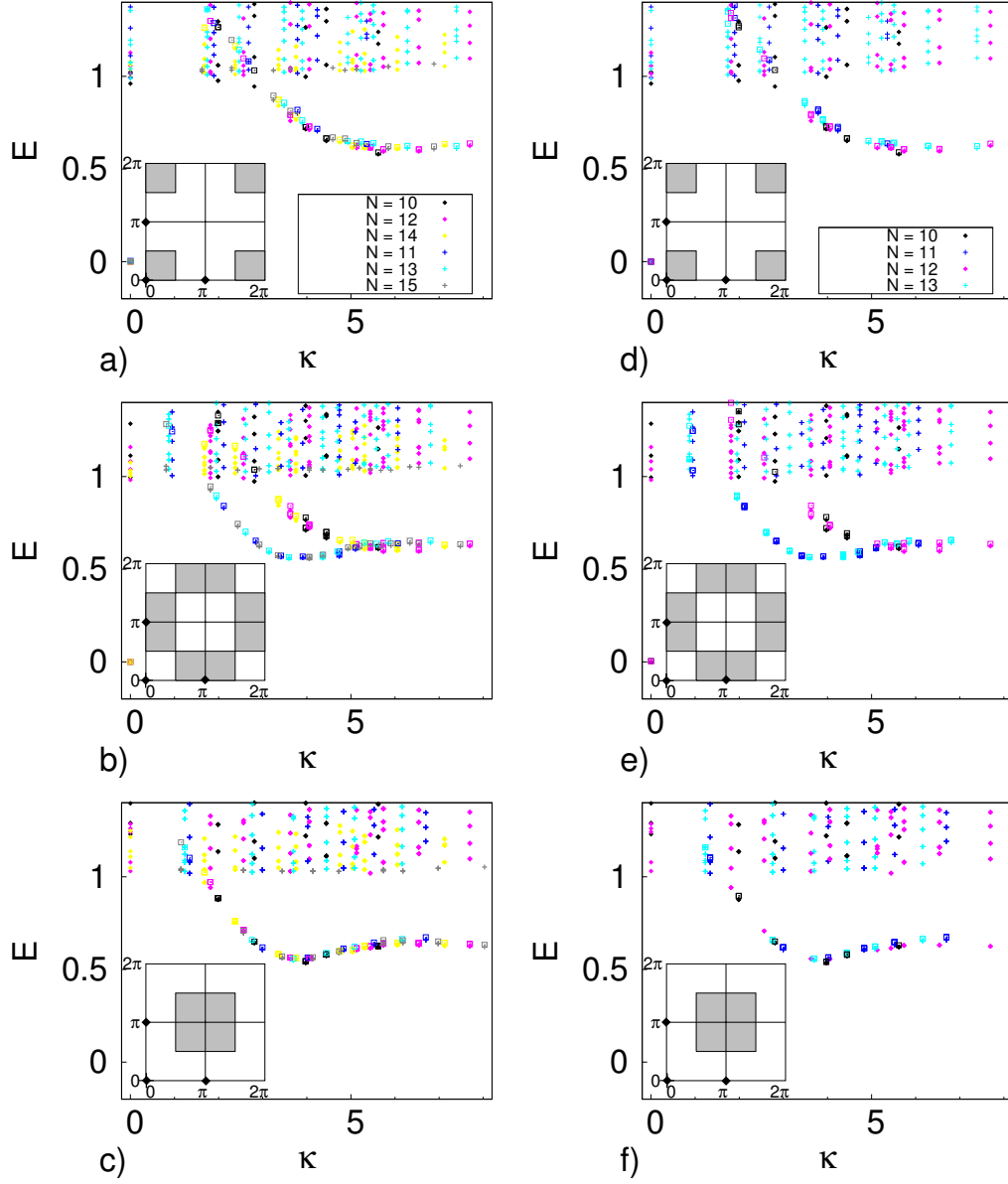


Figure 3.9: Low energy spectrum of the FQH on the torus as a function of the modulus of the momentum κ , for the model three-body contact interaction. We compare the energy of the trial states obtained by symmetrization (hollow squares) to the result of exact diagonalization (filled squares and crosses). The variational states are obtained by symmetrizing a decoupled bilayer system (a, b, c) or a single layer system defined on the $(2T)_x$ torus (d, e, f). The energies of these last states differ by less than a percent from the energies of the states obtained by the symmetrization of a system defined on the $(gT)_y$ system. We thus only show the former. See Sec. 3.1.4 for details on the construction of the trial states. In each graph, we show a different domain of the Brillouin zone, which is highlighted in gray in the inset. The black dots (respectively crosses) in the inset represent the Moore-Read ground states for N even (respectively odd). In each domain, κ is defined as the distance to the center of the domain (see also Eq. (3.35)).

Fractional Chern insulators beyond the Laughlin state

Contents

4.1	Magneto-roton mode above the Laughlin state	104
4.1.1	Identification of the neutral mode	104
4.1.2	Scaling of the gap above the Laughlin state	108
4.1.3	Writing a single mode approximation for fractional Chern insulators	109
4.1.4	Numerical benchmarking of the SMA for FCIs	111
4.2	Numerical observation of the composite fermion states in fractional Chern insulators	116
4.2.1	Microscopic model	117
4.2.2	Identifying the composite fermion states	117
4.2.3	Effect of a longer range interaction	121
4.3	Fractional Chern insulators with a Chern number $C > 1$. .	124
4.3.1	Chern insulators with $C > 1$ in the absence of interactions . .	124
4.3.2	Model $SU(C)$ fractional quantum Hall wave functions	127
4.3.3	Numerical study of some $C > 1$ fractional Chern insulators .	129

Chern insulators were introduced in Sec. 1.2 as the equivalent of the quantum Hall effect in a lattice system, in the absence of a magnetic field. As we have seen in Sec. 2.3, Chern insulators can host topologically ordered phases when the interaction between particles is strong. These phases are called fractional Chern insulators (FCIs). In particular, a phase akin to the Laughlin state has been predicted and numerically observed in several Chern insulator models. Likewise, one can wonder whether other features of the fractional quantum Hall effect are present in FCIs. In this chapter, we explore some aspects of fractional Chern insulators beyond the Laughlin state. In most cases, we will use the fractional quantum Hall effect (in its continuum version) as a basis to understand the physics of fractional Chern insulators. For example, there is a low energy mode above the Laughlin quasi-degenerate ground state in FCIs. In the first section of this chapter, we will analyze it and unveil its analogies with the magneto-roton mode above the Laughlin state in the continuum discussed in Sec. 3.2.1. Another relevant question is that of the emergence of other fractional quantum Hall model states in FCIs. Besides the Laughlin state,

the fractions explained by Jain's theory of composite fermions (as summarized in Sec. 2.1.4) are some of the most stable phases of the fractional quantum Hall effect. We numerically show the existence of these phases in Chern insulators in the second section of this chapter. Finally, Chern insulators offer the possibility of realizing a topological band with a Chern number larger than one without any additional degree of freedom, a feature that is absent in the quantum Hall effect. We study such $C > 1$ Chern insulators in the strongly interacting regime in the last section of this chapter. We numerically observe several topologically ordered phases, and draw a connection between these spinless phases and some spinful states of the fractional quantum Hall effect.

4.1 Magneto-roton mode above the Laughlin state

4.1.1 Identification of the neutral mode

As discussed in Sec. 3.2.1, there is a neutral low energy mode above any Laughlin $1/q$ state in the continuum. Without loss of generality, we can restrict our analysis to the bosonic $\nu = 1/2$ Laughlin state. As highlighted in Sec. 2.3.3, several Chern insulator lattice models can host the bosonic Laughlin state at filling $\nu^{FCI} = 1/2$, such as the kagome lattice [156], ruby lattice [71] and Haldane [60] models (see also Fig. 2.7 for a depiction of these lattice models). In this paragraph, we examine their low energy excitations, and prove that they are the lattice equivalent of the magneto-roton mode on the torus, as studied in Sec. 3.3.1.

We considered three representative models for Chern insulators: the ruby [71] and kagome [156] lattice models, and the Haldane model [60]. All three models have a lowest Bloch band characterized by a Chern number 1. The tight binding parameters that we use are defined in Ref. [98] (ruby lattice model), Ref. [136] (kagome lattice model) and Ref. [41] (Haldane model).

Since the ruby lattice model is used extensively in this study, we recall its definition. It has 5 different hopping parameters, corresponding to the real and imaginary parts of the hopping amplitude between different sites. The nearest neighbor hopping amplitude is $t = t_r + it_i$ for sites having the same parity, and $t_1 = t_{1r} + it_{1i}$ for sites having opposite parities. The hopping amplitude on the diagonal of the square is real and is noted t_4 . These various hopping terms lead to the Bloch Hamiltonian Eq. (2.56). To choose their value, we spanned the parameter space to find which value of the parameters yielded the largest many-body gap (the definition of this gap, and in particular the corresponding many-body Hamiltonian will be specified later in this section). The optimal values are different for fermionic and bosonic systems and respectively are

$$\begin{cases} t_r = 1, t_i = 1.2, t_{1r} = -1.2, t_{1i} = 2.6, t_4 = -1.2 & \text{for fermions} \\ t_r = 1, t_i = 1, t_{1r} = -1.4, t_{1i} = 2.4, t_4 = -1.46 & \text{for bosons} \end{cases} \quad (4.1)$$

While we did not study numerically the neutral mode above the fermionic Laughlin state, these optimal values will be useful in a later section of this chapter. When

using these parameters, the two lowest bands of this six band model are separated by a gap, and the lowest band has a Chern number equal to 1.

We consider N bosons on a Chern insulator lattice system with $N_x \times N_y$ unit cells and periodic boundary conditions, and use the lattice notations of Sec. 1.2.1.1. They interact via the on-site density-density interaction (2.54), which is projected onto the lowest band via the procedure described in Eq. (2.59). The filling fraction is defined with respect to the lowest band, i.e., $\nu^{FCI} = N/(N_x N_y)$, and chosen to be $\nu^{FCI} = 1/2$ for all numerical calculations in this section. It has been established that the ground state of these systems is a Laughlin-like phase (see Sec. 2.3.3). Their typical low energy spectrum (see Fig. 2.9) is a twofold almost degenerate ground state, separated by a gap from low energy excitations. In the cases of the ruby lattice models, the ground state energy splitting is barely noticeable, proving that it is less affected by finite-size effects.

A band of low energy excited states appear with a low density of states, in contrast with the high density of states in the continuum of higher energy excitations (which appears around energy $E \simeq 0.2$ in the ruby model – Fig 2.9a, and around $E \simeq 0.25$ in the Haldane model – Fig 2.9b). Depending on the model, the low energy excited states form different patterns: in the ruby model spectrum, a narrow, high density band ($E \simeq 0.1$) sits below a scattered cloud of states ($0.1 < E < 0.2$). In the case of the Haldane model, no such subtle pattern can be distinguished, and the states at energies $0.15 < E < 0.25$ all appear with a rather low density. Despite this model dependency, we want to show that the band of low energy excited states is similar to the neutral mode of the fractional quantum Hall effect, more precisely the magneto-roton mode above the Laughlin state described in Sec. 3.3.1. As pointed out in Sec. 2.3.3, the quantum numbers of the FCI and those of the fractional quantum Hall effect on the torus do not coincide. More precisely, the center of mass degeneracy provides an additional quantum number on the continuous torus, which is key to the identification of the magneto-roton mode, as we explain in the following paragraph.

We call BZ_{FCI} the lattice Brillouin zone defined in Eq. (1.49), which consists of $N_x \times N_y = N_\phi$ points. On the other hand, the reduced Brillouin zone for a filling fraction $1/2$ on the torus $\text{BZ}_{\text{FQH}}^{\text{red}, 1/2}$ was defined in Eq. (3.27) and contains N^2 points. Here, we will adopt a slightly different notation for the momentum quantum numbers that belong to $\text{BZ}_{\text{FQH}}^{\text{red}, 1/2}$, and add the superscript FQH to the usual $\mathbf{k} = (k_x, k_y)$ notation of the previous chapters. This should prevent any confusion between the lattice quantum numbers $(k_x, k_y) \in \text{BZ}_{\text{FCI}}$ (associated with the center of mass, non-projected, translation operators), and the FQH quantum numbers $\mathbf{k}^{FQH} = (k_x^{FQH}, k_y^{FQH}) \in \text{BZ}_{\text{FQH}}^{\text{red}, 1/2}$ (associated with the relative and center of mass translation operators projected onto the lowest Landau level). As explained in Sec. 3.3.1, the dispersion relation of the magneto-roton mode on the torus appears clearly when the low energy spectrum is plotted against the norm of the momentum $|\mathbf{k}^{FQH}|$, where $\mathbf{k}^{FQH} \in \text{BZ}_{\text{FQH}}^{\text{red}, 1/2}$, as can be seen in Fig. 4.1a. A mapping [25] between the N^2 FQH momenta and the N_ϕ lattice momenta was detailed in Sec. 2.3.3,

corresponding to the folding of $\text{BZ}_{\text{FQH}}^{\text{red},1/2}$ down to BZ_{FCI} . Following this procedure, we show the folded FQH magneto-roton spectrum for $N = 10$ bosons in Fig. 4.1b. In this representation, the magneto-roton mode consists of a highly degenerate low energy band (here, around $E \simeq 0.6V_0$), with a few states lying in the gap above the band. These more isolated states constitute the dispersive branch of the mode. The folding places states with a short and a long wavelength (in the FQH sense) in the same sectors. This obscures the identification of the magneto-roton mode as a single dispersing branch of states. Indeed, looking only at Fig. 4.1b, we could not identify the magneto-roton, as there is no "unfolding" procedure that would allow us to go back to Fig. 4.1a. This demonstrates the difficulties we will face to identify the dispersion relation of a potential magneto-roton mode in a FCI spectrum. Generically, FCIs do not have a center of mass translation symmetry that makes the relative momentum k_x^{FQH} a good quantum number in the FQH case. As a result, the FCI spectrum cannot be unfolded or resolved in this extra quantum number, and cannot be plotted as a function of $|\mathbf{k}^{\text{FQH}}|$ with $\mathbf{k}^{\text{FQH}} \in \text{BZ}_{\text{FQH}}^{\text{red},1/2}$.

Having noted these difficulties, we show that the low energy manifold of FCI excited states can nevertheless – to some extent – be identified to the FQH magneto-roton manifold. For a well chosen finite size FQH system, there is an energy separation between the magneto-roton and the continuum states (around $E \simeq 1$ in Fig. 4.1b), due to the quantization of momentum. In this case, the number of FQH magneto-roton states is well-defined. The same observation is valid in the FCI system of Fig. 4.1c, with an energy separation around $E \simeq 0.16$. In fact, the number of such states is the same in each momentum sector in Fig. 4.1b and Fig. 4.1c. More generically, the number of low energy excited states in all the FCI spectra that we looked at matches the number of magneto-roton states, as long as both these numbers are well defined. Indeed, such comparison relies on a clear separation between low and high energy excited states, which most often exists in the ruby and kagome lattice models, but not in the Haldane model, where the finite size effects are more important. Note that to obtain the same counting, the torus twisting angle θ has to be the same as the angle defined by the reciprocal lattice vectors of the FCI ($\theta = \pi/3$ for the kagome lattice and Haldane models, $\theta = 2\pi/3$ for the ruby lattice model). The equality between the numbers of states strongly suggests that the low energy excited states of the FCI spectra have the same nature as the magneto-roton states of the FQH. In the case of the ruby lattice model, where the finite size effects are least important, a one-to-one identification of some states is even possible in the dispersive part of the magneto-roton spectrum. This appears clearly in Fig. 4.1, in the respective energy ranges $0.11 < E < 0.16$ (FCI spectrum, Fig. 4.1c) and $0.65 < E/V_0 < 1$ (FQH spectrum (Fig. 4.1b)).

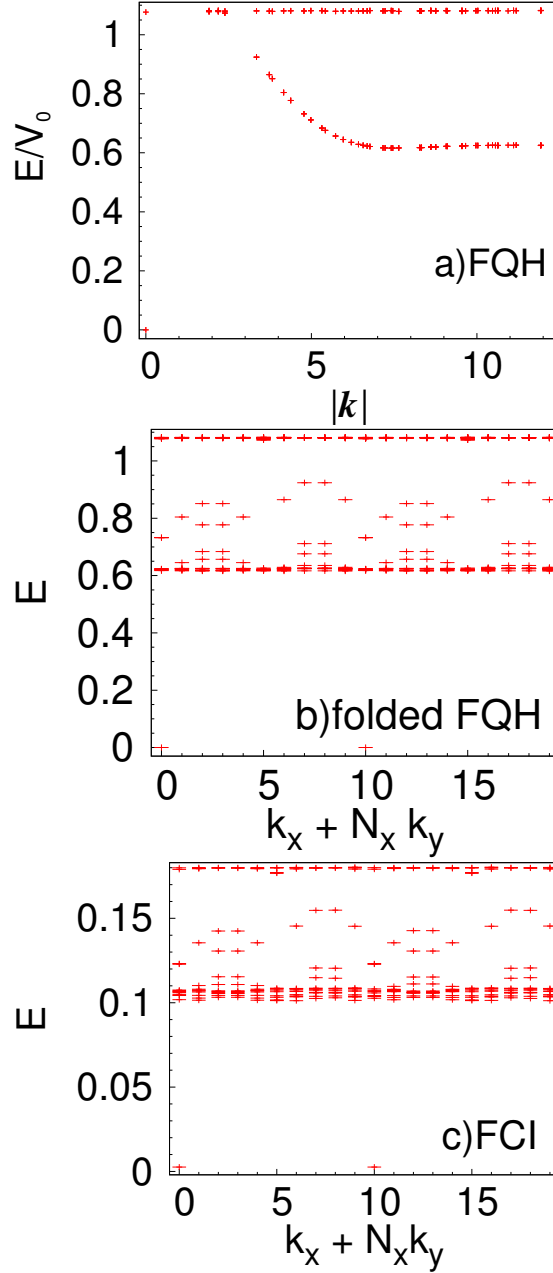


Figure 4.1: Low energy spectrum of the FQH on a torus of aspect ratio $L_x/L_y = 1.25$ with a twisting angle $\theta = 2\pi/3$, with $N = 10$, $N_\phi = 20$, as a function of (a) the modulus of the momentum and (b) the linear FCI momentum (using the FQH-to-FCI mapping). (c) Low energy spectrum of the ruby lattice model with $N = 10$ particles and $N_x \times N_y = 5 \times 4$. The FQH energies are given in units of the pseudopotential V_0 , while the FCI energies are given in units of t_r , the real part of the nearest-neighbor hopping amplitude.

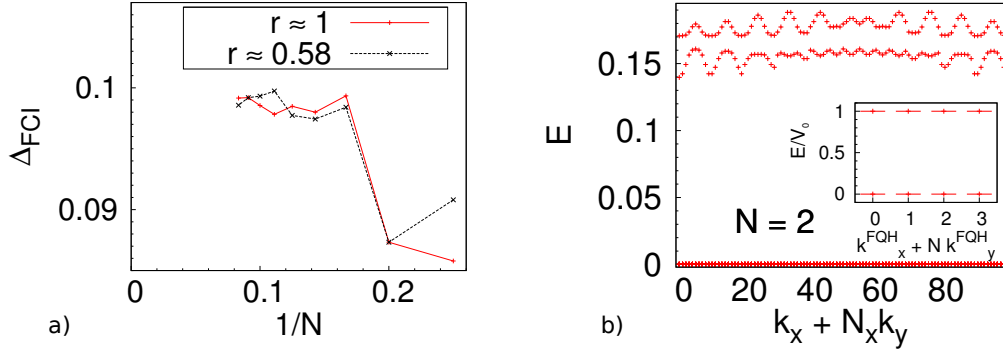


Figure 4.2: a) Gap of the ruby lattice Chern insulator model at a filling factor $\nu = 1/2$, for systems of aspect ratio as close to 1 as possible, in one case, and as close to 0.58 as possible. b) Full spectrum of two particles on a 10×10 ruby lattice Chern insulator model. The average of non-zero energies is around $E_{2\text{body}} \simeq 0.15$. The inset gives the energy spectrum of the corresponding FQH system. Once renormalized by the energy of the two-body problem, the asymptotic value of the gap falls within 2% of the value of the gap extrapolated for the FQH on the torus in Fig. 3.4b.

4.1.2 Scaling of the gap above the Laughlin state

We extract the many-body gap of the ruby lattice system (see Fig. 4.2). We want to extrapolate its thermodynamic limit value, as we did for a fractional quantum Hall system in Fig. 3.4b. The extrapolation is more difficult for a FCI system. As was initially pointed out in Ref. [131], and discussed in great details in Refs. [26] and [89], both extents N_x and N_y of the lattice should be large enough to prevent the formation of a charge density wave phase. As a consequence for a finite and generally small system size, the aspect ratio of the lattice greatly influences the value of the gap. In order to minimize this effect while studying the evolution of the gap with the system size, we follow the approach introduced in Ref. [89], and use tilted boundary conditions (see also Ref. [136] for a more detailed description). For any number of unit cells $N_s = N_x \times N_y$, this method allows us to obtain an aspect ratio close to the desired value. We look at the evolution of the gap for systems with aspect ratios r close to 1 and for systems $r \simeq 0.58$ in Fig. 4.2a. The choice of the value $r \simeq 0.58$ is rather arbitrary; it corresponds to the largest non-tilted lattice that we can numerically reach, namely with $N = 12$ particles ($N_s = 24 = 6 \times 4$). While one expects that $r \simeq 1$ should minimize the finite size effects, our system actually shows a small size dependence at either aspect ratio. It suggests that the correlation length in our system is small compared to both characteristic dimensions of the lattice, even for $r \simeq 0.58$. Note that the energy scale of the interaction in

¹We recall that in this chapter, k_x^{FQH} and k_y^{FQH} denote the FQH momentum quantum numbers, associated with the relative and center of mass translations in the lowest Landau level, and correspond to the k_x and k_y of the previous chapter.

the FCI is not as well defined as in the FQH case. The energy scale is parametrized by the gap in the spectrum of the interacting two-particle problem. The FQH two-body spectrum only has one single non-zero energy per momentum sector, which is almost \mathbf{k}^{FQH} independent (see the inset in Fig. 4.2b). The FCI system, on the other hand, has non-zero energy states with larger fluctuations (see Fig. 4.2b). This prevents us from performing an exact rescaling of the FCI spectra with respect to the two-particle energy scale. Nevertheless, taking the average two particle non-zero energy $E_{2\text{body}}$ as the energy scale leads to an extrapolated gap of 0.60(3), a value only 2% different from the FQH one.

4.1.3 Writing a single mode approximation for fractional Chern insulators

It is clear from Sec. 4.1.1 that the low energy mode above the Laughlin-like state in a fractional Chern insulator is the equivalent of the magneto-roton mode of the Laughlin state on the torus. In Sec. 3.3.1.2, we saw that this mode could be well approximated in the limit of long wavelengths by the so-called single mode approximation (SMA). Extending the SMA to FCI systems is a natural endeavor, given the similarity of the two systems. The results derived in this section are valid for a generic $\nu = 1/q$ filling factor.

According to Eq. (3.33), the SMA variational states are obtained by applying the density operator (projected onto the lowest Landau level) onto the Laughlin state. We use the notations of Sec. 1.2.1.1 for the lattice operators and states. To define a density operator (and subsequently project it to the lowest band $\mu = 0$), a geometrical choice about the embedding of the orbitals $\alpha = 1, \dots, m$ (where m is the number of atoms per unit cell) has to be made by fixing the position coordinate \mathbf{r}_α of each atom in the lattice unit cell. We define an embedding as the set $\{\mathbf{r}_\alpha\}_m$ of these coordinates. For instance, we choose the embedding of the kagome lattice model as

$$\{\mathbf{r}_\alpha\}_m = \{(0, 0), (1/2, 0), (0, 1/2)\}, \quad (4.2)$$

in units where the lattice spacing is unity (this is the same embedding as the one represented in Fig. 2.7c). In the same units, the ruby lattice model has the embedding corresponding to Fig. 2.7b:

$$\{\mathbf{r}_\alpha\}_m = \frac{1}{3 + \sqrt{3}} \left\{ \begin{array}{l} \left(\begin{array}{cc} -1 & , \quad \frac{-1+\sqrt{3}}{2} \end{array} \right), \\ \left(\begin{array}{cc} 1 & , \quad \frac{1+\sqrt{3}}{2} \end{array} \right), \\ \left(\begin{array}{cc} -1 - \sqrt{3} & , \quad \frac{-1-\sqrt{3}}{2} \end{array} \right), \\ \left(\begin{array}{cc} 1 & , \quad \frac{1-\sqrt{3}}{2} \end{array} \right), \\ \left(\begin{array}{cc} -1 & , \quad \frac{-1-\sqrt{3}}{2} \end{array} \right), \\ \left(\begin{array}{cc} 1 + \sqrt{3} & , \quad \frac{1+\sqrt{3}}{2} \end{array} \right) \end{array} \right\}. \quad (4.3)$$

The choice of embedding is an extra piece of information that is not contained in the Hamiltonian and determines whether or not the density operator shares certain spatial discrete symmetries with the Hamiltonian. For example, the choice Eq. (4.2) preserves the inversion symmetry of the kagome lattice Hamiltonian. The density operator $\tilde{\rho}_{\mathbf{k}}$, and its corresponding projection $\rho_{\mathbf{k}}$ in the band $\mu = 0$ are given by

$$\tilde{\rho}_{\mathbf{k}} = \sum_{\mathbf{r} \in \Lambda} \sum_{\alpha} e^{i\mathbf{k} \cdot (\mathbf{r} + \mathbf{r}_{\alpha})} c_{\mathbf{r}\alpha}^{\dagger} c_{\mathbf{r}\alpha}, \quad (4.4a)$$

$$\rho_{\mathbf{k}} = \sum_{\mathbf{q} \in \text{BZ}_{\text{FCI}}} \left[\sum_{\alpha} e^{i\mathbf{k} \cdot \mathbf{r}_{\alpha}} u_{\mathbf{q}+\mathbf{k},\alpha}^{0*} u_{\mathbf{q},\alpha}^0 \right] |0, \mathbf{k} + \mathbf{q}\rangle \langle 0, \mathbf{q}| \quad (4.4b)$$

When $\mathbf{q} = \frac{2\pi}{N_i} \tilde{\mathbf{e}}_i$ ($i = x, y$), the bracketed factor in Eq. (4.4b) can be identified to the Berry potential $\mathbf{A}_{\mathbf{B}}(\mathbf{k}) \cdot \tilde{\mathbf{e}}_i$. Hence, $\mathbf{A}_{\mathbf{B}}(\mathbf{k})$ also depends on the embedding, a piece of information not contained in the effective Hamiltonian. Still, as was discussed in Ref. [175], the embedding has to be properly chosen to obtain a large overlap of the model wave functions with exact diagonalization states. For any specific model, we will use the same embedding that maximizes the overlap with the model state. More precisely, we will use the embedding defined in Eq. (4.3) for the ruby lattice model, and the embedding of Eq. (4.2) for the kagome lattice model. These choices allow the density operator to preserve the inversion symmetry, which is a symmetry of the Hamiltonian.

Note that $\rho_{\mathbf{k}}$ does not go back to itself when \mathbf{k} is shifted by a reciprocal lattice vector

$$\mathbf{G} = 2\pi (\mathbf{G}_x/a_x, \mathbf{G}_y/a_y), \quad (\mathbf{G}_x, \mathbf{G}_y) \in \mathbb{Z}^2 \quad (4.5)$$

if the embedding displacements \mathbf{r}_{α} are not integer in units of the lattice spacing. Thus, \mathbf{k} in Eq. (4.4b) is not limited to BZ_{FCI} . In the case of the kagome lattice with the embedding (4.2),

$$\begin{aligned} \rho_{\mathbf{k}+\mathbf{G}} &= \rho_{\mathbf{k}+\mathbf{G}'} \\ \text{if } &\begin{cases} \mathbf{G}_x - \mathbf{G}'_x \bmod 2 = 0 \\ \mathbf{G}_y - \mathbf{G}'_y \bmod 2 = 0 \end{cases} \end{aligned} \quad (4.6)$$

yielding $4N_s$ independent density operators. The maximal number of linearly independent density operators (i.e. the number of values of \mathbf{k} that give linearly independent density operators) is limited by the number of bilinear operators $|0, \mathbf{k} + \mathbf{q}\rangle \langle 0, \mathbf{q}|$. Since both \mathbf{k} and \mathbf{q} can take as many different values as there are unit cells in the system (N_s), there are N_s^2 such bilinear operators. The embedding of the ruby lattice (as defined in Eq. (4.3)) is not commensurate with the lattice spacing, yielding the maximal number of independent density operators N_s^2 . The number of linearly independent density operators thus depends on the model's particular embedding, and there is an arbitrariness in using a specific embedding to obtain $\rho_{\mathbf{k}}$. Unless otherwise specified, we will work with incommensurate embeddings in the rest of this section.

As with the case of the FQH effect, a SMA trial state is obtained by acting on a ground state α with the density operator $\rho_{\mathbf{k}}$

$$|\Psi_{\mathbf{k},\alpha}^{\text{SMA}}\rangle = \rho_{\mathbf{k}} |\Psi_{\alpha}\rangle. \quad (4.7)$$

Combining all N_s^2 possible values $\rho_{\mathbf{k}}$, and all q possible ground states yields a total of qN_s^2 trial states. As already specified at the end of Sec. 4.1.1, the total number of states in the FCI magneto-roton is equal to the total number of FQH magneto-roton states. In the FQH language, this number was $NN_{\phi} = N_{\phi}^2/q$, which becomes N_s^2/q in the FCI language. Again, we have q^2 more variational SMA states than needed to describe the magneto-roton mode. However, in contrast to the FQH effect, more than one magneto-roton state can reside in a sector of given $\mathbf{k} \in \text{BZ}_{\text{FCI}}$. Because of this additional degree of freedom, we need an additional index i to specify, for a given sector $\mathbf{k} \in \text{BZ}_{\text{FCI}}$, which state we aim to reproduce. To obtain a given state i in the momentum sector \mathbf{k} , we propose to act on the ground state α_i with the density operator $\rho_{\mathbf{k}+\mathbf{G}_i}$

$$|\Psi_{\mathbf{k},i}^{\text{mag-SMA}}\rangle = |\Psi_{\mathbf{k}+\mathbf{G}_i,\alpha_i}^{\text{SMA}}\rangle = \rho_{\mathbf{k}+\mathbf{G}_i} |\Psi_{\alpha_i}\rangle. \quad (4.8a)$$

where the reciprocal lattice vector \mathbf{G}_i and the momentum sector \mathbf{K}_{α_i} of the ground state α_i must satisfy the constraint

$$|\mathbf{k} + \mathbf{G}_i - \mathbf{K}_{\alpha_i}| < K_{\text{max}}, \quad (4.8b)$$

Here, K_{max} is a cutoff that is not fixed a priori, but sets a scale that *a priori* does not depend on the system size. We give a schematic representation of this constraint for the ruby system with $N = 10$ bosons in Fig. 4.3. Since K_{max} does not seem to depend on the system size, the area defined in Eq. (4.8b) is fixed, and contains a number of points that scales linearly with N_s . The number of pairs (α_i, \mathbf{G}_i) that satisfy Eq. (4.8b) thus grows more slowly than the number of states in the magneto-roton mode (which scales like $N \times N_s$). In spite of this, it will become clear in the next section that the number of states *accurately* described by the SMA is the same in the FQH and the FCI systems.

Finally, we note the similarity between Eq. (4.8) and its FQH counterpart Eq. (3.33). The main difference is that the SMA to the magneto-roton mode for the FCI contains more free parameters, such as the embedding and the cutoff K_{max} . This is the result of the lower translational symmetry and the higher degree of model dependence. We shall see in the next paragraph that the SMA for the FCI magneto-roton mode does not stand behind the FQH SMA, even quantitatively.

4.1.4 Numerical benchmarking of the SMA for FCIs

We now want to numerically test the accuracy of the SMA as an approximation to the FCI magneto-roton mode, and in particular the validity of the criterion Eq. (4.8). While this benchmarking is in principle similar to that performed for the SMA on the torus in Sec. 3.3.1.2, it is in practice more complicated, as we will see below.

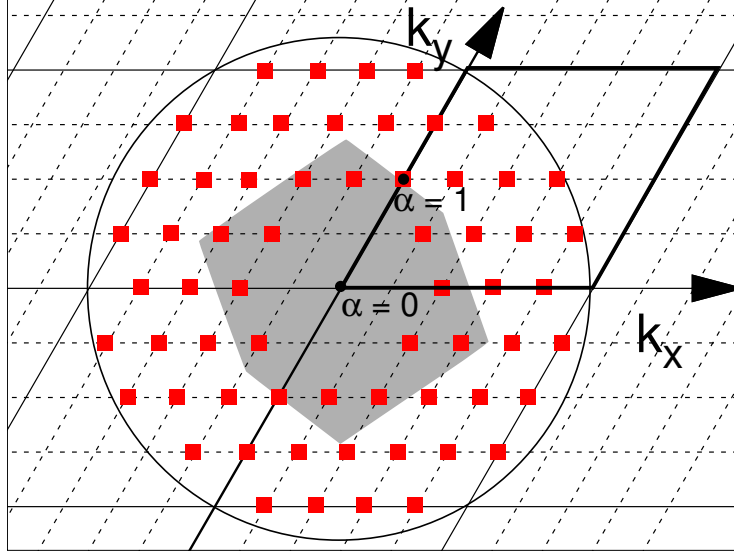


Figure 4.3: Schematic representation of the SMA construction rule Eq. (4.8b) for the ruby FCI model with $N = 10$ particles around the first ground state $\alpha = 0$. The dashed lines represent the reciprocal lattice, while the solid lines represent the limits of each Brillouin zone (\mathbf{G} takes a different value in each of these zones). The bold lines mark the limits of the first Brillouin zone BZ_{FCI} ($\mathbf{G} = 0$), while the grey area corresponds to the first Brillouin zone when constructed as the Wigner-Seitz cell of the reciprocal lattice. The center of mass momentum of each of the two ground states is indicated by a black dot. We draw a red square for each SMA state satisfying $|\mathbf{k} + \mathbf{G} - \mathbf{K}_0| < K_{\text{max}}$, with the position of \mathbf{K}_{max} represented by a circle. Note that the density operator at zero momentum is equal to the identity, such that there is no SMA state in the sector of the ground state. In the immediate vicinity of the ground state (six points here), there are SMA trial states, but their overlap with the exact states are low since the magneto-roton mode merges with the continuum at these momenta. Note that both these features are common to the FCI and FQH SMA.

In evaluating the accuracy of the SMA to the magneto-roton mode of the FQH states, we were able to take advantage of the fact that states for which the SMA is a good or a poor approximation are naturally separated into small and large momenta \mathbf{k}^{FQH} in the Brillouin zone, respectively. The story is not as simple for FCIs. As illustrated in Fig. 4.1, the spectrum of the FCI magneto-roton mode on the ruby lattice model can be very well reproduced by folding the spectrum of the FQH magneto-roton mode on the torus down to the Brillouin zone of the FCI. Unfortunately, the separation of small and large momenta is lost under this folding, because both small and large $\mathbf{k}^{FQH} \in \text{BZ}_{\text{FQH}}^{\text{red}, 1/2}$ may fall on the same $\mathbf{k} \in \text{BZ}_{\text{FCI}}$. In other words, even if the SMA as an approximation to the magneto-roton mode in the FCI performs as good as in the FQH case, it is in general not possible to establish a correspondence between the (folded) magneto-roton and the SMA states.

As was already stressed in this section, it is impossible to “unfold” the eigenstates of the FCI to an enlarged Brillouin zone in any meaningful way, because of the lower translational symmetry of the FCI. It is thus impossible to reconstruct a non-degenerate magneto-roton dispersion (with one eigenstate per momentum quantum number) for the magneto-roton mode from the *exact eigenstates* of the FCI. In contrast, we should remember that the *SMA states* of the FCI, as determined by the selection criterion (4.8), carry the reciprocal lattice vector \mathbf{G} as an additional momentum quantum number. This additional information allows to unfold the SMA spectrum. Indeed, \mathbf{G} corresponds to the information that is lost in the modulo operation of Eq. (2.61), during the folding. Using the retrieved \mathbf{G} , we can write the unfolded quantum numbers

$$\begin{aligned} k_x^{FQH} &= k_x + G_x N_x \\ k_y^{FQH} &= k_y + G_y N_y \end{aligned} \quad (4.9)$$

We can thus access the unfolded SMA relation dispersion by representing the SMA energy as a function of the norm of the vector $\mathbf{k} + \mathbf{G}$ (see Fig. 4.4). The exact eigenstates do not carry a vector \mathbf{G} , so that no such procedure could be applied to them. Note that the word “quantum number” should be used with caution when referring to \mathbf{G} , since it does not correspond to an exact symmetry of the problem. Strictly speaking, \mathbf{G} is not a quantum number, but merely a labeling of the states.

We now turn to the interpretation of the cutoff K_{max} introduced in Eq. (4.8b). In general, the projected density operator $\rho_{\mathbf{k}}$ is not periodic under $\mathbf{k} \rightarrow \mathbf{k} + \mathbf{G}$, with \mathbf{G} a reciprocal lattice vector. However, two SMA states generated with density operators at \mathbf{k} and at $\mathbf{k} + \mathbf{G}$ are not orthogonal and can in fact have a large overlap. For the ruby lattice model, and for all system sizes that we have looked at, we find that the SMA states $|\Psi_{\mathbf{G}, \alpha}^{\text{SMA}}\rangle$ such that

$$\text{or } \begin{cases} G_x \neq 0 \\ G_y \neq 0 \end{cases} \quad (4.10)$$

have a large overlap with the α ground state ($\langle \Psi_{\alpha} | \Psi_{\mathbf{G}, \alpha}^{\text{SMA}} \rangle > 0.5$). The vector \mathbf{G}^0

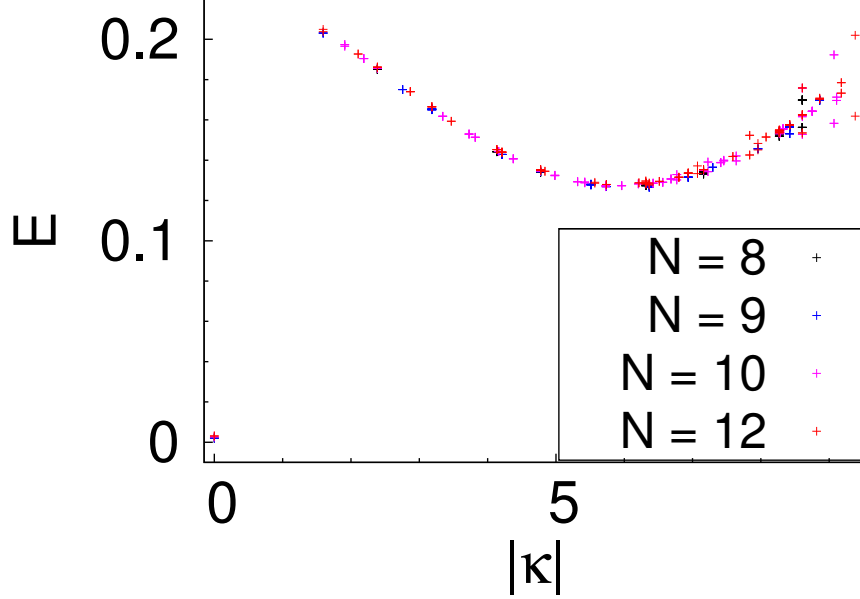


Figure 4.4: Magneto-roton mode of the FCI system with up to $N = 12$ bosons, at half filling, obtained using the SMA as defined in Eq. (4.8). We only show the states that obey the inequality defined in Eq. 4.8b.

defined by

$$\mathbf{G}^0 = (2\pi, 0) \quad (4.11)$$

(or equivalently $\mathbf{G}^0 = (0, 2\pi)$) thus naturally sets the value of the cut-off parameter K_{\max} to

$$K_{\max} = |\mathbf{G}^0 - \mathbf{K}_{\alpha}| \quad (4.12)$$

as represented in Fig. 4.3 for $\mathbf{K}_{\alpha_i} = 0$. Taking into account the scaling parameter introduced in Eq. (3.28) due to the angle $\theta = 2\pi/3$ of the reciprocal lattice vectors of the ruby model, this leads to

$$K_{\max} = \frac{4\pi}{3^{1/4}} \quad (4.13)$$

$$\simeq 9.5 \quad (4.14)$$

We represented the SMA dispersion relation in Fig. 4.4 accordingly, leaving out the points falling outside of the circle of center \mathbf{K}_{α_i} and radius K_{\max} . Note that within this circle, SMA states with the same $\mathbf{k} - \mathbf{K}_{\alpha_i}$, but different \mathbf{G} s have very small overlaps ($\langle \Psi_{\mathbf{k}+\mathbf{G},\alpha_i}^{\text{SMA}} | \Psi_{\mathbf{k}+\mathbf{G}',\alpha_i}^{\text{SMA}} \rangle < 0.1$).

Having specified this set of rules, we are now equipped to evaluate the numerical accuracy of the SMA to the FCI magneto-roton mode. We call $|\kappa|$ the norm of the

momentum vector $\mathbf{k} + \mathbf{G} - \mathbf{K}_\alpha$

$$|\boldsymbol{\kappa}| = |\mathbf{k} + \mathbf{G} - \mathbf{K}_\alpha| \quad (4.15)$$

When the variational energy of the FCI SMA states selected by criterion (4.8) are plotted as a function of $|\boldsymbol{\kappa}|$, one obtains an excellent agreement with the SMA dispersion of the FQH [see Fig. 4.5 (a)]. Remarkably, the minimum of the FCI and FQH magneto-roton modes fall exactly at the same value of $|\boldsymbol{\kappa}|$. Similarly to the FQH case, only the SMA states with $|\boldsymbol{\kappa}| < 2\pi$ accurately approximate an exact eigenstate that belongs to the magneto-roton mode. Interestingly, almost no finite size effect is visible, even though FCIs are in general more susceptible to finite size effects than FQH systems. As pointed out in the previous section, imposing a cutoff K_{\max} leads to generating less SMA modes than there are magneto-roton states. Fortunately, this does not reduce the number of magneto-roton states that are *accurately* described by the SMA, as the cutoff lies at a larger value of $|\boldsymbol{\kappa}|$ than the minimum of the mode. We extract the energy minimum of the SMA mode, and compare it to the value obtained in Sec. 4.1.1. This variational value overestimates the value of the gap by about 20%, similar to the FQH SMA. We note that the overlap values are not significantly smaller in the FCI case than their FQH counterparts. On average, the FCI overlaps are 5% smaller than the FQH overlaps.

To address the question of the validity of the selection rule Eq. (4.8), we can consider the larger variational subspace obtained by applying any bilinear operator onto each ground state, as was performed in Sec. 3.3.1.2 in the FQH case. However, diagonalizing the Hamiltonian in the full bilinear subspace is not conceivable in the FCI case. Indeed, this method mixes large and small $|\mathbf{k} + \mathbf{G}|$ in the same momentum sectors. This leaves us with a spectrum that cannot be unfolded, and the variational states that give an acceptable approximation of the magneto-roton mode cannot be identified. However, one can compute the overlap of each exact magneto-roton eigenstate with the full bilinear subspace. Similarly to the FQH case, this overlap is only a few percents higher than that of the SMA states with the exact eigenstates, validating the SMA approach.

Finally, we would like to highlight a crucial difference between the cases of the FQH effect and the FCI: the density operator used to construct the SMA is uniquely defined for the former, while it contains the freedom to choose an embedding for the latter. The choice of embedding will in general influence the quality of the SMA. Particularly pathological is the case in which the orbital displacement vectors \mathbf{r}_a is 0. Then, the projected density operators share the periodicity of the reciprocal lattice in momentum space and will not suffice to build enough variational states for the SMA. To our knowledge, no model for which such an embedding is natural hosts a robust Laughlin-like phase. The kagome lattice model has half integer \mathbf{r}_a in units of the lattice constant, and thus presents some commensurability effect. However, even in this case, all SMA states within a circle of radius $K_{\max} = |\mathbf{G}^0 - \mathbf{K}_\alpha|$ are linearly independent. Unfortunately, its magneto-roton mode is not as well defined as that of the ruby lattice system. Unsurprisingly, the eigenstates have a smaller overlap with the bilinear subspace (0.8 at best), and there is a lot of mixing between

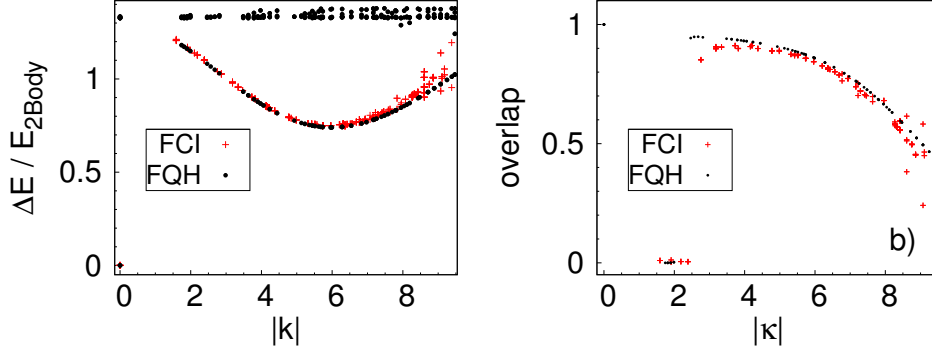


Figure 4.5: a) Magneto-roton mode of the FQH and ruby lattice FCI systems at half filling, with respectively up to $N = 13$ (FQH) and $N = 12$ (FCI) particles, as computed using the SMA, for $|\kappa| < K_{\max}$. For FCI systems, $|\kappa|$ was defined in Eq. (4.15). For FQH systems, it is just the norm of the vector \mathbf{k}^{FQH} . The FCI energies have been shifted by the ground state energy, and renormalized by the energy of the two-body problem $E_{2\text{body}}$ (as defined in Fig. 4.2b). b) Overlap of the SMA states of the FQH and FCI systems with the eigenstates obtained by exact diagonalization plotted as a function of $|\kappa|$. In the FCI case, there may not be a one to one correspondence between the SMA states and the exact eigenstates. We therefore give the overlap with the whole FCI magneto-roton subspace, while the FQH overlaps are with individual states.

the states originating from different ground states. The variational SMA states, in turn, have a maximum overlap of 0.53 with the exact eigenstates. Our efforts to tune the embedding away from the value given in Eq. (4.2) did not improve these overlaps significantly. Note that tuning the embedding for the ruby model would barely improve the overlaps in this case either. Indeed, they are already close to the maximal values that can be reached using all the bilinears originating from the same ground state.

4.2 Numerical observation of the composite fermion states in fractional Chern insulators

The Laughlin $1/3$ state and its bosonic $1/2$ counterpart are the most stable of all fractional quantum Hall states: it is thus not surprising that these were the first fractional Chern insulators to be numerically observed [110, 146, 131]. Subsequently, the Moore-Read and Read-Rezayi states were observed using many-body interactions [25, 166, 172]. As we saw in Sec. 2.1.4, the composite fermion construction explains the existence of a series of fractional quantum Hall states at filling fraction $\nu^{FCI} = p/(2p + 1)$ for fermions (and $\nu = p/(p + 1)$ for bosons). We investigated numerically the existence of a series incompressible phases at filling $2/5$ and $3/7$ for

fermions ($2/3$ and $3/4$ for bosons). Using an array of numerical evidence based on exact diagonalization and entanglement spectroscopy, we proved that these phases appeared with a high degree of stability on the ruby lattice model.

4.2.1 Microscopic model

We use the Chern insulator ruby lattice model, as depicted in Fig. 2.7b, and described in Sec. 2.3.2. We use the tight-binding parameters defined in Eq. (4.1), which yield a gapped lowest band with a Chern number equal to 1.

The fermions interact via a density-density nearest neighbor interaction H_{int}^f , which was written in Eq. (2.55). The bosons interact via an on-site density-density interaction H_{int}^b (see Eq. (2.54)). To get rid of the effect of band mixing, we project the interaction onto the lowest band. Further, we avoid the effect of dispersion by working in the flat-band limit, which was detailed in Sec. 1.2.1.2. This leads to the following projected, flat-band Hamiltonians (similar to Eq. (2.59)), for fermions and bosons, respectively

$$H^f = \sum_{\mathbf{k}, \mathbf{k}' \in BZ} |0, \mathbf{k}\rangle \langle 0, \mathbf{k}| H_{int}^f |0, \mathbf{k}'\rangle \langle 0, \mathbf{k}'| \quad (4.16a)$$

$$H^b = \sum_{\mathbf{k}, \mathbf{k}' \in BZ} |0, \mathbf{k}\rangle \langle 0, \mathbf{k}| H_{int}^b |0, \mathbf{k}'\rangle \langle 0, \mathbf{k}'| \quad (4.16b)$$

where $|0, \mathbf{k}\rangle$ are the Bloch states of the lowest band, and were defined in Sec. (1.2.1.1).

For comparison, we will also need the spectrum (and eigenstates) of the corresponding fractional quantum Hall states on the torus. They are obtained by diagonalizing an interaction Hamiltonian (the pseudopotential Hamiltonian \hat{V}_0 for bosons, \hat{V}_1 for fermions – see Eqs. (2.12) and (2.13) – or the Coulomb interaction) projected onto the lowest Landau level.

4.2.2 Identifying the composite fermion states

4.2.2.1 Characterizing the ground state from its degeneracy

In Ref. [98], we performed the exact diagonalization of the Hamiltonian (4.16) at filling fraction $\nu^{FCI} = 2/5$ and $3/7$ for fermions ($2/3$ and $3/4$ for bosons). We look for the signatures of an incompressible state in the energy spectrum, i.e. a low energy manifold separated by a large gap from the low energy excitations. On the torus, the composite fermion fractional quantum Hall states at filling fraction $\nu = p/(np + 1)$ ($n = 2$ for fermions, $n = 1$ for bosons) have an exact degeneracy $np + 1$, which is due to the center of mass degeneracy (see Sec. 2.2.3.1). In a finite size fractional Chern insulator, we thus expect to find a quasi-degenerate gapped ground state, with a quasi-degeneracy equal to $np + 1$. We show the low energy spectrum of the Hamiltonian (4.16) resulting from our exact diagonalization study in Fig. 4.6. We observe the expected 5-fold (Fig. 4.6a), 7-fold (Fig. 4.6b), 3-fold (Fig. 4.6c)

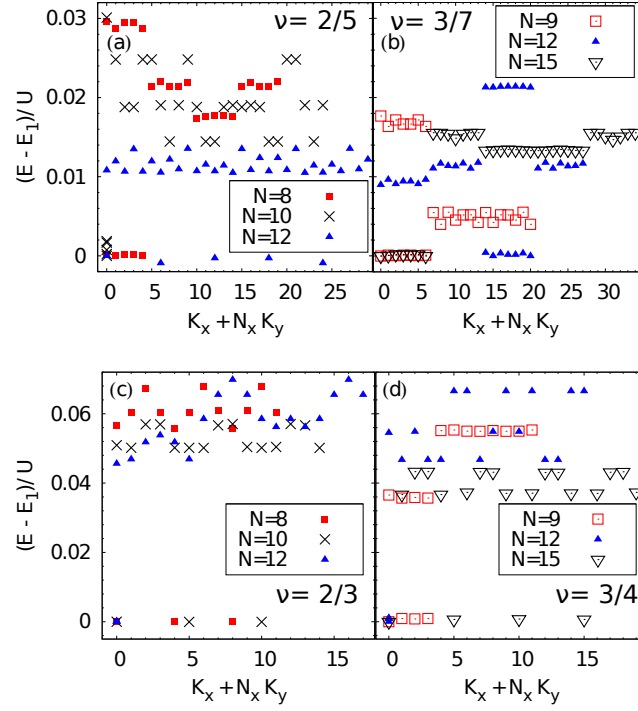


Figure 4.6: Low energy spectra on the ruby lattice for (from left to right, top to bottom) : $N = 8, 10, 12$ fermions at $\nu = \frac{2}{5}$ and $N_x = 5, 5, 6$ (a), $N = 9, 12, 15$ fermions at $\nu = \frac{3}{7}$ and $N_x = 7$ (b), $N = 8, 10, 12$ bosons at $\nu = \frac{2}{3}$ and $N_x = 4, 5, 6$ (c) and $N = 9, 12, 15$ bosons at $\nu = \frac{3}{4}$ and $N_x = 4, 4, 5$ (d). The energies are shifted by E_1 , the lowest energy for each system size. We only show the lowest energy per momentum sectors in addition to the degenerate groundstate (except for $N = 15$ where we only show one energy state per momentum sector). For $N = 12$ in Figs. (c) and (d), all groundstates occur in the momentum sector $K_x = K_y = 0$ and are almost perfectly degenerate.

and 4-fold (Fig. 4.6d) almost degenerate ground states. Note that the momentum sectors of the quasi-degenerate ground states match with the sectors that can be predicted using the FQH-to-FCI mapping described in Sec. 2.3.3. These features of the low energy spectrum (quasi-degeneracy, presence of the gap) are consistent for all the system sizes for which they could be computed. Attempting to extrapolate the many-body gap in the thermodynamic limit seems complicated here. Indeed, the gap is very sensitive to the aspect ratio of the system (a property we already discussed in Sec. 4.1.1), which varies by a great amount in the systems that were studied here. This is mainly due to the fact that, in Ref. [98], the aspect ratio was set to N_x/N_y , where N_x and N_y are the numbers of unit cells in the x and y direction, due to the choice of boundary conditions. As was later mentioned in Ref. [89] (and explained in detail in Ref. [136]), the use of tilted boundary conditions can relax this constraint and allow more freedom in fixing the choice of the aspect

ratio. Unfortunately, this method was only developed after this work was already made, and thus has not been used to extrapolate the gap at the time, but only later to extract the thermodynamic value of the gap above the Laughlin state on the ruby lattice (see Fig. 4.2).

4.2.2.2 Characterization of the charged excitations from energetics

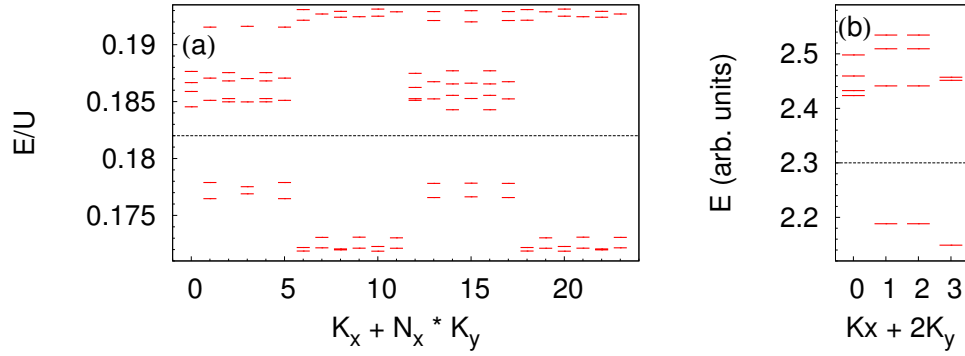


Figure 4.7: Low energy spectra for $N = 10$ fermions on a $(N_x, N_y) = (6, 4)$ ruby lattice (a) and its FQH counterpart for fermions on a torus with the Coulomb interaction and $N_\Phi = 24$ flux quanta in the reduced Brillouin zone (b). Both systems are one flux (or one site) less than the $\nu = \frac{2}{5}$ groundstate and thus embed two quasielectrons. For the FQH plot, we only display the sectors that are not related by the 12-fold center of mass translation symmetry. The number of states per momentum sector below the gap (depicted by the dashed line) in the FCI spectrum can be deduced from the FQH spectrum using the FQH-FCI mapping. The momentum quantum numbers labeling the FQH spectrum are the relative momentum along the x direction and center of mass momentum along the y direction, as defined in Sec. 2.2.3.1.

We now turn to the characterization of the charged excitations of the ground state. As was discussed in Sec. 2.2.4, the number of states for a given number of quasiparticle or quasiholes is a signature of topological order: a given topological order is associated with a specific number of quasihole and quasiparticle states. Nucleating quasiparticle or quasihole excitations can thus help us to identify the topological order of the ground state. Even in the continuum, there is no exclusion principle to predict the number of quasiparticle or quasihole excitations of a composite fermion state. We thus rely on the direct comparison of the number of states on the continuum (fractional quantum Hall) and lattice (fractional Chern insulator) sides to determine the topological nature of the FCI phase.

Quasiholes can be nucleated in a fractional Chern insulator system by removing particles from the system, or by enlarging the system (i.e. by adding unit cells

to the original system). Likewise, quasiparticles are nucleated by increasing the number of particles or by removing unit cells. For example, one can generate two quasielectrons at filling $\nu = 2/5$ with $N = 10$ fermions by looking at the system on a 6×4 ruby lattice (i.e. one unit cell less than the groundstate). Fig. 4.7a shows the corresponding low energy spectrum which possesses a clear gap. We compare it to the energy spectrum of the identical FQH system (see Fig. 4.7b): the FQH-FCI mapping perfectly relates the two countings below the gap. We have observed similar results for both bosons and fermions, for both quasielectrons and quasiholes. While the observation of these features is required, it is not a definitive proof of the topological nature of these states. As discussed in Ref.[26], a charge density wave (CDW) state could have a similar counting structure.

4.2.2.3 Entanglement spectroscopy

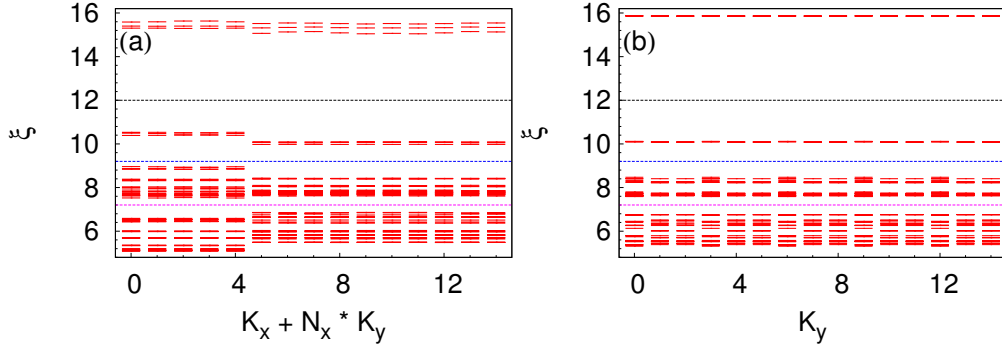


Figure 4.8: PES of bosonic FCI on the ruby lattice (a) and FQH system with delta interaction (b) at $\nu = \frac{2}{3}$, $N = 10$ and $N_A = 3$. We observe several gaps in both spectra (each depicted by a line). The counting below each of these gaps obeys the FQH-to-FCI mapping. The counting below the largest (and topmost) gap corresponds to the number of Moore-Read quasihole states. The number of states below the middle gap is related to the Gaffnian [148] state.

To remove the ambiguity between a possible CDW state and a fractional Chern insulator, we can use the entanglement spectroscopy methods detailed in Sec. 2.4. More specifically, we use the particle entanglement spectrum (PES) of Sec. 2.4.2, which allows us to probe the quasihole excitations using only the almost degenerate ground state. The density matrix is written as a sum of the projectors onto the quasi-degenerate ground state (see Eq. (2.69)). We obtain the reduced density matrix ρ_A by tracing over $N_B = N - N_A$ particles of the system (see Eq. (2.68)). We note $e^{-\xi}$ the eigenvalues of the reduced density matrix ρ_A .

Since there is no formula to count the number of quasihole excitations of composite fermions states, we directly compare the PES of the FCI to that of the FQH state. Even in the continuum, the composite fermion states have a finite entanglement gap – unlike the Laughlin state, and other states that are the exact ground states of

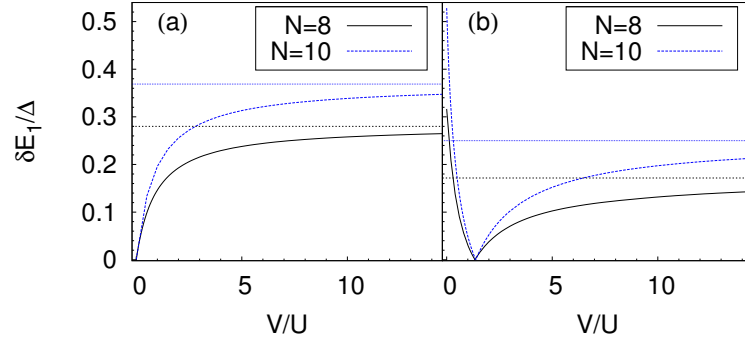


Figure 4.9: Evolution of $\frac{\delta E_1}{\Delta}$ with increasing two-body nearest neighbor repulsion V in the bosonic ruby lattice system for $N = 8$ and $N = 10$ at filling factor $\nu = 2/3$ on a $N_x = N/4, N_y = 4$ lattice. (a) We use the band parameters defined in Eq. (4.1) that produce the lowest ratio $\frac{\delta E_1}{\Delta}$ when only the on-site interaction is applied. (b) We have set the band parameters to the values described in Ref. [71] that lead to the flattest lowest band in the ruby lattice model. For both Figs a and b, the horizontal line is guide for the eyes that gives the asymptotic value when $U = 0$.

a local model Hamiltonian, such as the Moore-Read and Read-Rezayi states. For composite fermion states, it is not even guaranteed that the entanglement gap stays open. The lower part of the spectrum (below the gap) is the relevant part of the PES, since it corresponds to the highest weights in the reduced density matrix. We can expect the PES of the FCI composite fermion states to have, at best, the same (if not smaller) entanglement gap as the FQH composite fermion state. For example, the PES of the $\nu = 2/3$ bosonic system with $N = 10$ and a particle partition with $N_A = 3$ displays a clear entanglement gap (depicted by the black line in Fig. 4.8), with smaller gaps below the gap (depicted by a red and a blue line). This structure appears clearly for both the FQH and FCI PES. One can use the FQH-to-FCI mapping of quantum numbers to see that the number of states below these gaps are consistent, for all different gaps. Note that the number of states below these smaller gaps are respectively given by a (2,2) (blue line) and a (2,3) (red line) exclusion principle.

4.2.3 Effect of a longer range interaction

We also studied the stability of the bosonic CF state, focusing on the $\nu = \frac{2}{3}$ case, with an additional nearest-neighbor repulsion of amplitude $V > 0$. The total interaction is projected onto the lowest band, and we work in the flat-band limit, such that the total Hamiltonian is still given by Eq. (4.16b), where

$$H_{int}^b = U \sum_i : \rho_i \rho_i : + V \sum_{\langle i,j \rangle} : \rho_i \rho_j : \quad (4.17)$$

The bosonic CF state at $\nu^{FCI} = \frac{2}{3}$ is characterized by a nearly 3-fold degenerate groundstate separated from the rest of the spectrum by a many-body gap Δ , which

can either be direct or indirect. Upon introduction of a nearest-neighbor repulsion, the gap Δ decreases, and the groundstate degeneracy is lifted even more, with an energy spread δE_1 defined as the difference between the largest and the smallest energy in the ground state manifold. We have looked at the ratio $\frac{\delta E_1}{\Delta}$ when increasing the nearest neighbor interaction scale V . As shown in Fig. 4.9a, increasing V yields to a progressive destruction of the CF state. While we can still distinguish between the threefold degenerate groundstate and the first excited state at large V , the asymptotic value of $\frac{\delta E_1}{\Delta}$ seems to become larger with the number of particles. As a result, CF-like states are not stable against longer range interaction of a large amplitude. This is in agreement with a similar observation at the filling factor $\nu = 1/3$ [146, 172]. This result is not really surprising. Even in the FQH regime, the addition of longer range interaction to the Laughlin model interaction (using the Haldane's pseudopotentials of Sec. 2.1.2) will destroy the Laughlin phase. The instability that we observe in Fig. 4.9 has the same origin than the one in FQH. Note that a large amplitude V of the nearest neighbor interaction is necessary to destabilize the phase. It can be compared to the amount of longer range interaction that is necessary to destroy the composite fermion phase of the FQH on the torus at $\nu = 2/3$. On the torus, we consider the interaction

$$\hat{V} = \sum_M V_0 |M, 0\rangle \langle M, 0| + V_2 |M, 2\rangle \langle M, 2| \quad (4.18)$$

which penalizes the pairs of particles having a relative momentum 0 or 2 (as in Eq. (2.10), the summation is on the total momentum of the pair of particles). A phase transition occurs when the gap above the threefold (exactly degenerate) ground state vanishes. The evolution of the gap for a FQH system with respectively $N = 8$ and 10 bosons on the torus is shown in Fig. 4.10. We see that the gap closes around $V_2 \simeq 0.25V_0$ for both system sizes. This gives the range of stability of the FQH $\nu = 2/3$ state on the torus, a result that is original result to this manuscript (in particular it was not published in Ref. [98]). Note that it is difficult to quantitatively compare the stability of the FCI and FQH phases, since the mapping of the interaction (from the real space interaction on the lattice to the pseudopotential language) has a complicated form [92] (in particular, the ratio V/U is not identical to the ratio V_2/V_0). We would like to stress the meaning of "long range" in this context. Indeed, the Coulomb interaction (which best stabilizes the composite fermion states) is often considered a long range interaction. However, the projection of the Coulomb interaction to the lowest Landau level considerably reduces its range, because of the Gaussian decay of the electronic density, yielding a small V_2/V_0 ratio (see Fig. 2.2).

Note that changing the parameters of the tight-binding model will also cause the ratio $\frac{\delta E_1}{\Delta}$ to decrease. In fact, this quantity was used to optimize the band structure parameters, and the values defined in Eq. (4.1) are those that give the largest ratio $\frac{\delta E_1}{\Delta}$ at $\nu^{FCI} = 2/3$ for bosons (and at $\nu^{FCI} = 2/5$ for fermions). Going back to the effect of longer range interactions, we note that using another set of band parameters (those identified in Ref. [71] to produce a flattest lowest band in

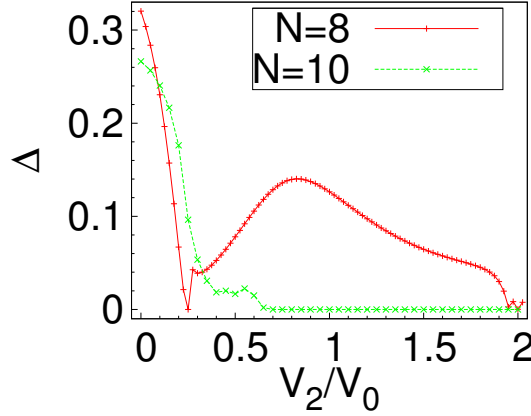


Figure 4.10: Evolution of the gap above the bosonic $\nu = 2/3$ state on the torus, for $V_0 = 1$ and different values of V_2 , where V_0 and V_2 are Haldane pseudopotentials, for systems with $N = 8$ and 10 bosons. For both system sizes, we observe a phase transition (phase closing) around $V_2 \simeq 0.25V_0$.

the ruby lattice model), we find a slightly different result. Adding some amount of V (here $V \simeq 1.35U$) seems to minimize $\frac{\delta E_1}{\Delta}$ (see Fig. 4.9b). This minimum is of the same order as in the case of the optimal band parameters. This suggests that one can play with a combination of either the interaction form or the band structure to optimize a given FCI.

We thus numerically identified the $2/5$, $3/7$ fermionic phases, as well as $2/3$ and $3/4$ bosonic phases in a fractional Chern insulator model, the ruby lattice model. In Ref. [98], we also showed that other Chern insulator models may host these phases, but with more visible finite size effects. These fractional topological phases were identified by relying on energetic signatures (degeneracy of the ground state and its charged excitations), as well as entanglement spectroscopy. This work contributed to the numerical confirmation of the emergence of fractional states in Chern insulators, and as such, had a relatively large impact. It was made shortly after the FQH-to-FCI mapping was proposed in Ref. [24]. It validated the mapping as a way to relate FCI and FQH quantum numbers away from the states of the Read-Rezayi series, since it was the first time it was used in a situation where the number of excitations could not be predicted by a counting principle. These states, as well as other fractions, were independently identified in Ref. [89], which confirmed their stability in slightly larger systems, and in other Chern insulator models. Finally, it completed an analytical study of the composite fermion states in fractional Chern insulators [109, 108].

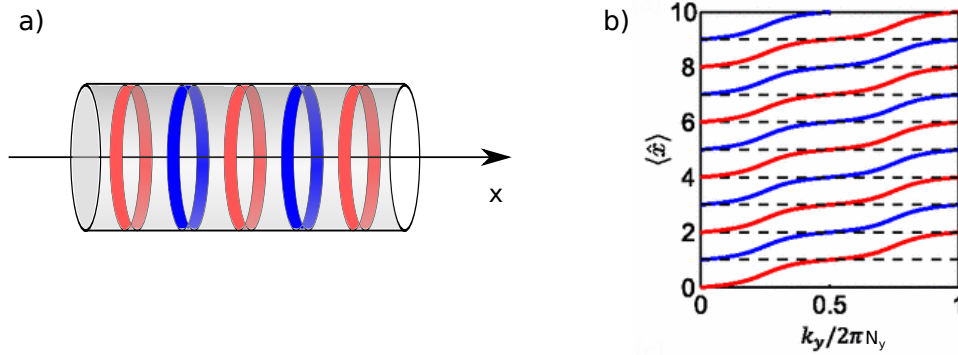


Figure 4.11: Wannier orbitals of a $C = 2$ Chern insulator on a cylinder geometry. a) Schematic representation of the Wannier orbitals, which are localized in the x direction, and extended in the y direction. The periodicity property Eq. (4.20) of these orbitals allows to separate them into two groups with a fictitious degree of freedom represented by the color red or blue. b) Evolution of the expectation value of the position operator projected into the lowest band for the red and blue Wannier orbitals. Each black dashed line represents the position of a lattice site. After the insertion of a unit flux quantum, the center of a given orbital has been shifted by two lattice spacings, in agreement with Eq. (4.20).

4.3 Fractional Chern insulators with a Chern number $C > 1$

In the absence of interactions, a $C > 1$ band is similar to C bands with a Chern number unity. When strong interactions are turned on, we can thus expect to reproduce some of the phases of the spinful fractional quantum Hall effect. We will see that even at the single-particle level, a $C > 1$ topological band is not strictly equivalent to C unit Chern number bands. As a result, Chern insulators with a $C > 1$ band may host some completely new phases, different from those of the fractional quantum Hall effect, when interactions are turned on. We will substantiate this claim with numerical evidence from exact diagonalization and a deep look at the entanglement spectrum.

4.3.1 Chern insulators with $C > 1$ in the absence of interactions

4.3.1.1 Wannier orbitals for the Chern insulators

The Bloch states are eigenstates of the single-particle Hamiltonian, and of the operators that translate the particle by a lattice vector. It can sometimes be advantageous to work in a basis of localized states, or Wannier states. There are many ways to define the Wannier states, due to the $U(1)$ gauge freedom of the Bloch states, but all definitions involve a spatial Fourier transform of the Bloch states to obtain eigen-

states of \hat{x} and \hat{y} , the position operators projected onto the band of interest. We consider an insulator with a lowest band that has a Chern number $C \neq 0$. Since the projected translation operators along two non-equivalent directions of the lattice do not commute (like the guiding center coordinates of a particle in a Landau level in Eq. (1.33)), it is not possible to define Wannier orbitals that are eigenstates of both \hat{x} and \hat{y} . There are thus no states that are localized in both directions in the $C \neq 0$ band of a Chern insulator.

However, there is no obstruction to defining Wannier orbitals that are localized in one direction and extended in the other direction [126, 35] (see Fig. 4.11a for a schematic representation of the Wannier orbitals on a cylinder). For $C = 1$, the 1D Wannier states are similar to the lowest Landau level quantum Hall wave functions ϕ_{0,k_y} defined on the cylinder in Eq. (1.37). The orbitals $\phi_{0,k_y=2\pi k_y/L_y}$ (where $k_y = 0, \dots, N_\phi - 1$) are localized around the line $x = \frac{2\pi l_B^2 k_y}{L_y} = \frac{L_x k_y}{N_\phi}$, while being completely delocalized (plane waves) in the y direction. The insertion of a unit flux quantum along the cylinder axis (x direction) corresponds to the addition of a vector potential \mathbf{A}' along the y direction

$$\mathbf{A}' = -\frac{2\pi\hbar}{eL_y}\mathbf{e}_y \quad (4.19)$$

This operation amounts to shifting the momentum k_y in the Hamiltonian Eq. (1.36) by $2\pi/L_y$. The lowest Landau level wave function $\phi_{0,k_y}(x, y)$ of Eq. (1.37) thus becomes $\phi_{0,k_y+2\pi/L_y}(x, y)$, which is equal to $\phi_{0,k_y}(x - L_x/N_\phi, y)$.

Going back to Chern insulators with an arbitrary Chern number, Barkeshli and Qi [16] detailed the single-particle physics of Chern insulators with $C > 1$ using this Wannier states formalism. Let us call $|W(k_y, n)\rangle$ the Wannier state localized around the position n in the x direction ($n = 0, \dots, N_x - 1$), and with a momentum k_y in the y direction ($k_y = 2\pi k_y/N_y$, with $k_y = 0, \dots, N_y - 1$). Barkeshli and Qi showed that the Wannier states $|W(k_y, n)\rangle$ of a Chern insulator obeyed twisted boundary conditions

$$|W(k_y + 2\pi/N_y, n)\rangle = |W(k_y, n + C)\rangle \quad (4.20)$$

Equivalently, the adiabatic insertion of a unit flux quantum along the x direction causes the Wannier orbitals to shift by C lattice spacings. Note that we proved this property in the previous paragraph for $C = 1$, in the case of the quantum Hall wave functions ϕ_{0,k_y} . We can illustrate this periodicity property for a $C > 1$ Chern insulator by looking at the expectation value of the projected position operator \hat{x} for the Wannier orbitals. Fig. 4.11b represents the evolution of the expectation value of \hat{x} for the Wannier orbitals as a magnetic flux quantum is inserted along the cylinder axis, for a $C = 2$ Chern insulator.

Thanks to the periodicity property Eq. (4.20) of the Wannier states, one can thus disentangle C copies of a $C = 1$ Chern insulator, and associate a fictitious $SU(C)$ degree of freedom to each copy. In the case of a $C = 2$ Chern insulator, Fig. 4.11 shows how the Wannier orbitals can be separated into two groups, the fictitious degree of freedom being represented by the color red or blue of the orbital. Note that

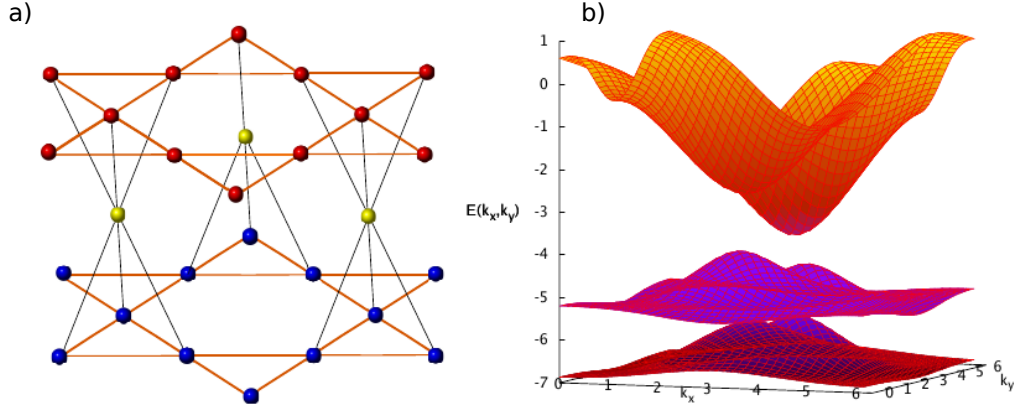


Figure 4.12: The pyrochlore lattice Chern insulator model with $p = 2$ layers of the kagome lattice. a) The lattice model. The two kagome layers are represented in red and blue, respectively, and the triangular layer in yellow. b) Three lowest bands of the single-particle spectrum of the pyrochlore lattice model with the tunneling parameters defined in Eq. (4.21). The band immediately above the lowest band is gapped and has a Chern number $C = 2$.

this picture is valid in the thermodynamic limit, but for a finite size system with periodic boundary conditions in both directions, commensurability effects might arise. Indeed, if the number of unit cells N_x in the x direction is not a multiple of C , the separation into C copies is no longer possible, since the insertion of a flux will mix the different fictitious degrees of freedom. For example, in Fig. 4.11a, $N_x = 5$, and the rightmost red Wannier orbital becomes the leftmost blue Wannier orbital after insertion of a unit flux quantum along the cylinder axis. In such finite system, the fictitious degree of freedom and the translations projected onto the lowest band are actually entangled, giving rise to a physics with no quantum Hall effect equivalent.

4.3.1.2 A simple microscopic model of a $C > 1$ Chern insulator

In our numerical study, we mostly used the simplified pyrochlore lattice model introduced in Ref. [159]. It consists of p kagome layers coupled through intermediate triangular layers. The kagome lattice Chern insulator model [156] was described in Sec. 2.3.2 (see in particular Eq. (2.57) for its Bloch Hamiltonian and Fig. 2.7c for the lattice structure). It contains nearest neighbor tunneling terms of complex amplitude $t_1 + i\lambda_1$. Between two kagome layers, there is an atomic plane forming a triangular lattice. The kagome and triangular layers are aligned in such a way that each atom of the triangular lattice falls at the same position as the atom 3 of each kagome lattice unit cell (see Fig. 2.7c for the numbering of atoms in the unit cell of the kagome lattice). Fig. 4.12a depicts the pyrochlore model for $p = 2$ kagome

layers. The number of bands in this model is equal to $3 + 4(p - 1)$ (3 bands for each single kagome layer, 1 additional band for each triangular layer). The triangular layers are coupled to the kagome layers via a nearest neighbor tunneling term of real amplitude t_\perp . For a wide range of parameters, the $(p - 1)^{\text{th}}$ band of this model is gapped, and has a Chern number equal to the number of kagome layers ($C = p$). We choose the following tunneling parameters, and $p = 2$ or $p = 3$

$$t_1 = 1, \lambda_1 = 0.83, t_\perp = -1.03 \quad (4.21)$$

These parameters yield a relatively flat $(p - 1)^{\text{th}}$ band (where the lowest band has a label 0) with Chern number $C = p$. The three lowest bands of the single-particle spectrum of this system is represented for $p = 2$ in Fig. 4.12b.

4.3.2 Model $SU(C)$ fractional quantum Hall wave functions

In the previous paragraph, we have seen that in some cases, a $C > 1$ Chern band is equivalent to a unit Chern number topological band, hosting particles with a fictitious $SU(C)$ degree of freedom. In the strongly interacting regime, we thus expect the $C > 1$ Chern insulators to host phases similar to the $SU(C)$ fractional quantum Hall effect. We review these phases in this paragraph.

The generalized Halperin $[m, n]$ states [64] are a series of abelian wave functions which generalize the Laughlin state to a system where the particles carry an additional $SU(C)$ degree of freedom. They write

$$\Psi_{[m, n]}^{SU(C)} = \Phi_m^{\text{intra}} \Phi_n^{\text{inter}} e^{-i \sum_{\alpha=1}^C \sum_{k_\alpha=1}^{N_\alpha} |z_{k_\alpha}^{(\alpha)}|^2 / (4l_B^2)} \quad (4.22)$$

where Φ_m^{intra} is the product of C Laughlin states, one for each component α

$$\Phi_m^{\text{intra}} = \prod_{\alpha=1}^C \prod_{k_\alpha < l_\alpha} \left(z_{k_\alpha}^{(\alpha)} - z_{l_\alpha}^{(\alpha)} \right)^m, \quad (4.23)$$

Φ_n^{inter} gives the correlation between components

$$\Phi_n^{\text{inter}} = \prod_{\alpha < \beta} \prod_{k_\alpha=1}^{N_\alpha} \prod_{k_\beta=1}^{N_\beta} \left(z_{k_\alpha}^{(\alpha)} - z_{k_\beta}^{(\beta)} \right)^n \quad (4.24)$$

and $z_{k_\alpha}^{(\alpha)}$ is the complex coordinate of the k^{th} particle of component α . m and n are two integers that characterize the strength of the correlations between particles of the same and different component, respectively. The $SU(C)$ $[m, n]$ Halperin states represent states with a total filling fraction

$$\nu = \frac{C}{m + (C - 1)n} \quad (4.25)$$

where the filling fraction for a multicomponent system is defined as the sum of the filling fractions for each component. On the torus, these states have a degeneracy

$$d = (m - n)^{C-1} (m + (C - 1)n) \quad (4.26)$$

When $n = m - 1$, the Halperin states are $SU(C)$ spin singlets. In this case, the filling fraction is

$$\nu = \frac{C}{(m-1)C+1} \quad (4.27)$$

and the degeneracy of the ground state on the torus is

$$d = (m-1)C+1 \quad (4.28)$$

As seen in Sec. 3.1.3, the Laughlin state can be used to build the non-abelian Read-Rezayi states, using the so-called projective construction. The projective construction can be generalized to write non-abelian $SU(C)$ spin singlet states [6] (NASS- k) starting from the $SU(C)$ $[m, m-1]$ Halperin states. It consists in separating the particles into k groups of N/k particles, writing a $SU(C)$ $[m, m-1]$ Halperin state for each group, and symmetrizing over the particle coordinate

$$\Psi_m^{SU(C),k} = \mathcal{S} \left(\prod_{i=0}^{k-1} \Psi_{[m,m-1]}^{SU(C)} \left(z_{1+iN/k}^{(1)}, \dots, z_{(i+1)N/k}^{(C)} \right) \right) \quad (4.29)$$

where \mathcal{S} operates the symmetrization over all particle coordinates. This state appears at filling fraction

$$\nu = \frac{Ck}{C(m-1)+1} \quad (4.30)$$

When $m = 2$, $\Psi_{m=2}^{SU(C),k}$ is simply called the NASS (non-abelian spin singlet). This state introduced in Ref. [6] for $C = 2$, and generalized to $C = 4$ in Refs. [134, 135].

The $[m, m-1]$ $SU(C)$ Halperin states and NASS- k states are the exact zero energy states of some model Hamiltonians. These model interactions are the $SU(C)$ symmetric versions of the model interactions of the $U(1)$ counterparts of these states, the Laughlin and \mathbb{Z}_k Read-Rezayi states. For example, the model interaction of the $[m, m-1]$ $SU(C)$ Halperin state can be written in terms of pseudopotentials (see Sec. 2.1.2) as

$$\begin{cases} V_l > 0 & \text{if } l < m-1 \\ V_l = 0 & \text{if } l \geq m-1 \end{cases} \quad (4.31)$$

such that it penalizes all pairs of particles with a relative momentum l strictly lower than $m-1$, no matter what spin they carry. Likewise, for bosons, the model interaction of the \mathbb{Z}_k Read-Rezayi states can be generalized to the spinful case. In this case, the contact interaction Eq. (2.36) couples $k+1$ bosons, irrespective of their spins (for fermions, the interaction is slightly more complicated [5]). The NASS- k state is the exact ground state of this model interaction.

The number of ground states and quasihole states for the Halperin and NASS- k states can be predicted using an exclusion principle [6, 42], which is a generalization of the spinless exclusion principle of Sec. 2.2.4. In the spinless case (see Sec. 2.2.4), we have defined admissible (k, r) partitions using the occupation basis. We can use another notation which defines each partition λ as a set of integers $\{\lambda_i\}_{1 \leq i \leq N}$ satisfying

$$\lambda_i \leq \lambda_{i+1} \quad (4.32)$$

such that a state of the Fock basis is proportional to $\mathcal{S}(z_1^{\lambda_1}, \dots, z_N^{\lambda_N})$ (as usual, the operator \mathcal{S} symmetrizes over all particle positions). In this language, the (k, r) principle translates into

$$\lambda_i - \lambda_{i+k} \geq r \quad (4.33)$$

In the spinful case, the partition λ describing a Fock state (as defined in Sec. 2.2.4) is replaced by a dressed partition (λ, σ) . The dressed partition gives the orbital index λ_i (with $i = 1, \dots, N$) and spin $(\sigma_i = 1, \dots, C)$ of the occupied orbits, such that

$$\begin{cases} \lambda_i > \lambda_{i+1} \\ \text{or} \\ \lambda_i = \lambda_{i+1} \text{ and } \sigma_i \geq \sigma_{i+1} \end{cases} \quad (4.34)$$

A $(k, r)_C$ admissible partition is a $SU(C)$ dressed partition that verifies the additional condition

$$\begin{cases} \lambda_i - \lambda_{i+k} \geq r \\ \text{or} \\ \lambda_i - \lambda_{i+k} = r - 1 \text{ and } \sigma_i < \sigma_{i+k} \end{cases} \quad (4.35)$$

If we set $C = 1$, we obtain the constraints imposed on the admissible partitions of the spinless fractional quantum Hall effect, as expressed in Sec. 2.2.4. The number of ground states and quasihole states in a system with N particles and N_ϕ flux quanta is given by the number of such $(k, r)_C$ admissible partitions. The $[m, m-1]$ $SU(C)$ Halperin spin singlets are the generalization of the Laughlin $1/m$ state, and obey a $(1, m)_C$ counting principle. By setting $C = 1$, one finds the usual $(1, m)$ exclusion principle of the Laughlin $1/m$ state. Likewise, the NASS- k state $\Psi_{m=2}^{SU(C), k}$ defined in Eq. (4.29) is the $SU(C)$ generalization of the \mathbb{Z}_k Read-Rezayi state, and obeys a $(k, 2)_C$ exclusion principle. Finally, note that for any given N and N_ϕ , any admissible $(k, r)_C$ dressed partitions (λ, σ) can be converted into a spinless partition λ' , such that for all $i = 1, \dots, N$

$$\lambda'_i = C\lambda_i + \sigma_i \quad (4.36)$$

It can be shown that the set of partitions λ' obtained from Eq. (4.36) is the same as the set of partitions obeying the $(k, C(r-1) + 1)_1$ exclusion principle.

4.3.3 Numerical study of some $C > 1$ fractional Chern insulators

4.3.3.1 Energetics

We use the tight-binding model described in Sec. 4.3.1.2, more particularly the $(p-1)^{th}$ band, which has a Chern number p . We consider N spinless bosons interacting via the following $(k+1)$ -body on-site interaction

$$H_{int, k}^b = U \sum_i : (\rho_i)^{k+1} : \quad (4.37)$$

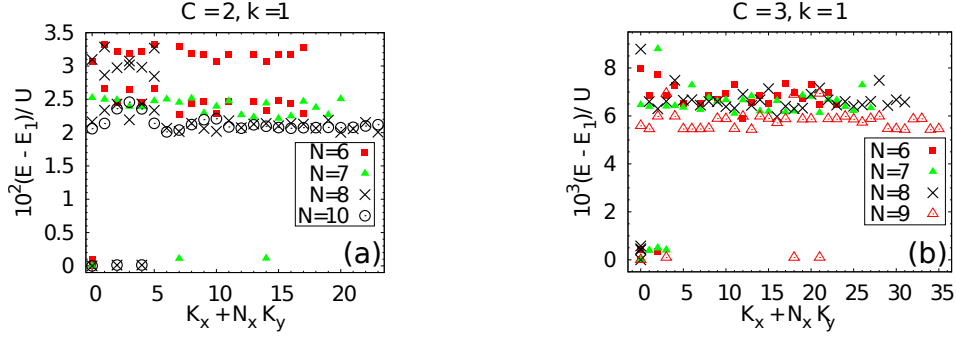


Figure 4.13: Low energy spectrum on the pyrochlore lattice with $C = 2$ (a) and $C = 3$ (b), as obtained by exact diagonalization of a two-body on-site interaction projected onto the lowest band (see Eq. (4.38) with $k = 1$). We observe a $(C+1)$ -fold almost degenerate ground state, with a gap to higher energy excitations.

For $k = 1$, $H_{int,k}^b$ is equal to H_{int}^b , the two-body density-density interaction defined in Eq. (2.54).

We assume that the p^{th} lowest bands are filled and inert. Again, the interaction is projected onto the band of interest (which has a band index $\mu = p - 1$), and the effect of dispersion is neglected using the flat-band limit (see Eq. (2.59)), such that the Hamiltonian writes

$$H_k^b = \sum_{\mathbf{k}, \mathbf{k}' \in BZ} |p-1, \mathbf{k}\rangle \langle p-1, \mathbf{k}| H_{int,k}^b |p-1, \mathbf{k}'\rangle \langle p-1, \mathbf{k}'| \quad (4.38)$$

Note the difference of definition for the filling fraction of the fractional Chern insulator and the $SU(C)$ fractional quantum Hall effect. The filling fraction ν^{FCI} in a fractional Chern insulator is defined with respect to the partially filled band, and does not depend on the Chern number C of said band. On the other hand, the filling fraction for the $SU(C)$ fractional quantum Hall effect corresponds to the total filling fraction for all values of $\sigma = 1, \dots, C$, such that the filling fraction of comparable FCI and FQH systems are related by

$$\nu^{FCI} = \frac{\nu}{C} \quad (4.39)$$

We perform the exact diagonalization of the Hamiltonian Eq. (4.38). We first use a two-body interaction ($k = 1$), and a filling fraction

$$\nu^{FCI} = \frac{1}{C+1} \quad (4.40)$$

For both $C = 2$ and $C = 3$, we observe a $C + 1$ quasi-degenerate ground state, with a clear gap to higher energy excitations, for all numbers of particles that are numerically accessible (see Fig. 4.13). We can nucleate quasi-hole excitations in this system by adding unit cells to the original system. We verified numerically that

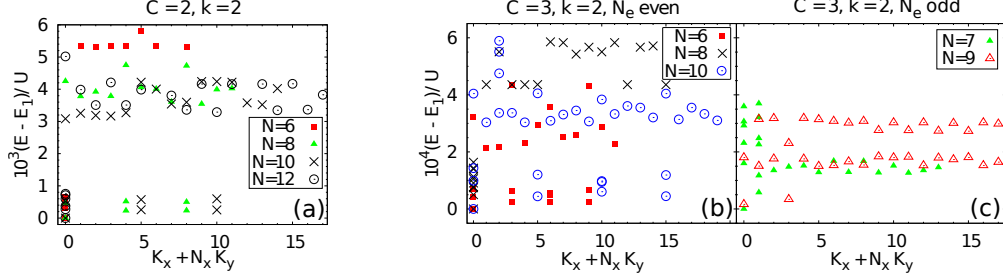


Figure 4.14: Low energy spectrum on the pyrochlore lattice with $C = 2$ (a) and $C = 3$ (b), as obtained by exact diagonalization of a three-body on-site interaction projected onto the lowest band (see Eq. (4.38) with $k = 2$). We observe a sixfold almost degenerate ground state for $C = 2$, with a gap to higher energy excitations. For $C = 3$, we observe a tenfold almost degenerate ground state when the number of particles N is even. No clear pattern can be extracted from the low energy spectrum when the number of particles is odd.

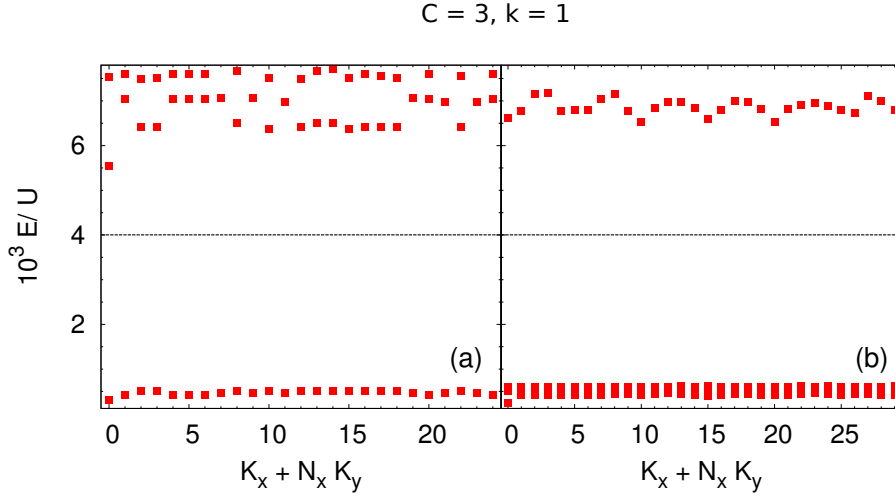


Figure 4.15: Low energy spectrum on the pyrochlore lattice with $C = 3$, as obtained by exact diagonalization of a two-body on-site interaction projected onto the lowest band (see Eq. (4.38) with $k = 1$). a) $N = 6$ bosons on a 5×5 lattice (one site added compared to the $\nu^{FCI} = 1/4$ ground state). b) $N = 7$ bosons on a 6×5 lattice (two sites added compared to the $\nu^{FCI} = 1/4$ ground state).

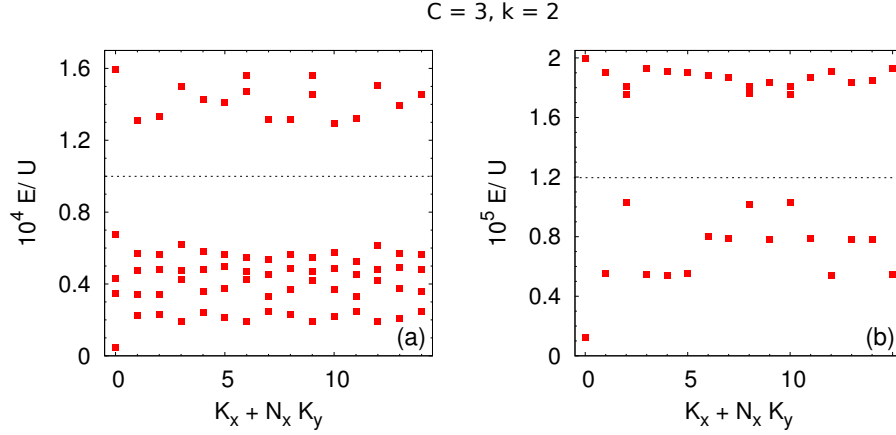


Figure 4.16: Low energy spectrum on the pyrochlore lattice with $C = 3$, as obtained by exact diagonalization of a two-body on-site interaction projected onto the lowest band (see Eq. (4.38) with $k = 2$). a) $N = 7$ bosons on a 3×5 lattice (one site added compared to the $\nu^{FCI} = 2/4$ ground state). b) $N = 7$ bosons on a 4×4 lattice (two sites added compared to the $\nu^{FCI} = 2/4$ ground state).

this operation leads to a gapped spectrum, where the total number of states below the gap is given by the $(1, C + 1)_1$ counting principle (see Fig. 4.15). This counting suggests an abelian spinless state, but could just as well be interpreted as a spinful $SU(C)$ state. Indeed, the $(1, C + 1)_1$ counting is related to the spinful $(1, 3)_C$ exclusion principle (which predicts the number of bosonic $SU(C)$ $[2, 1]$ Halperin states), via the mapping Eq. (4.36). Note that the filling fraction and the form of the interaction are compatible with the interpretation of our FCI phase as a spinful state. Indeed, the filling fraction $\nu^{FCI} = 1/(C + 1)$ can be compared to the filling fraction $\nu = C/(C + 1)$ of the bosonic $SU(C)$ $[2, 1]$ Halperin state. Moreover, the on-site density-density interaction Eq. (4.37) is similar to the delta interaction, which, in its $SU(C)$ symmetric version (expressed in terms of pseudopotentials in Eq. (4.31) with $m = 2$), is the model interaction for the $[2, 1]$ Halperin singlet state. Due to the equivalence Eq. (4.36) between spinless and spinful counting principles, it is difficult to determine the spinless or spinful nature of the FCI ground state. Also, we observe that only the total number of states between the spinful FQH and spinless FCI matches: the FQH-to-FCI mapping (see Sec. 2.3.3) fails to predict the counting per momentum sector.

A similar observation can be made for a three-body interaction ($k = 2$), and a filling fraction

$$\nu^{FCI} = \frac{2}{C + 1} \quad (4.41)$$

for both $C = 2$ and $C = 3$. At this filling fraction, we observe a gapped ground state, which is almost sixfold degenerate for $C = 2$, and almost tenfold degenerate for $C = 3$ for an even number of particles (see Fig. 4.14). Once quasiholes are nucleated

in the system, we also obtain a gapped low energy spectrum (see Fig. 4.16). The total degeneracy of both the ground state and quasihole states is compatible with a $(2, C+1)_1$ exclusion principle. This counting rule compares to the $(2, 2)_C$ spinful exclusion rule, which predicts the number of NASS states and of their quasihole excitations. Again, the filling fraction $\nu = 2C/(C+1)$ of the NASS state is compatible with that of the observed FCI state, and so is its model interaction (the $(k+1)$ -body contact interaction). Note that for $C = 2$, the filling fraction $\nu^{FCI} = 2/(C+1) = 2/3$ can only be realized for an even number of particles. On the other hand, for $C = 3$, the filling fraction $\nu^{FCI} = \frac{2}{C+1} = 1/2$ can be realized for either parity of the number of particles. The fact that the tenfold ground state only appears for an even number of particles suggests a paired state, in agreement with the possible interpretation of this state as a NASS.

Finally, we notice the absence of any commensurability effect between the number of particles N and the Chern number C in the ground state degeneracy. Indeed, the $SU(C)$ -singlet Halperin state appears only when N is a multiple of C . On the other hand, when $C = 2$ and $k = 1$, the threefold quasi-degeneracy appears even for N odd. Likewise, the fourfold quasi-degeneracy of the $C = 3$, $k = 1$ ground state appears even when N is not a multiple of 3. A similar observation holds true when $k = 2$: the necessity to distribute all fictitious degrees of freedom equally across all particles, coupled with the pairing, would have us expect a difference between the case where N is a multiple of $2C$, and the case where it is just a multiple of 2. We observe no such difference, which again limits the validity of the analogy of the $C > 1$ fractional Chern insulators with the $SU(C)$ fractional quantum Hall states.

The above numerical simulations and discussion reveal the difficulty to clearly identify the FCI $C > 1$ state as a spinful or spinless state, using only energetic arguments. While there is an apparent similarity between these states and the FQH $SU(C)$ singlet states, other arguments (like the absence of any commensurability effect between the number of particles and the Chern number) limit the validity of this analogy. In the next paragraph, we use particle entanglement spectroscopy to gain more insight into these phases.

4.3.3.2 Entanglement spectroscopy

We start by noting the specificities of the spinful FQH model states – compared to their spinless counterparts – with regard to particle entanglement spectroscopy. As seen in Sec. 2.4.2, the particle entanglement spectrum (PES) of the spinless FQH model state with N particles and N_ϕ flux quanta has a particular structure: for a particle partition with $N_A \leq N/2$, the number of non-zero eigenvalues of the reduced density matrix ρ_A is equal to the number of quasihole states in the system with N_A particles and the same number of flux quanta N_ϕ . This counting is equal to the number of (k, r) admissible partitions. For a spinful $SU(C)$ FQH state, however, constraints on the internal degree of freedom can modify the PES counting. Let us consider the case of a $SU(C)$ spin singlet, such as the $SU(C)$ $[2, 1]$ Halperin state. To reflect the $SU(C)$ symmetry, each dressed partition (λ, σ) of

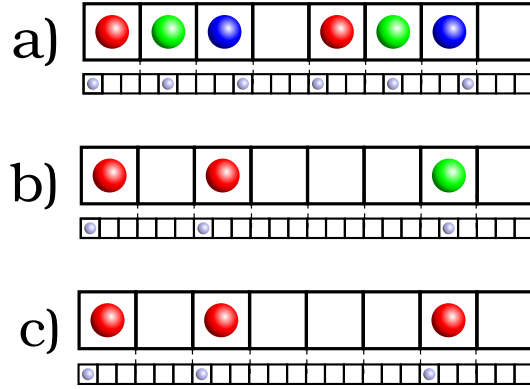


Figure 4.17: $(1,2)_3$ admissible partitions in the $SU(3)$ case (using the red, green and blue colors for each possible value of the internal degree of freedom) and their $(1,4)_1$ counterparts (in gray). Here we have chosen red to be $\sigma = 0$, green $\sigma = 1$ and blue $\sigma = 2$. (a) displays a typical admissible configuration for the groundstate of the $SU(3)$ Halperin state. (b) is an admissible configuration for the quasihole states that is present when computing the PES for the $N = 6$ particle groundstate. (c) is also an admissible configuration for the quasihole states but cannot be accessed through the PES from the $N = 6$ particle groundstate.

the ground state must contain the same number N/C of particles of each spin σ . Representing each spin σ with a different color, we give an example of such partition in Fig. 4.17a in the case where $C = 3$. When counting the number of $(k, r)_C$ ($(1, 2)_C$ in our example) admissible partitions, one should discard the partitions with more than N/C particles of the same spin. Indeed, these partitions do not exist in the ground state, and thus cannot appear in the PES. Fig. 4.17b and Fig. 4.17c both show $(1, 2)_3$ admissible partitions, but only the partition in Fig. 4.17b should be taken into account to predict the PES counting, since Fig. 4.17c has more red particles than appear in the ground state. The $SU(C)$ symmetry thus lowers the number of states in the PES of a $SU(C)$ ground state, compared to what is expected from the $(k, r)_C$ exclusion principle. On the other hand, no such constraint exists for the quasihole states, whose degeneracy is still given by the spinful $(k, r)_C$ or spinless $(k, C(r - 1) + 1)_1$ exclusion principle. Note that no discrepancy can be observed for $C = 2$, since the number of states in the partition A is always limited to $N_A \leq N/2 = N/C$. For $C = 3$, however, there are particle partitions such that $N/C < N_A \leq N/2$, such that the effects of the additional constraint can be observed in the PES of the ground state.

We have computed the PES of the almost degenerate ground states of all of our FCI systems (the procedure to obtain the PES of a degenerate ground state was detailed in Sec. 2.4.2). In all the cases where there is a clear ground state quasi-degeneracy in the energy spectrum, we observed an entanglement gap, and were able to count the number of states below it. For $C = 2$, the previous comment implies

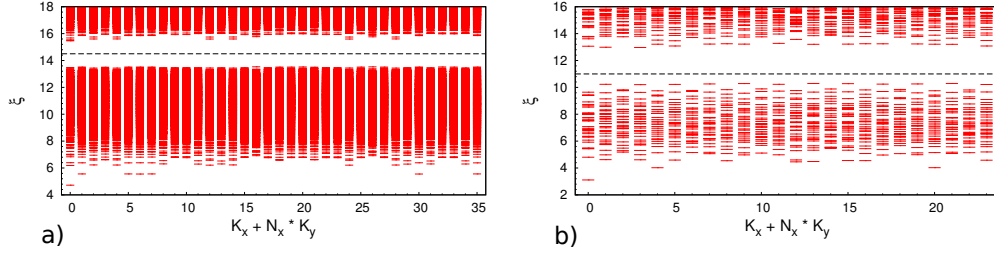


Figure 4.18: a) PES of the low energy groundstate manifold for $N = 9$ bosons on a 6×6 pyrochlore lattice with $C = 3$ and two body interaction, with $N_A = 4$. The number of states below the dotted line is 14364. This is 1575 states less than the $(1, 4)_1$ counting. This counting matches the counting obtained through the Halperin PES. b) PES of the low energy groundstate manifold for $N = 6$ bosons on a 6×4 pyrochlore lattice with $C = 3$ and two body interaction, with $N_A = 3$. The number of states below the dotted line is 680. It is lower than the $(1, 4)_1$ counting, but does not match the PES counting of the corresponding $SU(3)$ -singlet Halperin state.

that the PES counting of the $SU(2)$ FQH states and their spinless counterparts match. Consequently, we do not expect the PES to rule out or confirm the necessity of an internal $SU(2)$ degree of freedom to describe the $C = 2$ FCI ground state. We verified that the number of states below the entanglement gap was consistent with our observations of the Sec. 4.3.3.1. For $C = 2$ and $k = 1$, the number of states below the entanglement gap matches the spinful $(1, 2)_2$ quasihole counting, as well as the spinless $(1, 3)_1$ quasihole counting. This confirms the topological nature of the ground state. Note that the counting of the quasihole states in the energy spectrum is not sufficient to identify the phase since the spectrum of a charge density wave could have the same counting. As expected, the number of states is consistent with an interpretation of the ground state as a $SU(2)$ Halperin-like state, but also as a spinless state. Likewise, for $C = 2$ and $k = 2$, the number of states below the entanglement gap matches the spinful $(2, 2)_2$ counting, as well as the spinless $(2, 3)_1$ counting.

We now turn to the case $C = 3$, and a two-body interaction ($k = 1$). This is a particularly interesting case, since it is the smallest value of C where we can realize the inequality $N_A > N/C$. For $N_A \leq N/C$, we observe a clear entanglement gap above the expected $(1, 2)_3$ (or equivalently $(1, 4)_1$) counting. For $N_A > N/3$, there is an entanglement gap, but the counting below this gap is generally not given by a $(1, 4)_1$ counting rule. We first focus on the situation where both N_x and N_y are integer multiples of C . We observe the number of states reduction predicted above for the $SU(C)$ FQH singlets. In this case the number of states below the gap is the same as the number of states of the $[2, 1]$ $SU(3)$ -singlet Halperin PES. For example, the PES of the $N = 9$ bosons on a 6×6 lattice for $N_A = 4$ has a clear entanglement gap, with 14364 states below it (see Fig. 4.18a), the same number of states as the Halperin state PES. However, outside of these very specific conditions

(when at least one of the integers N_x, N_y is not a multiple of C), the PES counting is not that of the Halperin state. The number of states below the entanglement gap is either equal, or lower than the $(1, 4)_1$ counting.

As seen in Sec. 4.3.1.1, Chern insulators with a maximal commensurability (i.e. N_x and N_y are both multiples of C) are equivalent to $SU(C)$ quantum Hall systems. In these systems, the Wannier orbitals can be decoupled into C groups of colored orbitals, each mimicking the quantum Hall orbitals with a given spin $\sigma = 1 \dots C$ on the cylinder. It is thus not surprising to obtain the $SU(C)$ -singlet Halperin states in these systems when $SU(C)$ symmetric interactions are turned on. The PES counting in the other, less commensurate cases was originally not understood in Ref. [154]. However, subsequent articles [176, 175] have provided a clear explanation for these states. When one of the lattice dimensions N_x or N_y is a multiple of C , the color degree of freedom of the Wannier states and their translation quantum numbers can be disentangle. The price to pay is a shift of the Wannier states along the cylinder axis, which depends on their color. This system is equivalent to the multicomponent quantum Hall system where a spin-dependent magnetic flux has been inserted along the cylinder axis. Halperin states corresponding to this picture can be written, and Ref. [176] showed that our results in $C > 1$ fractional Chern insulators were consistent with the PES of these states.

When both N_x and N_y are incommensurate with C , the color degree of freedom of the Wannier states can no longer be disentangled from their translation quantum numbers. The non-interacting system behaves like a multilayer system where a topological defect connects the different layers. This picture is very similar to that of a multilayer system with twisted boundary conditions, as described in Sec. 3.1.4 and depicted in Fig. 3.1 for $C = 2$. It is thus tempting, following the arguments of the previous chapter, to try to unfold this twisted system into a C times larger, defect-free torus. Note that here, the $SU(C)$ invariant interaction would couple the different layers, preventing a simple transposition of the arguments of Sec. 3.1.4. However, in our numerical results, we almost always observe a $(1, C + 1)_1$ Laughlin counting below the PES entanglement gap. This suggests a connection between the $C > 1$ fractional Chern insulator and the Laughlin state living on some unfolded version of the Chern insulator, which would be interesting to explore.

In conclusion, the PES results bring additional arguments to support the realization of fractional phases in Chern insulators with $C > 1$. In some cases, the ground state can be identified to an equivalent $SU(C)$ -singlet fractional quantum Hall state. The numerical results obtained for a three-body interaction ($k = 2$), while not shown here, strongly suggest the apparition of a non-abelian state which compares to the NASS state in the case where both directions of the lattice are commensurate with C . Our numerical data also clearly shows the emergence in Chern insulators of fractional phases with no simple fractional quantum Hall equivalent. Beyond the identification of these states, our analysis shows the power of particle entanglement spectroscopy. Indeed, the use of PES allowed us to gain some crucial information on the nature of the phases that would be impossible to obtain from energetic signatures alone.

Fractional topological insulators with time-reversal symmetry

Contents

5.1	Microscopic model	138
5.1.1	One-body model	139
5.1.2	Coupling via the band structure	140
5.1.3	Form of the interaction	142
5.2	Phase diagram of a fractional topological insulator	145
5.2.1	Stability of the fractional phase at half filling with pseudospin conservation	145
5.2.2	Stability of the fractional phase at half filling without pseudospin conservation	150
5.3	Transition between the time-reversal symmetric FTI and the bilayer FCI	154
5.3.1	The bilayer fractional Chern insulator	154
5.3.2	Interpolation of the bilayer FCI and FTI phases	155

In the previous chapters of this manuscript, we have described systems that break time-reversal invariance either explicitly (due to the presence of a magnetic field) or implicitly (when the lowest band of an insulator carries a non-zero Chern number). We now focus on systems where time-reversal invariance is not only preserved, but is also at the root of the topological nature of the phase. The physics of non-interacting two-dimensional topological insulators was detailed in Sec. 1.3. In this chapter, we will study these systems in the presence of strong interactions. Indeed, these systems may host interesting, novel phases, with properties as varied and rich as those of their time-reversal breaking counterparts (studied in Chapters. 2,3,4). So far, all the properties observed experimentally in time-reversal invariant topological insulators are explained with single-particle physics arguments. Unlike the fractional quantum Hall case, we thus cannot rely on any experimental observation to guide us in our search of fractional topological phases.

On the analytical side, most models are based on a pair of chiral-antichiral fractional quantum Hall states. The simplest example of such phase consists of two bosonic Laughlin $1/2$ states with opposite chiralities, a model which realizes the

double-semion topological order (a semion model – the Laughlin $1/2$ state, for instance – realizes a topological order with only two topological sectors, corresponding to two abelian quasiparticles). While there are predictions [94, 95] concerning the stability of this phase against perturbations, numerical simulations are necessary to measure the extent of this stability. It raises the question of how to realize the toy model of Fig 1.12 in a somewhat realistic manner. Indeed, how do we realize an experimental situation where different species of electron (carrying a fictitious spin degree of freedom) are subjected to opposite magnetic fields (see the situation described in Sec. 1.3.1)? We will see that Chern insulators, since they suppress the need for a magnetic field, provide a good solution to this problem. More specifically, we study a phase made of two copies of a fractional Chern insulator with opposite chiralities, with strong interactions within each copy, such that each copy realizes the Laughlin state.

5.1 Microscopic model

As seen in Sec. 1.3.1, the simplest way to realize a time-reversal invariant topological insulator is to consider two copies of the quantum Hall effect with opposite chiralities. For a more realistic setting, we consider two copies of a Chern insulator instead of the continuous quantum Hall system. For example, the model which describes the HgTe/CdTe topological insulator in Sec. 1.3.2.1 is based on two copies of the square lattice model with two orbitals per unit cell. However, as shown in Ref. [172], this Chern insulator model does not host a very stable Laughlin phase. Our goal here is to study the influence of diverse coupling terms on this simple type of FTI. We thus need to start from a model exhibiting a clear signature of this phase in the decoupled limit, otherwise model-dependent artifacts might obscure the effects of the coupling. Consequently, our Chern insulator choice should be motivated by the possibility to realize a robust Laughlin phase, rather than the pursuit of the most realistic model. In that sense, the kagome lattice model [156] described in Sec. 2.3.2 and depicted in Fig. 2.7c is a good choice, since it hosts a stable bosonic Laughlin phase at $\nu^{FCI} = 1/2$, as well as a stable fermionic Laughlin phase at $\nu^{FCI} = 1/3$ [172], with small finite size effects. The other reason to choose this model is its simplicity, since nearest-neighbor hopping terms with the proper complex amplitude are sufficient to see a clear signature of the Laughlin phase.

The simplest fractional topological phase we could study is made of two copies of the Laughlin $1/2$ state (for a bosonic phase) or two copies of the Laughlin $1/3$ state (for a fermionic phase). Generating the energy spectrum for the fermionic phase or for the bosonic phase has a very similar computational cost. Indeed, the number of configurations with N bosons at half filling is C_{3N}^N , and is thus the same as the number of fermionic configurations at third filling with the same number of particles. We choose the bosonic model, which will allow us to choose a simpler interaction term. As seen in Sec. 2.3.2, the simplest interaction terms allowing the $1/2$ (bosonic) and $1/3$ (fermionic) Laughlin states to appear are respectively

the on-site and nearest-neighbor interactions. As a result, the simplest coupling interaction between copies is a purely on-site interaction for bosons, and is thus parametrized by a single number. For fermions, we could in principle choose a purely on-site coupling term as well. However, there is no reason not to consider a nearest-neighbor interaction coupling the fermions in different copies, since the fermions within one copy interact via this interaction.

5.1.1 One-body model

The kagome lattice Chern insulator is the building block of our model. We define the amplitude of the nearest-neighbor tunneling term (noted $|t_1 + i\lambda_1|$ in Eq. (2.57)) as the energy unit. Without loss of generality, we can thus fix this amplitude to 1, and write $e^{i\varphi}$ the *complex* amplitude of the tunneling term. Using this notation, the Bloch Hamiltonian Eq. (2.57) of the single copy writes

$$h_{\text{CI}}(\mathbf{k}) = \begin{pmatrix} & |1\rangle & |2\rangle & |3\rangle \\ \begin{pmatrix} 0 & e^{i\varphi}(1 + e^{-ik_x}) & e^{-i\varphi}(1 + e^{-ik_y}) \\ & 0 & e^{i\varphi}(1 + e^{i(k_x - k_y)}) \\ h.c. & & 0 \end{pmatrix} & |1\rangle \\ & |2\rangle \\ & |3\rangle \end{pmatrix} \quad (5.1)$$

where 1, 2 and 3 denote the orbital indexes (see Fig. 2.7c for the labeling of the orbitals in the kagome lattice). Except for $\varphi = 0$ and $\varphi = \pm 2\pi/3$ (at which the system is gapless), the model has two non-trivial bands with Chern number $C = \pm 1$, in addition to a trivial band ($C = 0$) (see Fig. 5.1a). For the sake of simplicity, we set $\varphi = \pi/4$. The model with $\varphi = \pi/4$ is known to stabilize a Laughlin-like phase when interactions are switched on, as shown numerically in the fermionic case in Ref. [172].

To build a two dimensional time-reversal invariant topological insulator, we put together two copies of this model. We define a pseudospin operator \hat{s} , and we use the eigenvalues $s_z = \pm 1/2$ of its projection to label the two copies. The i^{th} atoms of both pseudospins are geometrically at the same position as depicted in Fig. 5.1b. The action of the time-reversal operator \mathcal{T} on a wave function describing one particle depends on its spin: $\mathcal{T}^2 = -1$ for half integer spins, $\mathcal{T}^2 = 1$ for integer spins [20]. Strictly speaking, the time-reversal symmetry should thus act as $\mathcal{T}^2 = 1$ on the spinless bosons in each copy of our model. However, we choose to define \mathcal{T} as the antiunitary discrete symmetry that flips the pseudospin index of the bosons. Since the pseudospin \hat{s} has the algebra of an angular momentum with $s = 1/2$, the discrete symmetry operator \mathcal{T} is properly defined and verifies the property

$$\mathcal{T}^2 = -1 \quad (5.2)$$

This will allow us to use the results of Sec. 1.3.3, in particular the Kramer's theorem, a prerequisite to the definition of the \mathbb{Z}_2 topological invariant. While this is a misnomer, we will keep the name time-reversal operator for \mathcal{T} for simplicity.

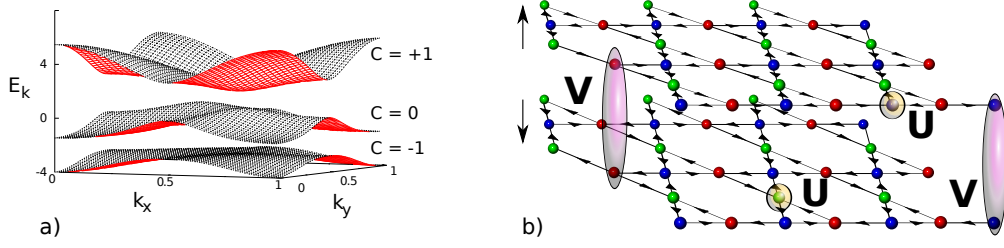


Figure 5.1: a) Band structure of the kagome lattice model with a nearest neighbor hopping phase $\varphi = \pi/4$. The three bands are separated by an energy gap, and have Chern number $C = -1, 0, +1$ respectively. b) Schematic representation of the interaction in our FTI kagome lattice system. The interaction strength is U between bosons within the same layer (identical pseudospin) and V between bosons in different layers (opposite pseudospin).

The single particle Bloch Hamiltonian for this model can be written in the form of a block matrix where the top left block acts on the particles with pseudospin up only while the bottom right block acts on the particles with pseudospin down. Time-reversal symmetry imposes on the Bloch Hamiltonian the constraint Eq. (1.97). This constrains the two diagonal blocks to be related by the relation Eq. (1.98). Taking this constraints into account, the Bloch Hamiltonian writes

$$H_R(\mathbf{k}) = \begin{pmatrix} h_{\text{CI}}(\mathbf{k}) & R \\ R^t & h_{\text{CI}}^*(-\mathbf{k}) \end{pmatrix} \begin{pmatrix} |\uparrow\rangle \\ |\downarrow\rangle \end{pmatrix} \quad (5.3)$$

The lattice has $N_s = N_x \times N_y$ unit cells with periodic boundary conditions. When interactions are switched on, the geometric aspect ratio of the system has a critical influence on the magnitude of the many-body gap, as mentioned in the case of FCIs in Sec. 4.1.2. In order to minimize this effect while studying the evolution of the gap with the system size, we follow the approach introduced used to obtain the scaling of the gap above the Laughlin state in the ruby lattice in Sec. 4.1.2 and use tilted boundary conditions. Using this technique, we choose a system geometry where the aspect ratio is very close to one for any number of unit cells N_s . In Fig. 5.2, we specify the geometry of all the systems used in this numerical study.

5.1.2 Coupling via the band structure

The off-diagonal 3×3 antisymmetric matrix R of the Bloch Hamiltonian Eq. (5.3) is a term that couples the two copies at the single-particle level. The time-reversal invariance condition forces this term to be antisymmetric

$$R = -R^t \quad (5.4)$$

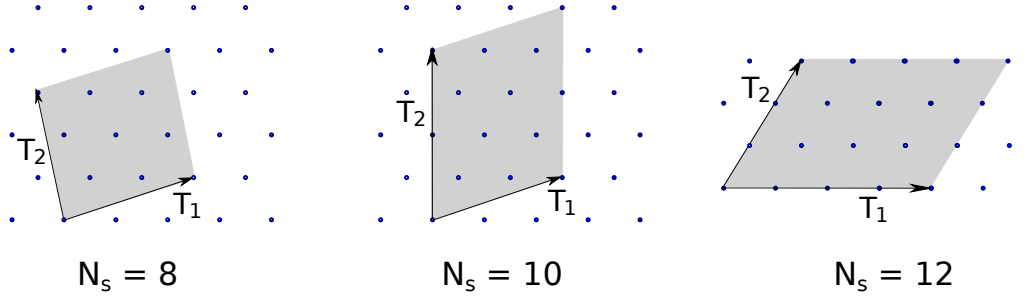


Figure 5.2: Geometry of the finite size systems used for exact diagonalization, materialized in gray on the triangular Bravais lattice. The system is periodic under any translation of the vectors \mathbf{T}_1 and \mathbf{T}_2 . For $N_s = 12$ unit cells, \mathbf{T}_1 and \mathbf{T}_2 are collinear to the Bravais lattice vectors. For $N_s = 8$ and $N_s = 10$ unit cells, we choose tilted boundary conditions (i.e. \mathbf{T}_1 and \mathbf{T}_2 are not collinear to the Bravais lattice vectors).

In realistic systems, the Rashba effect emerges from spin-orbit coupling (see Sec. 1.3.2.1), and is momentum dependent. In this article, we want to probe the effect of a term that couples the two layers at the single particle level, thus explicitly breaking the pseudospin symmetry (and, in most cases, the inversion symmetry) of the system. Since we are not tied to a physically realistic model, we will replace the Rashba term with a real, \mathbf{k} -independent matrix, to reduce the number of parameters to a minimum. Using this approximation, and the fact that $R^t = -R$, the coupling term is controlled by three parameters. We will study their influence independently. Examining how R transforms under spatial symmetry transformations shows us that there is a natural choice for one of the axes. The following coupling matrix

$$R_1 = \frac{1}{\sqrt{6}} \begin{bmatrix} 0 & 1 & -1 \\ -1 & 0 & 1 \\ 1 & -1 & 0 \end{bmatrix} \quad (5.5)$$

preserves the C_3 rotational invariance present in the kagome lattice model. For this reason, we choose R_1 to be one of the axes of the phase diagram. We define the two other directions R_2 and R_3 so that (R_1, R_2, R_3) is an orthonormal basis under the scalar product $(M, M') \rightarrow \text{Tr}(MM^t)$.

$$R_2 = \frac{1}{\sqrt{12}} \begin{bmatrix} 0 & 1 & 2 \\ -1 & 0 & 1 \\ -2 & -1 & 0 \end{bmatrix} \quad (5.6)$$

$$R_3 = \frac{1}{2} \begin{bmatrix} 0 & 1 & 0 \\ -1 & 0 & -1 \\ 0 & 1 & 0 \end{bmatrix} \quad (5.7)$$

The total coupling term as a function of the matrices R_i is given by

$$R = \alpha_1 R_1 + \alpha_2 R_2 + \alpha_3 R_3 \quad (5.8)$$

where $\alpha_1, \alpha_2, \alpha_3$ are real parameters. Note that generally, R breaks the inversion symmetry, even for $\alpha_2 = \alpha_3 = 0$. The one-body Hamiltonian has two symmetries with respect to $\alpha_1, \alpha_2, \alpha_3$ that we make explicit in the following.

– *Symmetry under the transformation $R \rightarrow -R$*

The Hamiltonians with opposite coupling terms H_R and H_{-R} are related by the following unitary transformation

$$H_R = U^\dagger H_{-R} U \quad (5.9)$$

with

$$U = \begin{bmatrix} I_3 & 0 \\ 0 & -I_3 \end{bmatrix} \quad (5.10)$$

where I_3 is the 3×3 identity matrix. Therefore the transformation $R \rightarrow -R$ is a symmetry of the Hamiltonian.

– *Symmetry under the transformation $\alpha_3 \rightarrow -\alpha_3$*

Rotating the lattice by an angle $2\pi/3$ and interchanging the sublattices 1 and 3 leaves the system invariant. In the Hamiltonian, this transformation changes the sign of α_3 . Consequently, the transformation $\alpha_3 \rightarrow -\alpha_3$ is a symmetry of the Hamiltonian.

Using both of these symmetries, we can reduce the parameter space to span by fixing the sign of two parameters. We choose $\alpha_1, \alpha_3 > 0$.

In principle, we do not expect that adding interactions to a topologically trivial insulator will create a fractional phase. Therefore, we need to address the stability of the topological phase at the single particle level before attacking the problem of the stability of a fractional topological phase. When $R = 0$, the single particle model is made of two decoupled Chern insulator copies, where one copy has a Chern number $+1$, the other -1 . According to Sec. 1.3.3.2, the decoupled model is thus a non-trivial insulator (the value of the \mathbb{Z}_2 topological invariant of the two lowest bands is one). Since R only contains real, \mathbf{k} -independent terms, increasing its strength to infinity will drive the system into a trivial phase. In the generic case ($R \neq 0$), the \mathbb{Z}_2 invariant can be effectively computed using the method developed in Ref. [180]. Fig. 5.3 shows some slices of the three dimensional phase diagram along the α_1 axis. Note that for $|\alpha_1| > 7$, our model is trivial for any value of α_2 and α_3 .

5.1.3 Form of the interaction

We consider N bosons interacting via an on-site interaction. The on-site interaction between bosons with the same pseudospin is necessary to the emergence of the double-semion phase in the decoupled limit. We note U its strength. There is also an interaction term of amplitude V between bosons with opposite pseudospins, which couples the two Laughlin copies. Unlike the tunneling term R , this term couples the two copies without breaking the pseudospin symmetry. Fig. 5.1 gives a schematic representation of this interaction. The interaction Hamiltonian writes

$$H_{\text{int}} = U \sum_{i,\sigma} : n_{i\sigma} n_{i\sigma} : + 2V \sum_i : n_{i\uparrow} n_{i\downarrow} : \quad (5.11)$$

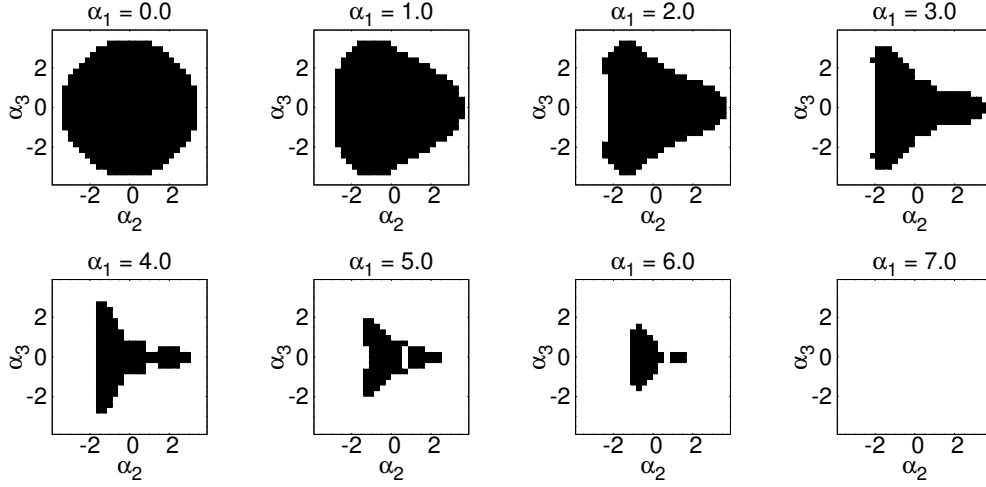


Figure 5.3: Different cuts of the single particle phase diagram along the C_3 invariant axis. The one body model is non-trivial in the black region of the phase diagram. α_1 is the amplitude of the C_3 invariant term and ranges from -7 to 7 , limits for which the kagome lattice model insulator is trivial for any value of α_2 and α_3 .

where $::$ denotes the normal ordering, and σ represents the pseudospin index (up or down). Following the same conventions as for the FCI systems, we define the filling fraction in a time-reversal symmetric topological insulator with respect to the partially filled two lowest bands, which together carry a \mathbb{Z}_2 invariant 1

$$\nu^{FTI} = \frac{N}{2N_s} \quad (5.12)$$

Note that, as already pointed out in Sec. 4.3.3.1, in conventional FQH systems, the filling fraction is usually defined with respect to the fully polarized Landau level $\nu = N/N_s = 2\nu^{FTI}$.

In Sec. 4.3.3.1, we used the flat-band limit (defined in Sec. 1.2.1.2) and projected the interaction to the lowest band (see Sec. 2.3.2) to remove the effect of band dispersion and band mixing in Chern insulators. We can define a very similar operation for a time-reversal symmetric topological insulator. The kagome lattice model with pseudospin 1/2 has six bands. The original Bloch Hamiltonian is

$$H(\mathbf{k}) = \sum_n E_n(\mathbf{k}) P_n(\mathbf{k}) \quad (5.13)$$

where $E_n(\mathbf{k})$ and $P_n(\mathbf{k})$ are the dispersion and the projector onto the n -th band, respectively. We remove the effect of dispersion by considering the flat-band Bloch Hamiltonian restricted to the two lowest bands $H(\mathbf{k}) = 1 - (P_0(\mathbf{k}) + P_1(\mathbf{k}))$. We thus consider the effective Hamiltonian:

$$H_{\text{eff}}(\mathbf{k}) = \mathcal{P}(\mathbf{k}) H_{\text{int}}(\mathbf{k}) \mathcal{P}(\mathbf{k}) \quad (5.14)$$

where $\mathcal{P}(\mathbf{k})$ is the projector onto the two lowest bands.

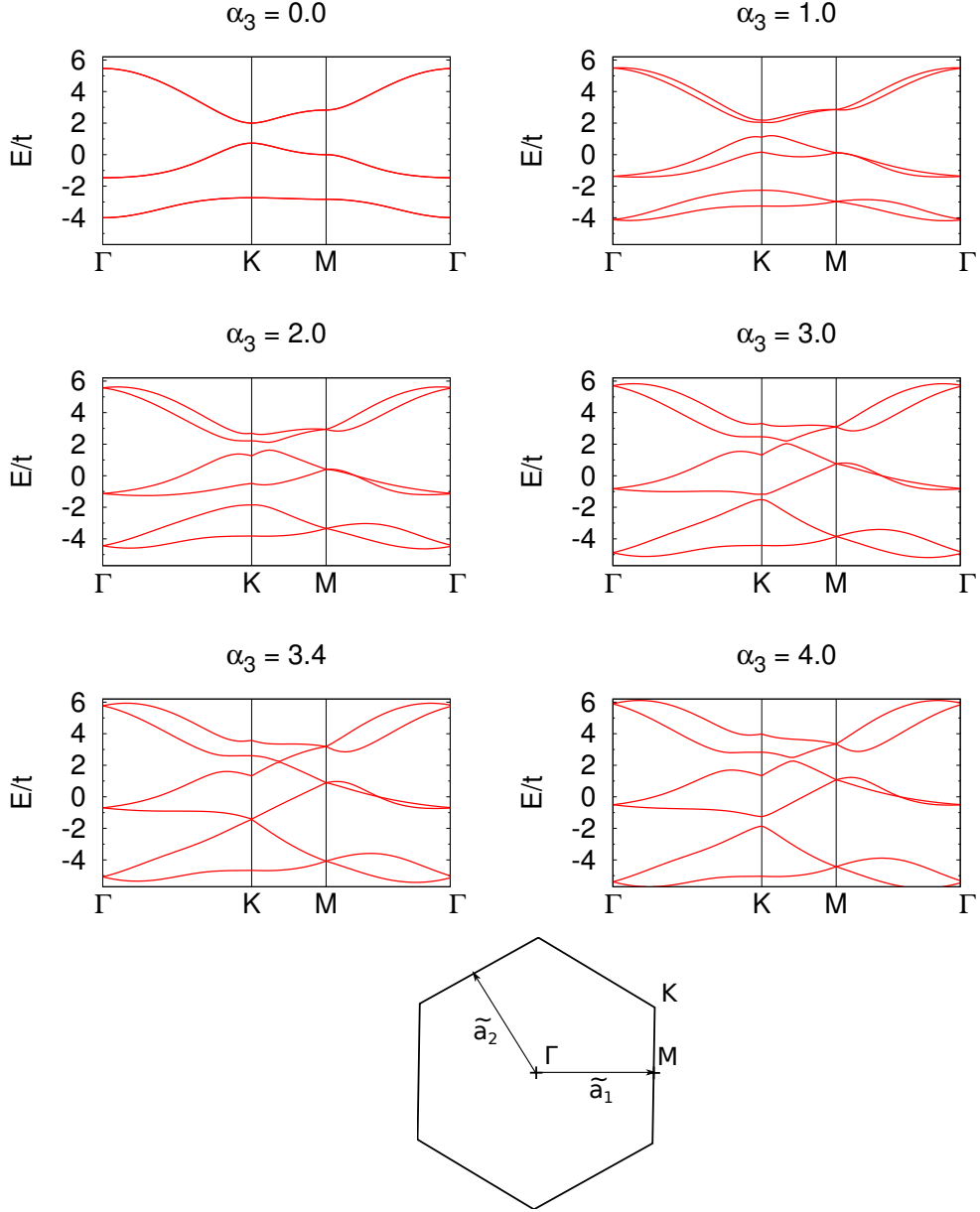


Figure 5.4: Band structure of the kagome lattice model with time-reversal symmetry along the high symmetry points Γ , K and M . The coupling term between the two kagome copies is set to $R = \alpha_3 R_3$ where R_3 is defined in Eq. (5.7). For $\alpha_3 = 0$ (decoupled kagome copies), there are three pairs of exactly degenerate bands, and the spectrum is identical to that of the single-layer kagome model. Introducing some coupling between the two kagome copies lifts this degeneracy, except at the inversion-symmetric points Γ and M . Indeed, the degeneracy of these points results from Kramer's theorem and is protected by time-reversal symmetry. The phase transition between the topological and trivial models is marked by a closing of the gap between the second and third lowest bands at $\alpha_3 \simeq 3.4$. The position of Γ , K and M in the first Brillouin zone is specified in the bottom panel. \tilde{a}_1 and \tilde{a}_2 are the reciprocal lattice vectors, such that two points related by an integer linear combination translation of these two points are equivalent.

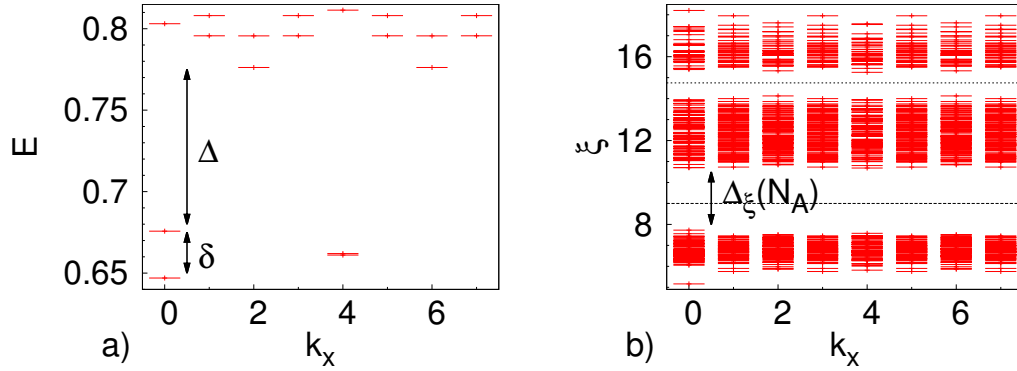


Figure 5.5: Half filling FTI phase at $N = N_s = N_x = 8$ ($N_y = 1$), in the case where there is no band structure coupling, and with an interlayer interaction of strength $V/U = 0.5$. *Left panel* Low energy spectrum. We observe an almost four-fold degenerate ground state lying in momentum sectors $(k_x, k_y) = (0, 0)$ (two states) and $(k_x, k_y) = (4, 0)$ (two states), with a gap Δ to higher excitations. The highest and lowest energy states of the ground state manifold have an energy splitting δ . *Right panel* PES of the ground state manifold, for a partition with $N_A = 4$ particles, in the sector $S_{zA} = 0$. The number of states below the lowest gap is 400. The number of states between the two dotted lines is 640. Both countings are simply related to the number of states in the PES of the FCI system with $N_\uparrow = 4$ bosons, $N_s = 8$, and $N_A^\uparrow = 2$ bosons in the A partition.

5.2 Phase diagram of a fractional topological insulator

5.2.1 Stability of the fractional phase at half filling with pseudospin conservation

5.2.1.1 Energy spectra

We first focus on systems where the two Chern insulators copies are only coupled by the interaction, and not at the band structure level ($R = 0$). We define S_z as the difference of population between the two layers:

$$S_z = \frac{N_\uparrow - N_\downarrow}{2} \quad (5.15)$$

where N_\uparrow (respectively N_\downarrow) is the number of particles with pseudospin up (respectively down). S_z is a good quantum number as long as no interlayer tunneling is allowed ($R = 0$). We diagonalize the interaction defined in Eq. (5.11). Since the interaction has been projected onto the two lowest bands, whose energies have been artificially set to 0, we can fix the value of U to 1 without loss of generality. We study the influence of the amplitude of the coupling interaction V on the low energy spectrum of the system.

When $V = 0$, the energy spectrum can be trivially deduced from the spectrum of the FCI with the same number of unit cells. Each FCI copy hosts an almost twofold

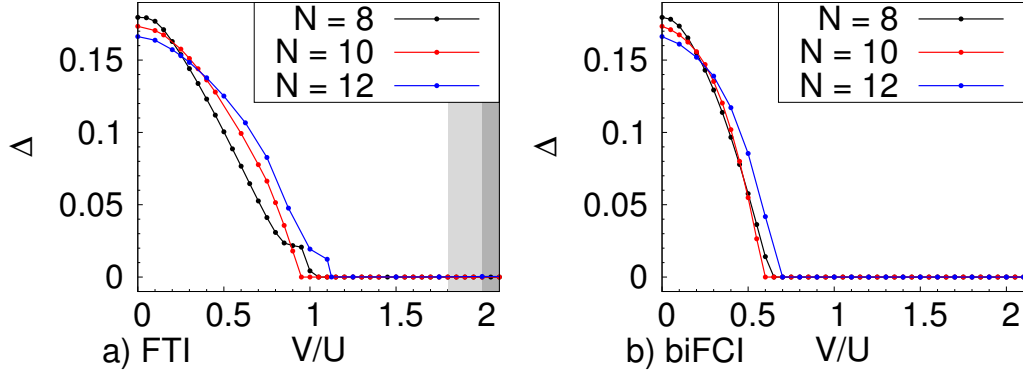


Figure 5.6: Evolution of the many-body gap of the systems with $N = 8, 10, 12$ bosons in a system with geometric aspect ratio close to one and $N_s = N$ unit cells. The gap is plotted as a function of the magnitude of the interaction between bosons of opposite pseudospin (V/U), for the time-reversal invariant FTI (a) and for the bilayer FCI (b). The shaded area in (a) corresponds to a full polarization of the FTI system, for $N = 10, 12$ (light grey) and $N = 8$ (dark grey). The bilayer FCI system only becomes fully polarized for values of V/U that are beyond the scope of this graph (the transition happens for $20 < V/U < 30$ depending on the system size).

degenerate Laughlin-like ground state manifold noted $\{\Psi_1^\sigma, \Psi_2^\sigma\}$ (where $\sigma = \uparrow, \downarrow$ is the pseudospin index). In the decoupled limit, the ground state manifold of the two copies thus consists of four almost degenerate states, which respectively write

$$\begin{cases} \Psi_1^\uparrow \otimes \Psi_1^\downarrow \\ \Psi_1^\uparrow \otimes \Psi_2^\downarrow \\ \Psi_2^\uparrow \otimes \Psi_1^\downarrow \\ \Psi_2^\uparrow \otimes \Psi_2^\downarrow \end{cases} \quad (5.16)$$

Note that due to the time-reversal symmetry, the down pseudospin wave functions are related to their up pseudospin counterparts by an operation of complex conjugation

$$\Psi_i^\downarrow = \left(\Psi_i^\uparrow\right)^* \quad i = 1, 2 \quad (5.17)$$

We call Δ the gap between the highest energy associated to this fourfold ground state and the first excitation. When we add some on-site interaction between bosons of opposite pseudospins, the gap is still clearly traceable (see Fig. 5.5a), but decreases. We plot Δ for different values of V/U (see Fig. 5.6a). We can also notice that the energy spread δ between the highest and lowest energy states of the ground state manifold increases. We keep track of the momentum sectors where the ground state manifold lies. These quantum numbers can be deduced from the ground state momentum sectors of the FCI system, which are known from the FQH on the torus

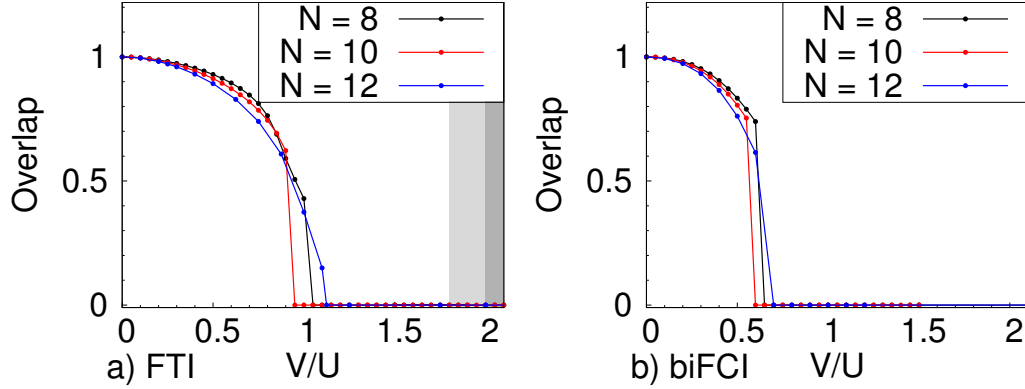


Figure 5.7: Overlap of the fourfold ground state wave function with the wave function of the decoupled system. Evolution of the overlap of the systems with $N = 8, 10, 12$ bosons and $N_s = N$ unit cells with respect to the magnitude of the interaction between bosons of opposite pseudospin (V/U), for the time-reversal invariant FTI (a) and for the bilayer FCI (b). The shaded areas correspond to the fully polarized phase as discussed in Fig. 5.6. We set the overlap to zero as soon as one of the four lowest lying states falls out of the expected momentum sectors.

through the FQH-to-FCI mapping described in Sec. 2.3.3. We set the gap to zero whenever at least one of the four lowest lying states in the spectrum does not lie in the expected momentum sector.

When V is sufficiently larger than U , it becomes more advantageous for the system to create some population imbalance between the two layers. In this case, the ground state is no longer characterized by a vanishing value of S_z , a situation which corresponds to a spontaneous breaking of the time-reversal symmetry. There is a limit where V/U is large enough that the system becomes fully polarized (all bosons occupy the same layer), as seen in Fig. 5.6a at $V/U = 1.8$ for $N = 8$ and at $V/U = 2.0$ for $N_s = 10, 12$. Our results show that the gap amplitude decreases slowly, and does not vanish until $V/U \simeq 1.0$. This suggests that the FTI phase is remarkably robust to the introduction of a coupling interaction. These results barely exhibit any finite size effect, as the range of stability does not show any significant variation from 8 to 10 to 12 particles.

We also computed the overlap of the ground state eigenvectors with the eigenvectors Eq. (5.16) of the decoupled system (see Fig. 5.7a). This shows that as long as there is a well defined ground state, the overlap remains close to 1, but drops to a value close to zero when the gap becomes smaller, thus confirming the results given in Fig. 5.6. Again, the results do not show any finite size effect.

5.2.1.2 Particle entanglement spectrum

As noted in Sec. 2.4.2, the energy spectrum alone does not allow one to distinguish a fractional topological phase from a charge density wave. Fortunately the particle

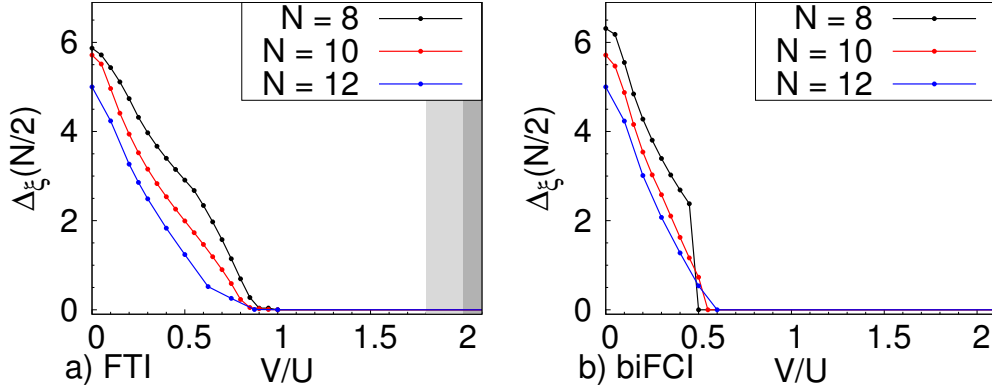


Figure 5.8: Evolution of the entanglement gap of the systems with $N = 8, 10, 12$ bosons and $N_s = N$ unit cells for a partition $N_A = N/2$, for the time-reversal invariant FTI (a) and for the bilayer FCI (b). V/U is the amplitude of the interlayer interaction. The shaded areas correspond to the fully polarized phase as discussed in Fig. 5.6.

entanglement spectrum (PES) can make this distinction. We consider a particle partition that keeps N_A particles in the reduced system, where N_A can be composed into the sum of N_A^\uparrow particles with pseudospin up and N_A^\downarrow with pseudospin down

$$N_A = N_A^\uparrow + N_A^\downarrow \quad (5.18)$$

As seen in Sec. 2.4.2, the particle partition preserves the geometrical symmetries of the original state. On top of the usual momentum quantum numbers, noted k_{xA} , k_{yA} , the population imbalance in the reduced system

$$S_{zA} = \frac{N_A^\uparrow - N_A^\downarrow}{2} \quad (5.19)$$

is also a good quantum number, as long as S_z is a good quantum number in the original system.

When the entanglement spectrum is gapped, the number of states below the gap is a signature of a given topological phase, because it is related to the number of quasihole excitations, a hallmark of the fractional phase. This statement was made in Sec. 2.4.2 and reaffirmed throughout the manuscript. Indeed, it helped us identify the composite fermion states in FCIs in Sec. 4.2.2.3, and was critical to characterize the fractional phases in $C > 1$ Chern insulators in Sec. 4.3.3.2. We expect this property to carry over to the FTI phase. We note the existence of an entanglement gap in the decoupled limit ($V = 0$). The number of states below this gap can be predicted by the number of states below the entanglement gap of the FCI PES. Let us first consider one FCI copy at half filling, say the pseudospin up FCI copy. We call $\mathcal{N}^{\text{FCI}}(N_A^\uparrow, \mathbf{k}_A^\uparrow)$ the number of states below the entanglement gap in the momentum sector $\mathbf{k}_A^\uparrow = (k_{xA}^\uparrow, k_{yA}^\uparrow)$ of this single copy. We can also define a

similar counting $\mathcal{N}^{\text{FCI}}(N_A^\downarrow, \mathbf{k}_A^\downarrow)$ for the pseudospin down FCI copy. In terms of the FCI quantum numbers, the FTI quantum numbers write:

$$k_{xA} = (k_{xA}^\uparrow - k_{xA}^\downarrow) \bmod N_x \quad (5.20)$$

$$k_{yA} = (k_{yA}^\uparrow - k_{yA}^\downarrow) \bmod N_y \quad (5.21)$$

The minus sign in Eqs. (5.20) and (5.21) comes from the time-reversal invariance of the system. It has the same origin as the sign in the one-body Hamiltonian that acts on the pseudospin down $h_{\text{CI}}^*(-\mathbf{k})$. For a given N_A and a given S_{zA} , Eqs. (5.18) and (5.19) fix the values of N_A^\uparrow and N_A^\downarrow . Naively, the FTI PES counting with a cut (N_A, S_{zA}) is thus the following in the \mathbf{k}_A sector

$$\mathcal{N}_A^{\text{FTI}}(\mathbf{k}_A) = \sum'_{\mathbf{k}_A = \mathbf{k}_A^\uparrow - \mathbf{k}_A^\downarrow} \mathcal{N}_A^{\text{FCI}}(N_A^\uparrow, \mathbf{k}_A^\uparrow) \times \mathcal{N}_A^{\text{FCI}}(N_A^\downarrow, \mathbf{k}_A^\downarrow) \quad (5.22)$$

where the sum has to be taken over all the FCI momentum sectors that satisfy the constraints of Eq. (5.20) and (5.21). The symbol \sum' means that the momentum constraint has to be taken modulo (N_x, N_y) .

As pointed out in Sec. 4.3.3.2, additional constraints can reduce the number of eigenvalues of the PES when the ground state manifold possesses an additional symmetry preserved by the particle partitioning. Here the ground state has $S_z = 0$, which results in the following constraint

$$\begin{aligned} N_A^\uparrow + N_B^\uparrow &= N^\uparrow = N/2 \\ N_A^\downarrow + N_B^\downarrow &= N^\downarrow = N/2 \end{aligned} \quad (5.23)$$

where the B indices refer to the B partition. Note that for a ground state with a degeneracy $d \neq 1$, the PES counting is not the same in partitions A and B

$$\mathcal{N}_A^{\text{FCI}}(N_A^\uparrow, \mathbf{k}_A^\uparrow) \neq \mathcal{N}_B^{\text{FCI}}(N_B^\uparrow, \mathbf{k}_B^\uparrow) \quad (5.24)$$

As a result, $\mathcal{N}_A^{\text{FTI}}(\mathbf{k}_A) \neq \mathcal{N}_B^{\text{FTI}}(\mathbf{k}_B)$, and the number of states below the gap in the FTI system reduces to

$$\mathcal{N}^{\text{FTI}} = \min(\mathcal{N}_A^{\text{FTI}}, \mathcal{N}_B^{\text{FTI}}) \quad (5.25)$$

We check that in the fully decoupled case, the PES has the expected counting. We note $\Delta_\xi(N_A)$ the smallest of the entanglement gaps in all sectors (S_{zA}, \mathbf{k}_A) (see Fig. 5.5b).

$$\Delta_\xi(N_A) = \min\{\Delta_\xi(N_A, S_{zA}, \mathbf{k}_A)\} \quad (5.26)$$

We follow the evolution of $\Delta_\xi(N_A)$ upon increasing interlayer interaction V/U . In addition to the persistence of the entanglement gap, the consistent counting below this gap with increasing V/U allows us to conclude to the stability of the FTI phase in a significant interval of V/U . In Fig. 5.8a we show the evolution of the entanglement gap for three system sizes ($N = 8, 10, 12$). We show the evolution of

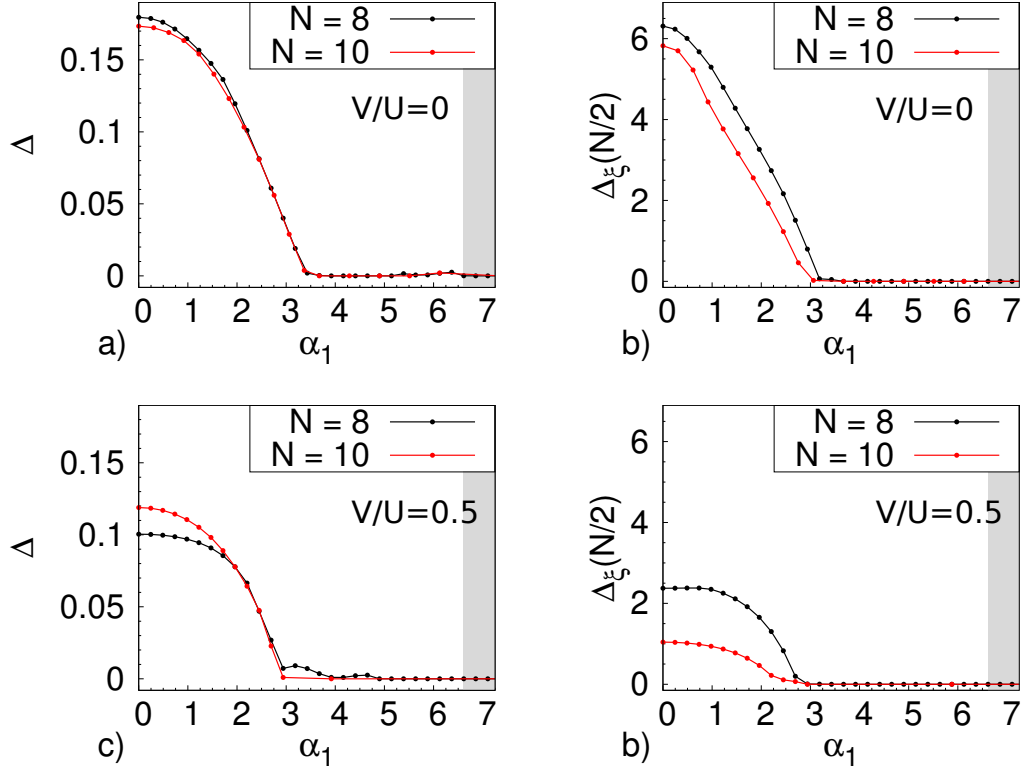


Figure 5.9: Stability of the FTI phase at half filling upon addition of a C_3 symmetry preserving coupling term of amplitude α_1 , in the absence of interlayer interaction ($V/U = 0$, a and b), and with $V/U = 0.5$ (c and d). The systems have $N = 8$ and $N = 10$ particles, $N_s = N$ unit cells. The shaded area corresponds to the region where the one-body model is a trivial insulator. a and c: Evolution of the many-body gap with α_1 . b and d: Evolution of the PES gap with α_1 , for a particle partition $N_A = N/2$.

$\Delta_\xi(N_A = N/2)$, as this gives the most conservative estimation of the stability of the phase ($N_A = N/2$ gives the smallest entanglement gap). These results confirm the topological nature of the fourfold ground state for values of the interlayer interaction up to $V/U \simeq 0.8$, with negligible finite size effects. Note that similar results were obtained in a recent paper [46] using a continuous model.

5.2.2 Stability of the fractional phase at half filling without pseudospin conservation

We now investigate the system where the two kagome lattice layers are coupled via both the interaction and the inversion symmetry breaking term R . We study here the influence of the magnitude of this coupling term on the stability of the fractional phase at half filling. S_z is no longer a good quantum number, which dras-

tically increases the computational effort compared to the situation in the previous paragraph. For instance at $N = 12$, the dimension of the largest subspace was 1.3×10^7 previously, it is now 7.0×10^7 . For $N = 10$, the dimension of the largest subspace raises from 4×10^5 to 2×10^6 . Meanwhile, we have a larger parameter space to explore, with α_1 , α_2 , α_3 , and V/U that can all vary independently. We will limit ourselves to systems with $N = 8$ and 10 particles.

We first study the stability of the topological phase in the direction $\alpha_2 = \alpha_3 = 0$, for different values of α_1 . In this case, the inversion symmetry is broken, but the C_3 rotational invariance is preserved. The evolution of the gap Δ is represented Fig. 5.9a, c for the systems with respectively $N = 8$ and $N = 10$ particles. We also compute the PES of these systems. The evolution of the entanglement gap is represented in Fig. 5.9b, d for partitions with $N_A = N/2$ particles. We use two different values of the interlayer interaction: $V/U = 0$ (a and b) and $V/U = 0.5$ (c and d). We observe that the energy gap and the entanglement gap survive in roughly the same regions (the gap closing occurs around $\alpha_1 \simeq 3.0$). Note that the energy gap Δ vanishes for similar values of α_1 for both interactions, although it takes very different values at $V/U = 0$ and $V/U = 0.5$ when $R = 0$. The stability region of the FTI lies well within the topological region of the one-body model (which is roughly $\alpha_1 \in [0, 6.5]$, as seen in Fig. 5.3). Interestingly, it covers a significant part (more than a third) of the non-interacting topological insulator stability zone.

We also look at the stability of the topological phase at half filling along two different planes: $\alpha_2 = 0$ and $\alpha_3 = 0$. We plot the gap Δ (see Fig. 5.10) and the PES gap (see Fig. 5.11) of the $N = 10$ system. The boundary between the trivial and topological regions in the one-body model is shown as a dotted line on the same graph. Again, the FTI stability regions covers a large part of the one-body TI stability zone. Phase diagrams are presented for both $V/U = 0$ and $V/U = 0.5$. We can then see how the FTI phase survives the introduction of both types of interlayer coupling (i.e. interaction and inversion symmetry breaking term) for a significant amplitude of both terms. Interestingly, the gap vanishes for similar values of α_1 , α_2 and α_3 for both values of the interaction, although for $R = 0$, the gaps at $V/U = 0$ and at $V/U = 0.5$ have very different values. Indeed, the ratio of the gaps at $V/U = 0$ and at $V/U = 0.5$ is 0.56 at $N = 8$ and 0.69 at $N = 10$. As expected, the FTI stability regions are of similar area and lie in the same zone of the phase diagram for both the $N = 8$ (not represented) and $N = 10$ (Fig. 5.10) systems. This is a good indication that the FTI phase might survive the coupling beyond the finite size case.

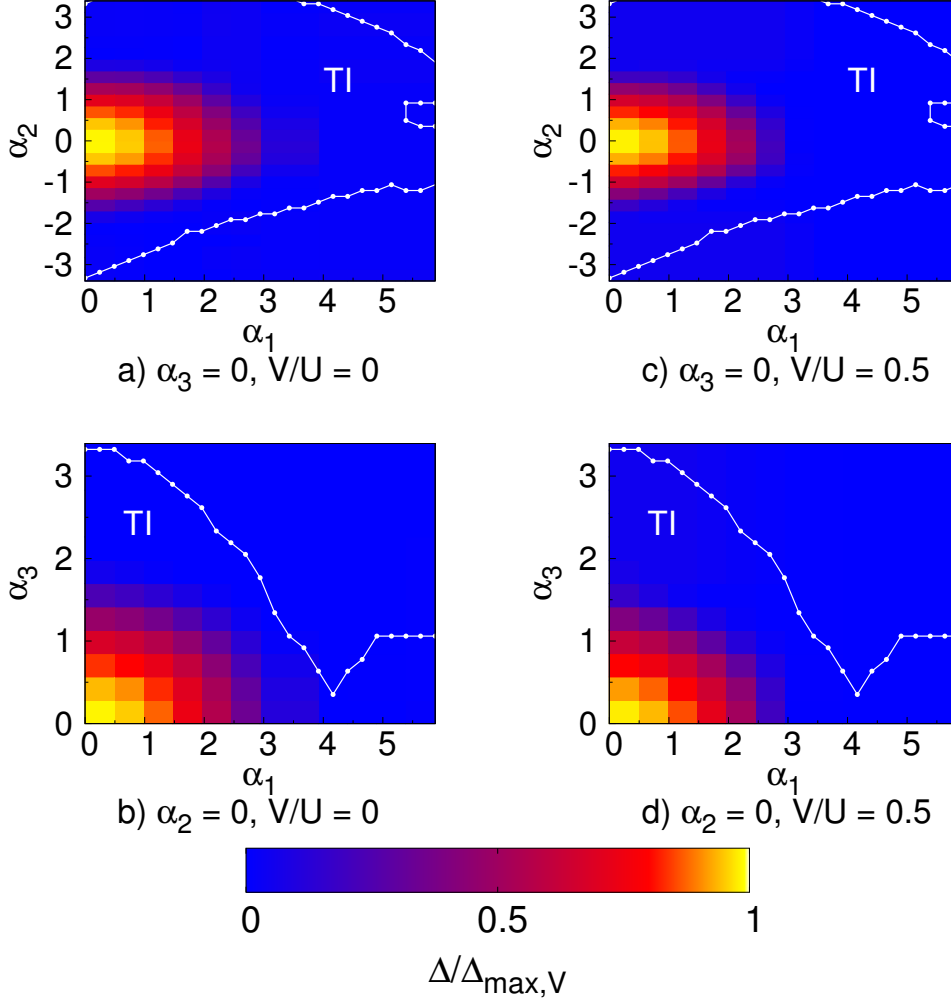


Figure 5.10: Gap of the kagome lattice model topological insulator at half filling with $N = 10$ bosons, in the plane $\alpha_3 = 0$ (a and b) and in the plane $\alpha_2 = 0$ (c and d), for $V/U = 0$ (a and c) and $V/U = 0.5$ (b and d). $\Delta_{\max,V}$ is the amplitude of the gap in the case where $R = 0$, with an interlayer interaction is V . We use the symmetries of the system with respect to the coupling elements α_i and show only the zones $\alpha_1 > 0$ and $\alpha_3 > 0$. The dotted line indicates the boundary between the trivial and topological insulator phases in the non-interacting model.

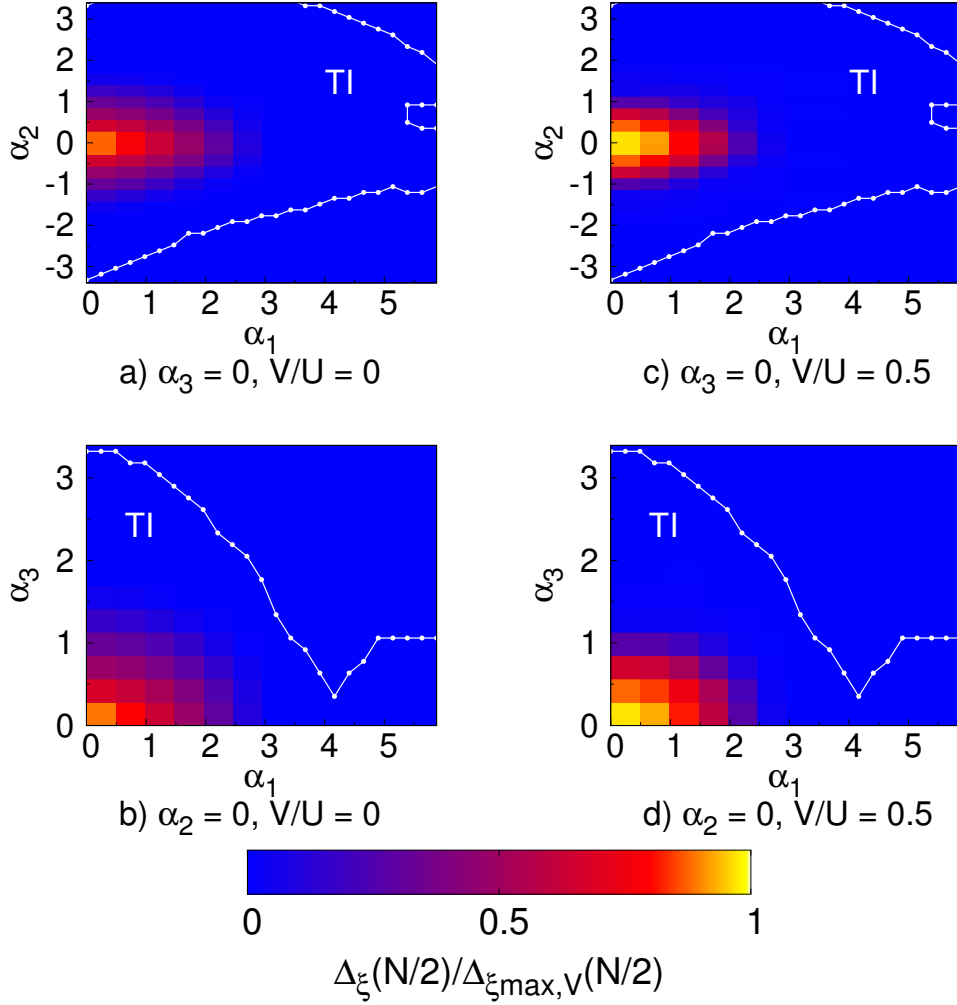


Figure 5.11: PES gap of the kagome lattice model topological insulator at half filling with $N = 10$ bosons, in the plane $\alpha_3 = 0$ (a and b) and in the plane $\alpha_2 = 0$ (c and d), for $V/U = 0$ (a and c) and $V/U = 0.5$ (b and d). $\Delta_{\xi\max,V}(N/2)$ is the amplitude of the PES gap in the case where $R = 0$, with an interlayer interaction is V). The number of particles in the partition is $N_A = 5$. We use the symmetries of the system with respect to the coupling elements α_i and show only the zones $\alpha_1 > 0$ and $\alpha_3 > 0$. The dotted line indicates the boundary between the trivial and topological insulator phases in the non-interacting model.

5.3 Transition between the time-reversal symmetric FTI and the bilayer FCI

5.3.1 The bilayer fractional Chern insulator

The study we carried out can be repeated for a system of two Chern insulators with identical chiralities for pseudospin up and down. The physics of this system is the same as the physics of the bilayer fractional quantum Hall effect. We limit ourselves to the case where S_z is a good quantum number (no interlayer tunneling term). The single-particle Hamiltonian reads

$$H_{\text{Bilayer}}(\mathbf{k}) = \begin{pmatrix} h_{\text{CI}}(\mathbf{k}) & 0 \\ 0 & h_{\text{CI}}(\mathbf{k}) \end{pmatrix} \begin{pmatrix} |\uparrow\rangle \\ |\downarrow\rangle \end{pmatrix} \quad (5.27)$$

where $h_{\text{CI}}(\mathbf{k})$ is defined in Eq. (5.1). This system breaks time-reversal symmetry. Consistently with the definition of ν^{FTI} , its filling fraction is defined with respect to the two lowest bands, and is thus different from the FQH bilayer filling fraction ν by a factor of two ($\nu^{\text{biFCI}} = \nu/2$).

The interaction Hamiltonian is unchanged and given by Eq. (5.11). At $\nu^{\text{biFCI}} = 1/2$ and $V = 0$, the ground state of the bilayer FCI is similar to the $SU(2)$ [2,0] Halperin state [64] (see Eq. (4.22)), which is fourfold degenerate on the torus. When the two layers are completely decoupled, the energy spectrum of the bilayer FCI and that of the FTI are identical, due to the inversion symmetry of the kagome lattice model. Therefore, the starting point of the stability analysis is exactly the same in both cases from an energetics perspective. For the same reasons, the PES of the two phases are also identical in the decoupled limit.

We perform exact diagonalizations on the bilayer FCI system. Again, we expect a fourfold quasidegeneracy of the ground state. We look at the many-body gap Δ , and at the ground state manifold energy splitting δ to see how well defined the ground state is. The evolution of the gap for systems with $N = 8, 10$ and 12 particles is shown Fig. 5.6b, and also exhibits negligible finite size effects. At $V/U \simeq 0.5$, it is no longer possible to distinguish a clear low energy manifold from higher energy excitations. This transition occurs near $V/U \simeq 1.0$ in the FTI system. We also looked at the overlap of the low energy manifold with the ground state of the decoupled system (see Fig. 5.7b). As expected, the overlap decreases faster in the case of a bilayer FCI than in the case of a FTI.

Note that for $V/U = 1.0$, the bilayer system recovers a full $SU(2)$ symmetry. Such a symmetry is absent in the FTI case. Indeed, the non-interacting time-reversal symmetric topological insulator breaks the $SU(2)$ symmetry, such that the FTI system is never $SU(2)$ symmetric, even when the interaction Eq. (5.11) is. This tends to indicate that the stability of the FTI is not trivially supported by the stability of the FCI phase, but rather that the time-reversal invariance plays a crucial role. We conjecture that the relative lack of stability of the bilayer FCI phase might be

explained by the emergence of a competing $SU(2)$ symmetric phase. A model wave function based on the Jain spin singlet state [107] was proposed to describe the analogous continuum FQH system at the $SU(2)$ symmetric point. Ref. [171] showed that some longer range interaction (corresponding to the V_2 Haldane pseudopotential) was required to stabilize this phase. Note that in a continuum FQH system, the $SU(2)$ symmetry is preserved by the addition of a pseudopotential interaction term V_1 coupling the bosons in different layers (the bosons in the same layer are not sensitive to this interaction, as pointed out in Sec. 2.1.2). The interaction containing both the V_0 and V_1 pseudopotentials was recently proposed to stabilize the Moore-Read state in a bilayer FQH system in Ref. [184]. However, in our model, we have not observed any coherent signature of either the Jain spin singlet or the Moore-Read state (or any ground state manifold with a well defined quasidegeneracy).

There is another striking difference between the bilayer FCI and the FTI phase diagrams at large interlayer interaction. As discussed in Sec. 5.2.1.1, at large V/U , we expect the system to be fully polarized. In the FTI case, such a transition occurs around $V/U \simeq 2$. For the bilayer FCI, the transition happens at a value that is one order of magnitude greater ($V/U = 26.4, 21.8$ and 19.6 for respectively $N = 8, 10, 12$). This is another fundamental characteristic that differentiates the phase diagrams of these two systems.

We also computed the PES of the ground state of the FCI bilayer system discussed in section 5.3.1. The number of states below the gap is the same as for the time-reversal invariant FTI, due to the inversion symmetry of the kagome lattice model. As we can see in Fig. 5.8b, $\Delta_\xi(N_A = N/2)$ decreases much faster than it does in the time-reversal symmetric case for all the system sizes that we have looked at. This confirms the results from the energy spectrum study, in so far as it gives additional evidence that the time-reversal invariance is crucial to the stability of the FTI phase.

5.3.2 Interpolation of the bilayer FCI and FTI phases

As pointed out in the previous section, when the two FCI copies are decoupled, the energy spectra of the FTI and bilayer FCI systems are identical. Moreover, when the interlayer interaction V/U is sufficiently large to obtain a fully polarized phase ($S_z = N/2$), these two systems are also equivalent. Indeed, in these conditions, the FTI hosts a chiral phase which is the same (up to an overall complex conjugation) as the phase appearing in the bilayer system. The object of this paragraph is to further reveal the symmetry between the FTI and the bilayer FCI systems by studying the transition between them. This also serves as a test of the bulk stability of the FTI phase against perturbative breaking of the time-reversal invariance. We use a real parameter λ to tune the transition at the one-body level from the time-reversal invariant system ($\lambda = 0$) to its bilayer FCI counterpart ($\lambda = 1$). Combining the Hamiltonians defined in Eqs. (5.3) and (5.27), the interpolating one-body Hamiltonian writes

$$H_\lambda(\mathbf{k}) = (1 - \lambda) H_{R=0}(\mathbf{k}) + \lambda H_{\text{Bilayer}}(\mathbf{k}) \quad (5.28)$$

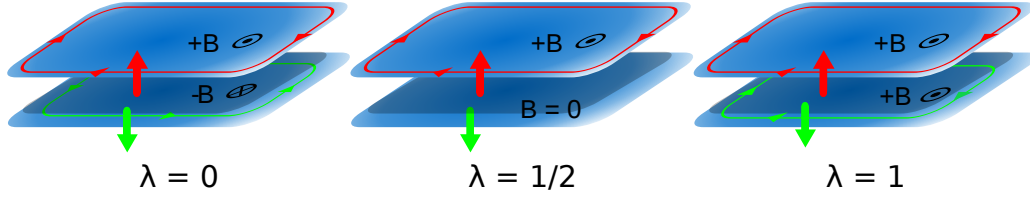


Figure 5.12: Schematic interpretation of the interpolation procedure between a FTI and a bilayer FCI system in terms of a FQH bilayer system with varying magnetic fields

Our system is similar to a bilayer FQH system where the magnetic field \mathbf{B}_\uparrow acting on the upper layer would be constant and equal to \mathbf{B} , while one would tune the magnetic field \mathbf{B}_\downarrow in the lower layer from $-\mathbf{B}$ ($\lambda = 0$) to $+\mathbf{B}$ ($\lambda = 1$) as depicted in Fig. 5.12. Note that the case $\lambda = 1/2$ corresponds to a zero magnetic field (i.e. to a topologically trivial phase) in the second layer, and thus to a phase transition of the one-body model. Although this is a convenient analogy, some difficulties would arise in the numerical implementation of this procedure in a FQH system. Indeed, one cannot tune the intensity of the magnetic field in one layer while keeping the filling fraction and the area of the system constant, as these quantities are mutually constrained. This is the major advantage of our setup based on two Chern insulators, as opposed to a continuous model such as the one used in Refs. [46, 143], where only the two extreme cases (time-reversal invariant FTI and bilayer FCI) could be studied.

The interaction Hamiltonian is unchanged and given by Eq. (5.11). We repeat the exact diagonalization study of Secs. 5.2.1.1 and 5.3.1, with varying interlayer interaction V/U and varying λ . We look at the gap Δ to see how well defined the fourfold quasidegenerate ground state is. The resulting phase diagram is given in Fig. 5.13. As expected, the decoupled system ($V/U = 0$) is invariant under the transformation $\lambda \rightarrow (1 - \lambda)$, stressing the symmetry between the FTI and the bilayer FCI phases. Interestingly, for $V/U < 0.4$, both systems are affected similarly by a change in λ ; their respective gaps close around $\lambda \simeq 0.4$ (FTI) and $\lambda \simeq 0.6$ (bilayer FCI). Once again, we observe that the FTI phase is more stable than the bilayer FCI one, as a function of both λ and V/U . Similar features can be observed in the phase diagram plotted using the system with $N = 8$ bosons.

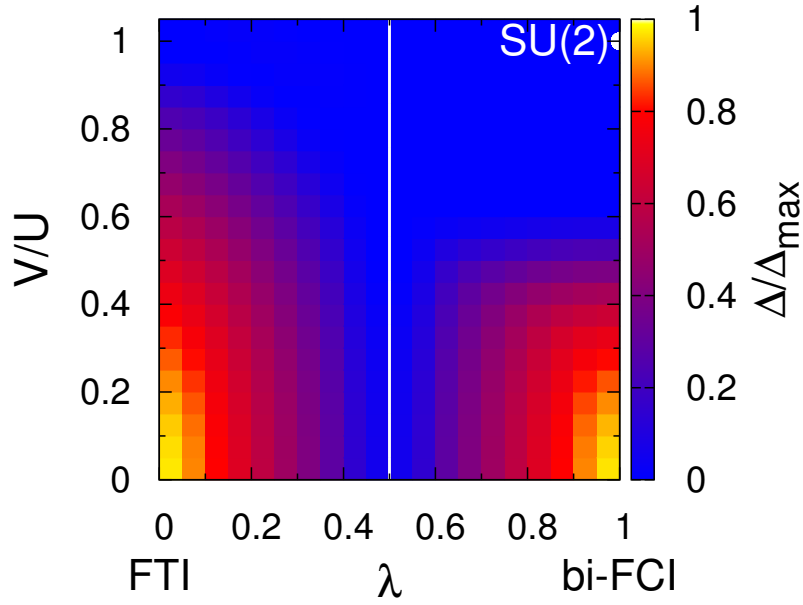


Figure 5.13: Gap of the bilayer kagome lattice system with $N = 10$ bosons undergoing a transition (parametrized by λ) from time-reversal invariant FTI (left) to the bilayer FCI phase (right), for varying values of the interlayer interaction V/U . Note that the one-body gap closes at $\lambda = 1/2$, a transition line which is marked in white on the phase diagram. The white dot marks the position of the $SU(2)$ invariant point. Δ_{\max} is the amplitude of the gap of the decoupled system with $\lambda = 0$. Along the line $V/U = 0$, the diagram is symmetric under the transformation $\lambda \rightarrow 1 - \lambda$.

Conclusion

During my PhD, I tried to determine the emergence conditions of topologically ordered phases hosting exotic fractionalized excitations. These phases may be used as qubits for decoherence-free quantum computation, a great motivation for this type of research. The fractional quantum Hall effect is so far the only experimental example of such phase, and finding other systems that support fractionalized excitations is one of the main goals of this field. While the experimental realization of fractional Chern insulators remains out of reach, their theoretical prediction in various models, and the better understanding of their emergence is a big progress in this direction.

I have studied the fractional quantum Hall effect on the torus as a guide to the physics of fractionalized phases on a genus 1 surface. I focused on the Read-Rezayi states on the torus, and in particular how they could be written starting from the Laughlin state. Given that the multilayer approach of previous works misses several of these states, I highlighted the necessity to consider a system with twisted boundary conditions, and provided a practical implementation. Indeed, unfolding this system into a single layer torus allowed me to write a very simple implementation of the projective construction, which holds in any geometry. Note that the projective construction is more than a mathematical curiosity, and suggests that non-abelian phases could be experimentally realized using multilayer abelian systems. The key is to find a realistic physical phenomenon that implements the projection: it has been proposed that coupling the layers with a tunneling or interaction term might lead to this result, but strong evidence of this phenomenon remains elusive. In any case, my results suggest that one might need to add topological defects to this multilayer description to get the full picture. Moreover, the new projective construction might have some practical consequences. The Read-Rezayi states can be written as matrix product states (MPS), a very powerful approach for the Laughlin state, but that requires a lot more effort for the higher rank members of the Read-Rezayi series. The new form of the projective construction would be rather easy to implement in the MPS language, and would allow us to write the Read-Rezayi states in a much less costly way.

I also studied the neutral low energy modes above the Laughlin and Moore-Read states on the torus, using exact diagonalization, a variational approach (the single mode approximation), and the projective construction. I used my new understanding of the single mode approximation (SMA) on the torus to generalize it to a lattice system. Interestingly, this approach introduces an additional degree of freedom that allows one to unfold the FCI Brillouin zone into a Brillouin zone similar to the FQH one, an operation that cannot be performed from the exact spectrum. Applying the single mode approximation to a FCI state yields a dispersion relation with a clear minimum. In FQH systems, this minimum is the precursor of the gap closing that occurs at the transition with the Wigner crystal phase. Studying a similar

phase transition in FCIs would be especially insightful, in particular to determine the presence or absence of a commensurability effect between the lattice spacing of the Wigner crystal and that of the underlying lattice. The SMA can be applied to a state obtained using exact diagonalization, with the limits of this technique in terms of system size. By writing a wave function for the Laughlin state on the lattice, we could also use the SMA to obtain variational magneto-roton states. Monte-Carlo simulations would then allow us to obtain the approximated low energy spectrum for much larger system sizes.

I numerically studied the emergence conditions of the composite fermion states in fractional Chern insulators, using exact diagonalizations as well as entanglement spectroscopy. This was the first observation of a fractional Chern insulator that was not in the same universality class as the Laughlin state. It brought more evidence of the great stability of fractional Chern insulators, and of the validity of the mapping between FQH and FCI quantum numbers.

I then turned to Chern insulators with a Chern number larger than one. Using similar tools, I proved that these models host phases akin to the multicomponent fractional quantum Hall effect (or Halperin states), but also phases with no equivalent in the fractional quantum Hall effect. There is a strong analogy between the $C > 1$ Chern band of a lattice system with a number of unit cells incommensurate with C and the twisted torus introduced in Chapter 3. While unfolding this torus in the presence of an $SU(C)$ symmetric interaction seems complicated, arguments based on the number of numerically observed quasihole states seem to indicate a profound relation between this phase and the Laughlin state defined on a single layer. More generally, I would like to study the realistic implementation of topological defects in interacting topological phases. Since theoretical proposals [15] exist in traditional condensed matter systems, it would be interesting to look for similar constructions in cold atoms.

Finally, I studied the stability of a fractional topological insulator with the time reversal symmetry. I showed that the double-semion phase present in the decoupled limit survived at relatively large values of the interaction coupling strength, as well as relatively large values of the tunneling term, which explicitly breaks the S_z symmetry. According to Ref. [94, 95], the double-semion phase hosts counter-propagating edge states that are topologically protected against backscattering. Exact diagonalizations are not very well suited to the simulation of open systems, because the numerically accessible systems are too small to avoid the cross-talking of the two physical edges. We thus did not study the stability of edge states in our model. This question will necessitate the development of new numerical tools, such as methods based on the density matrix renormalization group (DMRG), which are better at simulating systems with a cylinder geometry. For two-dimensional systems, this technique allows to consider long (or even infinite) cylinders with a moderate perimeter. Using entanglement measurement, we may unveil the edge information encoded in the bulk of the system. We may thus hope to see a signature of the two counter-propagating edge modes, as was recently done in the context of the bosonic integer quantum Hall effect [68].

Fourier transform of the density operator on the torus projected onto the lowest Landau level

We consider a quantum Hall system defined on a rectangular torus T of lengths $L_x \times L_y$. In real space, the density operator projected onto the lowest Landau level writes

$$\hat{\rho}(\mathbf{r}) = \sum_{0 \leq j, j' < N_\phi} \Phi_{0,j}^*(x, y) \Phi_{0,j'}(x, y) c_j^\dagger c_{j'} \quad (\text{A.1})$$

where $\Phi_{0,j}(x, y)$ is the wave function describing a single-particle with momentum $2\pi j/L_y$ in the lowest Landau level. Using Eq. (1.45) with $n = 0$, $\Phi_{0,j}(x, y)$ writes

$$\Phi_{0,j}(x, y) = \mathcal{N}_0 \sum_{m=-\infty}^{\infty} e^{i \frac{(l_B^2 2\pi j / L_y + m L_x) y}{l_B^2}} e^{-\frac{1}{2l_B^2} (l_B^2 2\pi j / L_y + m L_x - x)^2} \quad (\text{A.2})$$

The component $\mathbf{k} = (\frac{2\pi k_x}{L_x}, \frac{2\pi k_y}{L_y})$ (k_x and k_y integers) of the Fourier transform of the projected density operator thus writes (up to some normalization factor)

$$\begin{aligned} \hat{\rho}_{\mathbf{k}} &= \int_T dx dy e^{-i \frac{2\pi k_x x}{L_x}} e^{-i \frac{2\pi k_y y}{L_y}} \sum_{j, j'=1}^{N_\phi} \Phi_{0,j}^*(x, y) \Phi_{0,j'}(x, y) c_j^\dagger c_{j'} \\ &= \int_T dx dy e^{-i \frac{2\pi k_x x}{L_x}} e^{-i \frac{2\pi k_y y}{L_y}} \\ &\quad \sum_{0 \leq j, j' < N_\phi} \sum_{m, m'=-\infty}^{\infty} \left(e^{i \frac{2\pi y}{L_y} \left((j'-j) + (m'-m) \frac{L_x L_y}{2\pi l_B^2} \right)} \right. \\ &\quad \left. e^{-\frac{1}{2l_B^2} \left((l_B^2 2\pi j / L_y + m L_x - x)^2 + (l_B^2 2\pi j' / L_y + m' L_x - x)^2 \right)} c_j^\dagger c_{j'} \right) \end{aligned} \quad (\text{A.3})$$

where c_j and c_j^\dagger respectively annihilate and create a particle in orbital j . We first compute the integral I_y over the coordinate y . We can use the quantification of the number of magnetic fluxes on the rectangular torus $L_x L_y = 2\pi N_\phi l_B^2$ (see Eq. (1.43)) to express it as

$$\begin{aligned} I_y &= \int_0^{L_y} dy e^{i \frac{2\pi y}{L_y} (j'-j + (m'-m) N_\phi - k_y)} \\ &= L_y \delta_{j'-j + (m'-m) N_\phi - k_y, 0} \end{aligned} \quad (\text{A.4})$$

where δ is the Kronecker symbol. Next, we use the identity

$$a^2 + b^2 = \frac{1}{2} ((a+b)^2 + (a-b)^2) \quad (\text{A.5})$$

which is valid for any two real numbers a and b , to write the argument of the Gaussian factor in Eq. (A.3) as

$$\begin{aligned} & -\frac{1}{2l_B^2} \left[(l_B^2 \frac{2\pi}{L_y} j + mL_x - x)^2 + (l_B^2 \frac{2\pi}{L_y} j' + m'L_x - x)^2 \right] \\ & = -\frac{1}{4l_B^2} \left[4 \left(l_B^2 \frac{2\pi}{L_y} (j + k_y/2) + mL_x - x \right)^2 + \left(l_B^2 \frac{2\pi}{L_y} k_y \right)^2 \right] \end{aligned} \quad (\text{A.6})$$

where we have used the constraint $j' - j + (m' - m)N_\phi - k_y = 0$ from Eq. (A.4). The Fourier transform of the density operator thus writes

$$\hat{\rho}_{\mathbf{k}} = \mathcal{N}_0^2 e^{-\frac{l_B^2}{4} \left(\frac{2\pi k_y}{L_y} \right)^2} \sum_{0 \leq j < N_\phi} \int_0^{L_x} dx e^{-i \frac{2\pi k_x x}{L_x}} \sum_{m=-\infty}^{\infty} e^{-\frac{1}{l_B^2} \left(l_B^2 \frac{2\pi}{L_y} (j + k_y/2) + mL_x - x \right)^2} c_j^\dagger c_{j+k_y} \quad (\text{A.7})$$

The sum over m can be absorbed into the integral by expanding the integration interval to \mathbb{R} , and since $e^{-i2\pi k_x m} = 1$, this yields

$$\hat{\rho}_{\mathbf{k}} = \mathcal{N}_0^2 e^{-\frac{l_B^2}{4} \left(\frac{2\pi k_y}{L_y} \right)^2} \sum_{0 \leq j < N_\phi} \int_{-\infty}^{+\infty} dx e^{-i \frac{2\pi k_x x}{L_x}} e^{-\frac{1}{l_B^2} \left(\frac{2\pi l_B^2}{L_y} (j + k_y/2) - x \right)^2} c_j^\dagger c_{j+k_y} \quad (\text{A.8})$$

We recognize the Fourier transform of a Gaussian, which is equal to

$$\hat{\rho}_{\mathbf{k}} = \mathcal{N}_0^2 e^{-\frac{l_B^2}{4} \left(\frac{2\pi k_y}{L_y} \right)^2} e^{-\frac{l_B^2}{4} \left(\frac{2\pi k_x}{L_x} \right)^2} \sum_{0 \leq j < N_\phi} e^{-\frac{i2\pi k_x}{N_\phi} (j + k_y/2)} c_j^\dagger c_{j+k_y} \quad (\text{A.9})$$

In conclusion, the Fourier transform of the projected density operator writes

$$\hat{\rho}_{\mathbf{k}} = \mathcal{N}_0^2 e^{-\frac{l_B^2}{4} \mathbf{k}^2} \sum_{0 \leq j < N_\phi} e^{-\frac{i2\pi k_x}{N_\phi} (j + k_y/2)} c_j^\dagger c_{j+k_y} \quad (\text{A.10})$$

Factorization of the three-body contact interaction

The three-body hard core Hamiltonian writes

$$H = \sum_{\mathbf{q}_1, \mathbf{q}_2} : \hat{\rho}_{\mathbf{q}_1} \hat{\rho}_{\mathbf{q}_2} \hat{\rho}_{-(\mathbf{q}_1 + \mathbf{q}_2)} : \quad (\text{B.1})$$

where $\hat{\rho}_{\mathbf{q}}$ is the $\mathbf{q}_i = \left(\frac{2\pi s_i}{L_x}, \frac{2\pi t_i}{L_y}\right)$ component of the Fourier transform of the density operator projected onto the lowest Landau level. Using the expression (A.10) of $\hat{\rho}_{\mathbf{q}}$ derived in Appendix A, and setting $l_B = 1$, we can write

$$\begin{aligned} V_{j_1 \dots j_6} &= \sum_l \delta_{j_1 + j_2 + j_3, j_4 + j_5 + j_6 + lN_\phi} \\ &\sum_{s_1, s_2, t_1, t_2} \left\{ e^{-\frac{1}{2} \left(\frac{2\pi}{L_x}\right)^2 (s_1^2 + s_2^2 + s_1 s_2)} e^{-\frac{1}{2} \left(\frac{2\pi}{L_y}\right)^2 (t_1^2 + t_2^2 + t_1 t_2)} \right. \\ &\quad e^{-\frac{2\pi i}{N_\phi} \left[s_1(j_1 + \frac{t_1}{2}) + s_2(j_2 + \frac{t_2}{2}) - (s_1 + s_2)(j_3 - \frac{t_1 + t_2}{2}) \right]} \\ &\quad \left. \times \sum_{\tilde{t}_1 \tilde{t}_2} \delta_{j_4 - j_1, t_1 + \tilde{t}_1 N_\phi} \delta_{j_5 - j_2, t_2 + \tilde{t}_2 N_\phi} \right\} \end{aligned} \quad (\text{B.2})$$

The interaction can be reexpressed

$$\begin{aligned} V_{j_1 \dots j_6} &= \sum_l \delta_{j_1 + j_2 + j_3, j_4 + j_5 + j_6 + lN_\phi} \\ &\sum_{s_1, s_2, t_1, t_2} \left\{ e^{-\frac{1}{2} \left(\frac{2\pi}{L_x}\right)^2 (s_1^2 + s_2^2 + s_1 s_2)} e^{-\frac{1}{2} \left(\frac{2\pi}{L_y}\right)^2 (t_1^2 + t_2^2 + t_1 t_2)} \right. \\ &\quad e^{-\frac{2\pi i}{N_\phi} [s_1(j_4 - j_3 + t_2/2)]} \\ &\quad e^{-\frac{2\pi i}{N_\phi} [s_2(j_5 - j_3 + t_1/2)]} \\ &\quad \left. \times \sum_{\tilde{t}_1 \tilde{t}_2} \delta_{j_4 - j_1, t_1 - \tilde{t}_1 N_\phi} \delta_{j_5 - j_2, t_2 - \tilde{t}_2 N_\phi} \right\} \end{aligned} \quad (\text{B.3})$$

To rewrite the sum over s_1 and s_2 , we use the Poisson summation formula

$$\sum_{n=-\infty}^{\infty} f(n) = \sum_{\tilde{n}=-\infty}^{\infty} \int_{-\infty}^{\infty} dx f(x) e^{-i2\pi \tilde{n}x} \quad (\text{B.4})$$

The sum over s_1 and s_2 becomes

$$\sum_{\tilde{s}_1, \tilde{s}_2} \int ds_1 ds_2 \left\{ e^{-\frac{1}{2} \left(\frac{2\pi}{L_x} \right)^2 (s_1^2 + s_2^2 + s_1 s_2)} e^{-\frac{2\pi i}{N_\phi} [s_1(j_4 - j_3 + t_2/2)]} e^{-2\pi i s_1 \tilde{s}_1} e^{-\frac{2\pi i}{N_\phi} [s_2(j_5 - j_3 + t_1/2)]} e^{-2\pi i s_2 \tilde{s}_2} \right\} \quad (\text{B.5})$$

$s_1^2 + s_2^2 + s_1 s_2$ is the square norm of a vector \mathbf{s} of coordinates s_1 and s_2 , on a plane spanned by two basis vectors forming an angle of $\pi/3$ radians. A change of coordinates to an orthonormal basis allows us to separate the Gaussian factors. We call (a, b) the coordinates of \mathbf{s} in the new basis, such that

$$s_1^2 + s_2^2 + s_1 s_2 = \|\mathbf{s}\|^2 = a^2 + b^2 \quad (\text{B.6})$$

We choose the following a and b :

$$a = s_1 \cos \frac{\pi}{12} + s_2 \sin \frac{\pi}{12} \quad (\text{B.7})$$

$$b = s_1 \sin \frac{\pi}{12} + s_2 \cos \frac{\pi}{12} \quad (\text{B.8})$$

Conversely,

$$s_1 = \frac{2}{\sqrt{3}} \left(a \cos \frac{\pi}{12} - b \sin \frac{\pi}{12} \right) \quad (\text{B.9})$$

$$s_2 = -\frac{2}{\sqrt{3}} \left(a \sin \frac{\pi}{12} - b \cos \frac{\pi}{12} \right) \quad (\text{B.10})$$

where we have used the identity

$$(\cos \frac{\pi}{12})^2 - (\sin \frac{\pi}{12})^2 = \frac{\sqrt{3}}{2} \quad (\text{B.11})$$

Eq. B.5 becomes

$$\begin{aligned} \sum_{\tilde{s}_1, \tilde{s}_2} \int da \, e^{-\frac{2\pi}{N_\phi} \frac{2}{\sqrt{3}} a \left(\cos \frac{\pi}{12} (j_4 - j_3 + t_2/2) - \sin \frac{\pi}{12} (j_5 - j_3 + t_1/2) \right)} \\ e^{-2\pi \frac{2}{\sqrt{3}} a \left(\cos \frac{\pi}{12} \tilde{s}_1 - \sin \frac{\pi}{12} \tilde{s}_2 \right)} e^{-\frac{1}{2} \left(\frac{2\pi}{L_x} \right)^2 a^2} \\ \int db \, e^{-\frac{2\pi}{N_\phi} \frac{2}{\sqrt{3}} b \left(-\sin \frac{\pi}{12} (j_4 - j_3 + t_2/2) + \cos \frac{\pi}{12} (j_5 - j_3 + t_1/2) \right)} \\ e^{-2\pi \frac{2}{\sqrt{3}} b \left(-\sin \frac{\pi}{12} \tilde{s}_1 + \cos \frac{\pi}{12} \tilde{s}_2 \right)} e^{-\frac{1}{2} \left(\frac{2\pi}{L_x} \right)^2 b^2} \end{aligned}$$

where the integrals over a and b are decoupled and are each the Fourier transform of a Gaussian, thus respectively equal to

$$\begin{aligned} e^{-\frac{2L_x^2}{3} \left(\left(\tilde{s}_1 + \frac{1}{N_\phi} (j_4 - j_3 + t_2/2) \right) \cos \frac{\pi}{12} - \left(\tilde{s}_2 + \frac{1}{N_\phi} (j_5 - j_3 + t_1/2) \right) \sin \frac{\pi}{12} \right)^2} \\ e^{-\frac{2L_x^2}{3} \left(-\left(\tilde{s}_1 + \frac{1}{N_\phi} (j_4 - j_3 + t_2/2) \right) \sin \frac{\pi}{12} + \left(\tilde{s}_2 + \frac{1}{N_\phi} (j_5 - j_3 + t_1/2) \right) \cos \frac{\pi}{12} \right)^2} \end{aligned}$$

This product of two Gaussian factors can be simplified into

$$e^{-A^2} e^{-B^2} e^{+AB} \quad (\text{B.12})$$

where

$$\begin{aligned} A &= L_x \sqrt{\frac{2}{3}} \left(\tilde{s}_1 + \frac{1}{N_\phi} (j_4 - j_3 + t_2/2) \right) \\ B &= L_x \sqrt{\frac{2}{3}} \left(\tilde{s}_2 + \frac{1}{N_\phi} (j_5 - j_3 + t_1/2) \right) \end{aligned} \quad (\text{B.13})$$

and we have used the identity

$$\cos \frac{\pi}{12} \sin \frac{\pi}{12} = 1/4 \quad (\text{B.14})$$

The expression B.12 can in turn be transformed into

$$e^{-\frac{1}{3}(2A-B)^2} e^{-\frac{1}{3}(2B-A)^2} e^{-\frac{1}{3}(2A-B)(2B-A)} \quad (\text{B.15})$$

After these simplifications, the interaction reads

$$\begin{aligned} V_{j_1 \dots j_6} &\propto \sum_l \delta_{j_1+j_2+j_3, j_4+j_5+j_6+lN_\phi} \\ &\sum_{t_1, t_2} e^{-\frac{1}{2}(X_{t_1}^2 + X_{t_2}^2 + X_{t_1} X_{t_2})} \\ &\sum_{\tilde{s}_1, \tilde{s}_2} e^{-\frac{2}{9}Y^2} e^{-\frac{2}{9}Z^2} e^{-\frac{2}{9}YZ} \\ &\times \sum_{\tilde{t}_1 \tilde{t}_2} \delta_{j_4-j_1, t_1-\tilde{t}_1 N_\phi} \delta_{j_5-j_2, t_2-\tilde{t}_2 N_\phi} \end{aligned} \quad (\text{B.16})$$

where

$$\begin{aligned} Y &= ((2\tilde{s}_1 - \tilde{s}_2)L_x + 2X_{j_4} - X_{j_3} - X_{j_5} + X_{t_2} - X_{t_1}/2) \\ Z &= ((2\tilde{s}_2 - \tilde{s}_1)L_x + 2X_{j_5} - X_{j_3} - X_{j_4} + X_{t_1} - X_{t_2}/2) \end{aligned}$$

and we have used the notation $X_j = \frac{2\pi j}{L_y}$. Finally, we note the identity

$$\begin{aligned} &\frac{2}{9}(Y^2 + Z^2 + YZ) + \frac{1}{2}(X_{t_1}^2 + X_{t_2}^2 + X_{t_1} X_{t_2}) \\ &= \frac{1}{9} \left((Y + \frac{3}{2}X_{t_1})^2 + (Z + \frac{3}{2}X_{t_2})^2 + (Y + \frac{3}{2}X_{t_1})(Z + \frac{3}{2}X_{t_2}) \right. \\ &\quad \left. + (Y - \frac{3}{2}X_{t_1})^2 + (Z - \frac{3}{2}X_{t_2})^2 + (Y - \frac{3}{2}X_{t_1})(Z - \frac{3}{2}X_{t_2}) \right) \end{aligned} \quad (\text{B.17})$$

Using this identity allows us to separate creation and annihilation indexes in the expression of the interaction

$$\begin{aligned} V_{j_1 \dots j_6} &\propto \sum_l \delta_{j_1+j_2+j_3, j_4+j_5+j_6+lN_\phi} \\ &\sum_{\tilde{s}_1, \tilde{s}_2} \sum_{\tilde{t}_1, \tilde{t}_2} e^{-A_0^2} e^{-A_1^2} e^{-A_0 A_1} e^{-A_0'^2} e^{-A_1'^2} e^{-A_0' A_1'} \end{aligned} \quad (\text{B.18})$$

where

$$\begin{aligned}
 A_0 &= \frac{1}{3} \left(\underbrace{(2\tilde{s}_1 - \tilde{s}_2 + \tilde{t}_2 - 2\tilde{t}_1)}_{k_r} L_x + 2X_{j_1} - X_{j_3} - X_{j_2} \right) \\
 A_1 &= \frac{1}{3} \left(\underbrace{(2\tilde{s}_2 - \tilde{s}_1 + \tilde{t}_1 - 2\tilde{t}_2)}_{k_s} L_x + 2X_{j_2} - X_{j_1} - X_{j_2} \right) \\
 A'_0 &= \frac{1}{3} \left(\underbrace{(2\tilde{s}_1 - \tilde{s}_2 + \tilde{t}_1 + \tilde{t}_2)}_{k'_r} L_x + lL_x + 2X_{j_4} - X_{j_5} - X_{j_6} \right) \\
 A'_1 &= \frac{1}{3} \left(\underbrace{(2\tilde{s}_2 - \tilde{s}_1 + \tilde{t}_1 + \tilde{t}_2)}_{k'_s} L_x + lL_x + 2X_{j_5} - X_{j_4} - X_{j_6} \right)
 \end{aligned}$$

The sum over $\tilde{s}_1, \tilde{s}_2, \tilde{t}_1, \tilde{t}_2$ can be replaced by a sum over k_r, k_s, k'_r, k'_s where all of these indexes must have the same rest in the euclidean division by 3.

$$\begin{aligned}
 V_{j_1 \dots j_6} &\propto \sum_l \delta_{j_1+j_2+j_3, j_4+j_5+j_6+lN_\phi} \\
 &\sum_{g=0,1,2} \left\{ \sum_{k_r, k_s=g \bmod 3} e^{-A_0^2} e^{-A_1^2} e^{-A_0 A_1} \right. \\
 &\quad \left. \sum_{k'_r, k'_s=g \bmod 3} e^{-A_0'^2} e^{-A_1'^2} e^{-A'_0 A'_1} \right\}
 \end{aligned} \tag{B.19}$$

A similar procedure can be used to factorize the hard core interaction of an arbitrary number n of bosons. We give here the result of this factorization without demonstration. For n particles with momenta $X_{j_1} \dots X_{j_n}$, the relative momentum of the particle i writes

$$\tilde{X}_{j_i} = X_{j_i} - \frac{1}{n} \sum_{l=1}^n X_{j_l} \tag{B.20}$$

For a generic n -body contact interaction, the factorized interaction coefficient writes:

$$\begin{aligned}
 V_{j_1 \dots j_{2n}} &\propto \sum_l \delta_{(j_1 + \dots + j_n), (j_{n+1} + \dots + j_{2n} + lN_\phi)} \\
 &\sum_{g=0,1, \dots, n-1} \left\{ \left(\sum_{k_{r_1}=g \bmod n} \dots \sum_{k_{r_{n-1}}=g \bmod n} \left[\prod_{0 \leq i \leq j}^{n-2} e^{-A_i A_j} \right] \right) \right. \\
 &\quad \times \left. \left(\sum_{k'_{r_1}=g \bmod n} \dots \sum_{k'_{r_{n-1}}=g \bmod n} \left[\prod_{0 \leq i \leq j}^{n-2} e^{-A'_i A'_j} \right] \right) \right\}
 \end{aligned} \tag{B.21}$$

where A_i and A'_i can be written using the relative momentum \tilde{X}_{j_i} of each particle

$$\begin{aligned} A_i &= \frac{1}{N} \left(k_{r_i} L_x + N \tilde{X}_{j_i} \right) \\ A'_i &= \frac{1}{N} \left((k'_{r_i} + l) L_x + N \tilde{X}_{j_{i+N}} \right) \end{aligned} \tag{B.22}$$

Bibliography

- [1] M. Aidelsburger, M. Atala, S. Nascimbène, S. Trotzky, Y.-A. Chen, and I. Bloch. Experimental realization of strong effective magnetic fields in an optical lattice. *Phys. Rev. Lett.*, 107:255301, Dec 2011. (Cited on page 27.)
- [2] M. Aidelsburger, M. Lohse, C. Schweizer, M. Atala, J. T. Barreiro, S. Nascimbène, N. R. Cooper, I. Bloch, and N. Goldman. Measuring the Chern number of Hofstadter bands with ultracold bosonic atoms. *Nature Physics*, 11:162–166, Feb. 2015. (Cited on pages 15, 27, 28, 29, 30 and 31.)
- [3] S. An, P. Jiang, H. Choi, W. Kang, S. H. Simon, L. N. Pfeiffer, K. W. West, and K. W. Baldwin. Braiding of Abelian and Non-Abelian Anyons in the Fractional Quantum Hall Effect. *ArXiv e-prints*, Dec. 2011. (Cited on page 58.)
- [4] P. Anderson. More is different. *Science*, 177(4047):393–396, 1972. (Cited on page xi.)
- [5] E. Ardonne, N. Read, E. Rezayi, and K. Schoutens. Non-abelian spin-singlet quantum Hall states: wave functions and quasihole state counting. *Nuclear Physics B*, 607:549–576, July 2001. (Cited on page 128.)
- [6] E. Ardonne and K. Schoutens. New class of non-abelian spin-singlet quantum hall states. *Phys. Rev. Lett.*, 82:5096–5099, Jun 1999. (Cited on page 128.)
- [7] D. Arovas, J. R. Schrieffer, and F. Wilczek. Fractional statistics and the quantum hall effect. *Phys. Rev. Lett.*, 53:722–723, Aug 1984. (Cited on pages 51 and 56.)
- [8] J. E. Avron, R. Seiler, and B. Simon. Homotopy and quantization in condensed matter physics. *Phys. Rev. Lett.*, 51:51–53, Jul 1983. (Cited on page 30.)
- [9] H. Bachmair, E. O. Göbel, G. Hein, J. Melcher, B. Schumacher, J. Schurr, L. Schweitzer, and P. Warnecke. The von klitzing resistance standard. *Physica E: Low-dimensional Systems and Nanostructures*, 20(1-2):14 – 23, 2003. Proceedings of the International Symposium "Quantum Hall Effect: Past, Present and Future". (Cited on page 3.)
- [10] M. Baraban, G. Zikos, N. Bonesteel, and S. H. Simon. Numerical analysis of quasiholes of the moore-read wave function. *Phys. Rev. Lett.*, 103:076801, Aug 2009. (Cited on page 58.)
- [11] M. Barkeshli, P. Bonderson, M. Cheng, and Z. Wang. Symmetry, Defects, and Gauging of Topological Phases. *ArXiv e-prints*, Oct. 2014. (Cited on page 83.)

- [12] M. Barkeshli, C.-M. Jian, and X.-L. Qi. Classification of topological defects in abelian topological states. *Phys. Rev. B*, 88:241103, Dec 2013. (Cited on page 83.)
- [13] M. Barkeshli, C.-M. Jian, and X.-L. Qi. Theory of defects in abelian topological states. *Phys. Rev. B*, 88:235103, Dec 2013. (Cited on page 83.)
- [14] M. Barkeshli, C.-M. Jian, and X.-L. Qi. Twist defects and projective non-abelian braiding statistics. *Phys. Rev. B*, 87:045130, Jan 2013. (Cited on page 83.)
- [15] M. Barkeshli, Y. Oreg, and X.-L. Qi. Experimental Proposal to Detect Topological Ground State Degeneracy. *ArXiv e-prints*, Jan. 2014. (Cited on page 160.)
- [16] M. Barkeshli and X.-L. Qi. Topological nematic states and non-abelian lattice dislocations. *Phys. Rev. X*, 2:031013, Aug 2012. (Cited on page 125.)
- [17] M. Barkeshli and X.-G. Wen. Anyon Condensation and Continuous Topological Phase Transitions in Non-Abelian Fractional Quantum Hall States. *Phys. Rev. Lett.*, 105(21):216804, Nov. 2010. (Cited on page xiv.)
- [18] A. Belavin, A. Polyakov, and A. Zamolodchikov. Infinite conformal symmetry in two-dimensional quantum field theory. *Nuclear Physics B*, 241(2):333 – 380, 1984. (Cited on page 57.)
- [19] E. J. Bergholtz and Z. Liu. Topological Flat Band Models and Fractional Chern Insulators. *International Journal of Modern Physics B*, 27:30017, Sept. 2013. (Cited on page 68.)
- [20] B. Bernevig and T. Hughes. In *Topological Insulators and Topological Superconductors*. Princeton University Press, 2013. (Cited on pages 18 and 139.)
- [21] B. A. Bernevig and F. D. M. Haldane. Generalized clustering conditions of jack polynomials at negative jack parameter α . *Phys. Rev. B*, 77:184502, May 2008. (Cited on pages 62 and 79.)
- [22] B. A. Bernevig and F. D. M. Haldane. Model fractional quantum hall states and jack polynomials. *Phys. Rev. Lett.*, 100:246802, Jun 2008. (Cited on pages 62 and 79.)
- [23] B. A. Bernevig, T. L. Hughes, and S.-C. Zhang. Quantum spin hall effect and topological phase transition in hgte quantum wells. *Science*, 314(5806):1757–1761, 2006. (Cited on pages xii, 33, 34, 38 and 39.)
- [24] B. A. Bernevig and N. Regnault. Emergent many-body translational symmetries of abelian and non-abelian fractionally filled topological insulators. *Phys. Rev. B*, 85:075128, Feb 2012. (Cited on pages xiii, xv, 69 and 123.)

- [25] B. A. Bernevig and N. Regnault. Emergent many-body translational symmetries of abelian and non-abelian fractionally filled topological insulators. *Phys. Rev. B*, 85:075128, Feb 2012. (Cited on pages 105 and 116.)
- [26] B. A. Bernevig and N. Regnault. Thin-Torus Limit of Fractional Topological Insulators. *ArXiv e-prints*, Apr. 2012. (Cited on pages 74, 108 and 120.)
- [27] P. Bonderson, A. E. Feiguin, and C. Nayak. Numerical calculation of the neutral fermion gap at the $\nu = 5/2$ fractional quantum hall state. *Phys. Rev. Lett.*, 106:186802, May 2011. (Cited on page 89.)
- [28] P. Bonderson, V. Gurarie, and C. Nayak. Plasma analogy and non-abelian statistics for ising-type quantum hall states. *Phys. Rev. B*, 83:075303, Feb 2011. (Cited on page 58.)
- [29] A. Cappelli, L. S. Georgiev, and I. T. Todorov. A Unified Conformal Field Theory Description of Paired Quantum Hall States. *Communications in Mathematical Physics*, 205:657–689, 1999. (Cited on page 54.)
- [30] A. Cappelli, L. S. Georgiev, and I. T. Todorov. Parafermion Hall states from coset projections of abelian conformal theories. *Nuclear Physics B*, 599:499–530, Apr. 2001. (Cited on pages xiv, 54 and 81.)
- [31] C. Chamon and C. Mudry. Magnetic translation algebra with or without magnetic field in the continuum or on arbitrary bravais lattices in any dimension. *Phys. Rev. B*, 86:195125, Nov 2012. (Cited on page 92.)
- [32] C.-Z. Chang, J. Zhang, X. Feng, J. Shen, Z. Zhang, M. Guo, K. Li, Y. Ou, P. Wei, L.-L. Wang, et al. Experimental observation of the quantum anomalous hall effect in a magnetic topological insulator. *Science*, 340(6129):167–170, 2013. (Cited on pages xii and 15.)
- [33] C.-Z. Chang, J. Zhang, X. Feng, J. Shen, Z. Zhang, M. Guo, K. Li, Y. Ou, P. Wei, L.-L. Wang, Z.-Q. Ji, Y. Feng, S. Ji, X. Chen, J. Jia, X. Dai, Z. Fang, S.-C. Zhang, K. He, Y. Wang, L. Lu, X.-C. Ma, and Q.-K. Xue. Experimental observation of the quantum anomalous hall effect in a magnetic topological insulator. *Science*, 340(6129):167–170, 2013. (Cited on page 26.)
- [34] J. G. Checkelsky, R. Yoshimi, A. Tsukazaki, K. S. Takahashi, Y. Kozuka, J. Falson, M. Kawasaki, and Y. Tokura. Trajectory of the anomalous Hall effect towards the quantized state in a ferromagnetic topological insulator. *Nature Physics*, 10:731–736, Oct. 2014. (Cited on page 26.)
- [35] S. Coh and D. Vanderbilt. Electric polarization in a chern insulator. *Phys. Rev. Lett.*, 102:107603, Mar 2009. (Cited on page 125.)
- [36] J. Dalibard. Introduction to the physics of artificial gauge fields. *ArXiv e-prints*, Apr. 2015. (Cited on page 64.)

- [37] J. Dalibard, F. Gerbier, G. Juzeliūnas, and P. Öhberg. *Colloquium* : Artificial gauge potentials for neutral atoms. *Rev. Mod. Phys.*, 83:1523–1543, Nov 2011. (Cited on page 27.)
- [38] R. de-Picciotto, M. Reznikov, M. Heiblum, V. Umansky, G. Bunin, and D. Mahalu. Direct observation of a fractional charge. *Physica B Condensed Matter*, 249:395–400, June 1998. (Cited on page 51.)
- [39] F. Delahaye, T. J. Witt, B. Jeckelmann, and B. Jeanneret. Comparison of quantum hall effect resistance standards of the ofmet and the bipm. *Metrologia*, 32(5):385, 1995. (Cited on page 3.)
- [40] P. Di Francesco, M. Pierre, and S. D. In *Conformal field theory*, Graduate Texts in Contemporary Physics. Springer-Verlag New York, 1997. (Cited on page 57.)
- [41] E. Dobardžić, M. V. Milovanović, and N. Regnault. Geometrical description of fractional chern insulators based on static structure factor calculations. *Phys. Rev. B*, 88:115117, Sep 2013. (Cited on page 104.)
- [42] B. Estienne and B. A. Bernevig. Spin-singlet quantum hall states and jack polynomials with a prescribed symmetry. *Nuclear Physics, Section B*, 857(2):185–206, 2012. (Cited on page 128.)
- [43] G. Fano, F. Ortolani, and E. Colombo. Configuration-interaction calculations on the fractional quantum hall effect. *Phys. Rev. B*, 34:2670–2680, Aug 1986. (Cited on page 48.)
- [44] M. Fremling, T. H. Hansson, and J. Suorsa. Hall viscosity of hierarchical quantum hall states. *Phys. Rev. B*, 89:125303, Mar 2014. (Cited on page 83.)
- [45] S. FUBINI and C. LÜTKEN. Vertex operators in the fractional quantum hall effect. *Modern Physics Letters A*, 06(06):487–500, 1991. (Cited on page 57.)
- [46] S. Furukawa and M. Ueda. Global phase diagram of two-component Bose gases in antiparallel magnetic fields. *Phys. Rev. A*, 90(3):033602, Sept. 2014. (Cited on pages 150 and 156.)
- [47] S. Geraedts, M. P. Zaletel, Z. Papić, and R. S. K. Mong. Competing Abelian and non-Abelian topological orders in $\nu = 1/3 + 1/3$ quantum Hall bilayers. *ArXiv e-prints*, Feb. 2015. (Cited on page xiv.)
- [48] S. M. Girvin and A. H. MacDonald. Off-diagonal long-range order, oblique confinement, and the fractional quantum hall effect. *Phys. Rev. Lett.*, 58:1252–1255, Mar 1987. (Cited on page 56.)
- [49] S. M. Girvin, A. H. MacDonald, and P. M. Platzman. Collective-excitation gap in the fractional quantum hall effect. *Phys. Rev. Lett.*, 54:581–583, Feb 1985. (Cited on pages xiv, 88 and 97.)

- [50] S. M. Girvin, A. H. MacDonald, and P. M. Platzman. Magneto-roton theory of collective excitations in the fractional quantum hall effect. *Phys. Rev. B*, 33:2481–2494, Feb 1986. (Cited on pages [xiv](#), [11](#), [88](#) and [97](#).)
- [51] A. Gómez-León, P. Delplace, and G. Platero. Engineering anomalous quantum hall plateaus and antichiral states with ac fields. *Phys. Rev. B*, 89:205408, May 2014. (Cited on page [27](#).)
- [52] M. Greiter, X. Wen, and F. Wilczek. Paired hall states. *Nuclear Physics B*, 374(3):567–614, 1992. (Cited on page [53](#).)
- [53] M. Greiter, X.-G. Wen, and F. Wilczek. Paired hall state at half filling. *Physical review letters*, 66(24):3205, 1991. (Cited on page [53](#).)
- [54] Z. Gu, H. A. Fertig, D. P. Arovas, and A. Auerbach. Floquet spectrum and transport through an irradiated graphene ribbon. *Phys. Rev. Lett.*, 107:216601, Nov 2011. (Cited on page [27](#).)
- [55] V. Gurarie and C. Nayak. A plasma analogy and berry matrices for non-abelian quantum hall states. *Nuclear Physics B*, 506(3):685 – 694, 1997. (Cited on pages [56](#) and [58](#).)
- [56] F. Haldane. “fractional statistics” in arbitrary dimensions: A generalization of the pauli principle. *Phys. Rev. Lett.*, 67:937–940, Aug 1991. (Cited on page [62](#).)
- [57] F. D. M. Haldane. Fractional quantization of the hall effect: A hierarchy of incompressible quantum fluid states. *Phys. Rev. Lett.*, 51:605–608, Aug 1983. (Cited on pages [44](#), [48](#), [51](#) and [77](#).)
- [58] F. D. M. Haldane. Many-particle translational symmetries of two-dimensional electrons at rational landau-level filling. *Phys. Rev. Lett.*, 55:2095–2098, Nov 1985. (Cited on page [59](#).)
- [59] F. D. M. Haldane. Many-particle translational symmetries of two-dimensional electrons at rational landau-level filling. *Phys. Rev. Lett.*, 55:2095–2098, Nov 1985. (Cited on page [91](#).)
- [60] F. D. M. Haldane. Model for a quantum Hall effect without Landau levels: Condensed-matter realization of the “parity anomaly”. *Phys. Rev. Lett.*, 61:2015–2018, Oct. 1988. (Cited on pages [xii](#), [15](#), [21](#), [31](#), [66](#) and [104](#).)
- [61] F. D. M. Haldane and E. H. Rezayi. Finite-size studies of the incompressible state of the fractionally quantized hall effect and its excitations. *Phys. Rev. Lett.*, 54:237–240, Jan 1985. (Cited on page [48](#).)
- [62] F. D. M. Haldane and E. H. Rezayi. Spin-singlet wave function for the half-integral quantum hall effect. *Phys. Rev. Lett.*, 60:956–959, Mar 1988. (Cited on page [53](#).)

- [63] E. H. Hall. On a new action of the magnet on electric currents. *American Journal of Mathematics*, 2(3):pp. 287–292, 1879. (Cited on page 2.)
- [64] B. I. Halperin. Theory of the quantized hall conductance. *Helv. Phys. Acta*, 56(1-3):75, 1983. (Cited on pages 51, 127 and 154.)
- [65] B. I. Halperin. Statistics of quasiparticles and the hierarchy of fractional quantized hall states. *Phys. Rev. Lett.*, 52:1583–1586, Apr 1984. (Cited on pages 51 and 56.)
- [66] B. I. Halperin, P. A. Lee, and N. Read. Theory of the half-filled landau level. *Phys. Rev. B*, 47:7312–7343, Mar 1993. (Cited on page 53.)
- [67] M. Haque, O. Zozulya, and K. Schoutens. Entanglement entropy in fermionic laughlin states. *Phys. Rev. Lett.*, 98:060401, Feb 2007. (Cited on page 72.)
- [68] Y.-C. He, S. Bhattacharjee, R. Moessner, and F. Pollmann. Bosonic Integer Quantum Hall effect in an interacting lattice model. *ArXiv e-prints*, June 2015. (Cited on page 160.)
- [69] M. Hermanns. Composite fermion states on the torus. *Phys. Rev. B*, 87:235128, Jun 2013. (Cited on pages 83 and 99.)
- [70] F. L. Hernandez-Marquez, M. E. Bierzychudek, G. R. Jones, and R. E. Elmquist. Precision high-value resistance scaling with a two-terminal cryogenic current comparator. *Review of Scientific Instruments*, 85(4):–, 2014. (Cited on page 3.)
- [71] X. Hu, M. Kargarian, and G. A. Fiete. Topological insulators and fractional quantum hall effect on the ruby lattice. *Phys. Rev. B*, 84:155116, Oct 2011. (Cited on pages 66, 104, 121 and 122.)
- [72] J. K. Jain. Composite-fermion approach for the fractional quantum hall effect. *Phys. Rev. Lett.*, 63:199–202, Jul 1989. (Cited on pages 83 and 99.)
- [73] J. K. Jain. Incompressible quantum hall states. *Phys. Rev. B*, 40:8079–8082, Oct 1989. (Cited on page 51.)
- [74] D. Jaksch and P. Zoller. Creation of effective magnetic fields in optical lattices: the hofstadter butterfly for cold neutral atoms. *New Journal of Physics*, 5(1):56, 2003. (Cited on page 27.)
- [75] B. Jeckelmann and B. Jeanneret. The quantum hall effect as an electrical resistance standard. *Reports on Progress in Physics*, 64(12):1603, 2001. (Cited on page 3.)
- [76] G. Jotzu, M. Messer, R. Desbuquois, M. Lebrat, T. Uehlinger, D. Greif, and T. Esslinger. Experimental realization of the topological Haldane model with ultracold fermions. *Nature*, 515:237–240, Nov. 2014. (Cited on pages 15 and 27.)

- [77] C. L. Kane and E. J. Mele. Quantum spin hall effect in graphene. *Phys. Rev. Lett.*, 95:226801, Nov 2005. (Cited on pages [xii](#) and [33](#).)
- [78] C. L. Kane and E. J. Mele. Z_2 topological order and the quantum spin hall effect. *Phys. Rev. Lett.*, 95:146802, Sep 2005. (Cited on page [33](#).)
- [79] A. Kitaev. Fault-tolerant quantum computation by anyons. *Annals of Physics*, 303(1):2 – 30, 2003. (Cited on pages [xiii](#) and [57](#).)
- [80] A. Kitaev. Periodic table for topological insulators and superconductors. *AIP Conference Proceedings*, 1134(1):22–30, 2009. (Cited on pages [xii](#) and [41](#).)
- [81] A. Kitaev and J. Preskill. Topological entanglement entropy. *Phys. Rev. Lett.*, 96:110404, Mar 2006. (Cited on page [71](#).)
- [82] T. Kitagawa, T. Oka, A. Brataas, L. Fu, and E. Demler. Transport properties of nonequilibrium systems under the application of light: Photoinduced quantum hall insulators without landau levels. *Phys. Rev. B*, 84:235108, Dec 2011. (Cited on page [27](#).)
- [83] K. v. Klitzing, G. Dorda, and M. Pepper. New method for high-accuracy determination of the fine-structure constant based on quantized hall resistance. *Phys. Rev. Lett.*, 45:494–497, Aug 1980. (Cited on pages [xi](#), [3](#) and [50](#).)
- [84] M. König, H. Buhmann, L. W. Molenkamp, T. Hughes, C.-X. Liu, X.-L. Qi, and S.-C. Zhang. The quantum spin hall effect: Theory and experiment. *Journal of the Physical Society of Japan*, 77(3):031007, 2008. (Cited on pages [xii](#), [33](#), [35](#), [36](#) and [38](#).)
- [85] M. König, S. Wiedmann, C. Brüne, A. Roth, H. Buhmann, L. W. Molenkamp, X.-L. Qi, and S.-C. Zhang. Quantum spin hall insulator state in hgte quantum wells. *Science*, 318(5851):766–770, 2007. (Cited on pages [xii](#) and [33](#).)
- [86] X. Kou, S.-T. Guo, Y. Fan, L. Pan, M. Lang, Y. Jiang, Q. Shao, T. Nie, K. Murata, J. Tang, Y. Wang, L. He, T.-K. Lee, W.-L. Lee, and K. L. Wang. Scale-invariant quantum anomalous hall effect in magnetic topological insulators beyond the two-dimensional limit. *Phys. Rev. Lett.*, 113:137201, Sep 2014. (Cited on page [26](#).)
- [87] X. Kou, L. Pan, J. Wang, Y. Fan, E. S. Choi, W.-L. Lee, T. Nie, K. Murata, Q. Shao, S.-C. Zhang, and K. L. Wang. Mapping the global phase diagram of quantum anomalous Hall effect. *ArXiv e-prints*, Mar. 2015. (Cited on pages [26](#) and [27](#).)
- [88] S. Kourtis, T. Neupert, C. Chamon, and C. Mudry. Fractional chern insulators with strong interactions that far exceed band gaps. *Phys. Rev. Lett.*, 112:126806, Mar 2014. (Cited on page [67](#).)

- [89] A. M. Läuchli, Z. Liu, E. J. Bergholtz, and R. Moessner. Hierarchy of fractional chern insulators and competing compressible states. *Phys. Rev. Lett.*, 111:126802, Sep 2013. (Cited on pages [xv](#), [108](#), [118](#) and [123](#).)
- [90] R. Laughlin. Elementary theory: the incompressible quantum fluid. In R. Prange and S. Girvin, editors, *The Quantum Hall Effect*, Graduate Texts in Contemporary Physics, pages 233–301. Springer US, 1987. (Cited on page [56](#).)
- [91] R. B. Laughlin. Anomalous quantum hall effect: An incompressible quantum fluid with fractionally charged excitations. *Phys. Rev. Lett.*, 50:1395–1398, May 1983. (Cited on page [46](#).)
- [92] C. H. Lee, R. Thomale, and X.-L. Qi. Pseudopotential formalism for fractional Chern insulators. *Phys. Rev. B*, 88(3):035101, July 2013. (Cited on pages [64](#) and [122](#).)
- [93] J. Leinaas and J. Myrheim. On the theory of identical particles. *Il Nuovo Cimento B Series 11*, 37(1):1–23, 1977. (Cited on page [55](#).)
- [94] M. Levin and A. Stern. Fractional topological insulators. *Phys. Rev. Lett.*, 103:196803, Nov 2009. (Cited on pages [138](#) and [160](#).)
- [95] M. Levin and A. Stern. Classification and analysis of two-dimensional abelian fractional topological insulators. *Phys. Rev. B*, 86:115131, Sep 2012. (Cited on pages [138](#) and [160](#).)
- [96] M. Levin and X.-G. Wen. Detecting topological order in a ground state wave function. *Phys. Rev. Lett.*, 96:110405, Mar 2006. (Cited on page [71](#).)
- [97] H. Li and F. D. M. Haldane. Entanglement spectrum as a generalization of entanglement entropy: Identification of topological order in non-abelian fractional quantum hall effect states. *Phys. Rev. Lett.*, 101:010504, 2008. (Cited on pages [xv](#), [72](#) and [73](#).)
- [98] T. Liu, C. Repellin, B. A. Bernevig, and N. Regnault. Fractional chern insulators beyond laughlin states. *Phys. Rev. B*, 87:205136, May 2013. (Cited on pages [xv](#), [xvi](#), [104](#), [117](#), [118](#), [122](#) and [123](#).)
- [99] Z. Liu, A. Vaezi, K. Lee, and E.-A. Kim. Non-Abelian phases in two-component $\nu = 2/3$ fractional quantum Hall states: Emergence of Fibonacci anyons. *ArXiv e-prints*, Feb. 2015. (Cited on page [xiv](#).)
- [100] A. Lopez and E. Fradkin. Fractional quantum hall effect and chern-simons gauge theories. *Phys. Rev. B*, 44:5246–5262, Sep 1991. (Cited on page [56](#).)
- [101] H. Min, J. E. Hill, N. A. Sinitsyn, B. R. Sahu, L. Kleinman, and A. H. MacDonald. Intrinsic and rashba spin-orbit interactions in graphene sheets. *Phys. Rev. B*, 74:165310, Oct 2006. (Cited on page [33](#).)

- [102] H. Miyake, G. A. Siviloglou, C. J. Kennedy, W. C. Burton, and W. Ketterle. Realizing the harper hamiltonian with laser-assisted tunneling in optical lattices. *Phys. Rev. Lett.*, 111:185302, Oct 2013. (Cited on pages 15 and 27.)
- [103] G. Möller, A. Wójs, and N. R. Cooper. Neutral fermion excitations in the moore-read state at filling factor $\nu = 5/2$. *Phys. Rev. Lett.*, 107:036803, Jul 2011. (Cited on pages 89, 90 and 97.)
- [104] R. S. K. Mong, M. P. Zaletel, F. Pollmann, and Z. Papić. Fibonacci anyons and charge density order in the 12/5 and 13/5 plateaus. *ArXiv e-prints*, May 2015. (Cited on page 54.)
- [105] G. Moore and N. Read. Nonabelions in the fractional quantum hall effect. *Nuclear Physics B*, 360(2–3):362 – 396, 1991. (Cited on pages 53 and 57.)
- [106] G. Moore and N. Seiberg. Classical and quantum conformal field theory. *Communications in Mathematical Physics*, 123(2):177–254, 1989. (Cited on page 57.)
- [107] N. Moran, A. Sterdyniak, I. Vidanović, N. Regnault, and M. V. Milovanović. Topological d -wave pairing structures in jain states. *Phys. Rev. B*, 85:245307, Jun 2012. (Cited on page 155.)
- [108] G. Murthy and R. Shankar. Composite Fermions for Fractionally Filled Chern Bands. *ArXiv e-prints*, Aug. 2011. (Cited on pages 68 and 123.)
- [109] G. Murthy and R. Shankar. Hamiltonian theory of fractionally filled chern bands. *Phys. Rev. B*, 86:195146, Nov 2012. (Cited on pages 92 and 123.)
- [110] T. Neupert, L. Santos, C. Chamon, and C. Mudry. Fractional quantum hall states at zero magnetic field. *Phys. Rev. Lett.*, 106:236804, Jun 2011. (Cited on pages xiii, 68 and 116.)
- [111] Q. Niu, D. J. Thouless, and Y.-S. Wu. Quantized hall conductance as a topological invariant. *Phys. Rev. B*, 31:3372–3377, Mar 1985. (Cited on page 17.)
- [112] K. Nomura and D. Yoshioka. Gap evolution in $\hat{I}_{\frac{1}{2}}=1/2$ bilayer quantum hall systems. *Journal of the Physical Society of Japan*, 73(10):2612–2615, 2004. (Cited on page xiv.)
- [113] T. Oka and H. Aoki. Photovoltaic hall effect in graphene. *Phys. Rev. B*, 79:081406, Feb 2009. (Cited on page 27.)
- [114] M. Oshikawa, Y. B. Kim, K. Shtengel, C. Nayak, and S. Tewari. Topological degeneracy of non-abelian states for dummies. *Annals of Physics*, 322(6):1477 – 1498, 2007. (Cited on page 61.)
- [115] M. Oshikawa and T. Senthil. Fractionalization, topological order, and quasi-particle statistics. *Phys. Rev. Lett.*, 96:060601, Feb 2006. (Cited on pages 61 and 62.)

- [116] K. Pakrouski, M. R. Peterson, T. Jolicoeur, V. W. Scarola, C. Nayak, and M. Troyer. Phase diagram of the $\nu = 5/2$ fractional quantum hall effect: Effects of landau-level mixing and nonzero width. *Phys. Rev. X*, 5:021004, Apr 2015. (Cited on page 54.)
- [117] W. Pan, J.-S. Xia, V. Shvarts, D. E. Adams, H. L. Stormer, D. C. Tsui, L. N. Pfeiffer, K. W. Baldwin, and K. W. West. Exact quantization of the even-denominator fractional quantum hall state at $\nu = 5/2$ landau level filling factor. *Phys. Rev. Lett.*, 83:3530–3533, Oct 1999. (Cited on page 53.)
- [118] Z. Papić. Solvable models for unitary and nonunitary topological phases. *Phys. Rev. B*, 90(7):075304, Aug. 2014. (Cited on page 81.)
- [119] Z. Papić, M. O. Goerbig, N. Regnault, and M. V. Milovanović. Tunneling-driven breakdown of the 331 state and the emergent pfaffian and composite fermi liquid phases. *Phys. Rev. B*, 82:075302, Aug 2010. (Cited on page xiv.)
- [120] Z. Papić, F. D. M. Haldane, and E. H. Rezayi. Quantum phase transitions and the $\nu = 5/2$ fractional hall state in wide quantum wells. *Phys. Rev. Lett.*, 109:266806, Dec 2012. (Cited on pages 54 and 94.)
- [121] S. A. Parameswaran, R. Roy, and S. L. Sondhi. Fractional chern insulators and the W_∞ algebra. *Phys. Rev. B*, 85:241308, Jun 2012. (Cited on pages 64 and 68.)
- [122] S. A. Parameswaran, R. Roy, and S. L. Sondhi. Fractional quantum Hall physics in topological flat bands. *Comptes Rendus Physique*, 14:816–839, Nov. 2013. (Cited on page 68.)
- [123] M. R. Peterson, Y.-L. Wu, M. Cheng, M. Barkeshli, Z. Wang, and S. Das Sarma. Abelian and Non-Abelian States in $\nu = 2/3$ Bilayer Fractional Quantum Hall Systems. *ArXiv e-prints*, Feb. 2015. (Cited on page xiv.)
- [124] W. Poirier and F. Schopfer. Resistance metrology based on the quantum hall effect. *The European Physical Journal Special Topics*, 172(1):207–245, 2009. (Cited on page 3.)
- [125] E. Prodan and F. D. M. Haldane. Mapping the braiding properties of the moore-read state. *Phys. Rev. B*, 80:115121, Sep 2009. (Cited on page 58.)
- [126] X.-L. Qi. Generic wave-function description of fractional quantum anomalous hall states and fractional topological insulators. *Phys. Rev. Lett.*, 107:126803, Sep 2011. (Cited on page 125.)
- [127] N. Read. Non-abelian adiabatic statistics and hall viscosity in quantum hall states and $p_x + ip_y$ paired superfluids. *Phys. Rev. B*, 79:045308, Jan 2009. (Cited on pages 56 and 58.)

- [128] N. Read and D. Green. Paired states of fermions in two dimensions with breaking of parity and time-reversal symmetries and the fractional quantum hall effect. *Phys. Rev. B*, 61:10267–10297, Apr 2000. (Cited on page [xiv](#).)
- [129] N. Read and E. Rezayi. Beyond paired quantum Hall states: Parafermions and incompressible states in the first excited Landau level. *Phys. Rev. B*, 59:8084–8092, Mar. 1999. (Cited on page [54](#).)
- [130] N. Read and E. H. Rezayi. Hall viscosity, orbital spin, and geometry: Paired superfluids and quantum hall systems. *Phys. Rev. B*, 84:085316, Aug 2011. (Cited on page [48](#).)
- [131] N. Regnault and B. A. Bernevig. Fractional chern insulator. *Phys. Rev. X*, 1:021014, Dec 2011. (Cited on pages [xiii](#), [68](#), [108](#) and [116](#).)
- [132] N. Regnault and T. Jolicoeur. Quantum hall fractions in rotating bose-einstein condensates. *Phys. Rev. Lett.*, 91:030402, Jul 2003. (Cited on page [92](#).)
- [133] N. Regnault and T. Jolicoeur. Quantum hall fractions for spinless bosons. *Phys. Rev. B*, 69:235309, Jun 2004. (Cited on page [92](#).)
- [134] J. W. Reijnders, F. J. M. van Lankvelt, K. Schoutens, and N. Read. Quantum hall states and boson triplet condensate for rotating spin-1 bosons. *Phys. Rev. Lett.*, 89:120401, Aug 2002. (Cited on page [128](#).)
- [135] J. W. Reijnders, F. J. M. van Lankvelt, K. Schoutens, and N. Read. Rotating spin-1 bosons in the lowest landau level. *Phys. Rev. A*, 69:023612, Feb 2004. (Cited on page [128](#).)
- [136] C. Repellin, B. A. Bernevig, and N. Regnault. F_2 fractional topological insulators in two dimensions. *Phys. Rev. B*, 90:245401, Dec 2014. (Cited on pages [xvi](#), [104](#), [108](#) and [118](#).)
- [137] C. Repellin, T. Neupert, B. A. Bernevig, and N. Regnault. Projective construction of the \mathbb{Z}_k Read-Rezayi fractional quantum Hall states and their excitations on the torus geometry. *ArXiv e-prints*, Apr. 2015. (Cited on pages [xv](#), [xvi](#), [84](#) and [87](#).)
- [138] C. Repellin, T. Neupert, Z. Papić, and N. Regnault. Single-mode approximation for fractional chern insulators and the fractional quantum hall effect on the torus. *Phys. Rev. B*, 90:045114, Jul 2014. (Cited on pages [xiv](#), [xvi](#) and [93](#).)
- [139] E. Rezayi, X.-G. Wen, and N. Read. Condensation of fractional excitons, non-Abelian states in double-layer quantum Hall systems and \mathbb{Z}_4 parafermions. *ArXiv e-prints*, July 2010. (Cited on page [xiv](#).)
- [140] E. H. Rezayi and F. D. M. Haldane. Incompressible paired hall state, stripe order, and the composite fermion liquid phase in half-filled landau levels. *Phys. Rev. Lett.*, 84:4685–4688, May 2000. (Cited on page [53](#).)

- [141] E. H. Rezayi and S. H. Simon. Breaking of particle-hole symmetry by Landau level mixing in the $\nu = 5/2$ quantized Hall state. *Phys. Rev. Lett.*, 106:116801, Mar 2011. (Cited on page 54.)
- [142] I. D. Rodriguez, A. Sterdyniak, M. Hermanns, J. K. Slingerland, and N. Regnault. Quasiparticles and excitons for the Pfaffian quantum Hall state. *Phys. Rev. B*, 85:035128, Jan 2012. (Cited on pages 89, 97 and 99.)
- [143] B. Roy, Z.-X. Hu, and K. Yang. Theory of unconventional quantum Hall effect in strained graphene. *Phys. Rev. B*, 87(12):121408, Mar. 2013. (Cited on page 156.)
- [144] L. Saminadayar, D. C. Glattli, Y. Jin, and B. Etienne. Observation of the $e/3$ fractionally charged Laughlin quasiparticle. *Phys. Rev. Lett.*, 79:2526–2529, Sep 1997. (Cited on page 51.)
- [145] A. P. Schnyder, S. Ryu, A. Furusaki, and A. W. W. Ludwig. Classification of topological insulators and superconductors in three spatial dimensions. *Phys. Rev. B*, 78:195125, Nov 2008. (Cited on pages xii and 41.)
- [146] D. N. Sheng, Z.-C. Gu, K. Sun, and L. Sheng. Fractional quantum Hall effect in the absence of Landau levels. *Nat Commun*, 2:389, Feb 2011. (Cited on pages xiii, 68, 116 and 122.)
- [147] S. H. Simon. Effect of Landau level mixing on braiding statistics. *Phys. Rev. Lett.*, 100:116803, Mar 2008. (Cited on page 56.)
- [148] S. H. Simon, E. H. Rezayi, N. R. Cooper, and I. Berdnikov. Construction of a paired wave function for spinless electrons at filling fraction $\nu = \frac{2}{5}$. *Phys. Rev. B*, 75:075317, Feb 2007. (Cited on page 120.)
- [149] M. Srednicki. Entropy and area. *Phys. Rev. Lett.*, 71:666–669, Aug 1993. (Cited on page 71.)
- [150] G. J. Sreejith, C. Tóke, A. Wójs, and J. K. Jain. Bipartite composite fermion states. *Phys. Rev. Lett.*, 107:086806, Aug 2011. (Cited on pages 89, 97 and 99.)
- [151] G. J. Sreejith, A. Wójs, and J. K. Jain. Unpaired composite fermion, topological exciton, and zero mode. *Phys. Rev. Lett.*, 107:136802, Sep 2011. (Cited on pages 89, 97 and 99.)
- [152] A. Sterdyniak, B. A. Bernevig, N. R. Cooper, and N. Regnault. Interacting bosons in topological optical flux lattices. *Phys. Rev. B*, 91:035115, Jan 2015. (Cited on page xv.)
- [153] A. Sterdyniak, N. Regnault, and B. A. Bernevig. Extracting excitations from model state entanglement. *Phys. Rev. Lett.*, 106(10):100405, Mar 2011. (Cited on pages xv, 72 and 73.)

- [154] A. Sterdyniak, C. Repellin, B. A. Bernevig, and N. Regnault. Series of Abelian and non-Abelian states in $C > 1$ fractional Chern insulators. *Phys. Rev. B*, 87(20):205137, May 2013. (Cited on pages [xv](#), [xvi](#) and [136](#).)
- [155] H. L. Stormer. Nobel lecture: The fractional quantum hall effect. *Rev. Mod. Phys.*, 71:875–889, Jul 1999. (Cited on page [43](#).)
- [156] E. Tang, J.-W. Mei, and X.-G. Wen. High-temperature fractional quantum hall states. *Phys. Rev. Lett.*, 106:236802, Jun 2011. (Cited on pages [66](#), [104](#), [126](#) and [138](#).)
- [157] J. C. Y. Teo, T. L. Hughes, and E. Fradkin. Theory of Twist Liquids: Gauging an Anyonic Symmetry. *ArXiv e-prints*, Mar. 2015. (Cited on page [83](#).)
- [158] D. J. Thouless, M. Kohmoto, M. P. Nightingale, and M. den Nijs. Quantized hall conductance in a two-dimensional periodic potential. *Phys. Rev. Lett.*, 49:405–408, Aug 1982. (Cited on pages [14](#) and [17](#).)
- [159] M. Trescher and E. J. Bergholtz. Flat bands with higher chern number in pyrochlore slabs. *Phys. Rev. B*, 86:241111, Dec 2012. (Cited on page [126](#).)
- [160] S. A. Trugman and S. Kivelson. Exact results for the fractional quantum hall effect with general interactions. *Phys. Rev. B*, 31:5280–5284, Apr 1985. (Cited on page [46](#).)
- [161] Y. Tserkovnyak and S. H. Simon. Monte carlo evaluation of non-abelian statistics. *Phys. Rev. Lett.*, 90:016802, Jan 2003. (Cited on page [58](#).)
- [162] D. C. Tsui, H. L. Stormer, and A. C. Gossard. Two-dimensional magneto-transport in the extreme quantum limit. *Phys. Rev. Lett.*, 48:1559–1562, May 1982. (Cited on pages [xi](#) and [42](#).)
- [163] A. Vaezi and M. Barkeshli. Fibonacci Anyons From Abelian Bilayer Quantum Hall States. *Phys. Rev. Lett.*, 113(23):236804, Dec. 2014. (Cited on page [xiv](#).)
- [164] K. von Klitzing. The quantized hall effect. *Reviews of Modern Physics*, 58(3):519–531, 1986. (Cited on page [4](#).)
- [165] H. Wang, D. N. Sheng, and F. D. M. Haldane. Particle-hole symmetry breaking and the $\nu = \frac{5}{2}$ fractional quantum hall effect. *Phys. Rev. B*, 80:241311, Dec 2009. (Cited on page [54](#).)
- [166] Y.-F. Wang, H. Yao, Z.-C. Gu, C.-D. Gong, and D. N. Sheng. Non-abelian quantum hall effect in topological flat bands. *Phys. Rev. Lett.*, 108:126805, Mar 2012. (Cited on pages [xiii](#) and [116](#).)
- [167] X. G. Wen and Q. Niu. Ground-state degeneracy of the fractional quantum hall states in the presence of a random potential and on high-genus riemann surfaces. *Phys. Rev. B*, 41:9377–9396, May 1990. (Cited on page [62](#).)

- [168] F. Wilczek. Magnetic flux, angular momentum, and statistics. *Phys. Rev. Lett.*, 48:1144–1146, Apr 1982. (Cited on page 55.)
- [169] R. Willett, J. P. Eisenstein, H. L. Störmer, D. C. Tsui, A. C. Gossard, and J. H. English. Observation of an even-denominator quantum number in the fractional quantum hall effect. *Phys. Rev. Lett.*, 59:1776–1779, Oct 1987. (Cited on page 53.)
- [170] R. L. Willett, C. Nayak, K. Shtengel, L. N. Pfeiffer, and K. W. West. Magnetic-field-tuned aharonov-bohm oscillations and evidence for non-abelian anyons at $\nu = 5/2$. *Phys. Rev. Lett.*, 111:186401, Oct 2013. (Cited on page 58.)
- [171] Y.-H. Wu and J. K. Jain. Quantum Hall effect of two-component bosons at fractional and integral fillings. *Phys. Rev. B*, 87(24):245123, June 2013. (Cited on page 155.)
- [172] Y.-L. Wu, B. A. Bernevig, and N. Regnault. Zoology of fractional chern insulators. *Phys. Rev. B*, 85:075116, Feb 2012. (Cited on pages 22, 64, 68, 116, 122, 138 and 139.)
- [173] Y.-L. Wu, B. Estienne, N. Regnault, and B. A. Bernevig. Braiding non-abelian quasiholes in fractional quantum hall states. *Phys. Rev. Lett.*, 113:116801, Sep 2014. (Cited on page 58.)
- [174] Y.-L. Wu, N. Regnault, and B. A. Bernevig. Bloch Model Wave Functions and Pseudopotentials for All Fractional Chern Insulators. *Phys. Rev. Lett.*, 110(10):106802, Mar. 2013. (Cited on pages xv and 64.)
- [175] Y.-L. Wu, N. Regnault, and B. A. Bernevig. Bloch model wave functions and pseudopotentials for all fractional chern insulators. *Phys. Rev. Lett.*, 110:106802, Mar 2013. (Cited on pages 110 and 136.)
- [176] Y.-L. Wu, N. Regnault, and B. A. Bernevig. Haldane statistics for fractional chern insulators with an arbitrary chern number. *Phys. Rev. B*, 89:155113, Apr 2014. (Cited on pages xv and 136.)
- [177] J. S. Xia, W. Pan, C. L. Vicente, E. D. Adams, N. S. Sullivan, H. L. Stormer, D. C. Tsui, L. N. Pfeiffer, K. W. Baldwin, and K. W. West. Electron correlation in the second landau level: A competition between many nearly degenerate quantum phases. *Phys. Rev. Lett.*, 93:176809, Oct 2004. (Cited on page 54.)
- [178] B. Yang, Z.-X. Hu, Z. Papić, and F. D. M. Haldane. Model wave functions for the collective modes and the magnetoroton theory of the fractional quantum hall effect. *Phys. Rev. Lett.*, 108:256807, Jun 2012. (Cited on pages 88, 89 and 91.)

- [179] Y. Yao, F. Ye, X.-L. Qi, S.-C. Zhang, and Z. Fang. Spin-orbit gap of graphene: First-principles calculations. *Phys. Rev. B*, 75:041401, Jan 2007. (Cited on page [33](#).)
- [180] R. Yu, X. L. Qi, A. Bernevig, Z. Fang, and X. Dai. Equivalent expression of F_2 topological invariant for band insulators using the non-abelian berry connection. *Phys. Rev. B*, 84:075119, Aug 2011. (Cited on page [142](#).)
- [181] S. C. Zhang, T. H. Hansson, and S. Kivelson. Effective-field-theory model for the fractional quantum hall effect. *Phys. Rev. Lett.*, 62:82–85, Jan 1989. (Cited on page [56](#).)
- [182] W. Zhu, S. S. Gong, F. D. M. Haldane, and D. N. Sheng. The Fractional Quantum Hall States at $\nu = 13/5$ and $12/5$ and their Non-Abelian Nature. *ArXiv e-prints*, May 2015. (Cited on page [54](#).)
- [183] W. Zhu, S. S. Gong, D. N. Sheng, and L. Sheng. Emergence of Non-Abelian Moore-Read state in double-layer bosonic Fractional quantum Hall system. *ArXiv e-prints*, Feb. 2015. (Cited on page [xiv](#).)
- [184] W. Zhu, S. S. Gong, D. N. Sheng, and L. Sheng. Possible non-Abelian Moore-Read state in double-layer bosonic fractional quantum Hall system. *Phys. Rev. B*, 91(24):245126, June 2015. (Cited on page [155](#).)
- [185] O. S. Zozulya, M. Haque, K. Schoutens, and E. H. Rezayi. Bipartite entanglement entropy in fractional quantum hall states. *Phys. Rev. B*, 76:125310, Sep 2007. (Cited on page [72](#).)